Josephson junctions in superconducting coplanar DC bias cavities
Fundamental studies and applications

Schmidt, F.E.

DOI
10.4233/uuid:d8dd6f55-d4f8-4f3e-bc15-09c324ea0860

Publication date
2020

Document Version
Final published version

Citation (APA)
Schmidt, F. E. (2020). *Josephson junctions in superconducting coplanar DC bias cavities: Fundamental studies and applications*. [Dissertation (TU Delft), Delft University of Technology]. https://doi.org/10.4233/uuid:d8dd6f55-d4f8-4f3e-bc15-09c324ea0860

Josephson junctions in superconducting coplanar DC bias cavities

Fundamental studies and applications

Josephson junctions in superconducting coplanar DC bias cavities

Fundamental studies and applications

Dissertation

for the purpose of obtaining the degree of doctor
at Delft University of Technology
by the authority of the Rector Magnificus, prof. dr. ir. T. H. J. J. van der Hagen
chair of the Board for Doctorates
to be defended publicly on
Friday 28 August 2020 at 12:30h

by

Felix Erik Schmidt

Master of Science Nanostructure Technology,
Julius-Maximilians-Universität Würzburg,
born in Cologne, Germany

This dissertation has been approved by the promotors.

Composition of the doctoral committee:

Rector Magnificus,	chairperson
Prof. Dr. G. A. Steele,	Delft University of Technology, promotor
Dr. A. Akhmerov,	Delft University of Technology, promotor
Independent members:	
Prof. Dr. C. Schönenberger,	University of Basel, Switzerland
Prof. Dr. P. Hakonen,	Aalto University, Finland
Prof. Dr. Y. Blanter,	Delft University of Technology
Dr. J. Prance,	Lancaster University, United Kingdom
Dr. T. van der Sar,	Delft University of Technology
Reserve member:	
Prof. Dr. H. S. J. van der Zant,	Delft University of Technology

Keywords: Graphene, Josephson junctions, Josephson inductance, superconducting microwave circuits, current detection, DC bias.

Printed by: Gildeprint.

Cover: Schematic circuit layout for the base layer of a shunt capacitor DC bias cavity.

Casimir PhD Series, Delft-Leiden 2020-15

ISBN 978-90-8593-442-4

An electronic version of this dissertation is available at
https://repository.tudelft.nl/.

Für Katrin und Felicitas

Remember, kids, the only difference between screwing around and science is writing it down.

Adam Savage, quoting Alex Jason in the 2012 MythBusters episode *Titanic Survival* [1]

Contents

Summary

This thesis investigates fundamental properties of Josephson junctions embedded in microwave circuits, and an application arising from this hybrid approach. We used the versatility of superconducting coplanar DC bias cavities to extract previously inaccessible information on phase coherent and subgap mechanisms of graphene Josephson junctions.

Chapter 1 gives an introduction to the technology of Josephson field effect transistors, among which graphene junctions show promise for future improvements in quantum computation. Together with an overview of the Josephson effect in superconducting-semiconducting systems, we introduce the concept of coplanar DC bias cavities for probing Josephson junctions at gigahertz frequencies.

In chapter 2, we describe the experimental methods developed for carrying out the subsequent measurements. We include details on fabrication, material properties and measurement setup.

Results of graphene Josephson junctions embedded in DC bias microwave resonators are presented in chapters 3 and 4. By following the resonance frequency and losses of the circuit, we are able to extract the junctions' Josephson inductance and subgap resistance. Studying the nonlinear power and bias current response reveals further information on the underlying loss mechanisms and current phase relation.

We turn to an application of our hybrid bias cavity – Josephson junction devices to detect small, low-frequency currents in chapter 5. Our device is competitive with state-of-the-art techniques for microwave radiation detection and, with minor modifications, should be able to outperform existing technologies by orders of magnitude.

Finally, we conclude the presented work in chapter 6 and provide an outlook on potential future research.

Samenvatting

Dit proefschrift onderzoekt fundamentele eigenschappen van Josephson-juncties ingebed in microgolf circuits en een toepassing die voortkomt uit deze hybride methode. We gebruikten de veelzijdigheid van supergeleidende coplanaire DC-bias-holtes om eerder ontoegankelijke informatie over fase coherente en subgap-mechanismen van grafeen Josephson-juncties af te leiden.

Hoofdstuk 1 geeft een inleiding tot de technologie van onder meer Josephson veldeffecttransistors wiens grafeen juncties veelbelovend zijn voor toekomstige verbeteringen in kwantum computers. Samen met een overzicht van het Josephson-effect in supergeleidende halfgeleidende systemen, introduceren we het concept van coplanaire DC-biasholtes voor het onderzoeken van Josephson-juncties bij gigahertz-frequenties.

In hoofdstuk 2 beschrijven we de experimentele methoden die ontwikkeld zijn voor het uitvoeren van deze metingen. We nemen details op over fabricage, materiaaleigenschappen en meetopstellingen.

De resultaten van grafeen Josephson-juncties ingebed in DC-bias microgolfresonatoren worden gepresenteerd in hoofdstukken 3 en 4. Door de resonantiefrequentie en verliezen van het circuit te meten, zijn we in staat om de Josephson-inductie en subgap-weerstand van de kruispunten af te leiden. Het bestuderen van de niet-lineaire kracht en biasstroming onthult meer informatie over de onderliggende verlies mechanismen en huidige fase relatie.

We wenden ons naar een toepassing van onze hybride bias-holte - Josephson-junctie-apparaten om kleine, laagfrequente stromen te detecteren in hoofdstuk 5. Ons apparaat concurreert met de allernieuwste technieken voor microgolfstralingdetectie en zouden, met kleine aanpassingen, in staat moeten zijn om de bestaande technologieën te overtreffen met een orde van grootte.

Ten slotte sluiten we het gepresenteerde werk in hoofdstuk 6 af en geven een kijk op potentieel toekomstig onderzoek.

Zusammenfassung

In dieser Dissertation untersuchen wir grundlegende Eigenschaften von in Mikrowellenschaltkreisen eingebetteten Josephson-Kontakten, sowie eine Anwendung, die aus diesem hybriden Ansatz folgt. Wir nutzten die Vielseitigkeit von supraleitenden koplanaren Gleichstromresonatoren um bisher nicht zugängliche Information über Phasenkohärente und Subgapwiderstände von Graphen Josephsonkontakten zu extrahieren.

Kapitel 1 beinhaltet eine Einleitung in die Technologie der Josephson-Feldeffekttransistoren, unter denen unter anderem Graphen vielversprechende Ansätze für zukünftige Verbesserungen für Quantencomputer zeigt. Gemeinsam mit einem Überblick über den Josephsoneffekt in supra-halbleitenden Systemen, legen wir einen Überblick auf koplanare Gleichstromresonatoren für die Untersuchung von Graphenkontakten bei Frequenzen im Gigahertzbereich.

In Kapitel 2 beschreiben wir die experimentellen Methoden, welche wir für die Durchführung der folgenden Experimente entwickelten. Dies beinhaltet Details zur Probenherstellung, Materialeigenschaften und dem Messaufbau.

Wir präsentieren Ergebnisse von in Gleichstrommikrowellenresonatoren eingebetteten Graphen Josephsonkontakten in Kapiteln 3 und 4. Durch Messung der Resonanzfrequenz und Verluste des Schaltkreises konnten wir die Josephsoninduktivität und den Subbandlückenwiderstand quantifizieren. Weitere Hintergründe der zugrunde liegenden Mechanismen der Mikrowellenverluste und der Strom-Phasenbeziehung konnten durch Analyse der nichtlinearen Leistungs- und Stromabhängigkeit des Schwingkreises gezogen werden.

Im Gegensatz zu den vorangegangenen grundlegenden Untersuchungen beschäftigen wir uns in Kapitel 5 mit der Anwendung der Kombination aus Gleichsstrombiasresonator und Josephsonkontakt zur Detektion kleiner, niedrigfrequenter Ströme. Unser Gerät ist mit den neuesten Techniken zur Detektion von Mikrowellenstrahlung konkurrenzfähig und sollte mit geringfügigen Änderungen in der Lage sein, vorhandene Technologien um Größenordnungen zu übertreffen.

Abschließend schließen wir die vorgestellte Arbeit in Kapitel 6 ab und geben einen Ausblick auf mögliche zukünftige Forschungen.

1

Introduction

1

1.1. COMPUTING WITH SEMI- AND SUPERCONDUCTING CIRCUITS

The invention of the metal oxide semiconductor field-effect transistor (MOSFET, see Fig. 1.1(a)) laid the ground for the information age, in large parts shaping the world to be what we know it as today. Pushed by continuous advances in material sciences, solid state physics and electrical engineering, the MOSFET is now the building block of all commercial computers. Owing largely to the success of scalability from integrated circuits, today's state-of-the-art microprocessors can host more than 39.54 billion transistors on a single chip, with physical dimensions down to a few tens of nanometers, see Fig. 1.1(b) [2]. With the increasing transistor density and shrinking physical dimensions came however the realization, that alternative computation architectures to the one based on semiconducting transistors might be needed to satisfy society's desire for computation power, as there might be a limit to how dense logic circuits could be packed with current technology. The slowing of Moore's law, originally predicting the doubling of transistor chip density every two years [3], is an important reminder of this challenge.

Already before the invention of the MOSFET, circuits on the basis of superconducting switches called "cryotrons" were envisioned as a competitive alternative to semiconducting computers [4, 5]. The discovery of Josephson junctions (JJs), weak links between two superconductors, depicted in Fig. 1.1(e), in 1962 [6, 7] spured additional interest due to the possibility of sensing extremely small magnetic fields, their low power consumption and high switching speeds [8]. In parallel to the development of MOSFETs, Josephson junctions were hence envisioned as building blocks for superconducting logic circuits, with IBM being one of the main drivers at the time [9]. In an attempt to combine the best of two worlds, the versatility of a high gain transistor, and the low dissipation of superconducting circuits, proposals were made in the 1980s to merge these two elements into the Josephson field effect transistor (JoFET), see Fig. 1.1(c) [10, 11].

While IBM eventually ceased to research Josephson junction computation due to an apparent supremacy of semiconducting computers [12], research continued at public institutions and universities, in part driven by Richard Feynman's ideas of building quantum machines to run complex calculations much more efficiently than any classical, MOSFET-based, computer [13]. The late twentieth century then saw the birth of first prototypes for a quantum computing architecture, and it was realized that Josephson junctions could form the basis of quantum bits [14]. Since then, global tech companies like IBM, Google, Microsoft and Intel are all heavily invested in this architecture, each following a slightly different path [15–18]. Superconducting quantum processors based on Josephson junctions embedded in microwave (MW) circuits, as pursued by IBM and Google, have culminated in the milestone of "quantum supremacy", i.e. the threshold at which a quantum processor can execute an algorithm that would be prohibitively costly in terms of computing time and money for a classical computer to perform [16]. As a side note, we would like to point out that the usefulness of Google's supremacy experiment, while still an impressive experimental achievement, is challenged and criticized by the IBM team [19].

Figure 1.1(f) shows an image of Google's "quantum supremacy" processor *Sycamore*. The building block of these processors are transmon qubits. These consist of a coplanar capacitance in series with superconducting quantum interference devices (SQUIDs), formed by two Josephson junctions in a loop. To tune the states of the transmons, magnetic flux is threaded through the SQUID loop, supplied via on-chip current bias lines in close proximity to the SQUIDs. While coherence times of several hundreds of microseconds show great potential

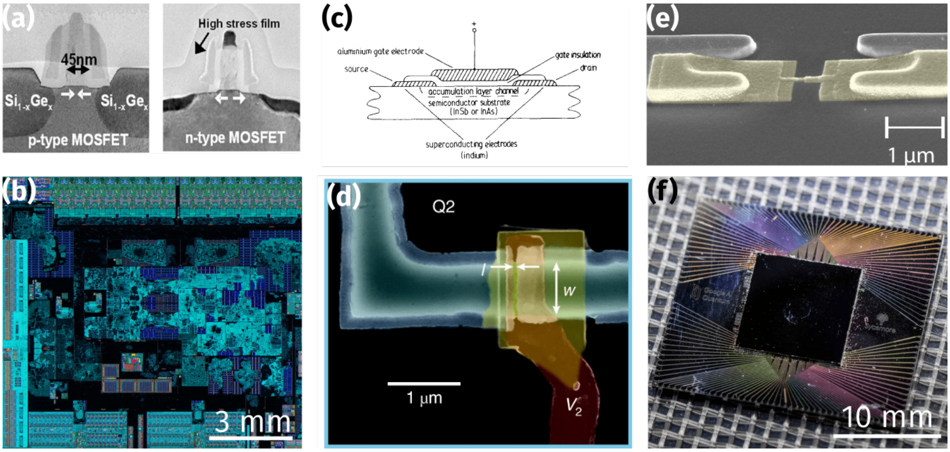

Figure 1.1: Semi- and superconducting based computing devices. (a) Cross-sectional TEM image of 45 nm node MOSFETs, the building block of semiconducting computers. Figure adapted from [24]. **(b)** Die shot of part of the I/O die of the microprocessor with currently highest number of transistors, in this case with 14 nm node: The *AMD Epyc Rome* with 8.34 billion transistors on the I/O die and 39.54 billion in total. Figure adapted from [25]. **(c)** Sketch of the first envisioned JoFET as hybrid between semiconducting transistors and superconducting Josephson junctions. Figure adapted from [10]. **(d)** SEM of a gatemon qubit, a potential building block for quantum computing on a hybrid super-semi approach. Figure adapted from [22]. **(e)** SEM of an aluminum oxide Josephson junction, the workhorse of state-of-the-art superconducting microwave quantum computing. Figure adapted from [26]. **(f)** Optical image of Google's "quantum supremacy" 53 qubit *Sycamore* quantum processor. Figure adapted from [27].

for future devices [20], standard transmons come with a few drawbacks: Already the very first implementation of a two-qubit transmon processor showed that magnetic fields can lead to significant cross talk coupling qubits several centimeters apart from each other [21]. Additionally, since the chips need to be operated at temperatures only fractions of a Kelvin above absolute zero in order to protect their coherence from thermal excitations, the cooling power of the refrigerator must not be exceeded. This can be problematic with high qubit numbers, since the Joule heating caused by the tuning current through all individual flux lines might exceed the cooling power. As the number of physical qubits increases, so does the challenge of shielding individual qubits from each other's bias lines, and retaining enough cooling power as to not induce thermal effects.

In contrast, replacing SQUIDs with the long-abandoned JoFET might be beneficial: Applying gate voltages instead of running a current through a wire does not lead to thermal dissipation, which removes the cooling power constraint. Additionally, cross-talk can be significantly reduced due to the nature of electric fields in gate capacitors being strongly confined to a small volume around the gate voltage lead. Finally, JoFETs have consistently performed well under application of in-plane magnetic fields. While the latter are not strictly necessary in transmon qubits (rather to be avoided) flux noise is one of the limiting factors of SQUIDs, to which JoFET-based qubits would be insensitive [22]. Even more important, magnetic field-compatible JoFETs are one of the requirements of qubits based on the Majorana architecture, which could result in significantly more coherent qubits due to their intrinsic topological protection [23].

As of now, there has been only very little research in integrating JoFETs in superconducting quantum computing. Recently, semiconductor nanowires and epitaxial 2DEGs were incorporated in transmon qubits, resulting in so-called "gatemons", see Fig. 1.1(d) [22, 28–31]. While coherence times are not yet at the same level as for standard transmons, gatemons show great promise and have gained significant interest in the scientific community. They not only provide a new way of controlling qubits [32], but also a path towards studying unconventional superconducting weak links at high frequencies [33].

In this thesis, we initially set out to explore how JoFETs based on graphene Josephson junctions (gJJs) could perform in superconducting microwave circuits. Since its discovery in 2004, graphene has shown versatile field effect applications and, already since very early on, gate-tunable superconductivity [34, 35]. With improvements in contact engineering and reduced film disorder, induced superconductivity in gJJs has been a testbed for Andreev physics, phase coherent mechanisms, quantum phase transitions and the interplay of superconductivity and magnetism [36]. Integrating gJJs in microwave circuits would thus be a first step towards the realization of gate-tunable superconducting microwave logic circuits. In order to retain information about the device's DC properties, and to directly link them to the microwave performance, we chose to combine both DC and MW in one device. To this end, we based our circuits on an architecture that allows simultaneous signal probing both with low and high frequencies: DC bias microwave cavities [37]. This not only allows for a detailed study of the junction's properties, but also enables applications based on current-biasing the sample.

1.2. JOSEPHSON EFFECTS IN SNS SYSTEMS

Josephson junctions are formed by a weak link between two superconducting electrodes, which must be sufficiently weak to sustain a phase difference $\delta = \phi_1 - \phi_2$ between the phases of the two electrodes, ϕ_1 and ϕ_2, respectively. Perhaps the simplest case of a JJ is a thin insulating tunnel barrier between two superconductors, the SIS JJ, see Fig. 1.2(a). Here, Cooper pairs can tunnel from one superconductor through the barrier to the other side, while acquiring a phase δ. The current flowing across this type of junction is given by the junction's current phase relation (CPR), which for an SIS JJ reads

$$I_{\mathrm{J}}^{\mathrm{SIS}}(\delta) = I_{\mathrm{c}} \sin \delta \,, \tag{1.1}$$

with the critical current I_{c}.

The situation is different in the case in which the weak link consists of a normal metal between two superconducting banks, an SNS junction. To support a supercurrent, the length of the normal metal must be smaller than the coherence length in the normal region, $L_{\mathrm{N}} < \xi_{\mathrm{N}}$, which in fact is much longer than the maximum thickness of the insulating barrier in the case of an SIS junction, where the thickness has to be smaller than the superconducting coherence length, $t \ll \xi_{\mathrm{S}}$ [38, 39]. The process of Andreev reflection at the interface between superconductors and normal metals lays the basis for understanding how an SNS junction works [40]. The process is sketched in Fig. 1.2(b): an electron impinging onto the super-normal interface from inside the normal region can only enter the superconductor in the form of a Cooper pair by being reflected as a hole with opposite spin and momentum. Vice versa, a Cooper pair travelling towards the normal region will decay into an electron travelling forward, and annihilate a hole travelling backwards with spin opposite to that of the electron. Inside the normal region, this will result in the formation of the so-called Andreev bound states (ABS) and a net

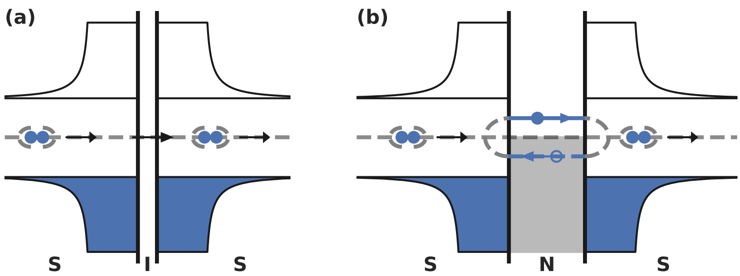

Figure 1.2: Cooper pair transport in SIS and SNS Josephson junctions. The density of states in a superconductor exhibits a gap of width 2Δ in energy around the Fermi level ϵ_F, with states below ϵ_F filled and states above unoccupied. **(a)** In an SIS Josephson junction, Cooper pairs, consisting of an electron and hole with opposite spins and momentum, can tunnel through a thin insulating barrier separating two superconducting banks. There are no states inside the insulating region. **(b)** In an SNS Josephson junction, the normal region exhibits a DOS that is filled up to ϵ_F. Unpaired electrons can enter the superconductor by Andreev reflection as a hole with opposite momentum. Conversely, Cooper pairs can enter the normal region by breaking into an electron and hole of opposite spin and momentum. This way, Andreev bound states form within the normal region and a net current flows across the junction.

current across the JJ.

The current-phase relation in SNS junctions takes on a significantly different form than the sinusoidal one in SIS junctions: For the simplest case of a one-dimensional SNS junction with perfect contact transparency $\tau_c = 1$ at the SN interface, each Andreev bound state has a ground state energy

$$E_i^{\mathrm{ABS}} = -\Delta\sqrt{1 - T_i \sin^2(\delta/2)} \tag{1.2}$$

with the gap energy in the superconducting regions Δ and channel transparency T_i, where T_i takes into account scattering inside the normal region [41, 42]. Scattering at the SN interface, i.e. $\tau_c < 1$, is not taken into account here in this simplified picture, as there is no closed analytical expression [40]. The energy of the excited ABS has opposite sign. Summing over all channels in the junction, the total Josephson potential is given by

$$U_J(\delta) = \Delta - \sum_i E_i^{\mathrm{ABS}} \approx E_J \frac{\delta^2}{2} - E_J \left(1 - \frac{3\sum T_i^2}{4\sum T_i}\right)\frac{\delta^4}{24} + \mathcal{O}(\delta^6) \tag{1.3}$$

where we Taylor-expanded Eq. 1.2 [43]. In the limit of low T_i, i.e. for an SIS junction, the energy would be given simply by $U_J^{\mathrm{SIS}}(\delta)/E_J = 1 - \cos(\delta) \approx \delta^2/2 - \delta^4/24$. Compared to the SIS case, we therefore find that the Josephson energy is reduced by a fraction depending on the channel transparency which will become important for gatemon qubits, see Ref. [43] and Chapter 4. We plot the ground and excited state energies of the ABS in Fig. 1.3(a). With increasing channel transmission, U_J exhibits stronger modulation and a closing band gap at $\delta = \pi$ with minimum separation $2\Delta\sqrt{1-\tau}$.

The corresponding relation between Josephson current and the respective phase drop

1

across the one-dimensional SNS JJ is

$$I_{\mathrm{J}}(\delta) = \frac{2e}{\hbar}\frac{\partial U_{\mathrm{J}}}{\partial \delta} = \frac{e\Delta}{2\hbar}\sum_i \frac{T_i \sin(\delta)}{\sqrt{1 - T_i \sin^2(\delta/2)}} \tag{1.4}$$

In addition, we can see that the JJ behaves as a strong nonlinear inductor, with inductance

$$\begin{aligned} L_{\mathrm{J}}(\delta) &= \frac{\hbar}{2e}\left(\frac{\partial I_{\mathrm{J}}}{\partial \delta}\right)^{-1} = \left(\frac{\hbar}{2e}\right)^2 \left(\frac{\partial^2 U_{\mathrm{J}}}{\partial \delta^2}\right)^{-1} \\ &= \frac{4\hbar^2}{e^2\Delta}\sum_i \frac{\left(1 - T_i \sin^2(\delta/2)\right)^{3/2}}{4T_i \cos(\delta)\left(1 - T_i \sin^2(\delta/2)\right) + T_i^2 \sin^2(\delta)}\,. \end{aligned} \tag{1.5}$$

Both quantities are depicted in Fig. 1.3(b,c). We can conclude two things: First, the larger the channel transmission, the stronger the forward skew of the current phase relation, defined as deviation of the CPR maximum from phase $\pi/2$, $S = 2\delta_{\max}/\pi - 1$, and corresponding deviation to the SIS case. Second, while also strongly nonlinear, the Josephson inductance of SNS junctions is significantly reduced compared to the SIS case, $L_{\mathrm{J}}^{\mathrm{SIS}}(\delta) = \hbar/(2eI_{\mathrm{c}}\cos\delta)$. On the other hand, for junctions where I_{c} remains constant, the increase in forward skew leads to a decrease in $\partial I_{\mathrm{J}}/\partial\delta$, and hence an increase in L_J around zero phase. After an inflection point at $\delta \approx 0.3\pi$, the SIS inductance is larger than the one at finite transmission, $L_{\mathrm{J}}^{\mathrm{SIS}} > L_{\mathrm{J}}(\tau)$. This is shown in Fig. 1.3(d,e). Since exact knowledge of the Josephson inductance is critical for operating transmon qubits, these deviations need to be investigated for future applications.

For a realistic SNS junction such as the two-dimensional graphene devices measured in this thesis, there are a number of effects that lead to deviations of the above presented mechanisms. The exact nature of the subgap density of states for example depends on size and geometry of the junction, as well as the contact transparency. If the junction is sufficiently wide such that the transport is no longer strictly one-dimensional, the ABS energy is reduced and moves closer to zero. The same holds for the case of long compared to short junctions, see Fig. 1.4: This can be understood qualitatively by an effective energy $E_{\mathrm{Th}^*} = \hbar v_{\mathrm{F}}/\Lambda < \Delta$ governing transport inside the junction, analogously to the Thouless energy [39, 44], with an effective length scale $\Lambda = L_{\mathrm{N}}/\tau$ and the Fermi velocity v_{F}. This quantity translates the dwell time of ABS inside the normal region to an energy which is responsible for the reduced effective superconducting gap and replaces Δ as the dominating energy scale [45]. Essentially, the longer the ABS spend in the normal region (either due to small v_{F} or large L_{N}), the stronger the reduction of the induced superconducting gap. In the case of a wide junction, i.e. two-dimensional transport, a transverse Thouless energy $E_{\mathrm{Th}^*}^{\|} = \hbar v_{\mathrm{F}}/\Lambda_{\|}$ with $\Lambda_{\|} = W_{\mathrm{N}}/\tau$ needs to be introduced. We can use these to discriminate between long/short and narrow/wide junctions: For a short JJ ($\xi > L_{\mathrm{N}}$), the induced gap is roughly given by the bulk gap of the superconducting leads, while for a long JJ ($\xi > L_{\mathrm{N}}$), the induced gap is given by the Thouless energy. In the direction parallel to the SN interface, if the junction is narrow ($\xi > W_{\mathrm{N}}$), the induced gap is given by the induced gap of the long/short case, while in a wide JJ ($\xi < W_{\mathrm{N}}$), the induced gap is influenced and reduced by $E_{\mathrm{Th}^*}^{\|}$. Finally, reduced contact transparency $\tau_{\mathrm{c}} < 1$ at the SN interface leads to the ABS detaching from the bulk gap at Δ even for zero phase difference [46].

Figure 1.4 shows the calculated subgap density of states (DOS) for a exemplary graphene Josephson junction in the short and long regime, i.e. $L_{\mathrm{N}} \ll \xi$ and $L_{\mathrm{N}} > \xi$. We find that for

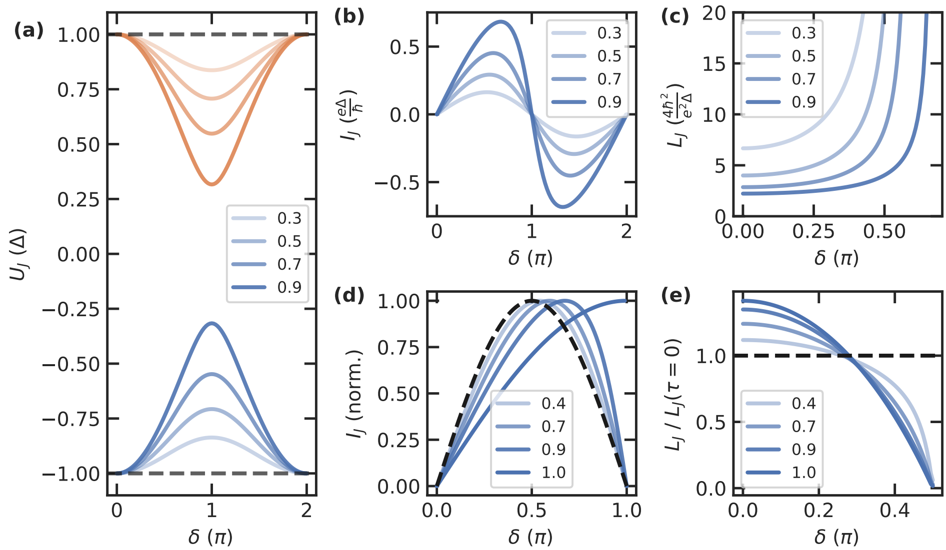

Figure 1.3: Channel transmission and nonsinusoidality. **(a)** Josephson energy of the ground (blue) and excited (orange) Andreev bound state for varying channel transmission τ as a function of phase drop across the Josephson junction. Increasing color intensity corresponds to increasing τ. Dashed line indicates the bulk gap $\pm\Delta$. **(b)** Josephson current for varying τ. Increasing transmission increases both amplitude and forward skewing of the CPR. **(c)** Josephson inductance as a function of phase. Due to the increased CPR slope for increasing τ around $\delta = 0$, the Josephson inductance decreases significantly. **(d)** Same as in **(b)**, but for constant critical current, hence only the forward skew increases. Dashed line: CPR of an SIS junction. **(e)** Josephson inductance as a function of transmission under the assumption of constant critical current as in **(d)**, compared to the case of an SIS junction (dashed line). Around zero phase, L_J increases with τ, while for large phase bias, the inductance of an SIS JJ is in fact larger than the one of a junction with finite transmission.

both cases the states with lowest energies are located at large parallel momentum $k_{\parallel}$, and that for the long junction, there are a number of subgap states below the bulk gap energy Δ. This significantly reduced gap can potentially absorb RF excitations, leading to dissipation and decoherence in microwave circuits. Finally, graphene shows strong angle-dependent transport due to Klein-tunneling at interfaces, which collimates charge carrier transport perpendicular to interfaces at pn junctions, which can further modify the DOS [47].

In order to build reliable, reproducible circuits out of SNS junctions, it is thus vital to characterize them not only in the DC, but also in the microwave regime, as this is where the inductance will be measurable. To this end, we placed our junctions in a circuit allowing for steady and high frequency signals to probe our device. These DC bias microwave circuits are described in the following section.

1.3. DC BIAS CAVITIES FOR PROBING JOSEPHSON JUNCTIONS

To probe the Josephson inductance, we make use of superconducting microwave resonators based on coplanar waveguides [48, 49]. These have been used extensively in the field of parti-

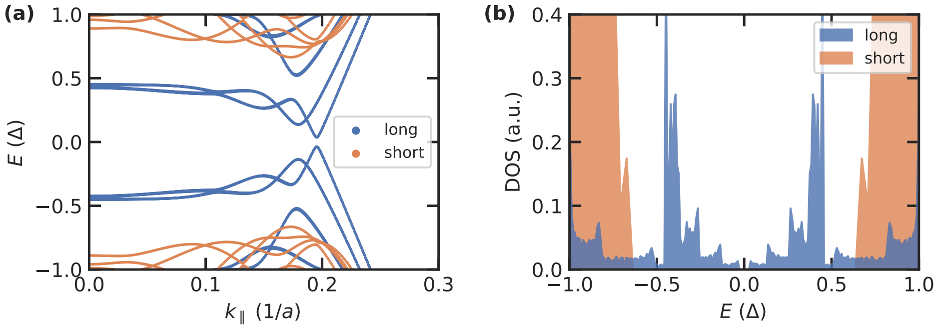

Figure 1.4: Realistic subgap states of a 2D graphene Josephson junction. Tight-binding simulations of a graphene Josephson junction show strong dependence of the subgap state energies on momentum parallel to the SN interface **(a)**, with lowest lying energies at large $k_\parallel$. While the short JJ (orange) shows an only slightly reduced minimum energy and DOS **(b)** compared to Δ, long junctions (blue) exhibit heavily reduced energy gaps.

cle detection and circuit (quantum) electrodynamics due to their intrinsic low loss originating from the fact that Cooper Pairs do not contribute any electrical resistance [50–53]. For probing the device under test both in the low and high frequency range (DC to several 10^9 Hz), our circuits need to sustain a stable resonance when biased with direct currents.

There is a variety of circuit architectures capable of this approach, such as using inductive coupling [54], direct leads at voltage nodes of a $\lambda/2$ resonator with matching length [55, 56] or lumped-element split-cavities [57]. In contrast, we based our design on an architecture previously developed in our group: the shunt capacitor DC bias cavity [37]. This circuit has several advantages over the previously mentioned ones: as no circuit symmetries need to be considered, the circuit layout is rather simple. Because the shunt capacitor is placed at the input port to the device, no additional port needs to be used to probe or excite the device under test (DUT), which prevents additional leakage channels. Finally, using a shunt capacitor provides a broadband signal port up to the self-resonance of the shunt capacitor, which is chosen to be well above the resonance frequency of the circuit. The reflection coefficient of this circuit is given by

$$S_{11} = -1 + \frac{2\kappa_\mathrm{e}}{\kappa_\mathrm{e} + \kappa_\mathrm{i} + 2i\Delta} \tag{1.6}$$

with the internal and external loss rates κ_i and κ_e and the detuning $\Delta = \omega - \omega_0$ [37]. In Fig. 1.5 we plot the reflection coefficient for various fractions of $\eta = \kappa_\mathrm{e}/\kappa_\mathrm{i}$, to illustrate the effects of over-, under- and critical coupling ($\eta > 1$, $\eta < 1$ and $\eta = 1$, respectively). For the signal to be strongest in terms of $|S_{11}|$, i.e. the absorption dip reaching zero, the shunt capacitor C_s should be designed such that $\kappa_\mathrm{e} = \kappa_\mathrm{i}$, with the external loss rate approximately given by

$$\kappa_\mathrm{e} = \frac{\omega_0}{Q_e} = \frac{2}{\pi\omega_0 Z_0^2 C_\mathrm{s}^2} \tag{1.7}$$

with external quality factor Q_e and transmission line impedance Z_0. Due to stray inductance of the shunt capacitor, there is an upper limit to the maximum feasible C_s we can use while

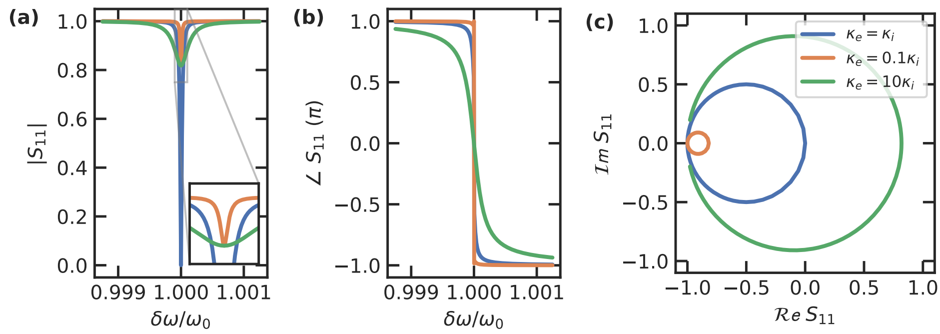

Figure 1.5: Effect of coupling ratio on the reflection coefficient of a DC bias cavity. Using Eq. 1.6, we can model the absolute value **(a)**, phase **(b)** and real and imaginary parts **(c)** of the reflection coefficient of a DC bias cavity. Colors denote the various coupling types: blue: critically coupled $\kappa_e/\kappa_i = 1$, orange: undercoupled $\kappa_e/\kappa_i = 0.1$, green: overcoupled $\kappa_e/\kappa_i = 10$. Strongest signal modulation in $|S_{11}|$ is achieved for critical coupling, while the other two cases have an identical minimum reflection coefficient.

keeping the self-resonance of the latter well above ω_0. In practice, this limits Q_e to approximately 100×10^3. However, when placing a JJ at the end of the TL, the internal loss rate can rise significantly. For this reason, we typically design our circuits such that they would be overcoupled in the case of a short to ground instead of a JJ, anticipating a rise in κ_i.

When probing Josephson junctions with the DC bias cavity, we need to calibrate the parameters of the microwave circuit prior to extracting quantitative information on the high frequency properties of the added JJ. Figure 1.6(a) depicts a schematic of the DC bias cavity with the relevant circuit parameters, including a second port to tune the DUT with a gate voltage. We perform the calibration by measuring a combination of open and shorted reference device with the same sample geometry, except with an open or short to ground in place of the JJ. Equipped with these values, we can proceed to study the influence JJ on the microwave circuit. For modeling, we use the open-source tool *Quite Universal Circuit Simulator* (QUCS [58]).

With an added Josephson junction with inductance L_J shorting the TL to ground, and neglecting R_sg and C_J, the shifted resonance frequency can be approximated by

$$\omega_0' = \omega_0 \frac{L_\mathrm{r} + L_\mathrm{J}}{L_\mathrm{r} + 2L_\mathrm{J}} \tag{1.8}$$

where L_r is the lumped TL resonator inductance including geometric and kinetic inductances, see Chapter 4 and Fig. 1.6(b). A complete analytical model of an RSCJ model parametrizing the JJ can be used for calculating junction-induced losses in the form of a subgap resistance, see Chapter 3 and Fig. 1.6. For very small R_sg, the Josephson inductance is effectively short-circuited, so both Q_i and f_0 approach the limit of no JJ. On the other hand, very large R_sg implies an open circuit with no losses other than the ones in the TL resonator, again approaching Q_i of the bare cavity and f_0 shifting the the value due to the added L_J. Intermediate resistance values suppress the resonance entirely. The shift in f_0 for large R_sg shows the frequency shift induced by L_J.

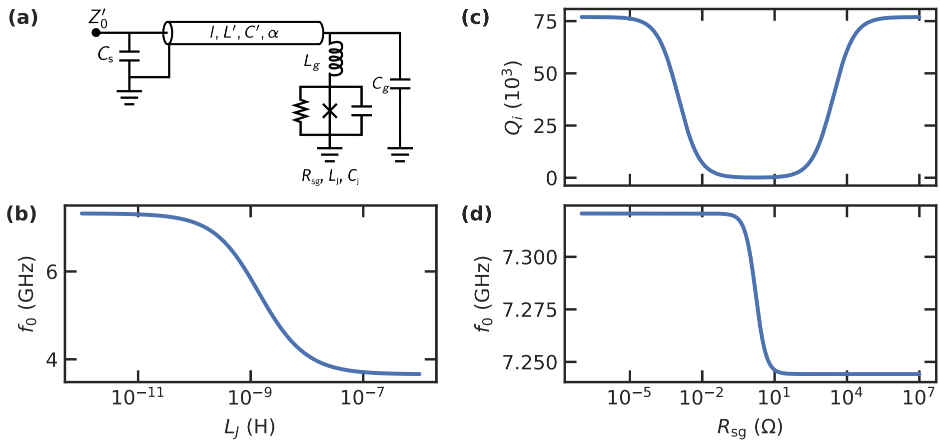

Figure 1.6: DC bias cavity shorted to ground by a parametrized top-gated graphene Josephson junction. **(a)** Fully parametrized circuit model. The transmission line is described by length l, inductance and capacitance per unit length L' and C' and attenuation α, and is coupled to an input impedance Z_0' via a shunt capacitance C_s. The Josephson junction is modeled as a network of linear lead inductance L_g together with an RCSJ model of subgap-resistance R_{sg}, junction capacitance C_J, nonlinear inductance L_J and gate capacitance C_g. In a realistic device (see Fig. 2.4), the gate electrode has capacitances to both the lead L_g and the transmission line. For simplicity, we model C_g as depicted here, and include additional capacitance in C_J. For simulating the device in *QUCS* however, we ignored L_g and C_g and used the following parameters (unless swept): $Z_0 = Z_0' = 50\,\Omega$, $C_s = 60\,\mathrm{pF}$, $l = 6\,\mathrm{mm}/\sqrt{\epsilon_r}$ with the dielectric constant of silicon $\epsilon_r = 11.7$, $\alpha = 1.002$, $L_J = 36\,\mathrm{pH}$, $C_J = 1\,\mathrm{fF}$, $R_{sg} = 1\,\mathrm{M\Omega}$. **(b)** Resonance frequency versus Josephson inductance with the other parameters fixed. Depending on the junction impedance, the fundamental cavity mode changes from $\lambda/2$ (small L_J) to $\lambda/4$ (large L_J). **(c,d)** Influence of subgap resistance on internal quality factor and resonance frequency. Small R_{sg} corresponds to a short, large R_{sg} to an open to ground in parallel to L_J. In both cases, the internal losses of the circuit are dominated by the transmission line attenuation. For intermediate values of R_{sg}, significant resistive damping effectively suppresses the circuit response. Panel **(d)** also illustrates the shift of f_0 when changing the boundary condition of the circuit, similar to the one due to L_J in panel **(b)**.

1.4. OUTLINE

In the following, we will show how DC bias cavities can be utilized to both extract information on the intrinsic microwave properties of a Josephson junction, and use the combination of cavity and junction to detect very small currents.

In chapter 2, we provide an overview on the experimental methods that we developed and used to enable the measurements presented later on. We detail the exfoliation and fabrication of graphene and boron nitride, and the fabrication of gJJs and superconducting CPW resonators. Additionally, a short introduction to the use of the superconducting alloy molybdenum-rhenium in Delft, together with a small study on its pros and cons, is supplied. The chapter closes with a brief introduction to thermal noise and the fridge wiring used to suppress the former during measurements.

In chapter 3, we present the first measurements of a graphene Josephson junction in the microwave regime. Motivated by the potential use of graphene in superconducting quantum circuits, we studied the Josephson inductance by tracking the resonance frequency, and extracted the subgap resistance from the added circuit losses of the JJ. Together with a detailed circuit characterization in both DC and the microwave regime, the results indicate that graphene Josephson junctions are indeed a feasible platform for circuit quantum electrodynamics.

In chapter 4, we take a closer look at the underlying mechanism governing the Josephson inductance of graphene Josephson junctions, i.e. their current-phase relation. Using the power and current bias dependence of our devices, we show that the CPR of diffusive and ballistic devices is forward-skewed, as is expected for these junctions. We quantify the resulting correction of the Josephson energy potential, which is crucial for the use of gJJs in microwave quantum circuits.

We switch from pure fundamental studies of the junction's characteristics to a circuit application in chapter 5. Instead of a graphene JoFET, we present a DC bias MW cavity coupled to an aluminum constriction Josephson junction, a so-called Dayem bridge [59]. Making use of the responsivity of the circuit's resonance frequency to bias current, we detect low-frequency currents with a minimum sensitivity of $8.9\,\mathrm{pA\,Hz^{-1/2}}$, comparable to state-of-the-art devices. With an analytical circuit model, we extrapolate orders of magnitude better values for improved device designs based on our circuit, which could eventually enable quantum limited current detection.

We close with a summary of all presented results and a possible way onwards in chapter 6. Appended to this thesis is a collection of additional DC data on graphene Josephson junctions and SQUIDs. There, we investigate features in the IV curves that occur as a result of the junction interacting with its electromagnetic environment: Fiske and Shapiro steps. The appendix additionally features tips and tricks for electron beam lithography, such as alignment and height measurements, specifications on the self-assembled low-pass and copper powder filters and miscellaneous source code.

2

Experimental methods

A significant, if not the major portion of an experimental physics thesis consists of the countless hours being spent on the (sometimes seemingless never ending) loop of device fabrication and device measurement. This chapter serves to give an insight into the methods and techniques being used to assemble functioning devices, together with a few tips and tricks that might be of use to other experimenters. While the backbone of this thesis was the use of the Kavli Nanolab Delft cleanroom, one of the biggest academic cleanrooms on the European continent, and all measurement presented in this thesis were performed in state-of-the-art dry dilution refridgerators, the methods are nonetheless extendable to smaller-scale laboratories.

The recipes and procedures regarding graphene heterostructures are based on extensive prior work of the group of Dr. Srijit Goswami at QuTech, TU Delft, and were further developed in close collaboration with Dr. Nikos Papadopoulos [60]. Recipes on DC bias cavities were developed together with Dr. Mark Jenkins. Fabrication was carried out in the Kavli Nanolab cleanroom of TU Delft.

2

2.1. DEVICE FABRICATION

2.1.1. THE ART OF MAKING ENCAPSULATED GRAPHENE DEVICES

Fabrication of graphene Josephson junctions is a tedious process: in contrast to integrated circuits, where the active materials are homogeneously deposited over an entire substrate, which enables massive parallel processing, the best graphene devices to date are not fabricated using scalable techniques, but rather each device is manually assembled and crafted. This requires significant efforts, since no two devices have the same exact shape, which often results in slightly different properties between devices.

The most promising wafer-scale graphene fabrication is achieved by chemical vapor deposition of single layer graphene on copper foils [61, 62]. However, only recently have such deposited films exhibited sufficiently low defect densities for high quality transport, which would otherwise result in inferior device quality [63, 64]. Additionally, device quality can be reduced by contaminations that are often encountered when transferring the graphene layer from its growth to the final substrate. Finally, even in the cases where transferred graphene itself only exhibits low defect and residue densities, patterning it into the final device shape almost exclusively contaminates it, most often via organic resist residues.

Since single layer graphene (SLG) is really only a single atom thick and thus all electronic transport takes place at its surface, contaminations on either side will result in charge carrier scattering and degrade the device performance. Till this day, the vast majority of devices with highest electronic quality, exhibiting phenomena such as ballistic transport, hydrodynamics, or superconductivity, rely on single layer graphene manually exfoliated from bulk graphite crystals [65–68].

Additionally, it is often required to tune the carrier density in the graphene layer, for which a gate electrode separated by a dielectric is needed. Because of the single-layer nature of graphene, it conforms very well to any surface roughness and is very sensitive to trapped charges in the dielectric layers. Significant efforts were put into removing the substrate entirely, thus freely suspending graphene. This, in conjunction with device annealing to burn off fabrication residues, can result in remarkably high-quality samples [69–75]. However, such devices are highly fragile and fabrication can be tedious [76]. On the other hand, finding an inert dielectric would ease fabrication needs. To this end, Dean *et al.* [77] realized the use of hexagonal Boron Nitride (BN) as the (until now) best dielectric and capping layer for graphene devices, showing vast improvements with respect to device mobility.

Like graphene, BN has a hexagonal lattice, albeit consisting of two sub-lattices of boron and nitride atoms with a lattice mismatch of 1 % to graphene. BN can be exfoliated from bulk crystals to thin insulating films of arbitrary layer number and signifcantly lower surface roughness than any other dielectric, making it a perfect match for graphene encapsulation. The highest quality BN crystals, i.e. the ones exhibiting the lowest charge defect density, are made by high pressure synthesis by Kenji Watanabe and Takashi Taniguchi at the *National Institute for Material Sciences* (NIMS), Japan [78, 79].

As confirmed by atomic force and scanning tunneling microscopy, SLG on BN exhibits significantly lower roughness compared to samples on SiO_2, until then the standard dielectric for graphene devices. In addition, variations in the local density of states of SLG on BN is reduced by a factor ten, while charge fluctuations are suppressed by a factor 100, as compared to SLG directly on SiO_2 [80, 81]. Complete screening of any trapped charges in the dielectric layer is possible with gate electrodes made of graphite instead of conventional metals [82, 83]. BN encapsulation even enables ballistic transport in very high quality CVD graphene devices [63].

Flake transfer procedures have since paved the way for the assembly of so-called van der Waals heterostructures, named so due to the van der Waals forces holding the flakes together. This has allowed for all kinds of exfoliatable crystals to be stacked, which enabled a new method of studying emergent phenomena such as induced spin orbit coupling, ferromagnetism or superconductivity [84, 85]. In this PhD thesis, however, we limit ourselves to the use of only SLG and BN to study induced superconductivity in the SLG. Even so, assembling a heterostructure of BN-G-BN, with subsequent patterning, and deposition of gate metals and dielectrics results in an extensive and long process, with processes varying between most research groups. In the following, we will detail the fabrication procedure used in the course of this thesis that resulted in the best measured devices.

SUBSTRATE CLEANING AND FLAKE EXFOLIATION

All BN-G-BN heterostructures are based on SLG and few-layer BN exfoliated from bulk highly oriented pyrolithic graphite (HOPG) and *NIMS* BN, respectively. Identifying flakes of suitable thickness is done by estimating the layer number and thickness from optical images. For optimal contrast [86], we used silicon substrates with 285 nm of dry chlorinated thermal SiO_2, diced into 6 mm × 6 mm pieces from 4 inch wafers from *NOVA Electronic Materials*. Details on dicing parameters are given in Sec. 2.3.1.

As mentioned earlier, any organic residues that come in contact with graphene will very likely lead to inferior device performance. Specifically, after dicing the chips, they need to be cleaned extensively in order to remove any leftovers from the dicing resist. To this end, diced chips are placed in a teflon holder and transferred through four 50 mL glass beakers filled with acetone, acetone, isopropyl alcohol (isopropanol, IPA) and IPA, each time ultrasonicated for 5 min. The chips can either be blow-dried one by one using high-pressure nitrogen gas, or by rinsing the teflon holder with the chips still on it in three water baths and placing it on a petri dish in an oven. To remove acetone and IPA residues, the chips are ultrasonicated for 5 min in nitric acid and blow-dried after rinsing in water. We found that an additional soft oxygen plasma to functionalize the SiO_2 surface (200 sccm of O_2, 600 W, 2 min, no cage in a *PVA Tepla 300*) just before, i.e. not more than 15 min prior to, flake exfoliation increased flake exfoliation yield, regardless of graphene or BN.

While there already exist fully automized exfoliation-to-heterostructure stations [87], we performed all of the following steps manually. Flake exfoliation is achieved by manually thinning down bulk crystals until micron-sized flakes of only one or two (SLG, BLG) or a few tens of layers (BN) thickness are left on a chip. We estimate that there are as many different ways of flake exfoliation as there are researchers working on this procedure. The procedure that worked best for us concerning BN exfoliation consists of placing individual BN crystallites (approximately a few 100 µm × 100 µm × 100 µm in volume) on a piece of *Scotch* tape *"Magic"* or *Nitto* tape[1], and subsequently folding over said piece of tape numerous times, such that one acquires a closed layer of thin BN crystallites. In the case of graphene, we would peel off a preferably closed film of graphite from a single 1 cm × 1 cm HOPG crystal with a piece of tape, followed by subsequent folding of the piece of tape until we acquired a homogeneous, yet closed film of thin graphite.

Once satisfied with the tape template, we used pre-cut 8 mm × 8 mm pieces of clean tape to peel off crystals from the template and press the side with crystals on the small piece of

[1] Nitto Processing Tape SWT20+ REACH R 280X100, bought from TELTEC GmbH

tape onto a previously cleaned substrate. After having kept pressure applied for approximately 30 s, we transferred the substrate with the tape still on to a hot plate and left the chip sit for 2 min to 5 min. We found highest flake densities for temperatures of 50 °C for *Nitto* and 100 °C for *Magic* tape. Finally, the chip was transferred off the hot plate, left to cool for 1 min and the tape was gently peeled off, while holding the substrate in place with a pair of tweezers. During this process, no further pressure should be applied to the tape as this usually results in lots of tape residues on the chip.

The process of exfoliation turns out to be a tradeoff between getting as many flakes as possible, and getting the lowest tape residues possibles. *Magic* tape has a higher adhesive strength, thus resulting in a higher flake density and predominantly large flakes (i.e. larger than 20 µm × 20 µm) compared to *Nitto* tape. On the other hand, this comes at the cost of more tape residues on both substrate and the individual flakes. Tape residues can lead to enhanced charge carrier scattering of graphene films, thus severely limiting device quality. Additionally, they increase the chance of bubble formation (see below), thus limiting the available sample space. Tape residues can be entirely removed by thermal annealing at 400 °C in an Ar + H_2 atmosphere. However, it proved extremely difficult to pick up or transfer flakes treated in this manner for heterostructure assembly. While we found that annealing at temperatures below 300 °C was still compatible with flake transfer, significantly less tape residues were removed this way. It is thus advisable to omit thermal annealing until the first lithography step and instead settle on a slightly lower exfoliation yield.

Heterostructure assembly

For assembling our BN-G heterostructures, we used the original transfer setup of Castellanos-Gomez *et al.* [88], upgraded with a heater stage capable of fast heating and cooling cycles between room temperature and 200 °C. The stage was additionally equipped with a small center hole to which a pump was attached via tubing. This allowed us to fix the substrates to or from which flakes were transferred via vacuum, avoiding glue residues from commonly used sticky tape which are notorious to remove after high temperatures. Heterostructures were assembled with a modified version of the procedures developed by Pizzocchero *et al.* [89] and Zomer *et al.* [90]. BN-G-BN structures are formed by repeated pick-and-place of SLG and few-layer BN (flake thickness between 10 nm to 50 nm). The process makes use of the change in viscoelasticity of an adhesive film on top of an elastic cushion of polydimethylsiloxane (PDMS), which is stuck to a microscope glass slide. Heating this transfer template above the glass transition temperature T_g of the polymer expands the cushion and allows the adhesive film to become viscous, thus conforming and adhering strongly to flakes covered by it. Cooling below T_g then solidifies the polymer and flakes will be picked up by lifting the transfer template.

We used two different adhesive films, either polypropylene carbonate (PPC) or polybisphenol carbonate (PC). We prepared the PPC solution by dissolving PPC acquired from *SigmaAldrich*[2] at a 15 % weight ratio in anisole[3] at 50 °C, while stirring with a fish magnet until everything was properly dissolved. The PC[4] was dissolved in chloroform[5] at a 6 % weight ratio. While

[2] Poly(propylene carbonate), average $M_n \sim 50,000$ by GPC. SigmaAldrich product no. 389021, CAS 25511-85-7, MDL MFCD00197919

[3] Anisole, ReagentPlus®, 99 %. SigmaAldrich product no. 123226, CAS 100-66-3, MDL MFCD00008354

[4] Poly(Bisphenol A carbonate), average $m_W \sim 45,000$ by GPC. SigmaAldrich product no. 181625, CAS 25037-45-0, MDL MFCD00084476

[5] Chloroform, anhydrous, ≥ 99 %, contains 0.5 % to 1.0 % ethanol as stabilizer. SigmaAldrich product no. 288306, CAS 67-66-3, MDL MFCD00000826

PPC requires lower working temperatures than PC, thus making it easier to align template and substrate, we have observed that temperatures above 110 °C resulted in fewer bubbles at the flake interfaces during transfer. The advantage of PC over PPC is that it is a much stronger adhesive, so the intermediate flake delamination (step 5) can be skipped. However, it needs to be kept in a fridge in order to not degrade, and cannot be spin-coated on the PDMS layer, whereas PPC can. Instead, a droplet of PC is placed on a 20 mm × 20 mm glass coverslip. A second coverslip is dropped on the first one, thus spreading the droplet in between. With care, but in a swift motion, we pull the top glass piece off, thus leaving behind a thin film of PC on the bottom glass slide, which can be peeled off using a piece of tape and placed on the PDMS stamp.

The adhesive film was placed on a droplet of PDMS which was stuck to a glass slide. Both glass slide and chip could be individually moved with micrometer screws. The following steps describe our typical working process for achieving high-quality interfaces using the PPC method:

1. Align the top BN flake with the center area of the PDMS/PPC template. Lower the glass slide such that the PPC touches the substrate. Take care that the PPC does not yet cover the flake, but touches down less than 100 µm away from it.

2. Increase the stage temperature above 55 °C. The PDMS/PPC will expand and cover the flake, and adhesion between BN and PPC increase significantly.

3. Turn off the stage heater and wait for the stage to cool below 40 °C (possibly with the help of a nitrogen gun). At this stage, the adhesion between BN and PPC should exceed that of BN and substrate. Now lifting the glass slide should rip the flake off the substrate. If at this stage the intended flake did not get picked up, repeating the process by heating to 80 °C to 90 °C and then cooling down should result in a much higher yield, at cost of longer waiting times for the stage to cool down.

4. Place the chip with the graphene flake on the stage and align the flake with the BN on the glass slide below now. Slowly lower the glass slide and set the stage temperature to 110 °C. The hot air and deflected slide will make it difficult to align the two flakes, so extra care has to be taken at this step. Once the stage has reached 110 °C, bring stage and glass slide in contact as slowly as possible until the interface passes the Gr and BN, preferably letting the expanding PDMS do the work.

5. Increase the stage temperature to 120 °C and then retract the glass slide, thus delaminating the top BN on the graphene flake.

6. Anneal the Gr/hBN stack at 170 °C for 15 min.

7. Place PPC/PDMS glass slide above the chip, turn off the stage heater and bring the polymer in contact once the temperature is below 70 °C to 80 °C.

8. Once the temperature drops below 40 °C, retract the glass slide. The Gr/hBn stack should get lifted off the substrate.

9. For assembling the BN-G-BN sandwich, repeat steps 4 - 8. If needed, transfer the sandwich to another substrate.

For flake transfer using PC, we follow the above steps, except that the transfer takes place at a base temperature of 110 °C instead of 40 °C, and to activate the adhesion to PC, heating to 130 °C to 140 °C instead of 80 °C to 90 °C is required.

Challenges of heterostructure assembly

Compared to interfacing van der Waals heterostructures with DC circuitry, numerous challenges arise for integration with RF devices. RF circuits in coplanar architecture, such as the ones in this thesis, need a metallic ground plane around the conducting lines, separated by micron-sized gaps. Due to the long-range interaction of electromagnetic fields, fabrication residues of any kind (metallic, dielectric, organic) should be avoided as much as possible to ensure reliable circuit operation.

That being said, the nature of flake transfer always introduces contaminations: for one, the polymer used for transfer has very strong adhesion to the metal areas of the shunts, ground planes and center conductors. While during stack assembly on oxidized silicon, the polymer would only touch the substrate at the start, when attempting to delaminate the heterostructure on the pre-patterned substrates, the polymer often ripped off the PDMS carrier and would also get delaminated, see Fig. 2.2(a). Additionally, van der Waals crystals have strong adhesion to the metals used in our work, which resulted in a number of residual flakes on the final chip surrounding the intended heterostructure. A long soak in NMP was able to remove the polymer at least visibly, but residual flakes had to be etched away in a separate step.

On the other hand, flake adhesion to the substrate itself was found to vary from good to extremely poor: We found that BN-G-BN stacks would often get washed away due to insufficient adhesion to sapphire substrates during processing. Due to the low adhesion of BN to sapphire and silicon nitride, many stacks were washed off the final substrates when dissolving the polymer. While the transfer yield of heterostructures on sapphire and silicon nitride was only as low as 50 % and 0 %, respectively, we did not observe this behaviour on silicon and silicon oxide surfaces, (see Fig. 2.2(b)), where all delaminated flakes would stick. Note that even adhesion promotion using HMDS (hexamethyldisilazane, $[(CH_3)_3Si]_2NH$) did not improve this issue.

When stacking flakes on top of each other, hydrocarbon gases and water, usually covering all surfaces in ambient conditions, can get trapped in between flakes [91], similar to air pockets encountered when placing protective covers on flat surfaces such as phone screens or windows. These bubbles can cluster together, reaching pressures of up to 1 GPa [92, 93] and resulting in local pseudomagnetic fields in excess of 300 T [94]. Bubbles are hence undesirable since they pose strong charge carrier scattering centers. Nevertheless, high substrate temperatures, both during and after assembly, can mobilize these gasses, allowing them to clear up large sample spaces by accumulating along flake defects. We have occasionally observed bubbles piercing the top BN and escaping from the stack when annealing the heterostructures at temperatures above 300 °C.

For these reasons, every single gJJ has to be designed by hand, since it is important to place the structure to be fabricated in an area without bubbles present in order to obtain a high-quality device. After stack placement on the final chip, we took several optical and atomic force microscope images to determine the graphene location with respect to alignment marks, and to identify bubble-free areas, see Fig 2.2(b). These combined images are loaded into the CAD software (we highly recommend *KLayout* [95], or alternatively *LibreCAD* [96]) to design the electrodes and gates for the gJJ, as shown in Fig 2.2(c).

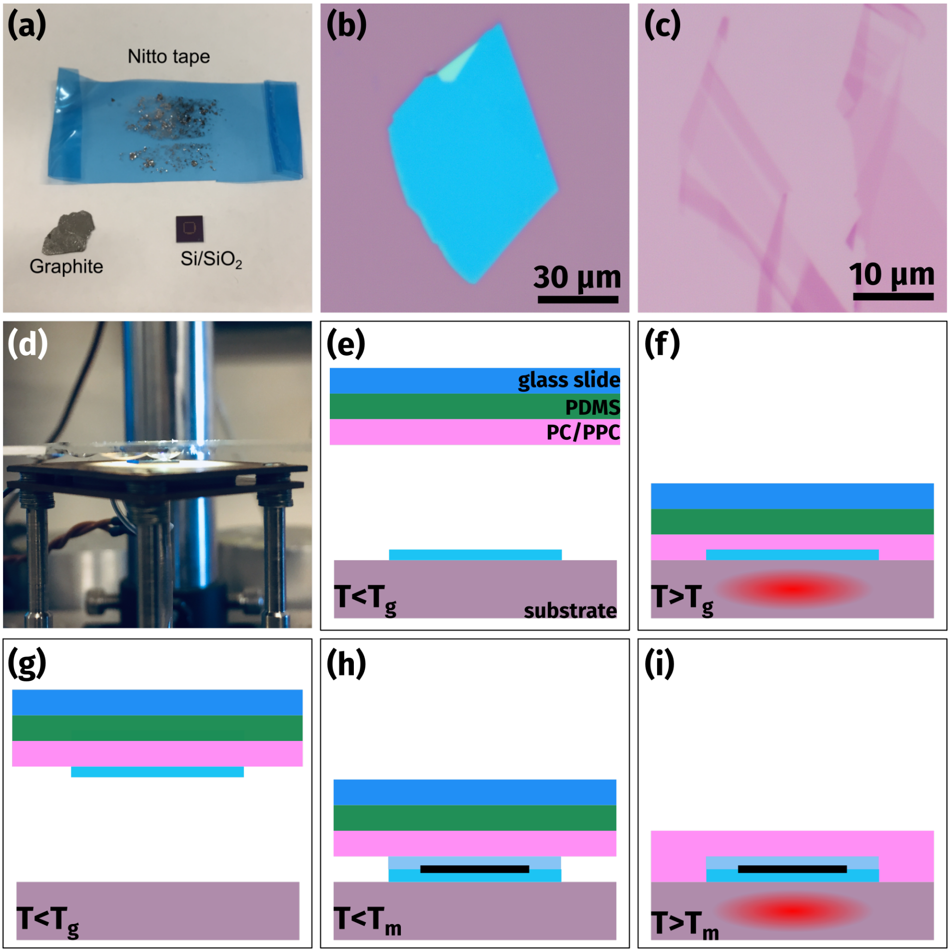

Figure 2.1: From bulk crystals to van der Waals heterostructures. **(a)** Bulk crystals of graphite, together with a piece of wafer adhesive tape used to thin down these crystals by repeated folding and opening of the tape. The tape is pressed on a 6 mm × 6 mm piece of silicon with 285 nm SiO_2 to enhance the optical contrast for monolayer graphene. Figure adapted from [60]. **(b)** Optical microscope image of a BN flake of approximately 30 nm thickness. **(c)** Optical microscope image of a thin flake of graphite, exhibiting regions of single and multilayer graphene. **(d)** Photograph of a glass slide with PDMS covered with a spun-on layer of PPC (approximately 1 µm to 2 µm thick), aligned to a silicon substrate mounted on the transfer stage. **(e-i)** Typical sandwich assembly cycle for creating multi-layered van der Waals heterostructures. **(e)** Polymer brought in contact with exfoliated flake on substrate at room temperature. **(f)** Heating substrate above glass transition temperature T_g enhances the adhesion of the flake to the polymer significantly above the adhesion to the substrate. **(g)** Subsequent cooling of the substrate leads to stiffening of the polymer. Combined with rapid lifting of the glass slide, usually solely induced by the thermally shrinking polymer, lifts the flake off the substrate. By repeating steps **(e)**-**(g)**, multiple flakes can be stacked on top of each other. **(h)** In order to deposit the finished heterostructure on a final substrate, the heterostructure is brought in contact with the substrate at room temperature, and the stage heated above the melting temperature of the polymer. Slow lifting of the glass slide leads to the structure remaining on the substrate, while the polymer can either remain fully stuck to the PDMS, or also remain on the substrate. **(i)** Polymer residues can be removed in organic solvents such as anisole, NMP, PRS3000 or chloroform.

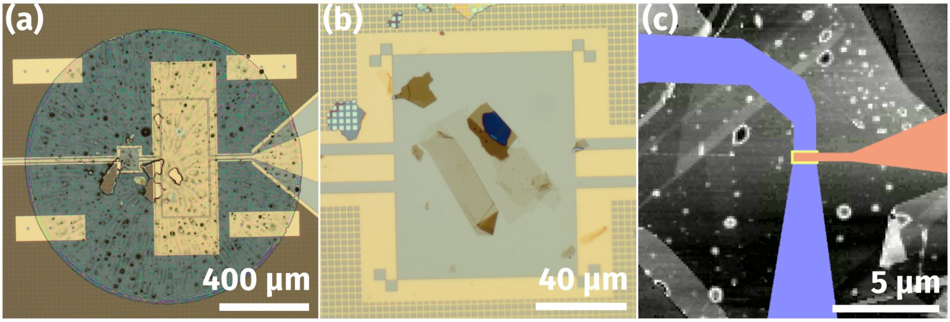

Figure 2.2: Fabrication issues associated with van der Waals assembly. (a) Due to the good adhesion of the polymer to metal surfaces, after flake deposition the polymer would often get delaminated and the chip needs to be thoroughly cleaned using wet chemistry solvents. **(b)** Due to the high adhesive strength of the PC and PPC, residual flakes around the assembled heterostructure are delaminated on the chip, requiring additional etching steps to clean the chip of these dielectrics. **(c)** AFM image (greyscale) of a heterostructure assembled via the PC method. Due to the significantly slower expansion of the polymer, gas and water molecules at the interfaces between the flakes are pushed towards the edges and fewer, but larger pockets are formed. Overlaid with the AFM image is the CAD file with contacts in blue, top-gate in red and gate dielectric in yellow, to design the metal layers with respect to the flake position.

Device patterning and arising challenges

Since the gJJ have to be individually designed are not fabricated scalably, we chose to first pattern the RF circuitry on either large silicon chips, or 2 inch sapphire wafers, and subsequently transfer the BN-G heterostructures on the final substrate, where they are patterned into the gate-tunable gJJ. Fabrication was carried out in the class 10000 (ISO 7) cleanroom of the *Kavli Nanolab Delft*, which offers class 100 (ISO 5) wet bench areas for sample processing. While the RF circuits could also have been fabricated using photolithography, we patterned all devices using electron beam lithography with either one of the *Raith EBPG 5200* or *5000+*. Dry-etching was done using *Leybold Heraeus Fluor* reactive ion etchers, dielectric deposition with PECVD in an *Oxford Instruments PlasmaPro 80*. Superconductors were deposited in sputtering systems from *AJA International, Inc.* and *Alliance Concept*.

The graphene Josephson junctions were fabricated using the etch-fill technique pioneered by Wang *et al.* [97], with added top-gates as in Refs. [44, 98]. Compared to fabrication on oxidized silicon, we encountered numerous challenges during fabrication that needed to be addressed before samples could be processed reliably. We chose NbTiN as superconductor for the contacts to graphene after the MoRe target in our lab ran empty, and since the use of NbTiN was well established in the neighboring group of Leo Kouwenhoven [99, 100].

We found that for ebeam lithography on sapphire substrates, a conductive charging layer on top of the bilayer PMMA in the form of Electra 92 (AllResist AR-PC 5091) was crucial to create high-resolution patterns, such as Josephson junctions with length by width of 0.5 μm × 5 μm. Without a conductive layer, the resist would consistently be exposed in the center of the junction, leading to a nano-short at this spot, see Fig. 2.3(a-c). This issue does not appear on silicon with or without oxide, since the band gaps of these materials are low enough for them to be somewhat conductive at room temperature. Failure to use a conductive layer during ebeam exposure of sapphire can even lead to physical damage to the EBPG in the case of sudden electrical discharge. Note that Electra 92 needs to be stored in a fridge and the bottle has to be warmed up to room temperature before being opened to avoid water condensation. Additionally, Electra needs to be washed off after ebeam exposure and before resist development in a simple water bath. Most importantly, the chip needs to be blow-dried from the water bath before development and should not be transferred from the water bath into the developer, as mixing either water and IPA, or water and developer can lead to overdevelopment of the resist.

Various samples also exhibited cracks in the resist after ebeam exposure and development, as shown in Fig. 2.3(d). These cracks were up to several tens of microns long and usually originated in sharp bends or corners of patterned structures, as well as from the edgebeads on bare chips coated with either PMMA or CSAR. They are most likely due to a combination of tensile film stress in the resist and insufficient resist adhesion to the substrate [101]: When a film does not properly adhere to the substrate, developer can peel off parts of the resist. Tensile stress in the resist accelerates this issue and can lead to long cracks, especially starting at sharp corners. Resist cracking could be avoided by changing the pattern shape to rounded corners and improving resist adhesion. One method was to coat the substrate with a monolayer of HMDS (hexamethyldisilazane, $[(CH_3)_3Si]_2NH$) from *MicroChemicals* from the gas phase prior to resist application. For this, we used the hotplate with integrated HMDS deposition system of a *Suss MicroTec Delta 80 RC*, with prebaking at 150 °C for 6 min. We found that this immensely helped against both cracks in various resists (PMMA, CSAR), regardless of whether the substrate was metallic or dielectric, and even under-etching of dielectrics with BOE. Alternatively, applying the resist to be spun on the chip and just letting the chip rest for 30 s to 60 s before spinning significantly improved resist adhesion as well. We speculate that the water layer present on all surfaces in ambient conditions needs this long to be replaced by the resist, which then stuck much better to the substrate. We note that for PMMA, cold development with a combination of IPA and water at a 3:1 ratio also solves the issue of cracking resists and can even improve feature resolution [102, 103]

Another issue commonly encountered during nanofabrication, in particular when performing lift-off, are so-called *dog-ears*. These are visible as metal parts sticking to the edges of patterned areas and are due to the side-coverage of the resist protecting other areas. Since sputtering leads to fairly isotropic deposition (compared to directional deposition with metal evaporation), sufficient resist undercut and thickness are necessary to facilitate liftoff. These requirements also restrict the minimum feature size that can be reliably patterned. Typically, a resist-to-metal ratio at least 3:1 allows stable liftoff. However, the etch-fill technique requires a careful balance between choosing a thick resist in order to have enough of it left after dry-etching for good liftoff, while making it as thin as possible to achieve for high-resolution patterning. A lower resist thickness can be chosen for lift-off if sufficient undercut is present, which is why a bilayer resist of PMMA was chosen. This undercut can be enhanced by longer development. Additionally, dry-etching at high pressures was found to be fairly isotropic and thus widening patterned structures and even increasing the undercut. Judging from optical images, this resulted in an undercut of approximately 100 nm to 150 nm. Some dog-ears could be removed by using an unused transfer template with PPC polymer, with which we were able to pull away some dogears which would then stick to the polymer. Using ultrasonication during liftoff typically works well with removing dog-ears. Due to the violent agitation and previously experienced problems with stack adhesion to the substrate, we opted against this procedure. Instead, we used the jet stream of syringes filled with PRS3000 inside the filled beaker in which

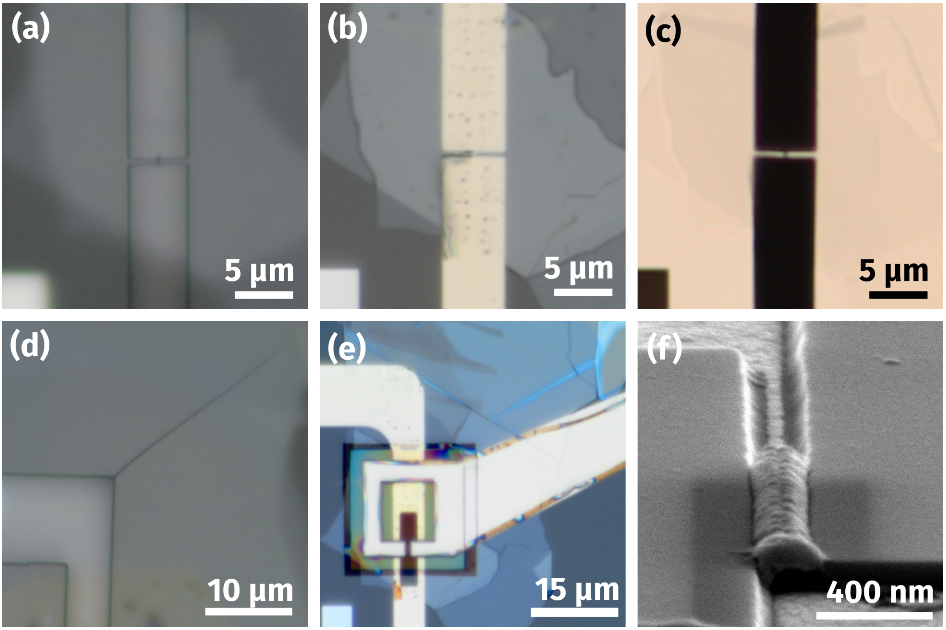

Figure 2.3: Challenges associated with gJJ fabrication. (a-c) Due to the insulating nature of sapphire, ebeam patterning can lead to the substrate charging up and overexposing parts of the resist. After developing **(a)**, dark spots in the resist in the gap center are due to developed resist due to charging effects. **(b)** After etching and lift-off, the junction is shorted in the center and dog-ears are visible to the right side, standing up. **(c)** Illumination through the backside of the sapphire substrate reveals a nanobridge short. **(d)** Insufficient resist adhesion to the substrate and resist tension can lead to cracks originating at sharp bends and extending several tens of microns. **(e)** Significant dog-ears after liftoff are visible as colored bands on top of the metal film of a top-gate extending over a graphene SQUID. **(f)** SEM image of two superconducting banks on sapphire, partially connected by two dog-ears across the gap.

the liftoff was happening, to aid the process.

The final process flow is shown in Fig. 2.4(a-f) and Tab. 2.1. As a trade-off between strong superconducting coupling and reliable sample fabrication, we designed all gJJ to be 500 nm long. Cross-sectional SEM showed side-angles of approximately 60° at the contact interfaces (see Fig. 2.4(g)), allowing for good overlap between metal contacts and graphene layer. We chose hydrogen silsesquioxane (HSQ, $[HSiO_{3/2}]_n$ [104]) as a spin-on gate dielectric due to its process reversibility, good step coverage and straightforward thickness variability. HSQ needs to be stored in a fridge, like Electra 92, and has to be warmed up to room temperature before applying on the sample. Once BN-G heterostructures would stick to the sapphire chip, and including the use of Electra 92, the yield of devices with gate-tunable supercurrents, was approximately 70 %.

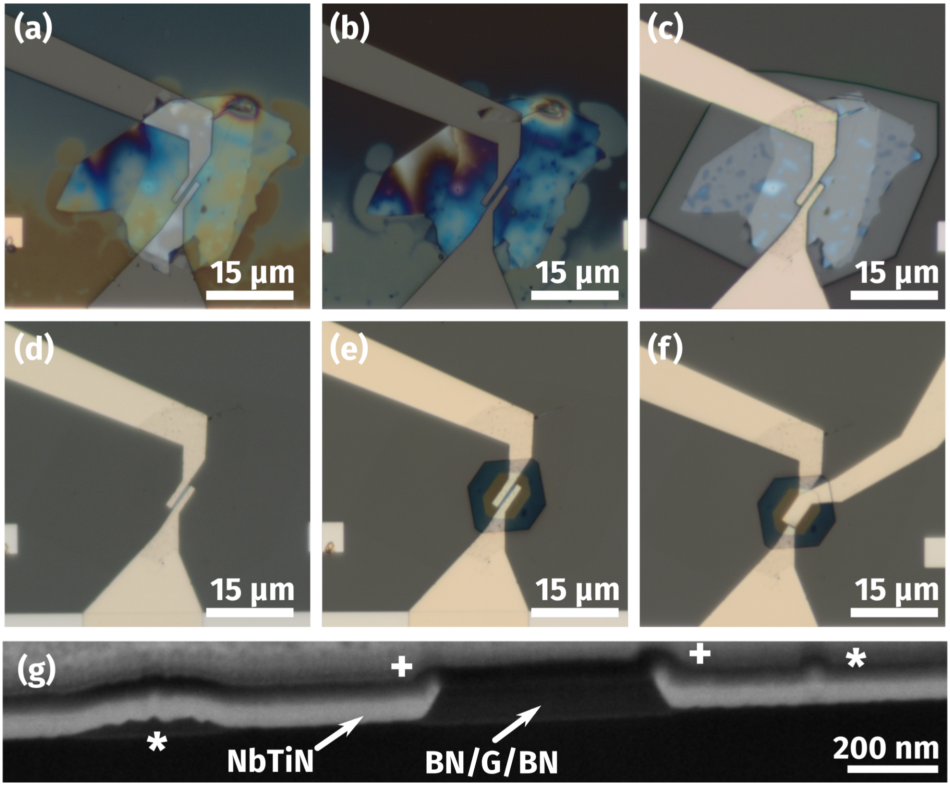

Figure 2.4: From stack to device: Fabrication of top-gated graphene Josephson junctions. **(a)** BN-G-BN sandwich on sapphire substrate. The optical micrograph is loaded into a CAD program and aligned with respect to the prepatterned markers. After electron beam exposure and development, the areas to be metallized are open, while the rest of the substrate remains covered by the resist. **(b)** In order to make galvanic contacts to the graphene layer, the chip is placed in a CHF_3 + O_2 plasma, which dry-etches the BN layer. Careful etch-rate calibration is required to not under-etch for good contact to the graphene while not over-etching so that enough PMMA is left for successful liftoff. **(c)** Sample after metallization and lift-off, with etch mask for shaping the stack into the final shape. **(d)** Sample after patterning into rectangular shape. Only the gJJ slab remains. **(e)** Bilayer HSQ covering the stack and metal leads as an insulating gate dielectric. **(f)** Finalized sample with superconducting gate electrode extending over the entire Josephson junction. **(g)** Cross-sectional SEM of a gJJ resting on silicon, contacted by NbTiN. Contact angles are approximately 60°. Defects such as bubbles (*) and dog-ears (+) are visible. Courtesy of Triantafyllia (Rose) Sermpeniadi/Conesa-Boj lab.

2

Table 2.1: Fabrication of side-contacted top-gated graphene Josephson junctions. Note that after washing off Electra 92, the chip needs to be blow-dried before developing the PMMA. Electra is not necessary needed for the top-gate dielectric and gate metal.

1.	**Making NbTiN contacts using etch-fill**
Ebeam resist (1/2)	PMMA 495 A4, 4000 rpm, bake 10 min at 185 °C
Ebeam resist (2/2)	PMMA 950 A3, 4000 rpm, bake 10 min at 185 °C.
Conductive resist	Electra 92, 2000 rpm, bake 90 s at 80 °C.
Ebeam patterning	1000 μC cm^{-2} + PEC
Wash off Electra 92	Rinse in water for 30 s to 60 s.
Development	MIBK:IPA (1:3) for 90 s, IPA 30 s.
Dry etching	CHF_3 + O_2 40 sccm+4 sccm @ 60 W, 80 μbar for 1 min (etch rate roughly 60 nm min^{-1})
Metal deposition	5 nm NbTi and 60 nm to 70 nm NbTiN
Liftoff	hot PRS 3000 @ 88 °C for a few hours, rinsing in IPA
2.	**Shaping the device:**
	Same resist, patterning and etching as for making the contacts, but with lower etch pressure (50 μbar) and no metal deposition.
3.	**Top-gate dielectric**
Ebeam resist	concentrated HSQ, 8000 rpm, bake 10 min at 90 °C in an oven.
Ebeam patterning	1000 μC cm^{-2}.
Development	MF322 for 1 min, MF322:H_2O (1:9) for 15 s, H_2O for 15 s. Repeat this process once.
4.	**Top-gate metal:**
	Same steps as for making the contacts, but no etching and with metal thickness of 80 nm to 120 nm.

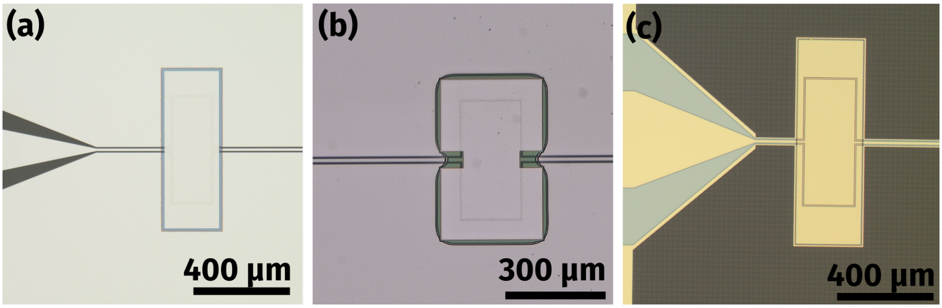

Figure 2.5: Finished current-bias microwave cavities. (a) DC bias cavity on sapphire with MoRe base and top layer and Si_3N_4 capacitor dielectric. **(b)** Device on silicon with aluminum base and top layer and Si capacitor dielectric. **(c)** Device on silicon with NbTiN base and top layer and Si_3N_4 capacitor dielectric. The third device features holes in the ground plane in an effort to reduce magnetic flux focusing and trap vortices.

2.1.2. FABRICATION OF DC BIAS CAVITIES

The process for fabricating DC bias cavities consists of three main steps:

- Deposit and pattern base layer (CPW, ground plane, shunt bottom part)
- Deposit and pattern shunt dielectric
- Deposit and pattern shunt top plate

For best fabrication results, a mono-layer of HMDS should be applied before every resist spinning, as described in Sec. 2.1.1. The use of Electra 92 for devices on sapphire is not strictly necessary due to the large feature size and the conducing metal base layer, but still recommended.

Care needs to be taken to ensure that there are no shorts in the shunt dielecric layer. Since the dielectric deposition using PECVD does not necessarily provide complete step coverage, the dielectric layer should be at least 30 % thicker than the base layer. We found this to be problematic when patterning the base layer using dry etching on silicon substrates because the dry-etch process can cut deep into the silicon substrate, increasing the step height to be covered by the dielectric. In this case, depositing a dielectric fill layer in the gaps slightly extending above the step edges, resulted in reliable device yield.

Instead of wet-etching the shunt capacitor dielectric, dry-etching using a $CHF_3 + O_2$ plasma at 60 W power and base pressure of 50 µbar yielded comparable results. However, the combination of plasma etching with negative ebeam resist often resulted in teflonization of the latter, severely complicating resist stripping afterwards. This can be avoided by either in-situ O_2 ashing, or by applying a thin PMMA layer below the negative ebeam resist, which can be stripped off the sample much easier. From a safety perspective, the plasma etch process is to be preferred over the use of BOE due to the much lower risk to the operator. Additionally, even though wet-etching seems to be a cleaner process compared to dry-etching, the obtained internal quality factors of samples fabricated using BOE did not consistently surpass those of dry-etched devices.

The RF circuits in Chapters 3 and 4 are fabricated as listed in Tab 2.2, while the one in Chapter 5 used Al:Si as superconducting layer and silicon as substrate and dielectric layer. In

Table 2.2: Fabrication of DC-bias superconducting microwave cavities. This is the recipe for the circuits in Chapters 3 and 4.

1.	**Deposit and pattern MoRe base layer**
Metal deposition	60 nm MoRe, 100 W, 60 sccm Argon flow.
Ebeam resist	AR-P 6200.13 (CSAR), 4000 rpm, bake 3 min at 155 °C.
Ebeam patterning	300 μC cm^{-2}.
Development	Pentylacetate for 60 s, MIBK:IPA (1:1) for 30 s, IPA for 15 s.
Dry etching	SF_6 + He 12.5 sccm+10 sccm @ 50 W, 10 μbar
Liftoff	hot PRS 3000 @ 88 °C for a few hours, rinsing in IPA
2.	**Deposit and pattern dielectric layer for shunt capacitor**
Dielectric deposition	PECVD 70 nm of Si_3N_4 @ 300 °C.
Ebeam resist	AR-N 7700.18, 3000 rpm, bake 1 min at 90 °C.
Ebeam patterning	210 μC cm^{-2}.
Development	MF321 for 60 s, MF321:H_2O (1:10) for 15 s (twice), H_2O for 15 s.
Wet etching	BOE 1 min
Strip resist	hot PRS 3000 @ 88 °C for a few hours, rinsing in IPA
3.	**Deposit top metal plate of shunt capacitor**
Ebeam resist (1/2)	PMMA 495 A4, 4000 rpm, bake 10 min at 185 °C.
Ebeam resist (2/2)	PMMA 950 A3, 4000 rpm, bake 10 min at 185 °C.
Ebeam patterning	1400 μC cm^{-2}.
Development	MIBK:IPA (1:3) for 90 s+ IPA 30 s.
Metal deposition	100 nm MoRe as described above.
Lift-off	hot PRS 3000 @ 88 °C for a few hours, rinsing in IPA

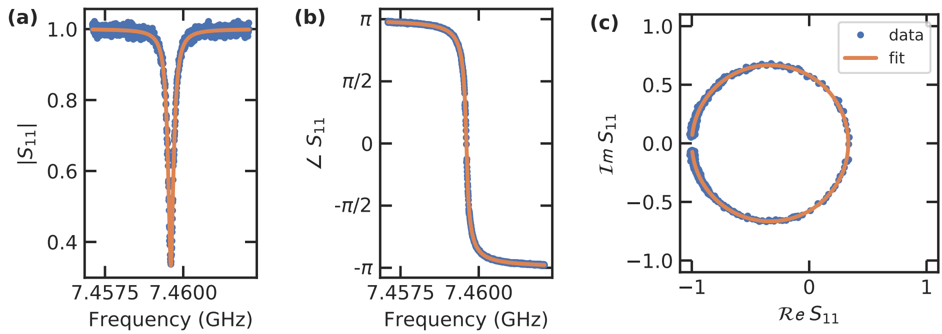

Figure 2.6: Reflection coefficient of the best fabricated DC bias cavity. Data (blue points) and fit (orange line) to the absolute value **(a)**, phase **(b)** and real and imaginary parts **(c)** of the reflection coefficient of a DC bias cavity with NbTiN base layer on silicon, the device in Fig. 2.5(c). The internal and external quality factors are $Q_i \approx 82\,439$ and $Q_i \approx 41\,209$.

terms of internal quality factor $Q_i = \omega_0/\kappa_i$, the best devices with sapphire substrate and MoRe base layer showed $Q_i \approx 41 \times 10^3$, while DC bias cavities out of aluminum on silicon substrates and shunt dielectric had $Q_i \approx 29 \times 10^3$. While not used for further measurements in this thesis, the reproducibly highest internal quality factors were achieved with sputter-deposited NbTiN on silicon after intensive wafer cleaning by our collaborators at *SRON* [105], and Si_3N_4 as dielectric with BOE patterning. Figure 2.6 shows the resulting reflection measurement of the best measured sample (see Fig. 2.5(c)), with an internal quality factor $Q_i \approx 82\,439$. In comparison, $\lambda/4$ side-coupled resonators from the same wafer fabricated in a single step exhibited internal quality factors exceeding 1 million.

Even higher device quality could be achieved with a low-loss dielectric such as Al_2O_3 and a more local deposition: We speculate that depositing dielectric on the entire chip area might degrade the film quality by damaging the superconducting layer in areas where voltage fluctuations are non-negligible, thus introducing defects such as two-level systems which can absorb radiation and lead to internal losses. Additionally, device patterning with dry-etching can physically roughen the superconducting base layer. Even wet-etching, such as with BOE, can leave behind defects. For example, we observed that ALD-deposited Al_2O_3 left micron-sized flakes on the chip, that could not entirely get dissolved in BOE. As an alternative, we propose local deposition by liftoff, as can be done with low-temperature PECVD or ALD. This could protect the surrounding circuitry and potentially reduce internal circuit losses.

2.2. CHROMOSOME-SHAPED OXIDATION OF MORE THIN FILMS

The use of MoRe as superconductor of choice for our devices has a rather anectodal reason: In 2012, Schneider *et al.* [106, 107] were searching for a superconductor able to withstand high magnetic fields as well as the growth conditions for carbon nanotube (CNT) fabrication, with good superconducting contacts. Initial attempts with NbTiN, then the superconductor of choice in the neighboring groups of Teun Klapwijk [108] and Leo Kouwenhoven [100], showed poor performance under CNT growth conditions, low CNT yield and high contact resistance. Rhenium, also previously used in the group of Leo Kouwenhoven [109], performed significantly better, but a material with even higher T_c was found in the form of molybdenum rhenium

(MoRe): MoRe turned out to survive the CNT growth, have a very closely matching work function to the one of CNTs, and yield larger T_c and I_c compared to rhenium.

MoRe was since the superconductor of choice for CNTs. Soon after, it was picked up by other groups, not only in the field of graphene [110], most notably after Calado *et al.* were able to show ballistic superconductivity in edge-contacted graphene [38], and has since been used in numerous groups with notable success, see Refs. [111–117].

However, it was often overlooked that devices made from MoRe began exhibiting peculiar "spots" visible under an optical microscope after a few days. We found that these were small "crystallites" growing on the surface of sputtered MoRe films, regardless of substrate (silicon, sapphire, or oxidized silicon) or film thickness (ranging from 20 nm to 200 nm). Growth of these structures seems to be forming by seed-growth of small islands less than 1 µm × 1 µm in size (see Figs. 2.7(c,d)) which would then diffuse on the surface and cluster together in chromosome-shaped strands (see Fig. 2.7(b)). This growth mechanism covers the entire film surface with small islands that lump together into bigger structures, as depicted in Fig. 2.7(a). Remarkably, some of the largest crystals grew even higher in the third dimension than the original MoRe film thickness.

In collaboration with the group of Dr. Conesa-Boj at TU Delft, we analyzed the atomic composition of these crystallites using EDX peak intensity. In Fig. 2.8 we show a qualitative analysis of the atomic composition of one of these structures. Here, a representative crystallite was imaged using SEM (Fig. 2.8(a)), and elemental maps corresponding to the spatial distribution of oxygen, silicon, rhenium, and molybdenum signals were obtained (Fig. 2.8(b-f)). The abundance of oxygen content in the areas of the crystallite hints at strong oxidation in these areas. At these locations, the signal originating from the silicon peak is reduced. This is expected, since due to the increase in thickness, less signal from the silicon substrate can reach the detector. Additionally, molybdenum signal is also weaker at these crystallites that at the area surrounding it, suggesting their poor content in molybdenum. In contrast to the reduced composition in silicon and molybdenum, the oxygen and rhenium signals become predominant at the crystal location, strongly hinting that those crystallites are mainly formed by some kind of rhenium oxide (ReO_x).

Further quantitative analysis could not be performed because the oxygen signal was too close to the zero loss peak. Additionally, a reliable separation of the bulk from the surface contributions for the rhenium and molybdenum peaks was not possible. Cross-sectional TEM and EDX could have lead to more insight, but were not performed. Our observation contrasts the one made on thin and bulk MoRe structures in literature, where MoO_3 and MoO_2 were found to be the dominant oxide [112, 118]. To the best of our knowledge, there is no literature on the observed ReO_x crystallites emerging from MoRe films. However, analysis of oxidized pure rhenium films showed similar crystallites, albeit not of the same size and with a slower growth rate and less uniform surface coverage [119, 120].

While the superconducting critical temperature of large structures of this film seemed to be unaffected by the growth, these structures can severely degrade the high-frequency response of superconducting circuits such as resonators or qubits, as dielectric losses can be one of the main reasons for qubit decoherence [121]. Moreover, since the crystallites physically move about on the film surface, they might interfere with patterned structures, leading to unintended defects in or even damage the electrical wiring.

We found that a 60 s dip of MoRe films in strong etchants, such as BOE, TMAH or TMAH-based developers such as MF321 or MF322, was enough to wash off these crystallites, as long

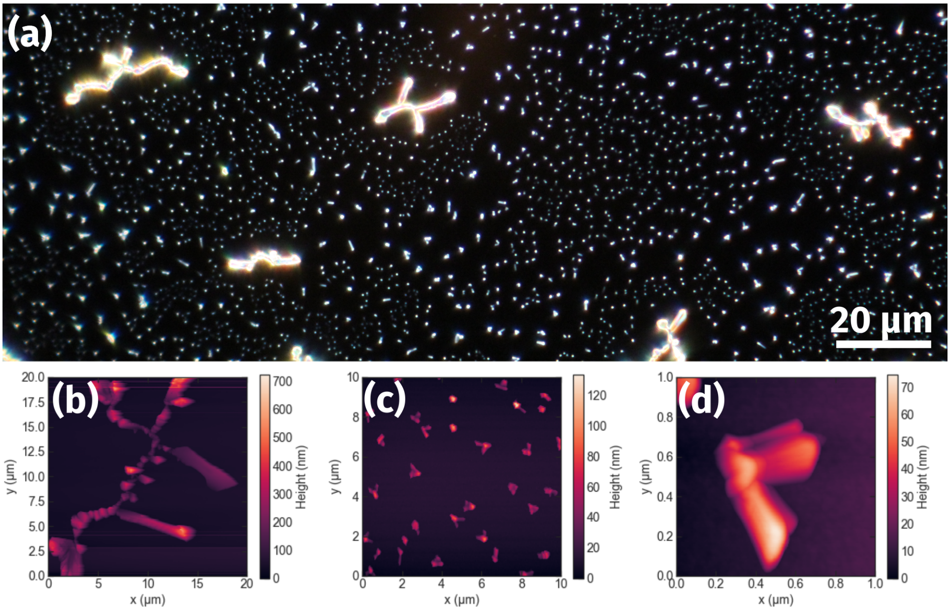

Figure 2.7: Chromosome-shaped oxidation of MoRe thin films. (a) Optical image of MoRe film under dark field illumination after two weeks in ambient conditions. **(b-d)** AFM images of several locations and types on the film: Small individual crystallites **(b)** serve as seed islands on the film surface **(c)**, which then agglomerate into chromosome-shaped strands **(d)**, covering the entire film surface **(a)**. MoRe film thickness was 100 nm.

as they were still in the seed phase and the density of big clusters was low. This corresponds to a storage time below three days in ambient conditions. Crystal seeding sets in almost immediately and is clearly visible under an optical microscope at 5x magnification after one day. The crystal growth can be slowed down significantly, but not completely suppressed, if films are stored in dry boxes with constant nitrogen flow. We estimate that one day in ambient conditions has the same effect as two weeks in nitrogen atmosphere.

Since the devices studied in this thesis did not require MoRe per se, we chose to not exclusively use this superconducting alloy after thorough investigation, but also make use of NbTiN or aluminum, depending on the specific circuit requirements.

2.3. Measurement setup

2.3.1. Device post-processing and packaging

Once device fabrication is finished, the sample has to be mounted on a chip carrier and contacted, so we can connect it to our measurement electronics. Our microwave PCBs are made for 10 mm $\times$ 10 mm chips. However, in order to better hold on to the chips during fabrication and to enhance the fabrication yield, samples are usually fabricated on larger substrates: The current bias cavities for the graphene devices presented in Chapters 3 and 4 were processed on a 2 inch wafer, and the cavities based on aluminum in Chapter 5 on 15 mm $\times$ 15 mm chips.

We dice the chips into the correct dimensions in the very last step, using a *Disco dicer*

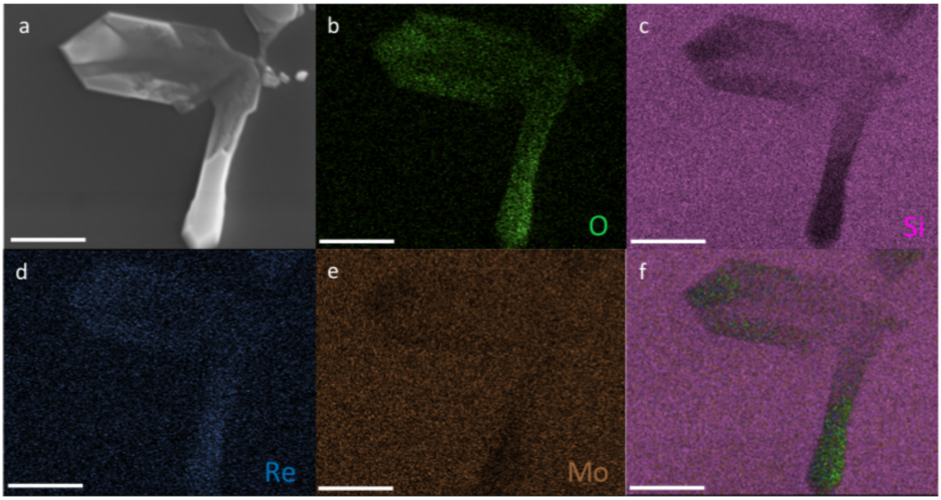

Figure 2.8: EDX spectra of MoRe crystallites on silicon substrate. a, SEM image of a region in the MoRe layer. **b-e,** EDX elemental maps of O, Si, Re and Mo respectively. **f,** Superposition of the **b-e** elemental maps. All scale bars 2 µm. Courtesy of Dr. Miguel Tinoco-Rivas/Conesa-Boj lab, TU Delft.

DAD 3220 from *Disco Hi-Tec Europe GmbH*. To protect the chip from dust during sawing, we spincoat photoresist[6] on the chip before dicing. Good resist-substrate adhesion is important because the water jet used to cool the blade can wash off the resist during dicing otherwise, potentially ruining weeks of delicate work in the cleanroom. Use of HMDS, or letting the resist sit on the chip to be diced for 1 min prior to spinning, is therefore strongly recommended.

The silicon chips were diced using a standard NBC blade at 3000 rpm and a feed speed of 5 mm s^{-1}, while for dicing sapphire we used a special diamond blade at 2000 rpm and 2 mm s^{-1}. For the devices presented in this thesis, we placed the diced chips in teflon holders inside beakers filled with PRS3000, heated the solution to 80 °C and subsequently put the beaker into an ultrasound bath at maximum power. After 5 min, the resist has then come off the sample, and we passed the chip through a series of PRS3000 and IPA baths to wash off any remains, and blow-dried using nitrogen.

For electrical measurements, the chips are wirebonded to PCBs that are mounted on copper boxes, see Fig. 2.9. The bottom part of the first generation copper boxes, on which the chip rests, had a simple flat base. However, we noticed that this led to cross-talk of devices across the entire chip, presumably due to electromagnetic box modes between substrate and copper base. To mitigate this spurious coupling, we removed most of the copper base to leave only two thin rails behind, to which the chips are glued with GE low temperature varnish. Wirebonding is done using a *Westbond 4000 "E"* system from *West•Bond Inc.* with bond wires from an AlSi alloy (99 %-1 %). To ensure good thermalization and electrical contact, we usually used three to four bonds for each bond pad, and as many bonds as would fit on the ground planes. An example of one of our devices that is mounted and wirebonded in a PCB, ready for measurement can be seen in Fig. 2.9. The connectors to go from the PCB to the outside world are

[6] HPR504, 4000 rpm, bake 60 s at 100 °C, approximately 1.2 µm thick

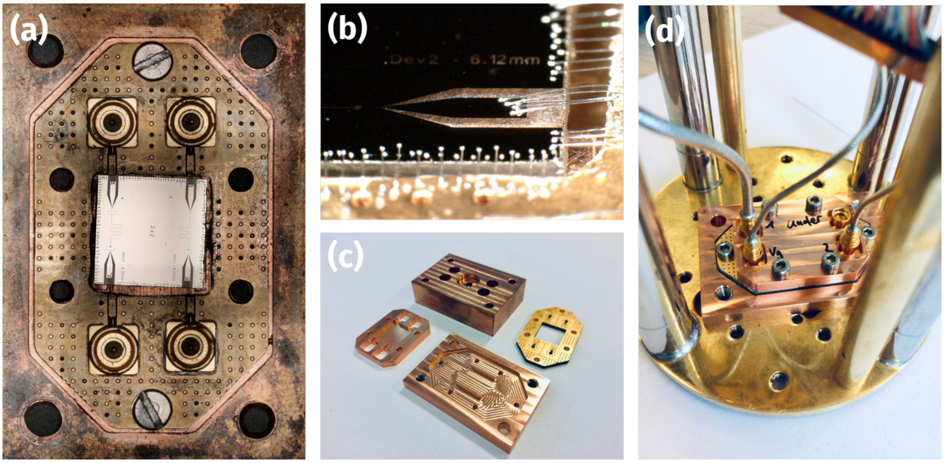

Figure 2.9: Device packaging for electrical measurements. (a) The 10 mm × 10 mm chip is mounted and wirebonded to a PCB, that is screwed onto a copper base. The four small holes around the chip are used to screw on a small copper lid, covering the chip. The four big holes at the edge of the copper base are used for mounting the chip in a cryostat, and to hold the top cover in place. Connectors for connecting the PCB to the outside world are surface mount SMP plugs. **(b)** Close-up of the bottom-right chip area, taken with ring illumination. The substrate is sapphire, hence the chip transparency. In the bottom right corner, one of the copper rails on which the chip sits is visible. **(c)** The individual parts of our sample holder (clockwise): PCB for 10 mm × 10 mm chips, copper base with rails to mount chip and PCB, small cover, large lid. **(d)** Sample enclosed and mounted in the bottom-loading puck of a *Triton* dilution fridge.

straight plug semi-detent SMP connectors[7].

2.3.2. Filtering and attenuation

Low frequency interference

Current and voltage fluctuations originating from room temperature electronics can carry the typical 50 Hz interference (also dubbed *mains hum*), along with other, high-frequency, components. In our lab, we suppress the mains hum by using battery-powered DC electronics for probing and biasing our circuits, the IVVI rack, made at *DEMO*[8] of TU Delft. The IVVI is controlled via an optical fiber connected to the measurement PCs.

Still, as shown in the Supplementary Material of Chapter 5, to properly suppress the mains hum, battery and mains powered equipment needs to be physically separated from each other. This requires separate grounds between the two, DC blocks for inner and outer conductor attached to all high-frequency lines, as well as placing the IVVI and mains powered equipment on separate racks.

Thermal excitation

Thermal excitation can contribute to quasiparticles in the superconductor, meaning introducing a population of unpaired electrons, compared to the lossless Cooper pairs. Table 2.3 lists the thermal energies and frequencies corresponding to typical temperatures in our setups.

[7] 19S102-40ML5 straight plug PCB, from *Rosenberger Hochfrequenztechnik GmbH & Co. KG*
[8] Dienst Elektronische en Mechanische Ontwikkeling, https://www.tudelft.nl/demo/

2

Table 2.3: Frequencies and energies of thermal noise.

Temperature	Thermal frequency	Thermal energy
300 K	6.25 THz	25.9 meV
50 K	1.04 THz	4.3 meV
4 K	83.3 GHz	345 µeV
1 K	20 GHz	86.2 µeV
100 mK	2 GHz	8.62 µeV
10 mK	208 MHz	862 neV

The origin of these excitations in the so-called Johnson-Nyquist noise due to the thermally activated motion of charge carriers in conductors, regardless of applied voltage [122, 123].

In order to neglect the influence of thermal effects on our circuits and for the superconductor to be in its thermal ground state, it is necessary to operate the devices at temperatures $T \ll T_c$. Since the superconducting gap voltages of NbTiN, MoRe and Al are 2.3 meV, 1.5 meV and 183 µeV, respectively, our experiments require access to the sub-Kelvin regime which is enabled by using dilution refrigerators. However, even with the devices mounted to the base plate of dilution refridgerators (the devices in Chapters 3 and 4 in a *Triton 200* from *Oxford Instruments*, the one in Chapter 5 in a *LD-400* from *Bluefors*), they still experience some active heat load due to the wiring connecting the sample to the room temperature electronics. This way, thermal noise can couple into the devices. It is therefore vital to suppress this noise by means of signal attenuation before reaching the sample, while not sacrificing too much signal-to-noise ratio.

While attenuating the input lines as much as possible seems to be a good idea at first, this is not necessary because the physical temperature of the lowest fridge stage, in our experiments the base temperature of $T_{\mathrm{MXC}} \approx 15$ mK, places a lower bound on the sample temperature, and therefore on the required lowest noise temperature. Additionally, due to low electron-phonon coupling at low temperatures, the electrons in the device most likely have a slightly higher temperature than the fridge itself, as cooling becomes inefficient at these temperatures [124]. Cooling below the fridge temperature is possible, but requires nuclear refrigeration in combination with further attenuation and low electron-phonon coupling [125, 126].

Since we will be probing our devices both at DC and with GHz frequencies, both low and high frequency lines need to be attenuated separately. Our DC lines are attenuated using home-made two-stage RC and copper powder filters (see Appendix C.2 for details). The RC filters have a cutoff frequency $f_{3\,\mathrm{dB}} \approx 30$ kHz and suppress higher frequencies up to 20 MHz. Above this range, radiation starts to leak through again, due to stray capacitance of the filter resistors and parasitic inductance of the capacitors, see Fig. 2.10(a,b). As shown in Fig. 2.10(a), a two-stage filter has a higher slope, −40 dB/decade compared to −20 dB/decade, while exhibiting only a slightly lower cut-off frequency. The radiation leaking through calls for additional, very high-frequency lowpass filters. We use home-made copper powder filters for this purpose, see Fig. 2.10(c,d). These consist of a long PCB trace encased in a copper box, which is filled with copper powder and epoxy, essentially forming a very long and lossy transmission line with very low resistance, suppressing frequencies above a few 100 MHz, as shown in Fig. 2.10(b).

We can estimate the effect of attenuation on the electron noise temperature [127]. With

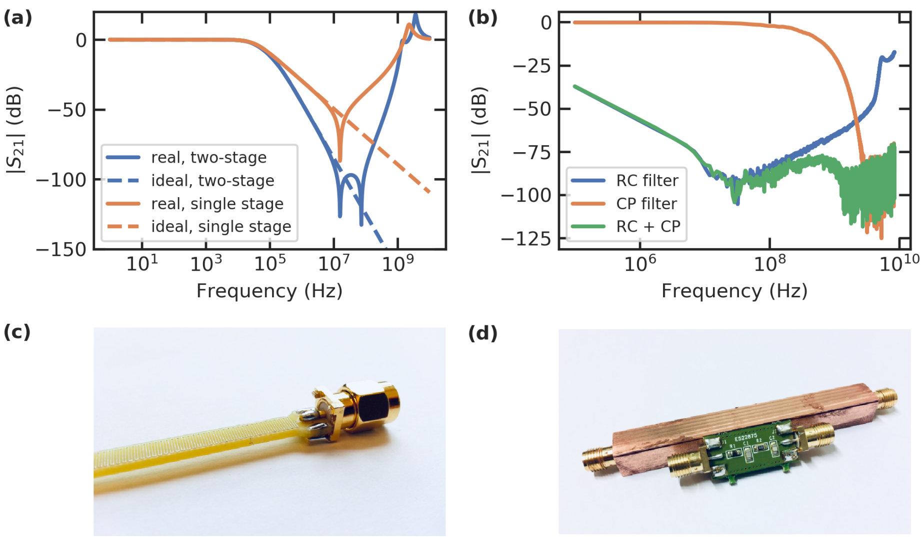

Figure 2.10: Electronic noise reduction using low-pass filters. (a) Simulated transfer function of single (orange) and two-stage (blue) RC low-pass filters. Dashed: ideal filter characteristic, solid: realistic behavior with stray capacitance and inductance. **(b)** Measured transfer function of combinations of two-stage RC lowpass and copper powder filters. Parasitic inductance and capacitances in the RC filter allow radiation to leak through at higher frequencies, which can be suppressed using copper powder filters. **(c)** Copper powder filter PCB with connector, without enclosure. The PCB trace is approximately 50 cm long. **(d)** Photograph of a two-stage RC filter of SMD 0812 elements and a fully assembled copper powder filter (see Appendix C.2 for details).

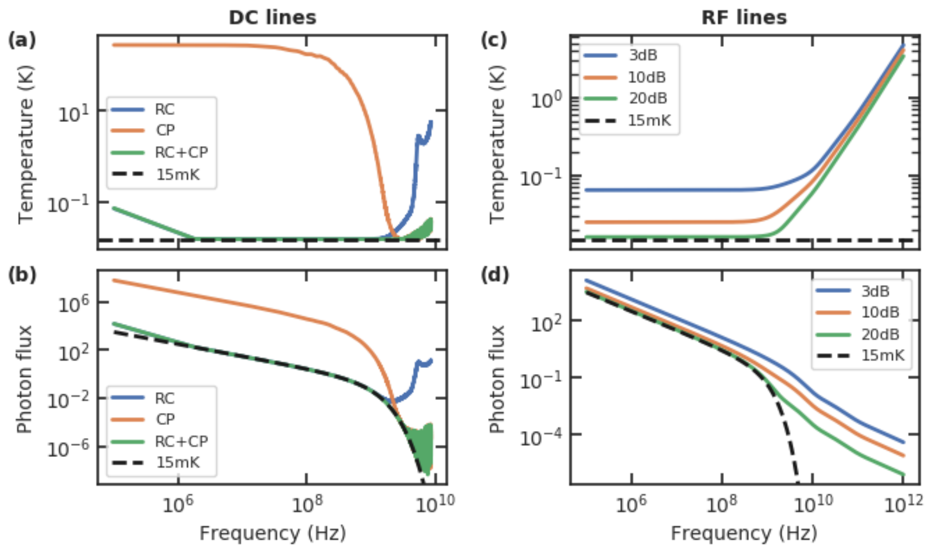

Figure 2.11: Reducing noise temperature through attenuation. **(a,b)** Calculated noise temperature **(a)** and corresponding photon flux **(b)** of the DC lines using typical low-pass filters for attenuation. **(c,d)** Calculated noise temperature **(c)** and corresponding photon flux **(d)** of the RF lines using attenuators of 3 dB, 6 dB, 10 dB, 20 dB at the 50 K, 4 K, 1 K, 100 mK, stages, respectively, together with additional attenuation between 3 dB to 20 dB at the 15 mK stage. Dashed black lines indicate a noise temperature of 15 mK and the corresponding thermal photon flux.

the Bose-Einstein distribution

$$n_{\mathrm{BE}}(f,T) = \frac{1}{e^{hf/k_{\mathrm{B}}T} - 1} \tag{2.1}$$

we can calculate the photon flux at frequency f due to thermal noise coming from T_1 transmitted through a bath at T_2 with transmission τ with the rate equation

$$n_{\mathrm{ph}}(f,T_1,T_2,\tau) = \tau n_{\mathrm{BE}}(f,T_1) + (1-\tau) n_{\mathrm{BE}}(f,T_2) \tag{2.2}$$

The noise temperature of the corresponding photon flux is then

$$T_n = \frac{hf}{k_{\mathrm{B}} \ln\left(\frac{n_{\mathrm{ph}}+1}{n_{\mathrm{ph}}}\right)} \tag{2.3}$$

Our dilution fridges have stages at 50 K, 4 K, 1 K, 100 mK and 15 mK. The DC line filters are placed at the lowest millikelvin stage, while the RF lines typically have attenuators of 3 dB, 6 dB, 10 dB, 20 dB and 3 dB to 20 dB, at the respective stages. In Fig. 2.11, we plot the expected noise temperature and corresponding photon flux for the DC and RF lines. The strong DC attenuation of both copper powder and RC filters ensures a noise temperature of 15 mK, limited by the mixing chamber plate, while without the copper powder filters, the noise temperature would reach 1 K for a few GHz. Assuming the RF attenuators are constant over the entire frequency range, the total distributed attenuation of 42 dB (using 3 dB at 15 mK) would not be enough to cool the electronic noise down to base temperature, but instead would level out at 85 mK at low frequencies. To reach base temperature, attenuation of 20 dB would be required at the mixing chamber, resulting in $T_n = 16$ mK with a total attenuation of 59 dB, see Fig. 2.11(c,d).

Additional attenuation can be gained however naturally from the intrinsic cabling loss, as well as additional components such as bias-tees, circulators or directional couplers, which we typically use in our measurements. In order to minimize the influence of noise coming from frequencies above 10 GHz, constant attenuation as described above is clearly not enough, which can be problematic for superconducting microwave qubits. For this, and also for reducing the effects of black-body radiation, high-frequency absorbing materials such as *Eccosorb* or *Aeroglaze* can be used [127–131]. However, we estimate that our devices are not limited by this loss mechanism, but instead intrinsic circuit losses, as detailed in the following chapters.

3

A BALLISTIC GRAPHENE SUPERCONDUCTING MICROWAVE CIRCUIT

Josephson junctions (JJ) are a fundamental component of microwave quantum circuits, such as tunable cavities, qubits and parametric amplifiers. Recently developed encapsulated graphene JJs, with supercurrents extending over micron distance scales, have exciting potential applications as a new building block for quantum circuits. Despite this, the microwave performance of this technology has not been explored. Here, we demonstrate a microwave circuit based on a ballistic graphene JJ embedded in a superconducting cavity. We directly observe a gate-tunable Josephson inductance through the resonance frequency of the device and, using a detailed RF model, we extract this inductance quantitatively. We also observe the microwave losses of the device, and translate this into sub-gap resistances of the junction at μeV energy scales, not accessible in DC measurements. The microwave performance we observe here suggests that graphene Josephson junctions are a feasible platform for implementing coherent quantum circuits.

This chapter was published in *Nature Communications* **9**, 4069 (2018) [44].

3.1. INTRODUCTION

The development of ultra-high mobility graphene with induced superconductivity has led to ballistic transport of Cooper pairs over micron scale lengths, supercurrents that persist at large magnetic fields and devices with strongly non-sinusoidal current-phase relations [38, 39, 132–134] While most measurements of such graphene Josephson junctions (gJJ) have been limited to the DC regime, Josephson junctions in general also play fundamental role in microwave circuits and devices such as qubits or quantum-limited amplifiers [135, 136].

In these microwave applications, the Josephson junctions used are almost exclusively based on double-angle evaporated aluminum-aluminum oxide tunnel junctions (AlOx) [137], resulting in amorphous superconductor-insulator-superconductor (SIS) barriers. Thus far, despite its robust and tunable superconductivity, graphene has not been implemented in this kind of microwave circuitry. Apart from potentially addressing some of the design and stability issues with AlOx junctions [138, 139], the use of gJJs in such circuits has the additional feature of allowing tunability of the junction properties through an electrostatic gate [28, 29, 38, 39, 132]. This feature can help address problems like on-chip heating and crosstalk in superconducting circuits where SQUIDs are used as tuning elements [140, 141].

Here, we present a superconducting microwave circuit based on a ballistic graphene JJ. The design of our device is such that it also allows DC access to the junction, allowing us to directly compare the DC and RF response of our circuit. While the gate-tunability enables us to directly tune the resonance frequency of the hybrid gJJ-resonator circuit, we also use the RF response to obtain additional information about the junction typically inaccessible through purely DC characterization.

3.2. RESULTS

3.2.1. CIRCUIT DESCRIPTION

The device presented here (Fig. 3.1) consists of a galvanically accessible graphene Josephson junction embedded in a superconducting coplanar waveguide cavity. The cavity superconductor is a molybdenum-rhenium (MoRe) alloy sputter-deposited on a sapphire substrate (Fig. 3.1(a)). The coupling to the external feedline is provided by a parallel plate shunt capacitor that acts as semi-transparent microwave mirror [37, 111]. In contrast to series capacitors often used as mirrors, the use of shunt capacitors allows us to probe the circuit with steady-state voltages and currents, enabling DC characterization of the gJJ. A circuit schematic of the device setup is depicted in Fig. 3.1(d). The gJJ is made from a graphene and hexagonal boron nitride (BN/G/BN) trilayer stack with self-aligned side contacts [89, 97] using a sputtered superconducting niobium titanium nitride (NbTiN) alloy. The stack is shaped into a junction of length $L = 500\,\mathrm{nm}$ and width $W = 5\,\mu\mathrm{m}$. Here, L and W denote the distance between the superconducting contacts and lateral extension, respectively. In order to tune the carrier density of the gJJ, a local DC gate electrode covers the junction and contact area. Optical micrographs of the device are shown in Figs.3.1(b,c) and a schematic cross-section of the gJJ is shown in Fig. 3.1(e). Measurements of a similar second device can be found in Supplementary Figs. 3.14 and 3.14.

3.2.2. DC CHARACTERIZATION

To compare our device with state-of-the-art gJJs, we first perform a purely DC characterization. We sweep the current-bias (I_{dc}) and measure the voltage across the gJJ for different applied

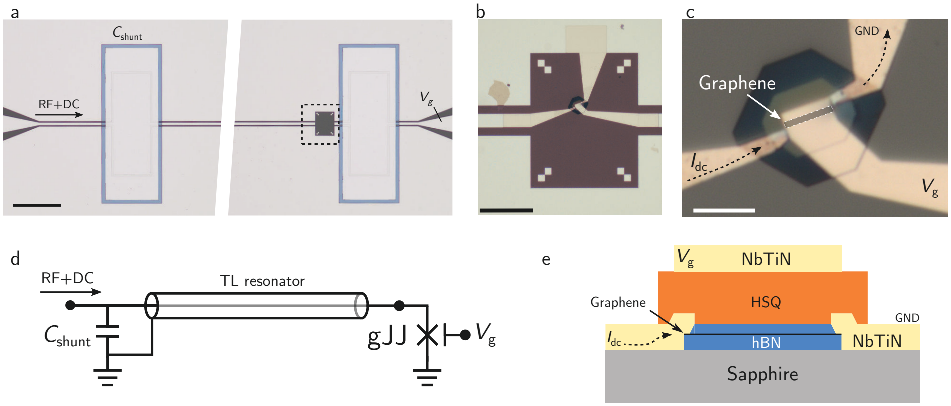

Figure 3.1: A gate tunable microwave cavity based on an encapsulated graphene Josephson junction. a, Optical micrograph of the microwave cavity before placing the hBN/G/hBN stack. Bright areas are MoRe, dark areas are sapphire substrate. Grey area around the parallel plate capacitors is the Si_3N_4 shunt dielectric. Scale bar 200 µm **b,** Optical micrograph of the gJJ. The cavity center line and the ground plane are connected through the gJJ and NbTiN leads. The gate line (right) extends over the entire junction. Scale bar 40 µm **c,** Close-up of panel (b) with the graphene channel indicated. Dark areas are HSQ for gate insulation. Scale bar 5 µm **d,** Sketch of the device circuit. The input signals are filtered and merged using a bias tee before being fed on to the feedline (see Methods section and Supplementary Fig. 3.5). **e,** Schematic cross-section of the gJJ with top-gate, not to scale.

gate voltages (V_g). The resulting differential resistance is plotted in Fig. 3.2(a) and clearly shows a superconducting branch that is tunable through V_g. The junction exhibits I_c in the range of 150 nA to 7 µA for $|V_g| < 30$ V with significantly lower I_c for $V_g < 0$ (p-doped regime) compared to $V_g > 0$ (n-doped regime). Comparing the bulk superconducting gap of our NbTiN leads with the junction Thouless energy, $\Delta/E_{th} \approx 1.52 > 1$, our device is found to be in the intermediate to long junction regime (see Supplementary Note 3.5.7 and Supplementary Figs. 3.16, 3.19 and 3.20).

While in the non-superconducting state (current bias far above the junction critical current I_c), the graphene junction shows a narrow peak in its normal resistance associated with low disorder at the charge neutrality point (CNP, at $V_g \approx -2$ V, see Fig. 3.2(b)), indicating high sample quality. Some hysteresis in the switching and retrapping currents can also be observed in the measurement (see Supplementary Note 5.7.4 for discussion). We furthermore observe oscillations in both the normal state resistance R_n and the switching and retrapping currents as a function of gate voltage for p-doping of the channel. We attribute these effects to the presence of PN junctions that form near the graphene-NbTiN contact. Each of the two NbTiN leads n-dopes the graphene near the respective contact while the main sheet is p-doped by the gate. The pair of PN junctions produce Fabry-Pérot interference effects that give rise to the observed oscillations in I_c and R_n. The characteristics of these oscillations indicate that our junction is in the ballistic regime [38, 39, 70, 115, 142–150].

3

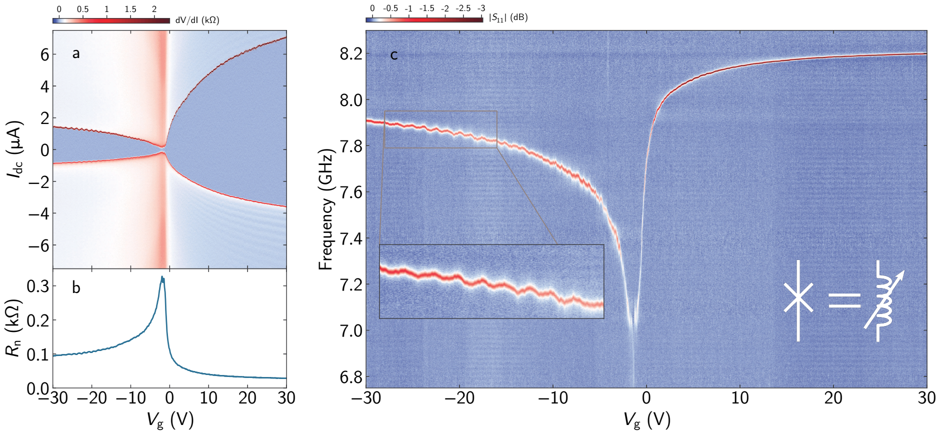

Figure 3.2: Observation of the Josephson inductance of a ballistic graphene superconducting junction. a, Differential resistance across the gJJ for a wide gate voltage range. Dark blue denotes area of zero resistance. The device shows signatures of FP oscillations on the p-doped side. **b,** Normal state resistance of the gJJ versus gate voltage. **c,** Microwave spectroscopy of the device in the superconducting state versus gate voltage, plotted as the amplitude of the reflection coefficient $|S_{11}|$ after background subtraction. The graphene junction acts as a tunable inductor in the microwave circuit, resulting in a cavity frequency that is tuned with gate voltage. Inset: The resonance frequency oscillates in phase with the oscillations in **(a)** and **(b)**.

3.2.3. Microwave characterization

Having established the DC properties of our junction, we turn to the microwave response of the circuit. Using a vector network analyser, we sweep a microwave tone in the 4 to 8.5 GHz range and measure the reflection signal S_{11} of the device for different applied gate voltages $|V_g| \leq 30$ V. The input powers and attenuation used correspond to an estimated intra-cavity photon number of at most 10-20 depending on operating frequency and linewidth. Further tests were performed at lower powers (down to approximately 0.02 intra-cavity photons) with negligible changes to the cavity line shape and width. More information on the measurement setup can be found in the Methods section and a detailed sketch in Supplementary Fig. 3.5. Figure 3.2(c) shows the resulting $|S_{11}|$. A clear resonance dip associated to our device can be tracked as a function of applied gate. The device exhibits a continuously tunable resonance frequency from 7.1 GHz to 8.2 GHz with higher frequencies at larger values of $|V_g|$.

3.2.4. Josephson inductance of the gJJ

The origin of the tunable circuit resonance frequency is the variable Josephson inductance of the graphene Josephson junction. The microwave response of a JJ can be modelled for small currents using an inductor with its Josephson inductance given by:

$$L_j = \frac{\Phi_0}{2\pi}\left(\frac{dI}{d\phi}\right)^{-1}, \tag{3.1}$$

where Φ_0 is the flux quantum. L_j depends on the superconducting phase difference ϕ across the junction and on the derivative of the current-phase relation (CPR). For small microwave

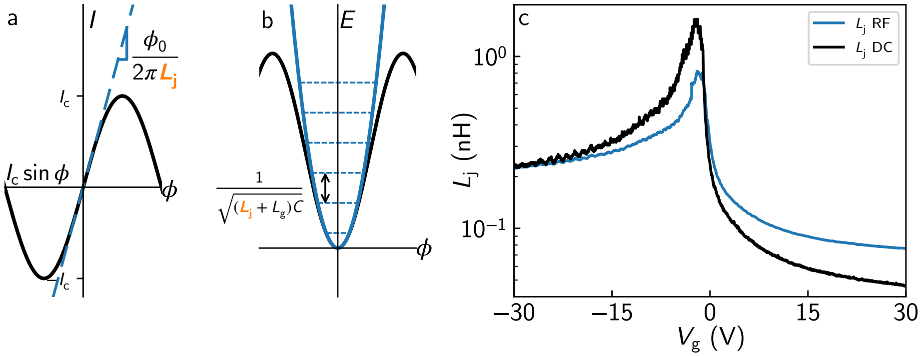

Figure 3.3: Josephson inductance extracted from RF and DC measurements. a, Schematic representation of L_j and its relation to the CPR of a Josephson junction. L_j can be understood as the slope of the current-phase relation around zero phase bias. **b,** Schematic representation of L_j extraction from the cavity resonance frequency. The potential energy near $\phi = 0$ is harmonic, with the fundamental frequency given by the junction inductance L_j and the cavity capacitance C and inductance L_g as $\omega = 1/\sqrt{(L_j + L_g)C}$. **c,** Comparison of Josephson inductance L_j extracted from DC measurements (black) and from the microwave measurements (blue). We attribute differences to deviations from a sinusoidal current phase relation (see main text for details). The error band from our fit of L_j can be found in Supplementary Fig. 3.8.

excitations around zero phase ($\phi \simeq 0$) and assuming a sinusoidal CPR, $I = I_c \sin\phi$, this derivative is $dI/d\phi = I_c$. This leads to an inductance $L_j = L_{j0} \equiv \frac{\Phi_0}{2\pi I_c}$ which can be tuned by changing the critical current of the junction. In the device presented here, this junction inductance is connected at the end of the cavity. When this inductance is tuned, it changes the boundary conditions for the cavity modes and hence tunes the device resonance frequency. The effect can be illustrated by taking two extreme values of L_j (see Supplementary Fig. 3.7): If $L_j \longrightarrow 0$ (i.e. $I_c \longrightarrow \infty$), the cavity boundary conditions are such that it is a $\lambda/2$ resonator with voltage nodes at both ends. If, on the other hand $L_j \longrightarrow \infty$ ($I_c \longrightarrow 0$), the cavity will transition into a $\lambda/4$ resonator with opposite boundary conditions at each end (a voltage node at the shunt capacitor and a current node at the junction end). This leads to a fundamental mode frequency of about half that of the previous case. Any intermediate inductance value lies between these two extremes. Due to the inverse relationship between I_c and L_j, the resonance frequency changes very quickly in certain gate voltage regions, having a tuning rate of up to $df_0/dV_g = 1.8\,\mathrm{GHz\,V^{-1}}$ at $V_g = -0.54\,\mathrm{V}$. This slope could potentially be further increased by increasing the gate lever arm, for example by choosing a thinner gate dielectric. We again note that the resonance frequency does not saturate within the measured range although the tuning rate at $|V_g| = 30\,\mathrm{V}$ is much lower. Additionally, by comparing Figs. 3.2(a) and 3.2(c), we can observe features in the RF measurements that are also present in the DC response. In particular, the Fabry-Pérot (FP) oscillations of I_c and R_n seen in the DC measurements result in a modulation of L_j, producing corresponding oscillations in the cavity frequency. By analysing the oscillation period in reciprocal space, we extract a FP cavity length of $L_c \approx 390\,\mathrm{nm}$ (see Supplementary Figs. 3.17 and 3.18). We can thus take L_c as a lower bound for the free momentum scattering and the phase coherence lengths, i.e. $l_{mfp}, \xi > L_c$.

Further analysis of the data presented in Fig. 3.2(c) can be used to perform a more quantitative analysis of the Josephson inductance of the gJJ as a function of gate voltage. As illustrated in Fig. 3.3(a) and equation (3.1), the Josephson inductance L_j is defined according to the slope of the CPR near $\phi = 0$ and sets the Josephson energy scale. For a given assumed CPR, the inductance can be deduced from a DC measurement of the junction I_c. When measuring the RF response of our device, the current in the junction oscillates with a very low amplitude around $\phi = 0$. This directly probes the CPR slope and the Josephson inductance at zero phase bias. This inductance L_j combined with the cavity inductance L_g and capacitance C determine the resonance frequency (Fig. 3.3(b)). An accurate calibration of the cavity parameters then allows us to extract L_j from our measured resonance frequency without assuming any specific CPR.

To accurately obtain L_j from our measurements, we calibrate the parameters of our RF model of the device using simulations and independent measurements, including effects of the kinetic inductance of the superconductor, the capacitance and inductance of the leads connecting the junction to the cavity, and the coupling to the external measurement circuit (see Supplementary Notes 3.5.1 and 3.5.2, Supplementary Fig. 3.6 and Supplementary Table 3.1) leaving only the junction characteristics as the remaining fit parameters. By fitting the microwave response of the circuit, we obtain the resonance frequency as well as internal and external Q-factors voltage. Using the model, we then translate this into an extracted inductance L_j of the junction for each gate voltage.

Figure 3.3(c) shows the resulting L_j obtained from the dataset in Fig. 3.2(c) compared to that obtained by assuming a sinusoidal CPR together with the DC switching currents from Fig. 3.2(a). At low negative gate voltages we find excellent agreement between the DC and RF models. As the gate voltage approaches the CNP, we observe clear differences, as the DC value of L_j from a sinusoidal CPR overestimates the inductance obtained from the RF measurements. For positive gate voltages, on the other hand, the DC value lies well below the one from our microwave measurements.

To understand the implications of these results, we start first with the p-doped regime. Since the gJJ is intermediate to long junction regime and has low contact transparency at high p-doping due to PN junctions at the contacts, it is expected to have a sinusoidal CPR. In this case, the DC values of I_c should correctly predict Josephson inductance. The clear agreement between the RF and DC values for L_j in this regime is remarkable, and suggests that we have an accurate RF model of the circuit that can be used to extract direct information about the nature of our junction. For high n-doping, the DC measurement yields much lower values of L_j than the ones obtained from our RF measurements. This is in agreement with the fact that high transparency and doping has been observed to produce forward skewing in gJJ CPR [98] which leads to an underestimation of L_j if a sinusoidal CPR is used in the DC calculation. On the other hand, the origin of the mismatch for V_g around the CNP is unclear. Although noise in the bias current can cause DC measurements to overestimate L_j, the noise present in our setup cannot account for this deviation. Alternatively, using the same logic as in the high n-doping case, this deviation could be accounted for with a backward skewed CPR. However, this is contrary to what has been reported in previous measurements on graphene [151].

3.2.5. Microwave losses in the gJJ

While tracking the resonance frequency as a function of gate voltage enables us to extract the Josephson inductance, the resonance linewidth provides information about the microwave losses of the gJJ. The resonance linewidth is also observed to depend on the gate voltage,

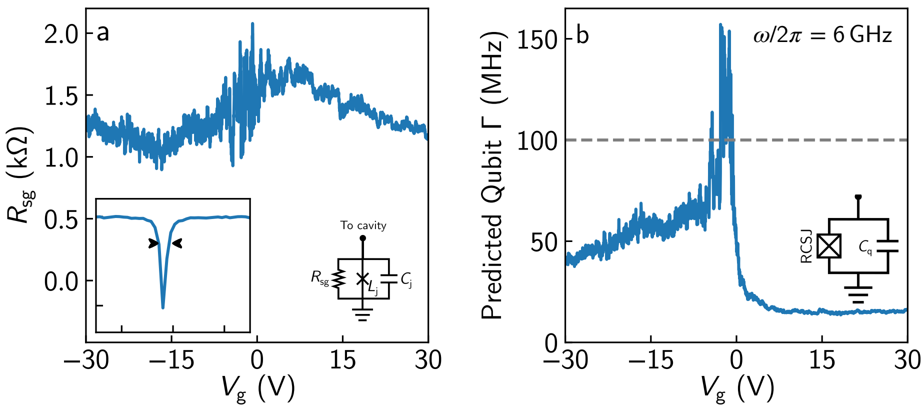

Figure 3.4: Subgap resistance from microwave cavity measurements. a, Extracted sub-gap resistance at as a function of gate voltage. The values are calculated by calibrating the cavity properties and using the junction model shown connected to the transmission line cavity to fit the observed cavity response. Inset shows the cavity response at $V_g = 30$ V. The horizontal and vertical axis divisions are 10 MHz and 10 dB respectively. **b,** Predicted linewidth for a graphene transmon qubit, obtained by taking the RCSJ parameters as a function of gate and adding a capacitance C_q such that the final operating frequency remains $\omega/2\pi = \left(2\pi\sqrt{(L_j(C_j + C_q))}\right)^{-1} = 6$ GHz. We assume the internal junction losses dominate the total linewidth. The horizontal line represents the anharmonicity of a typical SIS transmon $E_c/h =$ 100 MHz. In regions where the blue line falls under the dashed line, a gJJ transmon would be capable of operating as a qubit. The error bands for both panels can be found in Supplementary Fig. 3.9.

with minimum values of $\Gamma \sim 2$ MHz at high $|V_g|$ and a maximum of 80 MHz near the CNP. We use measurements of an identical circuit without the graphene junction as a benchmark to calibrate the internal and external cavity linewidths. Using this benchmark together with a model for the junction losses, we find the correct combination of junction parameters that provide the observed frequency and cavity linewidth. This allows us to quantify the amount of microwave losses attributable to the junction.

We describe the junction using the Resistively Capacitively Shunted Junction (RCSJ) model where the losses are parametrized by a dissipative element R_j. For voltages larger than the superconducting gap Δ the effective resistance $R_j = R_n$ is that of normal state graphene. The RF currents applied in our experiment, however, are well below I_c, and the associated voltages are also well below the bulk superconducting gap. In this regime, the correct shunt resistance for the RCSJ model is not the normal state resistance R_n but instead given by the zero-bias sub-gap resistance $R_j = R_{sg}$. This quantity, which ultimately determines the junction performance in microwave circuits, has not been observed before in graphene as it is only accessible through sub-microvolt excitations, which are difficult to achieve in DC measurements.

As shown in Fig. 3.4(a), the zero-bias sub-gap resistance is of the order of 1 kΩ to 2 kΩ and remains relatively flat on the range of applied gate voltages. We find that the ratio R_{sg}/R_n has values around 10-40, depending on gate voltage, with higher values in the n-doped regime. This ratio is often taken as figure of merit in SIS literature, as lower values of R_{sg} are detrimental to most applications since they imply higher leakage currents in DC and more dissipation in RF.

While R_{sg} of our device is lower than what would be implied by the coherence times in qubits based on low-critical-current oxide SIS junctions [152], the R_{sg}/R_n ratio is comparable to typical values from DC measurements of SIS devices with larger critical currents [153, 154].

The finite sub-gap resistance in superconductor-semiconductor devices is not fully understood, but is thought to originate from imperfect contact transparency, charge disorder and anti-proximity effects [46, 155]. While state-of-the-art SNS devices based on epitaxial semiconductors only recently exhibited hard induced gaps [156, 157], there are to our knowledge no reports of this on graphene devices, suggesting an interesting direction for future research. Another effect leading to finite sub-gap conductance is the size of our device, which is much larger and wider than usually employed junctions in microwave circuits. Depending on the ratio of Δ to the effective round-trip time of sub-gap states across the junction, the Thouless energy E_{th}, the sub-gap density of states can be non-negligible.

From previous reports [158], and from simulations of our channel (see Supplementary Note 3.5.7 and Supplementary Fig. 3.5), it is expected that there are a number of low-lying sub-gap states that could limit the value of R_{sg}. This suggests that the losses could be reduced (R_{sg} increased) by moving towards the short junction regime in which the energies of these states are increased and hence a harder gap forms. To maintain the same inductance L_j, the junction would also have to be made narrower to compensate for the higher critical currents associated with a shorter junction. This would presumably further enhance R_{sg} since low-lying sub-gap states typically originate from states with high transverse momentum. Given the fact that the geometry and aspect ratio of our junction is not at the limit of state-of-the-art fabrication capabilities, reducing the size is a promising step to reduce the losses in future gJJ based devices.

We finally analyse the potential performance of our device for circuit quantum electrodynamics (cQED) applications. We consider the performance of a hypothetical transmon qubit [159] using the inductance of our gJJ operating at $\omega/2\pi = 6$ GHz. Assuming that the qubit losses are dominated by R_{sg}, the quality factor of such a device is given by $R_{sg}/(\omega L_j)$ which in our case is of the order of a few hundred, a reasonable value considering further optimization steps can be taken. In order to qualify as a qubit, the resonator linewidth should be smaller the transmon anharmonicity, given by the charging energy E_c. In Fig. 3.4(b), we compare the predicted gJJ transmon linewidth Γ with a typical value for the anhamonicity of SIS transmon qubits, $E_c/h = 100$ MHz. For a wide range of gate voltages, we find that the predicted linewidth is smaller than the anhamonicity, $\Gamma < E_c/h$, a promising sign for qubit applications of the technology. We note, however, that the critical currents of this junction would be too high at large gate voltages (i.e. our Josephson inductances are too low), requiring a capacitor that would be too large to satisfy the condition $E_c/h \geq 100$ MHz and a resonant frequency of 6 GHz. To reduce the critical current (and increase the Josephson inductance), a narrower junction could be used, which could also increase the subgap resistance, further improving the performance. A more in-depth discussion on this point is included in Supplementary Notes 3.5.3–3.5.5 and Supplementary Figs. 3.10–3.12. We believe that implementing a graphene transmon qubit with good coherence times is feasible for future devices. We also note that while the ballistic nature of the junction is not crucial for its operation in the microwave circuit, the lack of electronic scattering in the channel offers a nice platform to better understand the loss channels in comparison to highly disordered systems, with a potential to use this knowledge in the future to optimize devices.

3.3. Discussion

In summary, we have measured a ballistic encapsulated graphene Josephson junction embedded in a galvanically accessible microwave cavity. The application of an electrostatic gate voltage allows tuning of the junction critical current as well as the cavity resonance frequency through the Josephson inductance L_j. While the DC response of the junction is broadly in line with previous work [38, 39, 132], the RF measurement of the cavity-junction system provides additional information on L_j and microwave losses in this type of junction. A comparison of the DC and RF derived values of L_j reveal deviations from sinusoidal current phase relations, including suggestions of features not previously observed, demonstrating that microwave probes can reveal new information about the junction physics. From the microwave losses of the resonance, we have extracted the junction sub-gap resistance and predicted that, with some optimization, it should be possible to make a coherent qubit based on a gJJ. From the physics of the proximity junctions, we have suggested a route towards improving the coherence potentially towards the current state-of-the-art, enabling a new generation of gate-tunable quantum circuit technology.

3.4. Methods

3.4.1. Fabrication of the microwave circuit

We closely follow a recipe published earlier [37, 111]. In short, a 50 nm film of MoRe is first sputtered onto a 2 in sapphire wafer (430 µm, c-plane, SSP from *University Wafers*). The coplanar waveguide (CPW) resonator is defined using positive e-beam lithography and dry-etching with an SF_6 + He plasma. We subsequently deposit 60 nm of Si_3N_4 for the shunt dielectric using PECVD and pattern this layer with a negative e-beam step and a CHF_3 + O_2 plasma. The top plate of the shunts consists of a 100 nm layer of MoRe which is deposited using positive e-beam lithography and lift-off. An additional shunt capacitor, identical to the one on the main input, is built on the gate line. This will filter RF noise on the gate line and suppress microwave losses through this lead. Finally, we dice the wafer into 10 mm $\times$ 10 mm pieces, onto which the BN/G/BN stacks can be deposited.

3.4.2. Fabrication of the gJJ

We exfoliate graphene and BN from thick crystals (HOPG from *HQ Graphene* and BN from *NIMS* [78]) onto cleaned Si/SiO_2 pieces using wafer adhesive tape. After identifying suitable flakes with an optical microscope, we build a BN/G/BN heterostructure using a PPC/PDMS stamp on a glass slide [89, 97]. The assembled stack is then transferred onto the chip with the finished microwave cavity. Using an etch-fill technique (CHF_3 + O_2 plasma and NbTiN sputtering), we contact the center line of the CPW to the graphene flake on one side, and short the other side to the ground plane. Clean interfaces between the NbTiN junction leads and the MoRe resonator body are ensured by maximizing the overlap area of the two materials and immediate sputtering of the contact metal after etch-exposing the graphene edge. The resistance measured from the resonator center line to ground is therefore due entirely to the gJJ. After shaping the device (CHF_3 + O_2 plasma), we cover it with two layers of HSQ [98] and add the top-gate with a final lift-off step.

3.4.3. MEASUREMENT SETUP

A sketch of the complete measurement setup is given in Supplementary Fig. 3.5. The chip is glued and wire-bonded to a printed circuit board, that is in turn enclosed by a copper box for radiation shielding and subsequently mounted to the mK plate of our dry dilution refrigerator. All measurements are performed at the base temperature of 15 mK. Using a bias-tee, we connect both the RF and DC lines to the signal port of the device while a voltage source is connected to the gate line.

We perform the microwave spectroscopy with a Vector Network Analyser (Keysight PNA N5221A). The input line is attenuated by 53 dB through the cryogenic stages, and 30 dB room temperature attenuators. Adding to these numbers an estimate for our cable and component losses results in a total attenuation on our input line of approximately 92 dB. The sample is excited with -30 dBm, so less than −122 dBm should arrive at the cavity. This corresponds to an estimated intra-cavity photon number of at most 10-20 depending on operating frequency and linewidth (see Supplementary Fig. 3.13). Test were run at $V_g = 30\,\mathrm{V}$ for powers down to −152 dBm, or approximately 0.02 photons, with negligible changes to the cavity line shape. Other gate voltages are expected to have even lower photon populations for with the same setup due to the lower internal cavity Q-factor. The reflected microwave signal is split off from the exciting tone via a directional coupler, a DC block, two isolators and a high-pass filter to reject any low-frequency noise coupling to the line. The signal is furthermore amplified by a 40 dB *Low-Noise Factory* amplifier on the 3 K plate, and two room-temperature *Miteqs*, each about 31 dB, leading to a total amplification of 102 dB. During all RF measurements, the bias current is set to zero.

The DC lines consist of looms with twelve twisted wire pairs, of which four single wires are used in the measurements presented here. The lines are filtered with π-filters inside the in-house built measurement rack at room-temperature, and two-stage RC and copper-powder filters, thermally anchored to the mK plate. To reduce the maximum possible current on the gate line, a 100 kΩ resistor is added at room-temperature. For the DC measurements presented, we turn the output power of the VNA off and current-bias the gJJ, while measuring the voltage drop across the device with respect to a cold ground on the mK plate.

3.4.4. DATA VISUALIZATION

To remove gate-voltage-independent features such as cable resonances, we subtracted the mean of each line for constant frequency with outlier rejection (40 % low, 40 % high) from the original data, resulting in Fig. 3.2(c). All figures representing data are plotted using *matplotlib* v2 [160].

3.4.5. DATA AVAILABILITY

All raw and processed data as well as supporting code for processing and figure generation is available in Zenodo with the identifiers `10.5281/zenodo.1296129` [161] and `10.5281/zenodo.1408933` [162].

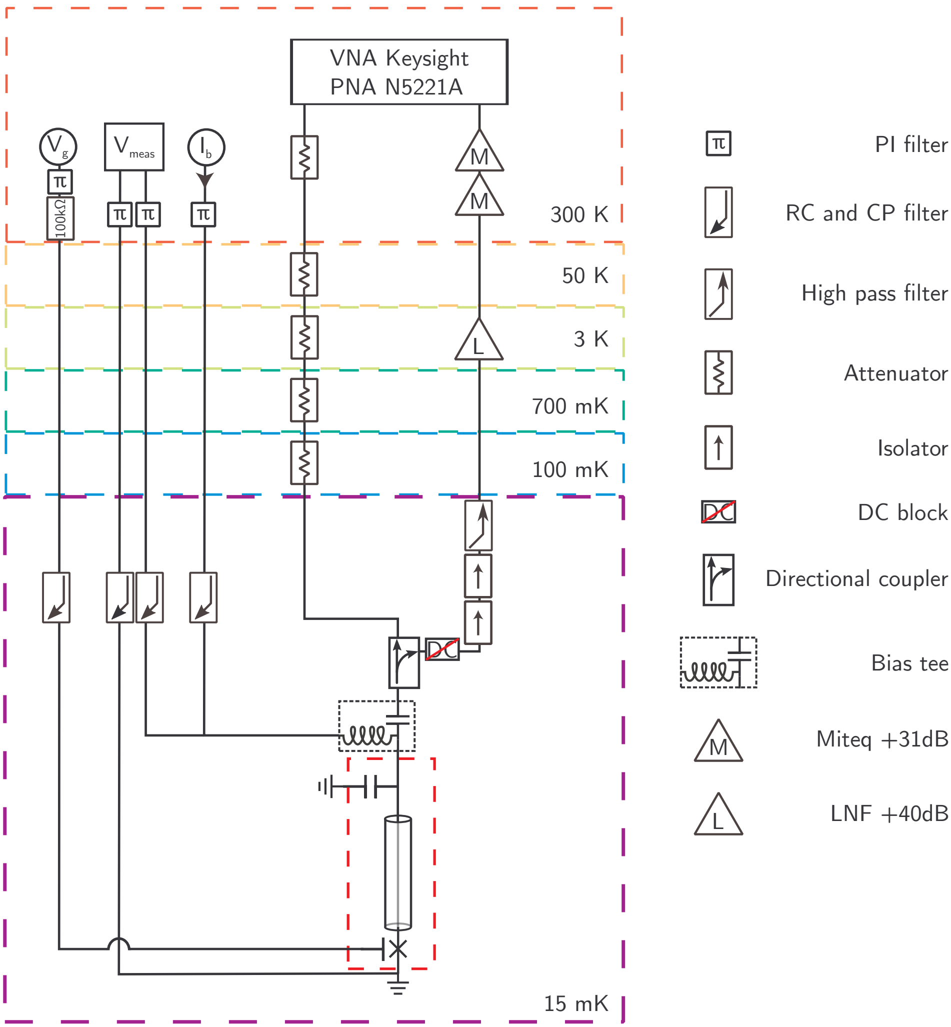

Figure 3.5: Sketched measurement setup. Dashed red box at the bottom marks device outline.

3

3.5. Supplementary Material: A ballistic graphene superconducting microwave circuit

3.5.1. Fitting routine for extracting the resonance frequency

The microwave response function of a capacitively shunted resonator in reflection geometry is given by [163]

$$\Gamma(\omega) = \frac{\kappa_{\mathrm{ext}} - \kappa_{\mathrm{int}} - 2i\Delta\omega}{\kappa_{\mathrm{ext}} + \kappa_{\mathrm{int}} + 2i\Delta\omega}, \tag{3.2}$$

where $\kappa_{\mathrm{ext,int}} = \omega_0/Q_{\mathrm{ext,int}}$ are the internal and external loss rates and $Q_{\mathrm{ext,int}}$ are the respective quality factors. $\Delta\omega = \omega - \omega_0$ is the frequency detuning from the resonance frequency ω_0.

The measured reflection coefficient must also include the effect of the connecting wires and devices between the network analyser and the device under test. The reflection coefficient is accordingly modified to incorporate this background:

$$S_{11} = B(\omega)\left(-1 + \frac{2\kappa_{\mathrm{ext}}e^{i\theta}}{\kappa_{\mathrm{ext}} + \kappa_{\mathrm{int}} + 2i\Delta\omega}\right) \tag{3.3}$$

The complex background $B(\omega)$ has the form:

$$B(\omega) = (a + b\omega + c\omega^2)e^{i(a'+b'\omega)}, \tag{3.4}$$

where a, b, c, a', b' are real parameters. We use this function to fit the measurement data and extract ω_0 and $\kappa_{\mathrm{ext,int}}$.

3.5.2. Extraction of parameters from microwave measurements

The schematic for the gJJ and cavity model can be seen in Supplementary Figure 3.6. A segment of a coplanar waveguide forms a cavity coupled on one side to an input line through a shunt capacitor. The far end of the transmission line (TL) segment has the gJJ modelled using an RCSJ model with an extra inductance and capacitance associated to the junction lead wires.

The parameters needed to characterize the system are described below, listed in Supplementary Table 3.1 and labelled in Supplementary Figure 3.6:

- The transmission line (TL) segment has a length l as well as a capacitance per unit length C' and inductance per unit length L'. TL losses are characterized by the attenuation parameter α. It is worth noting that $L' = L'_{\mathrm{g}} + L'_{\mathrm{k}}$ includes a geometric contribution, L'_{g}, and kinetic inductance contribution [164], L'_{k}.

- The effective value of the shunt capacitance C_{s}. Since C_{s} parametrizes the external cavity coupling, this includes contributions from both the shunt capacitor and the external circuit. The different connectors, wires, and other microwave components introduce impedance mismatches and cable resonances in the input/output lines, changing the external coupling. We use C_{s} to reabsorb most of these effects, hence making it frequency dependent.

- The characteristic impedance of the input line Z'_0 taken as 50 Ω, i.e., the VNA reference impedance.

- The gJJ is characterized by a junction inductance L_j, a junction capacitance C_j and subgap resistance R_sg.
- The junction leads also add a series inductance L_g and a shunt capacitance C_g.

With these inputs, the reflection response of the circuit can be calculated analytically and compared to the measured data. However, most of these parameters need to be calibrated and calculated first in order to deduce the junction parameters from the measurements. The different parameters and calibrations are set as follows:

- The cavity length is set by the design geometry of the cavity $l = 6119\,\mu\mathrm{m}$ and verified through microscope inspection.
- To determine the cavity L' and C' as well as the internal losses (related to α), several cavity measurements from the same batch as the final device were used. From fitting the fundamental mode resonances of these calibration samples we extracted values for L', C', α that we use for the final device. The samples used were:
  - A cavity with no junction at the end (Supplementary Figure 3.7(a)). This means that the fundamental mode frequency is approximately half that of the final device ($\lambda/4$ vs $\lambda/2$ boundary conditions). From this measurement and the physical geometry of the cavity, we deduce values for C', L'.
  - A cavity with a short at the end with the same shape as the final junction leads (Supplementary Figure 3.7(b)). This cavity was used to calibrate the loss parameter α associated to resistive and dielectric losses of the transmission line cavity. In principle, the losses are frequency dependent with higher losses at higher frequencies. Since this loss rate was obtained at the high end of the frequency range and is used for all our frequencies, the extracted loss rates are expected to overestimate the actual losses.
- The leads series inductance L_g and shunt capacitance C_g as well as the junction capacitance C_j were calculated using numerical simulation of the geometry (*COMSOL* v5.3 (COMSOL Inc., 2017) and *Sonnet* v16.54 (Sonnet Software Inc., 2017)). The contribution of the capacitances C_j and C_g are expected to be small compared to C_s. The impedances of these (parallel) capacitances are much larger than the typical impedances of the other circuit elements (L_j or R_sg for example).
- Additionally, L_g is swept between two extreme values given by our simulations representing a range of possible kinetic inductance values for NbTiN, the superconductor used in our leads. This gives the error band shown in Supplementary Figures 3.8 and 3.9.

With this, we are left with three free parameters: L_j, R_sg, C_s. These are determined from fitting the model to the microwave response of the final device as a function of applied gate voltage V_g. In broad terms, L_j sets the device resonance frequency, R_sg sets the internal quality factor (or loss rate) while C_s sets the external quality factor (or coupling). We note also that points around $V_\mathrm{g} = V_\mathrm{CNP}$ fall into a very undercoupled cavity regime, making the resonance peak visibility very low in some cases. This results in some of our fits not converging to the measured curve and producing absurd results. Since some of these peaks are not clearly

3

fittable given the measured background, we have opted to reject these few low visibility traces from the final fitted parameter plots.

3.5.3. Feasibility of a Graphene JJ transmon qubit

In this section we provide an additional discussion on the feasibility of a graphene based transmon qubit.

We first consider the device as presented in the main text. To calculate the anharmonicity of this device we use techniques from the black box quantization method [165]. According to this method, the value of the anharmonicity α is then given by

$$\alpha = \frac{2e^2}{L_\mathrm{j}\omega_0^2(\Im[Y'(\omega_0)])}, \tag{3.5}$$

where L_j is the Josephson inductance of the junction, ω_0 is the resonant frequency of the circuit, Y is the admittance of the circuit seen from the junction terminals (including its own admittance) and Y' its derivative with respect to frequency. The resonance frequency ω_0 then corresponds to the condition $\Im[Y(\omega_0)] = 0$ and the derivative at this point $Y'(\omega_0)$ can be computed.

As can be seen in Supplementary Figure 3.10, the calculated anharmonicity for our main device is always smaller than the measured linewidth. Therefore it does not qualify as a qubit in its current state.

3.5.4. Design scenario A – Measured graphene junction in fixed frequency transmon

While our device is not immediately a qubit, some improvements are possible. Most notably, the junction inductance is diluted by the cavity inductance, resulting in a low participation ratio in the total circuit inductance. We can therefore pose the question of what would the performance of a transmon be that contained only our graphene Josephson junction as its inductive element. This circuit is shown in the inset in Supplementary Figure 3.11(a) and consists of the junction in parallel with a shunt capacitor C_q. The value of this capacitance is set by the requirement that the frequency of the transmon be $\omega_0 = 2\pi \times 6$ GHz. Given the measured values of L_j as a function of applied gate voltage, we can then obtain the anharmonicity as:

$$\alpha = \frac{e^2}{2C_\mathrm{q}}. \tag{3.6}$$

The result is shown in Supplementary Figure 3.11(a) along with the projected linewidth of the device $\Gamma = (R_\mathrm{sg}C_\mathrm{q})^{-1}$. Although the situation is improved in this case, the anharmonicity is still substantially lower than the calculated linewidth. This is due to the fact that we are using a rather wide junction with a somewhat high critical current value and, therefore, a low inductance value. To keep the frequency at the chosen $\omega_0 = 2\pi \times 6$ GHz, the necessary capacitance is then too large to make a qubit. This could be resolved by making our junction narrower, hence increasing its inductance, as we shall see below.

3.5.5. Design Scenario B – Adjusted width graphene junction in fixed frequency and anharmonicity transmon

In this case we consider the same circuit as in the previous case. Now, however, we fix the capacitance so that the anharmonicity $\alpha = 100\,\mathrm{MHz}$. This sets the value of our capacitance $C_q \simeq 0.2\,\mathrm{pF}$. Since we also keep the requirement that $\omega_0 = 2\pi \times 6\,\mathrm{GHz}$, our junction inductance is fixed to a value of $L_j = (\omega_0^2 C_q)^{-1} \simeq 3.5\,\mathrm{nH}$. Given these requirements and the measured values of inductance for our device, we can deduce what junction width would be necessary at each gate voltage V_g to produce the required inductance.

Here we make the assumption that both L_j and R_{sg} scale with the inverse of the junction width, i.e., approximately as W^{-1}. This should be the case for L_j since $L_j \propto I_c^{-1} \propto R_n \propto W^{-1}$ since the $I_c R_n$ product in a ballistic junction is constant [42]. R_{sg} does not necessarily have to scale as R_n. It does, however, depend on the number of conduction channels available and on the graphene proximity gap. The number of channels should scale linearly with the width of the junction while the proximity gap should increase as high transverse momentum channels are suppressed. It is therefore reasonable to assume that R_{sg} scales at least as fast as L_j.

With these assumptions we can then calculate the required width and expected linewidth shown in Supplementary Figure 3.12. In this case there is an ample range of gate voltages that comply with the condition $\Gamma < \alpha$. The required junction widths are always above 100 nm, a limit that is within reach of state of the art fabrication techniques. It is on this basis that we propose that it is feasible to construct a graphene based transmon qubit.

3

3.5.6. Hysteresis of the junction switching current

The observed hysteresis in the switching current of our devices (see Figure 3.1(a) of main text, and Supplementary Figure 3.15(a)) could have various origins. A valid estimation of the relevant Stewart-McCumber parameter [166], $\beta_C = 2\pi I_c R^2 C/\Phi_0$, is not straightforward because there is always the question of how much capacitance of the leads going to the junction should be included. In principle, for example in DC measurements, even a portion of the wires going up the cryostat could be arguably relevant, up to a point where the inductance of these wires "chokes" the capacitance contribution.

We here discuss several estimates of possible relevant capacitances that could enter into β_C, where we assume a typical $R = 50\,\Omega$ and $I_s = 5\,\mu\mathrm{A}$. First, we note that the "geometric" capacitance of a parallel plate capacitor formed between the superconducting leads across the BN/G/BN stack yields a negligible value on the order of a few tens of atto Farads. More important is the "local" stray capacitance of the junction which we have simulated in *COMSOL* v5.3 (COMSOL Inc., 2017) and *Sonnet* v16.54 (Sonnet Software Inc., 2017). If we include the leads up to a distance of 5 µm from the junction, the relevant $C = 2\,\mathrm{fF}$ and $\beta_C = 0.08$. We also simulated the capacitance of the leads that go from the junction to the surrounding ground plane and to the CPW cavity, giving $C = 6.7\,\mathrm{fF}$ and $\beta_C = 0.25$. Of course, there is also likely a relevant capacitance contribution from the center conductor of the CPW to ground. For this, we can make a rough estimate of the total CPW center conductor capacitance of 909 fF and a resulting $\beta_C = 35$, reaching far into the underdamped regime. Finally, one could also include the shunt capacitor of 27 pF, which would give $\beta_C > 1000$. The last two are likely not completely relevant, since at the Josephson frequency associatated with the finite bias state of the junction ($\omega_P = \sqrt{2\pi I_c/(\Phi_0 C)} = 24\,\mathrm{GHz}$), the shunt capacitor will not charge through the inductance of the center wire of the cavity. More likely, the relevant β_C includes some reasonable contribution of the CPW capacitance: for example, assuming

$C = C_{\mathrm{CPW}}/10 = 90\,\mathrm{fF}$ would give a $\beta_{\mathrm{C}} = 3.4$ In addition to these damping effects, self-heating effects inside the SNS junction could further contribute to a hysteretic IVC [167, 168].

3.5.7. Simulation of sub-gap density of states

To gain further insight into the underlying mechanisms of our junction, we model the density of states (DOS) of a gJJ similar to our device with the software package *Kwant* v1.3 [169]. The relevant energies to consider are the bulk superconducting pairing potential Δ and the effective round-trip time of the Cooper pairs inside the junction, the Thouless energy $E_{\mathrm{th}} = \hbar v_{\mathrm{F}}/L$. From the critical temperature of our NbTiN leads (see Supplementary Figure 3.20) we estimate [166] $\Delta = 1.764 k_{\mathrm{B}} T_{\mathrm{c}} \approx 2\,\mathrm{meV}$. Our device is then placed in the intermediate to long regime, $\Delta/E_{\mathrm{th}} \approx 1.52 > 1$.

The modelled system consists of a discretized 2D honeycomb lattice with infinite boundary conditions in y-direction. The superconducting areas are implemented by setting the pairing potential of these regions to a finite value, effectively making the graphene itself superconducting. For the simulation shown we assume full SN coupling, corresponding to a contact transparency $Tr = 1$. The simulated system size was $L_{\mathrm{N}} = 60$ and $L_{\mathrm{SC}} = 300$ (both in units of the graphene lattice constant $a = 0.214\,\mathrm{nm}$), while we adjusted the pairing potential such that the junction is in the intermediate regime, i.e. $L_{\mathrm{N}}/\xi = \Delta/E_{\mathrm{th}} = 1.52$. The dispersion is obtained by solving the eigenvalue problem of the Hamiltonian discretized onto the implemented system and plotting the energy values as a function of transverse momentum $k_{\|}$ (see Supplementary Figure 3.16).

As expected, there are several Andreev Bound States (ABS) hosted below the bulk gap, significantly reducing $\Delta_{\mathrm{ind}} < \Delta_{\mathrm{bulk}}$ and opening possible dissipation channels for RF excitations. As the chemical potential $\mu \gg \Delta$, the subgap states do not change much with doping, in agreement with the relatively flat R_{sg} in Figure 3.4(b) of the main text. In two-dimensional JJs, the aspect ratio can also play a non-negligible role, as there can be a second effective Thouless energy related to the transverse length, or width of the junction, $E_{\mathrm{th}}^{\|} = \hbar v_{\mathrm{F}}/W_{\mathrm{N}}$. Hence, as the aspect ratio increases, the DOS below the bulk gap can rise significantly. Alternatively, one can understand this via the subgap dispersion: ABS with lowest energies are those exhibiting large transverse momentum because their effective path length is longer. The wider the junction, the longer the maximum direct paths across it become, thus the increase in subgap DOS. With $W_{\mathrm{N}}/L_{\mathrm{N}} \approx 10$, this is a contributing factor in our device.

Note that this discussion gets more complicated when considering the contact interfaces between the normal and superconducting parts, as for reduced contact transparencies the subgap states are even further pushed towards zero energy.

We confirm the validity of our simulation by calculating the energies of both infinite and finite systems for various scaling factors. The infinite system is the limit of the finite system with aspect ratio $L_{\mathrm{N}} \ll W_{\mathrm{N}}$. For a very narrow gJJ (lateral extension comparable or equal to distance between superconducting contacts), the DOS is much lower below the bulk gap compared to a very wide junction. The reason for this is the much higher level spacing for a narrow system that pushes additional states above the gap. Hence, to obtain a SNS system with hard and large induced gap, the normal part should be as narrow and short as possible.

We note that these peaks are not directly visible in our measurements, since instead of measuring the voltage drop across a current-biased JJ they require spectroscopy of the DOS via a tunnel probe, such as in Pillet *et al.* or Bretheau *et al.* [46, 170].

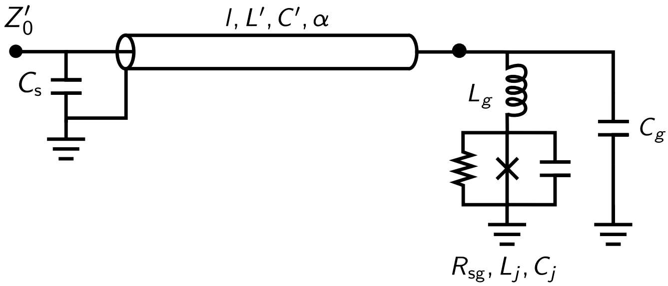

Figure 3.6: RF model for gJJ in cavity used for extraction of microwave parameters. For the fitting procedure see 3.5.2.

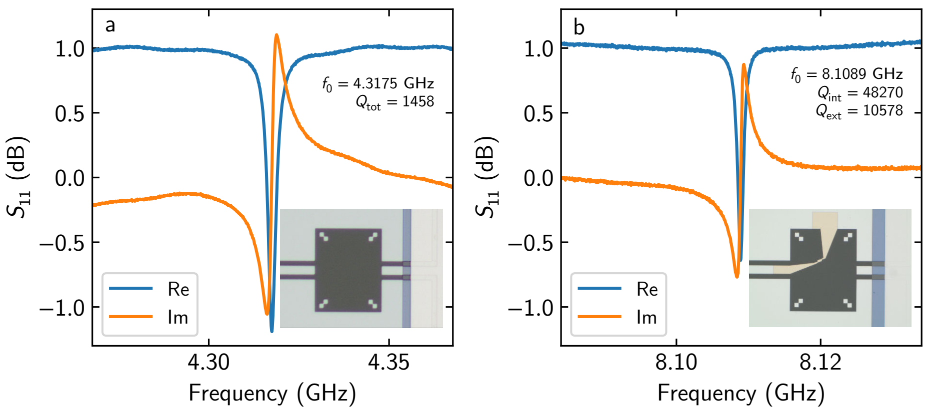

Figure 3.7: Reference samples for extraction of microwave parameters. a, Open-ended cavity measurement of the real (imaginary) part of the reflection coefficient plotted in blue (orange). Inset: Optical micrograph of junction area of the measured device (open end). **b,** Shorted-cavity measurement with same lead geometry as the actual gJJ sample. Inset: Optical micrograph of junction area of the measured device (connected to ground).

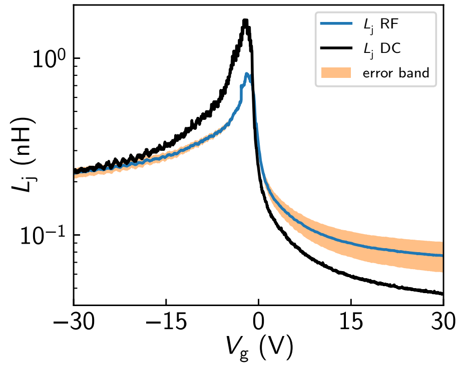

Figure 3.8: Josephson inductance extracted from RF and DC measurements, including error bands. We plot here the same quantities as in Figure 3.3 of the main text but include error bands corresponding to minimum and maximum values originating from uncertainties in the circuit. The scales are identical to the plots in the main text.

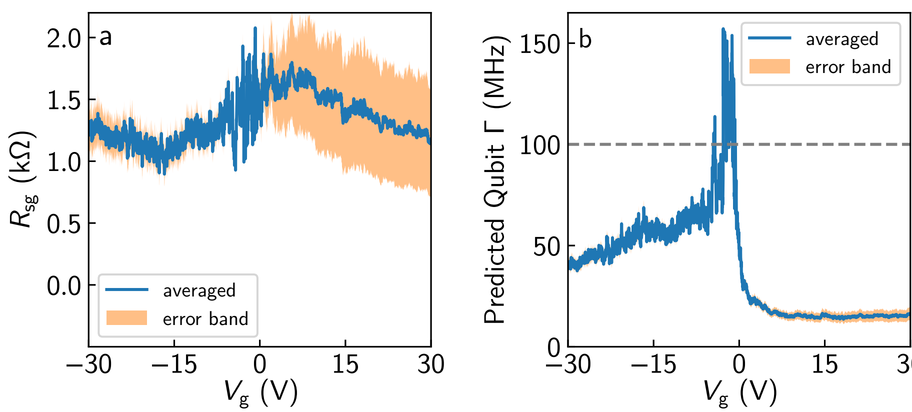

Figure 3.9: Subgap resistance from microwave cavity measurements, including error bands. We plot here the same quantities as in Figure 3.4 of the main text, but include error bands corresponding to minimum and maximum values originating from uncertainties in the circuit. The scales are identical to the plots in the main text. **a,** Subgap-resistance including error band. **b,** Corresponding linewidth of the hypothetical transmon with error band.

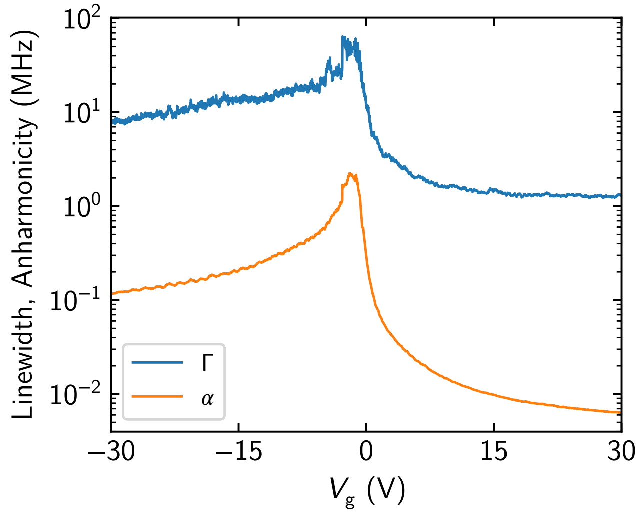

Figure 3.10: Anharmonicity and internal linewidth of current device, as described in 3.5.3. The calculated values of anharmonicity are always smaller than the measured linewidth meaning that this device cannot be considered a qubit in its current form.

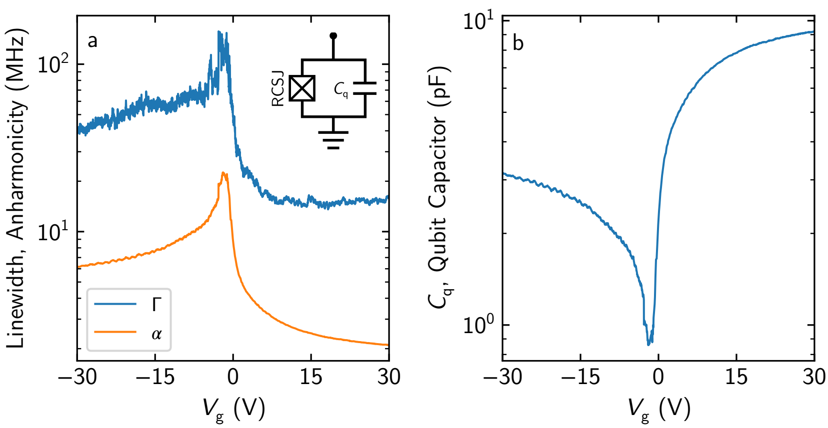

Figure 3.11: Anharmonicity and internal linewidth for design scenario A, as described in 3.5.4. a, We calculate the performance of the measured junction in a circuit such as the one shown in the inset. Setting the resonant frequency to $\omega_0 = 2\pi \times 6\,\text{GHz}$, we then calculate the anharmonicity and linewidth of this hypothetical device. Also in this case we find that calculated values of anharmonicity are always smaller than the linewidth. **b,** Required value of capacitance C_q to maintain a resonant frequency of $\omega_0 = 2\pi \times 6\,\text{GHz}$ as a function of V_g

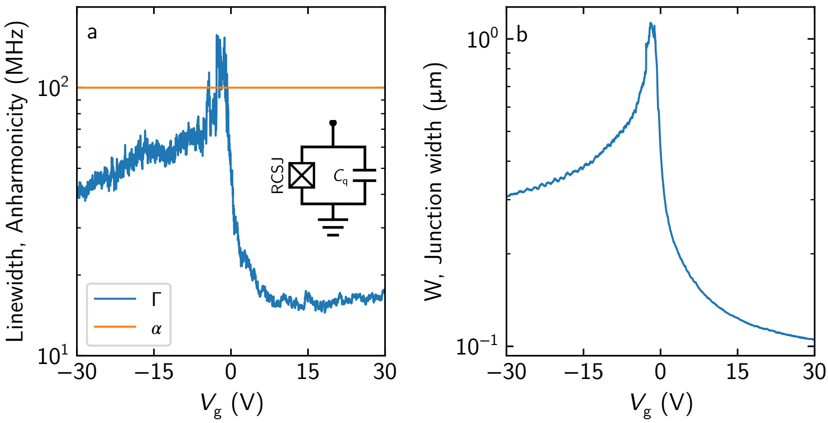

Figure 3.12: Anharmonicity and internal linewidth for design scenario B, as described in 3.5.5. a, We calculate the performance of a device whose capacitance and inductance are set by the requirement $\alpha = 100$ MHz and $\omega_0 = 2\pi \times 6$ GHz. This means scaling the junction width as a function of V_g. The expected linewidth Γ is shown along with the designed anharmonicity. **b,** Required junction width to maintain a resonant frequency of $\omega_0 = 2\pi \times 6$ GHz and $\alpha = 100$ MHz as a function of V_g.

l (TL length)	6119 µm
C' (Capacitance per unit length)	0.148 48 nF/m
L' (Total inductance per unit length)	0.619 838 µH/m
C_s (Shunt coupler capacitance)	~27 pF
Z_0 (TL Characteristic impedance)	64.611 Ω
Z_0' (Reference impedance)	50 Ω
v_{ph} (Phase velocity in TL)	$1.042\,38 \times 10^8$ m/s = 0.3477 c_0
$L_g' = \frac{\mu_0}{4}\frac{K(k_0'^2)}{K(k_0^2)}$ (Geometric inductance per unit length)	0.4277 µH/m
L_k' (Kinetic inductance per unit length)	0.1922 µH/m
L_k'/L' (Kinetic inductance fraction)	0.31
L_g (Geometric inductance of junction leads)	70 pH–100 pH
C_g (Geometric capacitance of junction leads)	4.7 fF
C_j (gJJ capacitance)	2 fF
α (Attenuation at 8.1089 GHz)	0.006 073 m^{-1}

Table 3.1: Transmission line, coupler and junction parameters with kinetic inductance correction included, as described in 3.5.2.

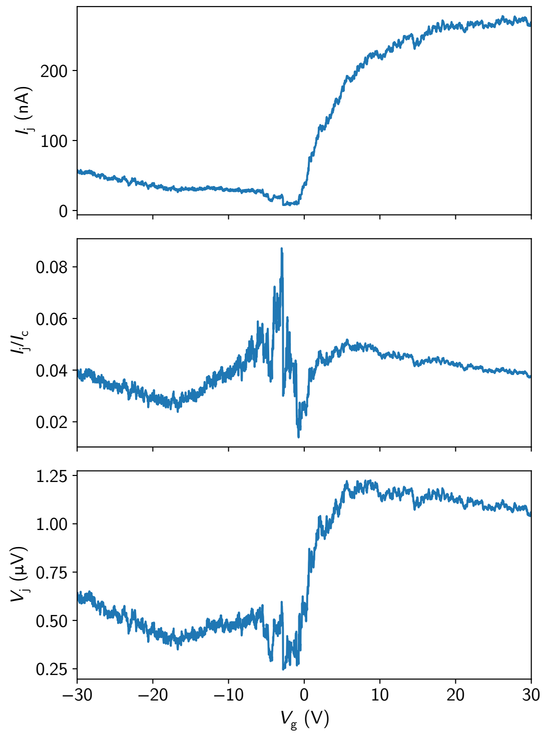

Figure 3.13: Current and voltage amplitude at junction for measurement in Figure 3.2(c) of main text. The input power at the device is estimated to be approximately −122 dBm. Currents are well below the measured critical current of the junction, even near the charge neutrality point. The average voltage across the junction induced by the microwave tone is lower than 1 μV.

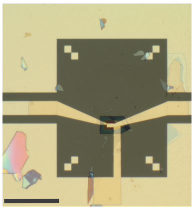

Figure 3.14: Microscope image of second graphene superconducting junction. The flakes around the device are hBN residues from the transfer process. Scale bar 40 μm.

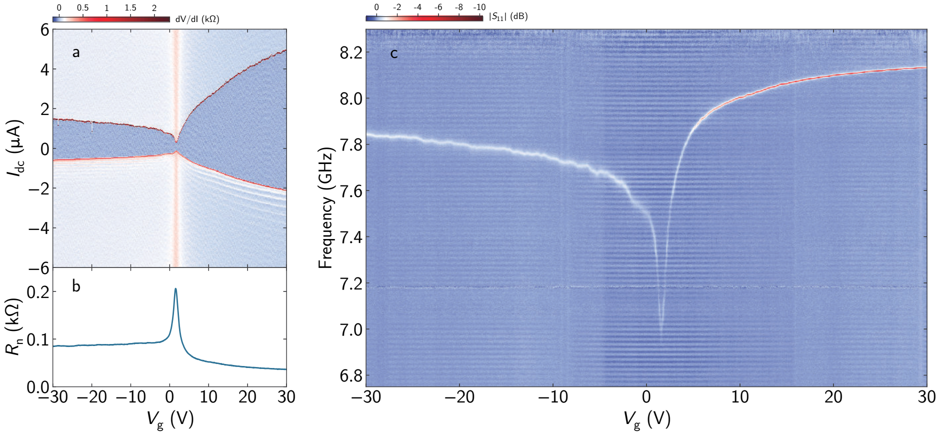

Figure 3.15: Observation of the Josephson inductance of a second graphene superconducting junction. **a,** Differential resistance across the gJJ (Supplementary Figure 3.14) for a wide gate voltage range. Dark blue denotes area of zero resistance. **b,** Normal state resistance of the gJJ versus gate voltage. **c,** Microwave spectroscopy of the device in the superconducting state versus gate voltage, plotted as the amplitude of the reflection coefficient $|S_{11}|$ after background subtraction. Remarkably, its performance is broadly similar to the main text device (see Figure 3.2 of main text), despite having been stored at room temperature in a nitrogen box for ten months before measurement.

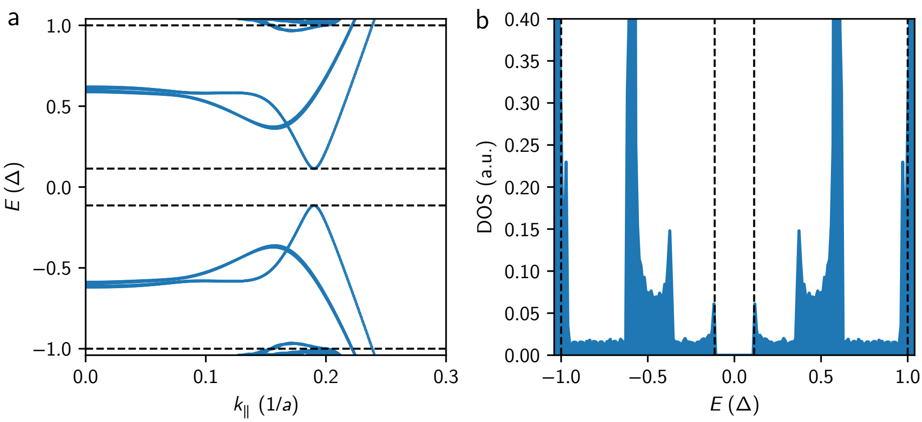

Figure 3.16: Dispersion and density of states of a gJJ, as described in 3.5.7. a, Simulated subgap dispersion for a graphene junction in the intermediate regime, $\Delta/E_{\text{th}} = 1.542$ with $L_{\text{N}} = 60$ and infinite lateral extension W_{N}. Energy is scaled with respect to Δ, $k_{\parallel}$ in terms of momentum parallel to the SN-interface. **b,** By binning the energy dispersion we obtain the density of states as a function of energy. Various subgap peaks originating from ABS with high transverse momentum occur, while a hard gap remains, as indicated by the dashed horizontal lines. The size of the hard gap is limited by the Thouless energies describing transport parallel and perpendicular to the SN interface. A narrow and short junction (L_{N}, $W_{\text{N}} \longrightarrow 0$, $\Delta \ll E_{\text{th}}$) would exhibit a larger induced gap.

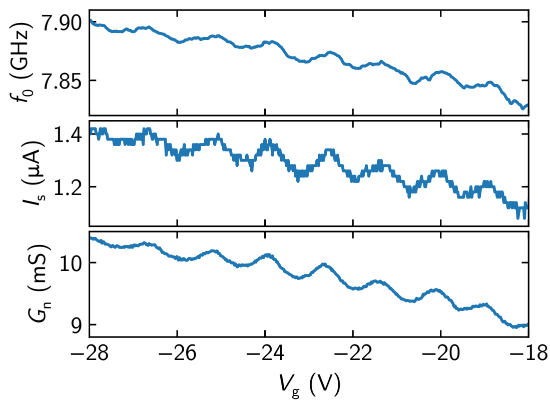

Figure 3.17: Correlating oscillations in DC and RF measurements. We observe reproducible and matching oscillations in-phase oscillations of resonance frequency, critical current and normal state conductance in the npn-regime. We attribute these to interfering electron waves partially reflected from the SN interfaces at the graphene-superconductor contacts: Since NbTiN slightly n-dopes the contact region (hence the asymmetry in R_n as a function of gate voltage), pn-junctions form at the interface once the graphene is driven into the p-doped regime by the gate voltage. In the case of ballistic transport across the graphene sheet, the different charge carrier trajectories interfere with each other. Varying the gate voltage leads to a change in Fermi wavelength and hence an alternation of constructive and destructive interference, resulting in reduced and suppressed conductance, supercurrent, or inductance. This is akin to Fabry-Pérot oscillations of light waves in free space, bound by two mirrors. The observation of these Fabry-Pérot oscillations in graphene-based systems is uniformly taken as evidence of ballistic transport [38, 39, 70, 115, 142–150]. We therefore conclude that our device is also in the ballistic regime. We analyse these oscillations in Supplementary Figure 3.18.

3

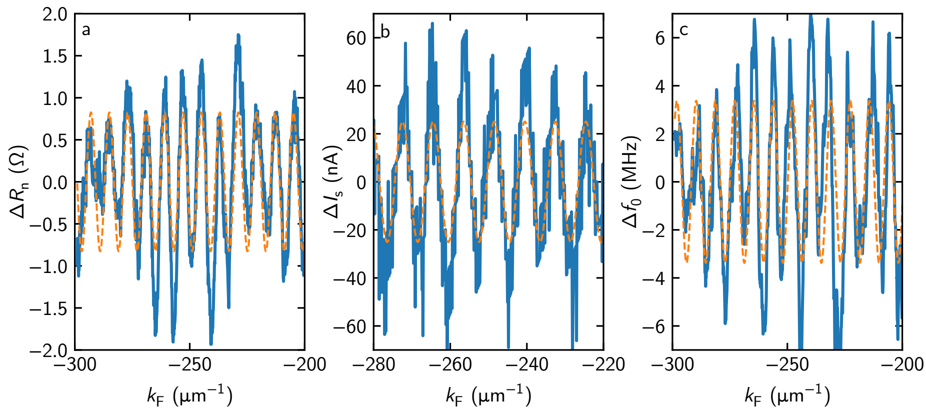

Figure 3.18: Fabry-Pérot oscillations in ballistic gJJ. We observe FP oscillations in **(a)** R_n, **(b)** I_c and **(c)** f_0. We can extract the length of the resonant cavity by fitting our oscillating signal with a sine, according to the resonance condition $2L_c = m\lambda_F, m \in \mathbb{N} \longrightarrow 2L_c k_F = 2\pi m$. After subtracting a slowly varying background with a third-order polynomial [38], the fits for R_n, I_c and f_0 (orange lines) independently yield $L_c \approx 390$ nm. This suggests a contact interface barrier of no more than 55 nm on each side. We can thus take L_c as a lower bound for the free momentum scattering and the phase coherence lengths, i.e. $l_{mfp}, \xi > L_c$.

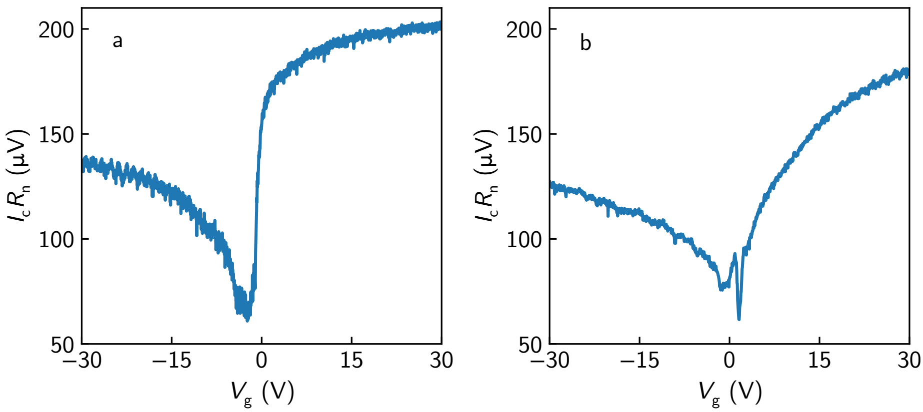

Figure 3.19: $I_c R_n$ product of gJJ devices. The $I_c R_n$ product in Josephson junctions is directly proportional to the gap voltage [166], with $I_c R_n \geq 2.08\Delta/e$ in the case of ballistic graphene junctions [42, 171]. **a,** In our main device, this quantity saturates at approximately 200 µV for high n-doping, drops to 50 µV around CNP, and reaches up to 130 µV for high p-doping. We take the small dependence on gate voltage in high doping regime as further indication of ballistic transport [71, 150]. Taking the bulk gap of the leads to be $\Delta = 1.764 k_B T_c = 2$ meV, our maximum $I_c R_n = 0.1\Delta$ which is much lower than the theoretically expected value. We attribute this to reduced contact transparency and our junction being in the long regime, where the Thouless energy $E_{th} = hv_F/L < \Delta$ is the dominant energy scale, limiting $I_c R_n$ [172]. Our observation matches that of various other groups [39, 71, 148, 150]. **b,** In contrast, the additional device lacks the saturating behaviour, and exhibits a lower $I_c R_n$ product. This, in addition to the absence of FP oscillations, leads us to conclude that the latter device is non-ballistic, possibly due to a slightly longer normal region, or residual dirt (such as bubbles) in the graphene channel.

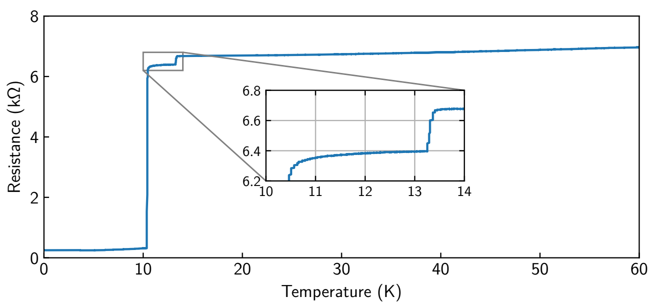

Figure 3.20: Critical temperature of MoRe and NbTiN. Resistance versus temperature of the gJJ sample, measured during the initial cooldown, for a current bias of 1 µA without any gate voltage applied. The two jumps at 10.5 K and 13.2 K correspond to the critical temperature of MoRe and NbTiN, respectively. Below $T_{c,MoRe}$, we measure a residual resistance of 250 Ω, which corresponds to the graphene sheet resistance for $V_g = 0$ V.

4

Probing the current-phase relation of graphene Josephson junctions using microwave measurements

We perform extensive analysis of graphene Josephson junctions embedded in microwave circuits. By comparing a diffusive junction at 15 mK *with a ballistic one at* 15 mK *and* 1 K*, we are able to reconstruct the current-phase relation.*

This chapter is based on previously unpublished data of the devices presented in Chapter 3. A preprint of this chapter is available at arXiv:2007.09795 [173]. Data and code to reproduce the calculations and figures presented here can be found on Zenodo [174].

4.1. Introduction

Josephson junctions (JJs) are widely used in microwave (MW) applications, such as quantum limited amplification and sensing, where JJs are exploited as nonlinear inductors. For the use of JJs in superconducting quantum information circuits, the junction nonlinearity has a major effect on the circuit requirements and capabilities [43]. However, the exact Josephson inductance can significantly differ between junctions: While JJs are generally non-linear elements, the specific non-linearity depends on the current-phase relation (CPR) which in turn is determined by the underlying physics inside the junction.

The current-phase relation is a fundamental property of the JJ, relating the supercurrent I_J flowing across a weak link between two superconducting banks with the phase difference δ between the two superconductors. It results from the first derivative of the Josephson energy potential with respect to phase, $I_\mathrm{J}(\delta) = (2e/\hbar)\partial_\delta V(\delta)$. For the ideal case of a JJ formed by a thin insulating tunnel barrier between two superconducting electrodes (SIS), the Josephson potential is given by $V(\delta)/E_\mathrm{J} = 1 - \cos\delta$ and the CPR has pure sinusoidal character as given by the first Josephson relation, $I_\mathrm{J}(\delta) = I_\mathrm{c}\sin\delta$ [6, 175].

4

However, in JJs formed by normal conductors between superconductors (SNS) such as graphene Josephson junctions (gJJs), transport across the JJ is governed by Andreev bound states (ABS), each with ground state energy

$$V_i(\delta)/\Delta_0 = 1 - \sqrt{1 - \tau_i \sin^2(\delta/2)} \tag{4.1}$$

with transmission probability τ_i and superconducting gap Δ_0 [41, 42]. Assuming a JJ with N channels of equal τ_i, i.e. $\tau = \sum \tau_i/N$, the corresponding CPR is given by

$$I_\mathrm{J}(\delta) = \frac{\pi\Delta_0}{2eR_\mathrm{n}} \frac{\sin\delta}{\sqrt{1 - \tau\sin^2(\delta/2)}}, \tag{4.2}$$

with the Boltzmann constant k_B and normal state resistance $R_\mathrm{n} = R_\mathrm{q}/N = h/(Ne^2) \approx 25.812\,\mathrm{k\Omega}/N$ [132, 176]. Here, R_q denotes the quantum Hall resistance and N the number of conducting channels. Depending on τ, the CPR can exhibit significant forward skew compared to the case of a purely sinusoidal CPR in SIS JJs. While the CPR of gJJs has been studied in the DC regime [98, 151], and gJJs have been successfully incorporated in MW circuits [44, 117, 177], the influence of the potentially skewed CPR has not been studied in the latter.

Here, we analyze the effect of a nonlinear CPR on the microwave performance of gJJ embedded in microwave circuits. Measuring two devices in different states, we compare the influence of scattering transport and temperature on the JJ nonlinearity. Our circuit design allows in-situ, and even simultaneous, DC and MW measurements, providing us with various measurement types to compare. The results show the usefulness of combining DC and MW in the same circuits for fundamental research on Josephson junction physics, which distinguishes it from pure MW CPR measurements [178].

4.2. Circuit characterization

Our circuit consists of a DC-bias microwave cavity formed by a coplanar waveguide (CPW) which is shunted by a large capacitor at the input, and shorted to ground on the far end by a gJJ that can be tuned with a gate voltage (V_g), see Fig. 4.1(a) and Refs. [37, 44, 179]. The superconducting base layer and shunt capacitor metal layers consist of DC-sputtered molybdenum-rhenium on a sapphire substrate, while the shunt capacitor dielectric layer is PECVD-SiN_x. The gate voltage lead is fed through a second shunt capacitor of the same geometry as the one at the input in order to suppress MW radiation leaking in through or out of the gate line. The MW wiring of both samples was fabricated on a single 2 inch sapphire wafer, after which the wafer was diced into 10 mm × 10 mm pieces onto which the individual gJJ were placed. The gJJ consist of boron nitride encapsulated single layer graphene with side-contacts of DC-sputtered niobium titanium nitride (NbTiN), fabricated via the etch-fill technique [44, 97]. The gJJ are designed to be 5 µm wide and separate the NbTiN leads by a length of 500 nm. Gate tunability is achieved by placing a third NbTiN lead extending over the entire gJJ, separated by a bilayer of HSQ. The circuit is wirebonded into a PCB that is mounted on the millikelvin plate of a dilution refrigerator and connected to the outside world via a bias-T, allowing both DC and MW characterization in the same setup. To suppress thermal excitations, the MW input line is heavily attenuated and all DC lines were equipped with π-filters in the room temperature battery powered electronics, as well as copper powder and two-stage RC filters thermally anchored to the millikelvin stage.

We measured two separate devices with nominally identical microwave circuits and junction designs: One of the devices exhibited signatures of ballistic transport in form of Fabry-Pérot-like oscillations, which we will refer to as the *ballistic device* (see Supplementary Material Sec. 4.6.1 and Fig. 4.5). This is the device presented in the main text of Ref. [44]. The other one, in lack of such features, will be called *diffusive device*, and corresponds to the reference sample of Ref. [44]. With a normal state resistance of both devices ranging between 35 Ω to 350 Ω, depending on gate voltage, we estimate around 74 to 740 conducting channels. This justifies the use of a single averaged transparency parameter τ in Eq. 4.1.

We extract the DC circuit parameters by applying a bias current to the JJ, using the CPW as a long capacitive lead and measuring the voltage drop across the gJJ. When exceeding a critical current, the JJ switches from the zero-voltage to the resistive state. We record this switching current I_c for varying gate voltages, as depicted in Fig. 4.1(b,c) for the two devices at a base temperature of 15 mK in the case of the diffusive, and both base temperature and 1 K for the ballistic device. In line with a minimum conductivity even at the CNP [42, 180–182], there remains a finite supercurrent in both samples, that cannot be pinched off completely. The DC switching current of the diffusive device ranges from a few hundred nA to 5.5 µA, similar to the ballistic device at 1 K. At base temperature, the maximum I_c of the ballistic device reaches up to 7.5 µA. Both samples exhibit significantly larger switching current for $V_g > V_{CNP}$ (n-doping) compared to $V_g < V_{CNP}$ (p-doping), where V_{CNP} denotes the gate voltage at the charge neutrality point (CNP) of the gJJ. We attribute this to a reduced contact transparency in the p-doped regime [44]. We measure $V_{CNP}^{diff} = 1.55$ V and $V_{CNP}^{ball} = -1.39$ V for the diffusive and ballistic sample, respectively. Discrepancies are presumably due to differences in residual doping during fabrication.

For high frequency signals, i.e. a few GHz, the gJJ behaves as a nonlinear inductor, with Josephson inductance

$$L_J = \frac{\hbar}{2e}\left(\frac{dI_J}{d\delta}\right)^{-1}, \tag{4.3}$$

which can be derived from the second Josephson relation, $\partial_t \delta = 2eV/\hbar$. The resonance frequency of a $\lambda/2$-resonator shorted to ground by such a Josephson inductance can be ap-

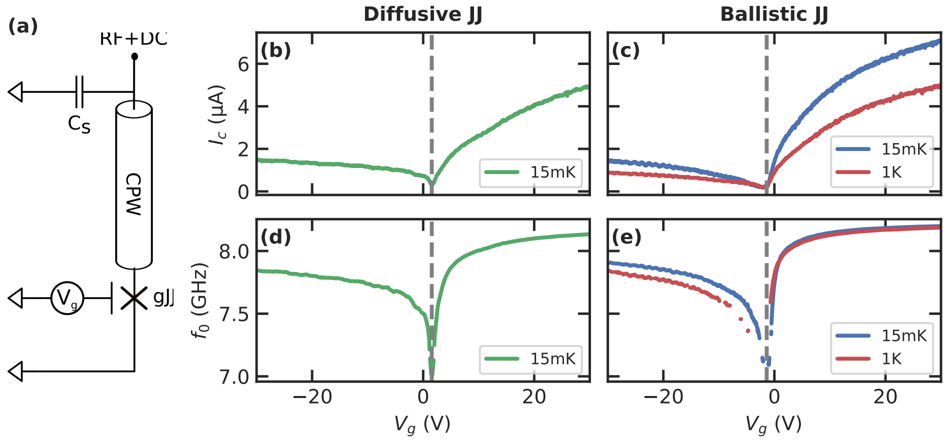

Figure 4.1: Simultaneous MW and DC measurements of ballistic and diffusive graphene Josephson junctions. (a) Measurement schematic. The gJJ shorts a coplanar waveguide transmission line to ground, which forms a gate-tunable $\lambda/2$-resonator. V_g is fed through an additional shunt capacitor (not shown). **(b,c)** Switching current for the diffusive **(b)** and ballistic Josephson junction **(c)**, at base-temperature of 15 mK (blue) and at 1 K (red). **(d,e)** Resonance frequencies versus gate voltage for the diffusive **(d)** and ballistic **(e)** device. The gate-tunable Josephson inductance changes the boundary condition of the $\lambda/2$-resonator, thus changing the resonance frequency of the circuit. Dashed grey lines indicate the charge neutrality point of each device, marked by the minimum critical current.

proximated by

$$f_0\left(I_b, I_c\right) = f_{\lambda/2}\frac{L_r + L_J\left(I_b, I_c\right)}{L_r + 2L_J\left(I_b, I_c\right)} \tag{4.4}$$

with L_r the bare CPW inductance and $f_{\lambda/2}$ the resonance frequency of the CPW without the JJ, see Supplementary Material Sec. 4.6.4. I_b is the bias current flowing through CPW and the JJ, I_c the critical current of the JJ. Depending on the impedance of the gJJ at the circuit resonance frequency, $Z_J = i\omega_0 L_J$, the fundamental mode hosted by the gJJ-terminated CPW varies between a $\lambda/2$ wave ($f_0 \rightarrow f_{\lambda/2}$) for small $Z_J \rightarrow 0$, while for $L_J \gg L_r$ the fundamental mode is $\lambda/4$ ($f_0 \rightarrow f_{\lambda/2}/2 = f_{\lambda/4}$).

The circuit response is measured by recording the reflection coefficient S_{11} of the cavity using a vector network analyzer, which excites the device through a series of attenuators and a directional coupler, and measures the reflected signal, amplified by low noise cryogenic and room temperature HEMTs. We fit the response using an analytical model to extract resonance frequency f_0 and internal (κ_i) and external loss rates (κ_e), see Supplementary Material Sec. 3.5.2. We observe gate-tunable resonance frequency f_0 between 7.0 GHz to 8.2 GHz, comparable for both devices, see Fig. 4.1(d,e). Due to the inverse nature of junction current and inductance, the large changes in I_c for $V_g > V_{CNP}$ only lead to minor changes in f_0 when comparing the hot and cold ballistic device. On the other hand, even small changes in the significantly smaller I_c for $V_g < V_{CNP}$ significantly reduce f_0 in this regime.

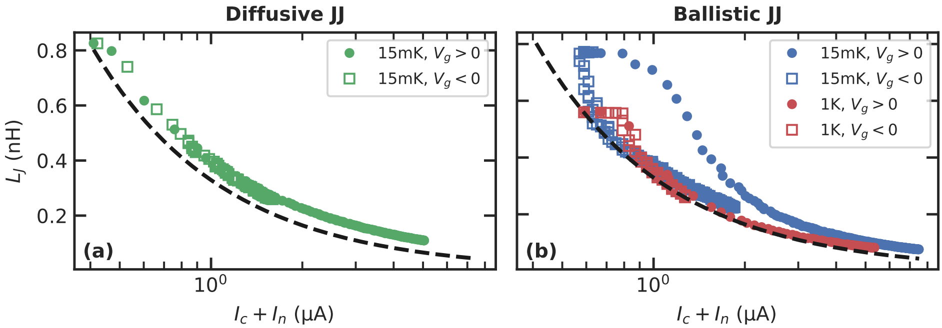

Figure 4.2: Evidence for non-sinusoidal CPR from deviation between Josephson inductance and critical current. MW-extracted L_J versus DC-measured I_c, corrected for estimates of current noise of 110 nA for the diffusive device at 15 mK **(a)** and 390 nA for the ballistic one at 15 mK and at 1 K **(b)** (blue and red, respectively). Full circles (empty squares) correspond to $V_g > V_{CNP}$ ($V_g < V_{CNP}$). Dashed line corresponds to an L_J calculated from I_c assuming a sinusoidal CPR. Values of L_J above the dashed line indicate a forward-skewed CPR, values below the dashed line would correspond to backwards skewing.

4.3. DEVIATIONS BETWEEN JOSEPHSON INDUCTANCE FROM DC AND MW MEASUREMENTS

Assuming a purely sinusoidal current-phase relation, the Josephson inductance can be extracted from the current phase relation via $L_J = \hbar/(2\pi I_c \cos\delta)$. However, depending on the exact shape of the CPR, L_J, and with it f_0, can significantly deviate from the above equations, see Supplementary Fig. 4.13. This leads to a reduced slope of the CPR around zero phase, which enhances L_J compared to the case of a sinusoidal CPR for the same value of I_c.

Instead of relying only on the DC measured values of I_c and the assumption of SIS CPR, we can directly extract L_J from the MW measurement of f_0. To calibrate the circuit parameters, we use additional measurements of reference devices shorted to with an open and a short to ground instead of a gJJ (see Supplementary Material Sec. 4.6.4 for details). From this, we extract $f_{\lambda/2} = 8.364$ GHz and $L_r = 3.671$ nH, which allows us to extract L_J via Eq. 4.4.

In Fig. 4.2, we plot the observed Josephson inductance together with the measured critical currents for the measured devices. As detailed in Supplementary Material Sec. 4.6.6, we estimate low-frequency current noise I_n to range between 110 nA to 390 nA in the setups used for measuring the diffusive and ballistic device, respectively. Without accounting for I_n, the observed L_J is significantly smaller than the SIS-CPR estimate from DC measurements of I_c, which, without any current noise, could only be explained by a backward-skewed CPR, see Supplementary Fig. 4.12. However, added to the measured values of I_c, this amount of current noise is sufficient to move all data points such that L_J is larger than expected from sinusoidal CPR for all I_c, matching the expected forward-skewed CPR regardless of diffusive or ballistic transport, or elevated temperatures.

The deviation is largest for the ballistic device at base temperature, and significantly reduced for the diffusive device, or at 1 K. This matches with the expectation of reduced forward skewing of the CPR at higher temperatures or lower transparencies: The skew is due to the phase coherence of Andreev bound states traversing the normal region between the superconducting banks multiple times (or, in a similar picture, multiple ABS crossing the normal region) which in turn means a longer phase coherence length is required to keep this contribution. As the phase coherence length is highly sensitive to temperature and scattering, an increase in either one of the last two results in both a reduction of switching current and forward skewing [151, 183–186].

In order to examine the underlying mechanisms further, we continue by studying the power and bias current dependence of our circuit.

4.4. PURE MW MEASUREMENTS OF THE JOSEPHSON NONLINEARITY

4.4.1. PROBING L_J VIA THE POWER DEPENDENCE

The nonlinear inductance of a Josephson junction consequently introduces nonlinear behavior to the overall circuit. Depending on the exact circuit design and participation ratio between Josephson and total circuit inductance, this nonlinearity is more or less diluted, yet finite so-called anharmonicity β, i.e. deviation from the ideal case of pure LC-resonator behavior, remains. Our circuit architecture allows us to extract this quantity directly and to calculate the expected CPR skew.

We can observe the anharmonicity of our DC bias circuit terminated with the diffusive gJJ by performing S_{11} measurements at high drive powers for a series of different gate voltages, as shown in Fig. 4.3 for $V_g = 10$ V. At very low drive powers, β has negligible effect on the circuit response, which can still be described by a purely harmonic oscillator here. With increasing on-chip power P_{in}, the resonance frequency experiences a down-shift, and both amplitude and phase of S_{11} start to get skewed towards lower frequencies. Once P_{in} exceeds a critical threshold, the resonator response bifurcates, which can be seen by the discontinuity in the data. For reference, all other measurements of this device were performed at $P_{in} \approx -131.4$ dBm, still in the linear regime and with a maximum current at the junction of $I_{MW} \approx 3.0$ nA well below the critical current, see Supplementary Material Fig. 4.10.

Using the previously determined parameters f_0, κ_i and κ_e, we can model the data by solving the equation of motion of a harmonic oscillator with an additional third order term in the cavity field with amplitude β,

$$\alpha = \left[-i\left(\Delta + \beta|\alpha|^2\right) - \frac{\kappa}{2}\right]\alpha + \sqrt{\kappa_e}S_{in}\,, \tag{4.5}$$

where S_{in} is the field amplitude of the drive, Δ the frequency detuning and $\kappa = \kappa_i + \kappa_e$, as detailed in Supplementary Material Sec. 4.6.5.

Best agreement between data and model is reached when introducing nonlinear dissipation in the form of increasing internal linewidth that grows with the square root of the drive power, $\delta\kappa_i/\kappa_i(0) = \gamma\sqrt{P_{in}}$, see Supplementary Section 4.6.5 and Supplementary Figs. 4.8 and 4.9. This is in contrast with circuits incorporating standard aluminum oxide JJs, where nonlinear dissipation with increasing power is usually absent [187].

There are several dissipation mechanisms known in superconducting microwave circuits that depend on drive power, such as on-chip heating [188–190], dielectric losses [121, 191–193], or subgap losses [194–196]. Heating of the circuit itself is unlikely since f_0 should tune significantly stronger due to a reduced I_c at elevated temperatures, with potentially significant influence on f_0, c.f. Fig. 4.1, which we did not observe for any of the gate voltages. Moreover, the power dissipated on-chip is extremely small and very unlikely to cause even local heating.

Losses due to electric dipole moments of two-level systems are also unlikely the source of the observation, as these are known to be activated for decreasing drive excitation volt-

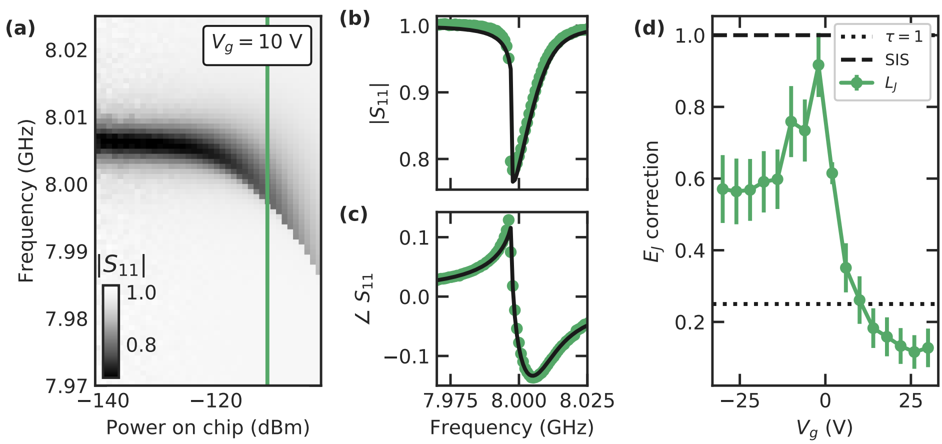

Figure 4.3: Extracting the anharmonicity coefficient. (a) Absolute value of the reflection coefficient S_{11} versus frequency for increasing drive power. Due to the circuit nonlinearity, the resonator experiences a downshift and bifurcation at elevated drive powers. Solid lines indicate linecuts in **(b)** and **(c)**. **(b-c)** Absolute value **(b)** and phase **(c)** of S_{11} for P_{int} = -110 dBm as indicated in **(a)**. Black lines are fits. **(d)** Josephson energy correction for measured gate voltages. Dots: data as extracted from fits as in **(b-c)** and L_{J}, dashed line: SIS limit, dotted line: $\tau = 1$ limit. Values below the dashed line indicate forward skewed CPR.

ages [191–193]. Moreover, TLS mainly reside in disordered dielectric materials. However, there is only dielectric volume present at the shunt capacitor dielectric and the gJJ (encapsulating BN and HSQ top-gate). Here, the circuit has voltage nodes and voltage fluctuations, which could activate the TLS, are expected to have negligible effect on the circuit performance.

We therefore attribute the source of the observed nonlinear damping to low-lying subgap states within the induced superconducting gap in the gJJ. These subgap states can be due to e.g. intransparent superconductor-normal contacts, or Andreev bound states with large transverse momentum, polluting the bulk superconducting gap and leading to microwave loss [44]. As the drive power increases, these subgap states get populated, resulting in an internal loss rate that grows with the square root of the input power, see Supplementary Fig. 4.9. Loss mechanisms in similar SNS systems, with normal metal weak links, have shown similar effects [183, 194], but they have not been observed before in gJJ.

The β term in Eq. 4.5 is due to the anharmonicity of the microwave cavity for high drive powers which is evident when expanding the Josephson energy potential to higher orders,

$$V_J(\delta) \approx E_{\mathrm{J}}\frac{\delta^2}{2} - E_{\mathrm{J}}\left(1 - \frac{3\sum\tau_i^2}{4\sum\tau_i}\right)\frac{\delta^4}{24} + O(\delta^6)\,, \tag{4.6}$$

where $E_{\mathrm{J}} = \Delta_0 \sum \tau_i/4$ [43]. Compared to the case of an SIS junction, depending on τ the fourth-order correction

$$\Gamma = 1 - 3\tau/4 \tag{4.7}$$

can vary between 1 for SIS to 0.25 for $\tau = 1$. In Fig. 4.3(d), we plot this quantity as the ratio of the measured value of the anharmonicity coefficient β_{meas} and the one expected from a $\lambda/2$

resonator shorted to ground by a Josephson junction, approximately given by $\beta_{\text{th}} = f_0 p^3/2$ with the participation ratio between Josephson and total inductance $p = L_J/(L_r + L_J)$ [197, 198].

For a broad range of gate voltages, the correction lies between the two extremes of no and full forward skewing. However, for $V_g > 5\,\text{V}$, this value drops below the minimum of 0.25 as expected from Eq. 4.6. While this is unexpected, we note that without knowing exactly how many ABS channels are active in the JJ, it is not possible to extract a number for τ, as the measured anharmonicity coefficient only returns information on $\sum \tau_i = N\tau$. Additional experiments, such as extracting the transparency for each channel from multiple Andreev reflection via voltage-biased measurements [46, 199–201], or direct measures of both E_J and the anharmonicity coefficient in transmon qubits [22, 28–30], would be required to draw further conclusions.

4.4.2. Probing L_J via the bias current dependence

4

A second way of reconstructing the CPR is by means of analyzing the bias current dependence of the high frequency circuit response, as this allows for a direct measure of $L_J(I_b)$. We model the bias current dependence of both the ballistic and diffusive device at 15 mK using Eqs. 4.3 and 4.4 under the assumption of a general CPR according to Eq. 4.2 and using τ and I_c as a free parameters, as shown in Fig. 4.4(a) (see Supplementary Material Sec. 4.6.6 for details).

Compared to a Josephson inductance with sinusoidal CPR, the measured data requires additional Josephson inductance, pushing f_0 to lower frequencies, which is provided by a CPR with same I_c, but forward skewed (see Supplementary Material Fig. 4.13). The lower limit of the resonance frequency at zero bias current is given by a fully forward skewed CPR with $\tau = 1$, which yields maximum L_J for the same I_c as a fully sinusoidal CPR. For all gate voltages, the measured data lies between these two extremes. Fixing L_r and $f_{\lambda/2}$ as the earlier calibrated values, and including a forward skewed CPR in our model, we are able to fit the measured f_0, which allows us to extract a CPR-transparency parameter $\tau(V_g)$.

As the bias current increases, so does the internal linewidth of the S_{11} resonance, see Supplementary Material Sec. 4.6.6 and Fig. 4.11. This is most likely due to the previously mentioned current noise on our DC lines, which modulates the resonance frequency around the value set by f_0. Due to the measurement time, the recorded trace then shows a widened resonance dip, that even resembles a split-dip feature at high responsivity to bias current, $G_1 = \partial f_0/\partial I_b$. We therefore chose to omit bias current measurements of gate voltages where the resonance frequency was not clearly visible, which is the reason for some missing datapoints in Fig. 4.4.

From the remaining data, we extract an average channel transmission $\tau_{\text{diff}} = 0.64 \pm 0.18$ and $\tau_{\text{ball}} = 0.77 \pm 0.14$ for the diffusive and ballistic device, respectively, at base temperature. With skew defined as the deviation of the CPR maximum from phase $\pi/2$, $S = 2\delta_{\max}/\pi - 1$, the corresponding values are $S_{\text{diff}} = 0.20 \pm 0.09$ and $S_{\text{ball}} = 0.27 \pm 0.15$ for the diffusive and ballistic device, respectively, as plotted in Fig. 4.4(b). We note that this is comparable to the results obtained from DC-measurements of the CPR [98, 151]. Overall, the skewness seems to be constant for both devices, except for the region around CNP, where skewness seems to be significantly higher than elsewhere.

Corrections to E_J amount to 0.52 ± 0.13 for the diffusive and 0.42 ± 0.10. This is an important result for future use of gJJs in applications such as qubits, as this correction plays an important role in the circuit's anharmonicity and coherence times [43].

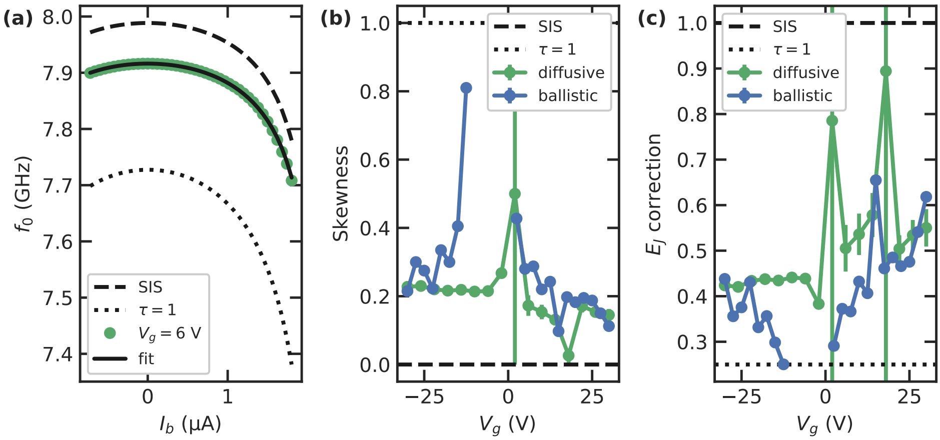

Figure 4.4: Observation of the skewness of the current phase relation by measuring the DC current dependence of the linear response of the Josephson inductance. Fitting the bias current dependence **(a)**, we can extract the junction transparency and corresponding CPR skew **(b)** for the diffusive (green) and ballistic (blue) gJJ device versus gate voltage. A Josephson inductance with underlying SIS-CPR would result in high f_0 and small frequency tuning, while maximum skew provides a lower bound on f_0. **(d)** Using τ, we calculate the correction factor to E_J following Eq. 4.7 for both devices, indicating significant forward skewing in both samples. Dashed lines: Underlying sinusoidal CPR, dotted lines: maximally skewed CPR with $\tau = 1$ (see Supplementary Material Fig. 4.13).

4.5. CONCLUSION

In summary, we were able to extract evidence of a forward-skewed current phase relation in graphene Josephson junctions by embedding them in superconducting microwave circuits. Using a combination of drive power and bias current measurements, our results show that scattering of charge carriers, as well as elevated temperature, reduce the CPR skew and with it the circuit anharmonicity via the change in nonlinearity of the JJ itself.

Our circuit architecture is an attractive candidate for analyzing the CPR of exotic JJs, such as ferromagnetic or topological ones [176, 202–205]. Moreover, the influence of high microwave powers on the CPR can be studied straightforwardly, as this only requires repeating the bias current measurements at various powers. Additionally, the combination of bias current and power dependence should allow to trace out a larger part of the CPR than just around zero phase.

The observed nonlinear damping might unfortunately limit applications of graphene Josephson junctions for cQED. Devices such as parametric amplifiers need to be operated at high drive powers, which, with nonlinear damping, no longer result in quantum-limited amplification.

4.6. SUPPLEMENTARY MATERIAL: INDUCTANCE AND CURRENT-PHASE RELATION OF GRAPHENE JOSEPHSON JUNCTIONS

4.6.1. CLASSIFICATION AS DIFFUSIVE OR BALLISTIC JJ

As stated in the main text, we define the device as ballistic or diffusive in the presence or absence of Fabry-Pérot-like oscillations. In Fig. 4.5, we plot these oscillations after removing a third order background from the data to remove the overall gate-voltage tuning dependence. Both at base temperature and at 1 K, we observe high-frequency, highly correlated oscillations in all of f_0, I_c and $G_n = R_n^{-1}$ for the *ballistic* device, which justifies its classification as such. The oscillation period allows an estimate of a cavity length of 390 nm for the ABS inside the JJ [44]. For the same voltage range, however, the *diffusive* device only shows a low-frequency trend originating from the deviation about the removed background, thus lacking the ballistic feature.

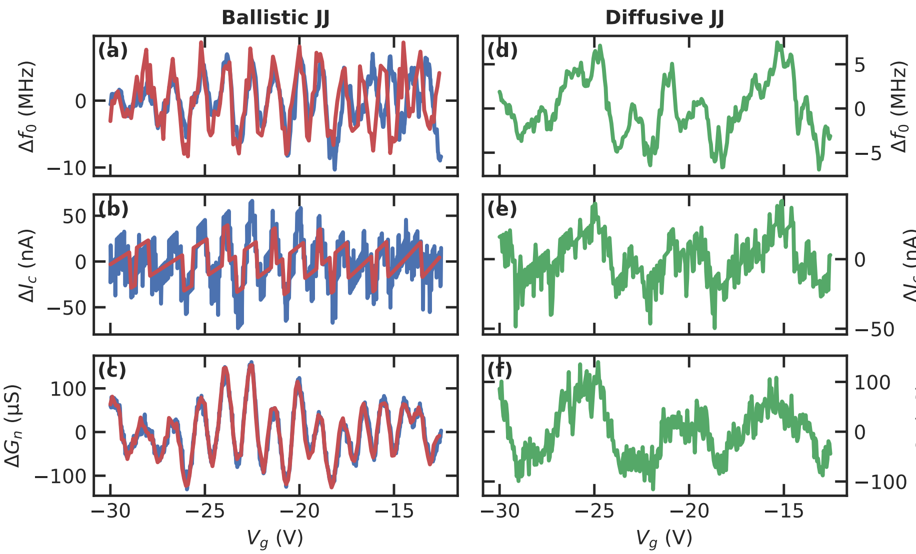

Figure 4.5: Fabry-Pérot oscillations in the ballistic device. (a-c) Oscillations in the resonance frequency, DC-switching current and normal state conductance as a function of gate voltage for the ballistic device at base temperature (blue) and 1 K (red). **(d-f)** For the diffusive device, no such features are observed, only a slowly varying background, justifying the classification as *diffusive* device.

4.6.2. ESTIMATION OF THE FRIDGE ATTENUATION

We can estimate the attenuation of our MW input line by using the cryogenic HEMT as a calibrated noise source. The HEMT noise power is given by

$$P_{\mathrm{HEMT}} = 10 \log \left(\frac{k_{\mathrm{B}} T_{\mathrm{HEMT}}}{\mathrm{mW}} \right) + 10 \log \left(\frac{\Delta f}{\mathrm{Hz}} \right) , \tag{4.8}$$

with the Boltzmann constant k_{B}, the noise temperature of the HEMT $T_{\mathrm{HEMT}} = 2\,\mathrm{K}$ as specified by the manufacturer and the measurement bandwidth $\Delta f = 100\,\mathrm{Hz}$. The resulting noise power is $P_{\mathrm{HEMT}} = -175.59$ dBm. Additionally, we can calculate the average background signal arriving at the VNA by averaging all S_{11} traces in the areas off-resonant to the cavity, which leaves the background unaltered in power. Doing so, we extract an average signal and standard deviation, which yields the signal-to-noise ratio at the VNA, $\mathrm{SNR}_{\mathrm{VNA}} = 43.85$ dB, for a VNA output power of -20 dBm. Assuming 2 dB of cable loss between sample and HEMT, we arrive at an attenuation of 111.74 dB of our VNA input line,

4.6.3. EXTRACTING I_c AND f_0

The DC switching current (Fig. 4.1(b,c)) is taken as the current at which $\partial V/\partial I_b$ is maximum, where V is the measured voltage drop across the JJ. Noise or interference on the DC lines could lead to a reduction of the measured I_c compared to the true value. To get a more accurate estimation of I_c together with a good understanding of the noise sources, switching histograms are the preferred measurement method. The necessary setup was however not available at the time of measurement.

To extract resonance frequency and loss rates from the MW data, we fit the reflection coefficient to the following model (see Ref. [37] for a derivation):

$$S_{11}(\omega) = -1 + \frac{2\kappa_e}{\kappa + 2i\Delta}, \tag{4.9}$$

where $\kappa = \kappa_e + \kappa_i$ denoting the total, external and internal loss rates, respectively, and $\Delta = \omega - \omega_0$ with resonance frequency $\omega_0 = 2\pi f_0$. The measured S_{11} is usually distorted by a setup-related microwave background of the following shape:

$$B(\omega) = \left(a + b\omega + c\omega^2\right) e^{i(a'+b'\omega)}, \tag{4.10}$$

and with additional rotation by angle θ in the complex plane, the measured S'_{11} is:

$$S'_{11}(\omega) = B(\omega)\left(e^{i\theta}\left(S_{11}(\omega)+1\right) - 1\right) \tag{4.11}$$

The origin of the microwave background and phase rotations are impedance mismatches in the wiring originating from various non-ideal circuit elements (e.g. connectors, attenuators, directional couplers, wirebonds). Standing waves can form in some segments of the wiring which interfere with the measured signal, thus producing an oscillating measurement background. To remove this background for the gate voltage sweeps (Fig. 4.1(d,e)), we pick the measurement trace at the CNP as the one with only background signal, as the MW resonance is extremely broad and effectively not present here. We then divide the other traces by this trace, resulting in a much cleaner signal. For measurements based on bias current sweeps, see Fig 4.4(a), we take the MW background as the S_{11} trace at $I_b > I_s$. Here, the JJ switched to the normal state and the MW resonance is not present in the measurement. In order to remove MW background from the power dependence, we mask the regions in which there are resonances for the various powers and gate voltage setpoints, and average the remaining traces. This way, we obtain a power and frequency map of the MW background, which we use for removing background signal from power traces, such as the one in Fig. 4.3(a).

4.6.4. EXTRACTING f_R, L_R AND L_J

We can derive an expression for the circuit resonance frequency depending on the other parameters by using the impedances defined in Fig. 4.6. The circuit impedance as seen from the

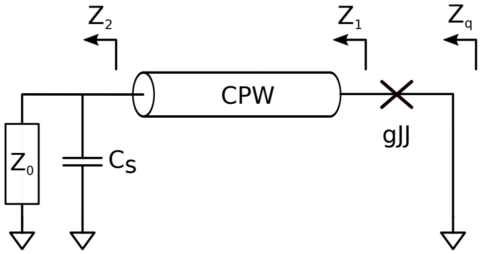

Figure 4.6: Derivation of resonance frequency. We define the three impedances Z_1, Z_2 and Z_q as seen from the CPW towards the input port, from the gJJ towards the CPW, and as the parallel circuit impedance. The gJJ can further be modeled via an RCSJ-model, and an additional gate capacitance (not shown, see text for details).

JJ towards the CPW, Z_1, the input impedance as seen from the CPW towards the input port, Z_2, and the overall parallel circuit impedance Z_q are:

$$Z_1 = Z_0 \frac{Z_2 + Z_0 \tanh \gamma l}{Z_0 + Z_2 \tanh \gamma l} \tag{4.12}$$

$$Z_2 = \left(\frac{1}{Z_{C_s}} + \frac{1}{Z_0} \right)^{-1} = \left(i\omega C_s + \frac{1}{Z_0} \right)^{-1} \tag{4.13}$$

$$Z_q = \left(\frac{1}{Z_J} + \frac{1}{Z_1} \right)^{-1} = \left(\frac{1}{i\omega L_J} + \frac{1}{Z_1} \right)^{-1}, \tag{4.14}$$

with the CPW length l, the complex CPW loss per unit length $\gamma = \alpha + i\beta$, and the transmission line impedance Z_0. Note that the junction impedance Z_J can be further extended by an RCSJ model and should include additional capacitance for the gate and inductance for the contact electrodes, as described in Ref. [44]. Assuming negligible losses in the CPW on resonance, $\gamma l \approx i\beta l = i\pi\omega_0/\omega_r$, i.e. the CPW only acts as a phase shifter. The resonance condition of the above circuit is for the imaginary part of the admittance $Y = 1/Z_q$ to be zero, which yields

$$0 = \Im \left[\frac{1}{i\omega_0 L_J} + \frac{1}{Z_0} \frac{Z_0 + iZ_2 \tan(\pi\omega_0/\omega_r)}{Z_2 + iZ_0 \tan(\pi\omega_0/\omega_r)} \right] \tag{4.15}$$

We can approximate the above by a similar method as the authors of Refs. [206–208]: Assuming a large shunt capacitance at the input, such that $Z_2 \approx 0$ and expanding the tangent, we arrive at the expression stated in Eq. 4.4. This assumption is justified since $C_s \approx 27$ pF for our devices, such that both $Z_2 \approx 0.2\,\Omega \ll Z_0 = 50\,\Omega$. We find that for all values of L_J, including the range in our experiments, the approximation differs by less than 0.2 % from the analytical solution (see below).

We extract the circuit parameters from our measurement data in the same fashion as described in the Supplementary Material of Ref. [44]: In short, we use a reference device with no junction at the end to calibrate f_r and L_r, a reference device shorted to ground to calibrate the transmission line losses, and finite-element simulations to deduce additional inductances and capacitances of the leads and gate electrode. This allows us to extract the Josephson inductance directly from the observed resonance frequency, regardless of the underlying CPR. As shown in Fig. 4.7, while there are significant deviations of Eq. 4.4 to the measured $f_0(I_c)$, all

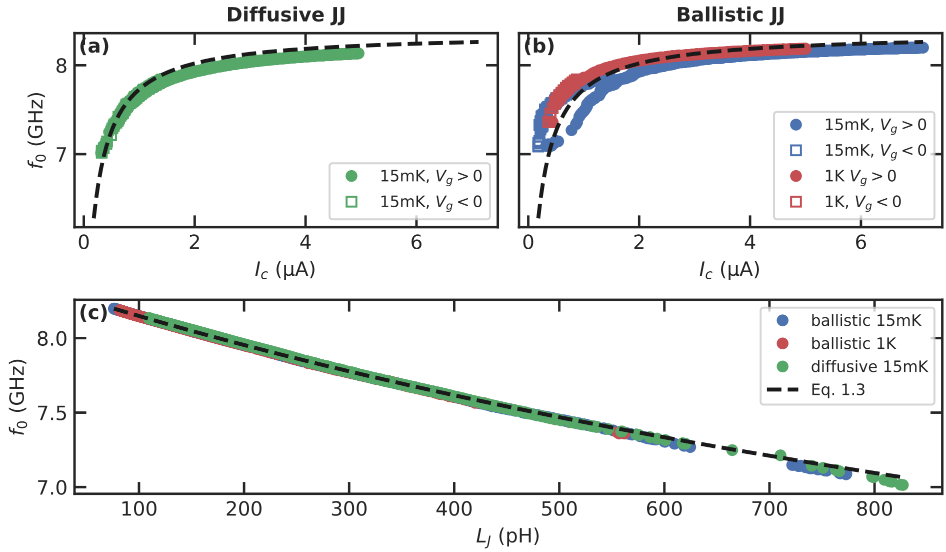

Figure 4.7: Resonance frequency vs switching currents for two different gJJ devices. Both the diffusive device at low temperature **(a)** and the ballistic device at 1 K (**(b)**, red) show monotonically increasing f_0 versus DC-extracted switching currents. In contrast, for low temperatures, the ballistic gJJ (**(b)**, blue) exhibits multi-valued $f_0\,(I_s)$ for gate voltages larger (full circles) and smaller (empty squares) than the charge neutrality point. The multivalued behavior in the ballistic device at low temperature presumably originates from significant differences in junction transparency between n- and p-doping, and only allows for a fit for $V_g > 0$. This is not observed at higher temperature or for the diffusive device. Dashed lines correspond to Eq. 4.4 under assumption of sinusoidal CPR. **(c)** Resonance frequency as a function of observed Josephson inductance, showing good matching to Eq. 4.4.

measured devices fall on a single curve when plotted as a function of L_J, which verifies this approximation.

4.6.5. Device response to drive power

Following the method described in Ref. [179], the equation of motion of the amplitude field $\alpha(t)$ of a resonator with weak anharmonicity β written in the frame rotating with the drive S_{in} is given by Eq. 4.5, from which the steady-state solution $\partial\alpha_0/\partial t = 0$ results in the polynomial function

$$\beta^2\alpha_0^6 + 2\Delta\beta\alpha_0^4 + \left(\Delta^2 + \frac{\kappa^2}{4}\right)\alpha_0^2 - \kappa_e|S_{in}|^2 = 0\,, \tag{4.16}$$

which we can solve and use to calculate the expected reflection coefficient as our model,

$$S_{11} = -1 - \frac{\sqrt{\kappa_e}}{S_{in}}\alpha_0\,. \tag{4.17}$$

to fit the measurement data. We reduce the number of free parameters of this function from five to two by fixing ω_0 and κ_e as the values extracted at lowest drive power and calculating S_{in}

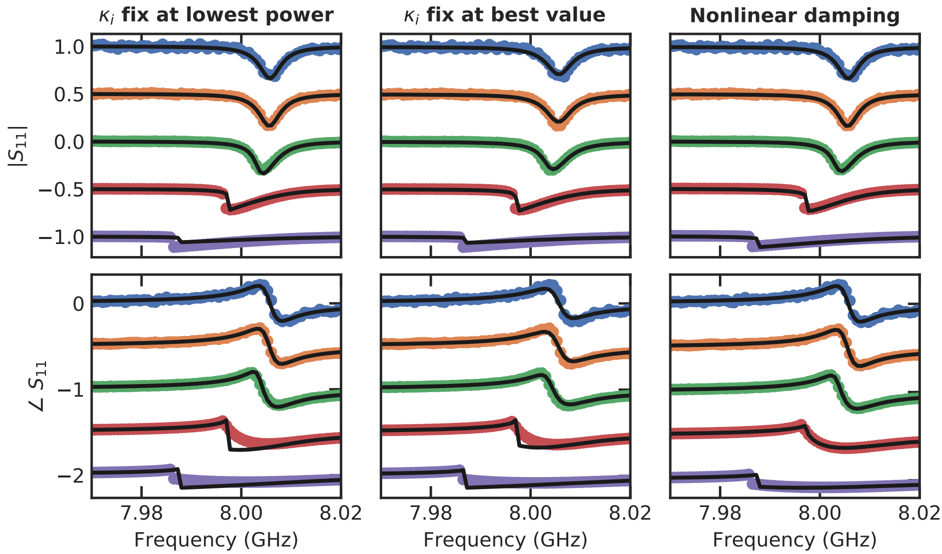

Figure 4.8: Anharmonicity fit assuming different cases for κ_i. Fixing κ_i to be the value at lowest drive power (first column) results in significantly worse fit than introducing it as constant, but free parameter (second column). However, best agreement between data and model is reached when introducing nonlinear damping (third column and Fig. 4.4). Linecuts and colors correspond to the ones in Fig. 4.4.

from the fridge attenuation, see Supplementary Section Sec. 5.7.1. The remaining parameters are β and κ_i, where the internal loss rate can in fact depend on the drive power, $\kappa_\mathrm{i} = \kappa_\mathrm{i}(S_\mathrm{in})$. Fixing the loss rate to be constant throughout the fit does not lead to a good fit to the data, as shown in Fig. 4.8. Our algorithm first fits the measured data to return constant β and κ_i, and uses these as initial values for a fit to extract the power dependent loss rate.

We can fit the thus extracted change in internal linewidth using a linear growth in drive field S_in or square-root dependence on drive power,

$$\kappa_\mathrm{i} = \kappa_\mathrm{i}(0)\left(\gamma\sqrt{P_\mathrm{in}} + 1\right) \tag{4.18}$$

as shown in Fig. 4.9(a). This strongly suggests internal losses originating from sub-gap states populated by the drive field. Over the range of measured gate voltages, the increase in loss is roughly constant, with slightly larger values for positive compared to negative gate voltages, see Fig. 4.9(b).

Following Ref. [179], we can approximate the current across the junction via the intracavity photon number when driving the device on resonance by combining the input power together with the total and external cavity linewidths:

$$I_0 = \sqrt{\frac{16 P_\mathrm{in} \kappa_\mathrm{e}}{L_\mathrm{r} \kappa^2}} \tag{4.19}$$

In the high-power regime, we estimate the internal linewidths growing according to Eq. 4.18, with the coefficient γ averaged over all gate voltages. In Fig. 4.10, we show the estimated

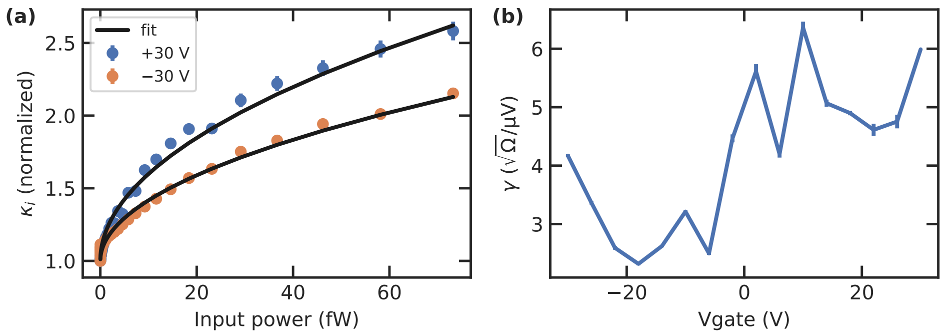

Figure 4.9: Nonlinear damping in the gJJ. (a) The internal linewidth of the diffusive device grows with the square root of the input power, regardless of gate voltage. **(b)** The extracted fit parameter γ is slightly lower for p-doping compared to n-doping. γ is related to the subgap losses.

currents at the diffusive gJJ for low and high MW powers. While in the case of low powers (all measurements except for the once in Fig. 4.3) the current at the junction is much smaller than I_c, for large drive powers we begin to sample a greater region of the CPR.

4.6.6. Device response to bias current

Increasing loss rate

In addition to an increase in κ_i for high drive powers as discussed in the main text, the internal loss rate of our circuit also depends on bias current. We observe an increasing loss rate for increasing bias current, see Fig 4.11. Possible origins of this phenomenon are low-frequency noise on the DC electronics, as this artificially widens the measured cavity resonance if the measurement time is greater than the inverse noise frequency. Additionally, phase-slip events might occur at larger rates if the Josephson energy potential is tilted, as compared to zero bias current.

The current noise amplitude can be calculated in two ways: As shown in Fig. 4.11(a), the reflected signal exhibits a double-peak for bias currents close to I_c, in addition to an increase in linewidth. This strongly suggests low-frequency current noise, modulating the resonance about the fixed bias current faster than the measurement scan. From the peak spacing and the measured responsitvity $G_1 = \partial f_0/\partial I_b$, i.e. the change in resonance frequency versus bias current, we can compute the current noise as

$$\Delta I_n = \frac{\Delta f_0}{\left(\frac{\partial f_0}{\partial I_b}\right)} \tag{4.20}$$

From this, we estimate $\Delta I_n \approx 270$ nA due to low-frequency noise for the ballistic device.

Similarly, the increase in total linewidth can be fitted as a linear function of G_1,

$$\kappa_i(I_b) = \kappa_i(0) + I_n \frac{\partial f_0}{\partial I_b}\,, \tag{4.21}$$

resulting in an upper bound for the total corresponding bias current induced losses, see Fig. 4.11(b). For the ballistic device, we extract a total corresponding current noise $I_n \approx 390$ nA

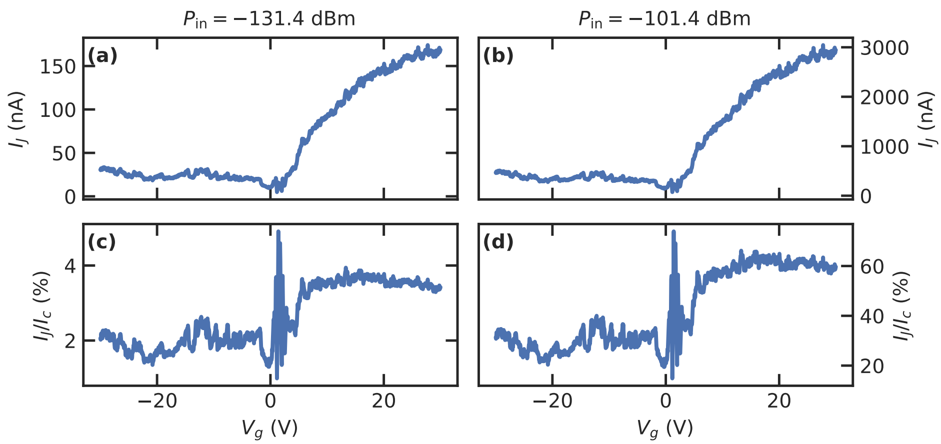

Figure 4.10: Current across the diffusive graphene Josephson junction. **(a,b)** Current across the JJ for varying gate voltage at reference power **(a)** and maximum drive power **(b)**, calculated via Eq. 4.19. **(c,d)** Ratio of current across the JJ to DC-measured switching current for varying gate voltage at reference power **(c)** and maximum drive power **(d)**. Note the different scales for the left and right column.

for the ballistic, and $I_n \approx 110$ nA for the diffusive device. This leads us to believe that the setup used for the ballistic device was better isolated against current noise than the one for the diffusive device. Still, some contribution due to processes such as phase slip events is necessary to explain the excess noise obtained from the increase in total linewidth.

Since this current noise also leads to an artificial reduction in the measured I_c, this leads to a rescaling of the current axis of Fig. 4.2. Adding the respective estimates of I_n to the measured I_c results in Fig. 4.12. In this case, all measured values of L_J are larger than the ones extrapolated from I_c and a sinusoidal CPR, hinting at an overall forward skewed CPR over the full gate voltage range in both devices. Additional measurements in the form of statistics on the switching current [36, 209, 210] could result in more information on this matter, but were not performed at the time.

Extracting τ

Figure 4.13 illustrates the effect of a forward skewed CPR on the Josephson inductance and resonance frequency dependence on bias current. Since a higher skew results in a reduced slope of the CPR, Eq. 4.3 tells us that L_J must therefore be increased at zero phase (and current). Consequently, for the same DC bias microwave circuit with parameters $f_{\lambda/2}$ and L_r, a JJ with larger forward skew and L_J pushes the initial resonance frequency further downwards than in the case of sinusoidal CPR.

Without any knowledge on the junction transparency τ, fitting data of a CPW cavity with JJ exhibiting a potentially nonsinusoidal CPR can lead to significant deviations from the true circuit parameters. It is therefore essential to use a fixed set of parameters for f_{λ_2} and L_r, as described in Sec. 4.6.4. To fit the bias current dependence data for extracting τ, we keep these values fixed and only allow τ and I_c to vary within reasonable boundaries, i.e. $\tau \in [0, 1]$ and $I_c < \max I_b$. Due to the significant current noise, the cavity resonance gets very broad and begins to resemble a double-dip feature, which makes extraction of reliable values for small

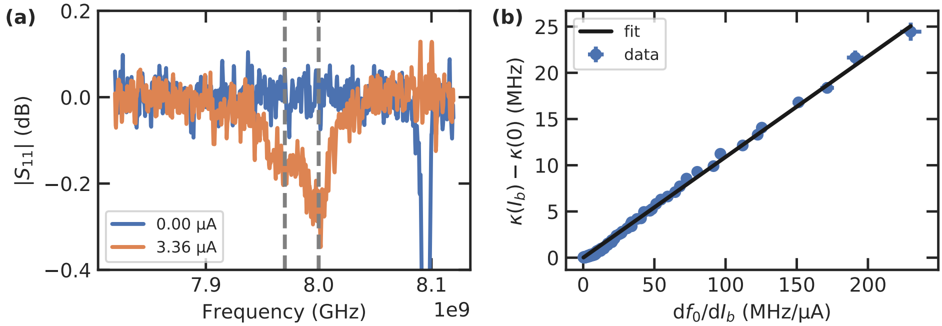

Figure 4.11: Internal loss rate for increasing bias current. **(a)** Compared to the case of zero bias (blue), large bias currents lead to a splitting of the reflected signal in two separate dips (orange). The peak spacing and eq. 4.20, we can extract a current noise of approximately 270 nA. **(b)** Difference in total loss rate compared to zero bias current shows a linear increase as a function of responsivity G_1, which can be fitted using eq. 4.21. Increasing loss rate with bias current could originate from low-frequency noise and/or phase slip events.

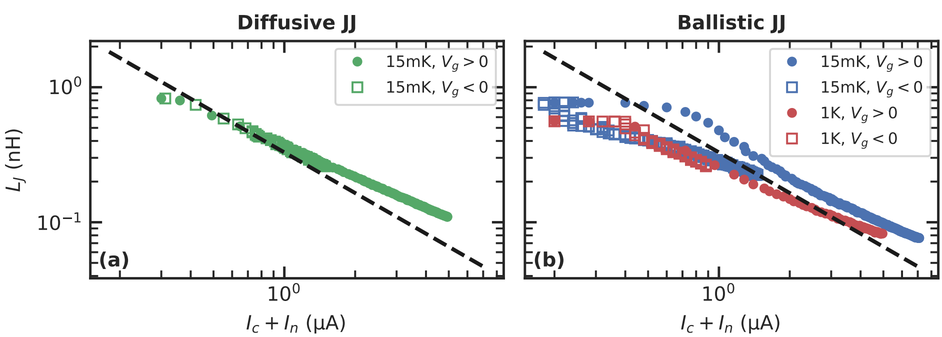

Figure 4.12: Josephson inductance and critical currents without added current noise. Without accounting for DC current noise, a significant portion of the measured L_J drop below the SIS limit of a sinusoidal CPR.

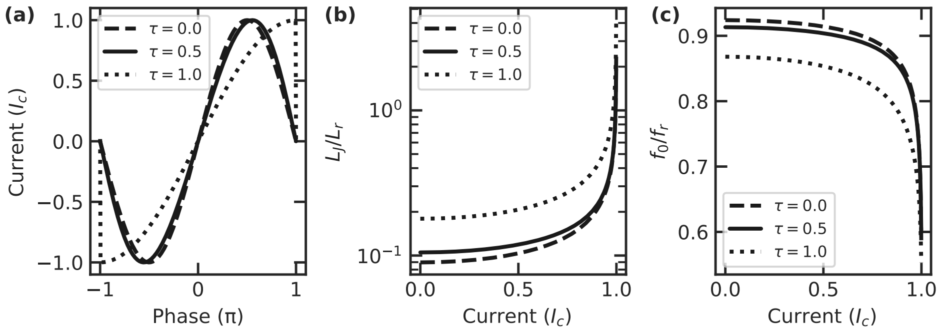

Figure 4.13: Predicted influence of the junction transparency on the bias current dependence. **(a)** CPR for various $\tau = 0$ (solid), $\tau = 0.5$ (dashed) and $\tau = 1.0$ (dash-dotted). **(b-c)** Josephson inductance **(b)** and resonance frequency **(c)** normalized to the calibrated values of L_r and f_r, respectively. Each linestyle corresponds to an underlying CPR as calculated in **(a)**, each with a simulated $I_c = 1\,\mu A$. Increased forward skewing of the CPR leads to a reduced slope and higher Josephson inductance, which in turn reduces the resonance frequency and increases the tuning.

gate voltages increasingly difficult. For this reason, we chose to omit gate voltages below the CNP from further analysis.

5

Current detection using a Josephson parametric upconverter

We present the design, measurement and analysis of a current sensor based on a process of Josephson parametric upconversion in a superconducting microwave cavity. Terminating a coplanar waveguide with a nanobridge constriction Josephson junction, we observe modulation sidebands from the cavity that enable highly sensitive, frequency-multiplexed output of small currents for applications such as transition-edge sensor array readout. We derive an analytical model to reproduce the measurements over a wide range of bias currents, detunings and input powers. Tuning the frequency of the cavity by more than 100 MHz *with DC current, our device achieves a minimum current sensitivity of* $8.9\,\mathrm{pA}/\sqrt{\mathrm{Hz}}$*. Extrapolating the results of our analytical model, we predict an improved device based on our platform, capable of achieving sensitivities down to* $50\,\mathrm{fA}/\sqrt{\mathrm{Hz}}$*, or even lower if one could take advantage of parametric amplification in the Josephson cavity. Taking advantage of the Josephson architecture, our approach can provide higher sensitivity than kinetic inductance designs, and potentially enables detection of currents ultimately limited by quantum noise.*

A preprint of this chapter is available at arXiv:2001.02521 [179]. Data and code to reproduce the calculations and figures presented here can be found on Zenodo [211].

5.1. Introduction

Ultra-low noise radiation detection has applications in astronomy, particle physics, and quantum information processing. In particular, transition edge sensors (TES) allow for broadband radiation detection with exceptionally low noise equivalent power [212] and photon number resolution [213, 214]. To read out the small changes in current of TES in response to radiation absorption, highly sensitive current amplifiers such as superconducting quantum interference devices (SQUIDs) can be used with sensitivities as low as $4\,\mathrm{fA}/\sqrt{\mathrm{Hz}}$ [215]. However, with the increasing number of TES to be read out simultaneously in multipixel detectors, SQUID amplifiers significantly increase system cost and complexity, especially when employing frequency-domain multiplexing to reduce the number of necessary amplifiers [216].

An example of recently developed current detectors as a replacement of SQUIDs are kinetic inductance parametric upconverters (KPUPs), also referred to as microwave kinetic inductance nanowire galvanometers, which rely on the changing kinetic inductance L_k of a narrow superconducting wire embedded in a microwave circuit in response to a DC bias current, with state of the art devices reaching current sensitivities $\mathcal{S}_I$ between $5\,\mathrm{pA}/\sqrt{\mathrm{Hz}}$ to $10\,\mathrm{pA}/\sqrt{\mathrm{Hz}}$ [217–219]. One could potentially achieve a higher response from such a cavity detector by replacing the nanowire kinetic inductance element with a Josephson junction (JJ), enabling detection of currents using a Jospheson parametric upconverter (JPUP). This would also enable the incorporation of processes such as Josephson parametric amplification, which allows signals to be amplfied with quantum limited noise [220], directly in the readout cavity.

5

Typically, the integration of JJs in superconducting microwave circuits is technologically more demanding due to the additionally needed fabrication steps to avoid aging effects and low coherence at microwave frequencies [193, 221–223]. The intrinsically large Kerr-nonlinearity of JJs [224] can additionally place an upper limit on the device power allowed for circuit operation, which calls for either large critical current JJs with additional fabrication challenges [225], or appropriate circuit design for sufficiently diluting the nonlinearity to provide stable device operation.

Here, we provide experimental realisation of a JPUP based on a hybrid combination of a direct current (DC) accessible microwave cavity in coplanar waveguide (CPW) geometry [37, 44]. The design uses a constriction JJ fabricated in the same step and layer as the microwave cavity which simplifies the fabrication procedure and allows for high cavity drive powers [226–229]. We show device operation by converting kHz current signals to the GHz range, and reproduce the data with an analytical model for a wide range of bias currents, drive detunings and drive powers. Our device achieves performance comparable to KPUP technology, with the potential to provide enhanced current sensitivity with a more optimized design. Ultimately, by using Josephson parametric amplification in the same cavity as used for sensing, the JPUP could sense low frequency currents with a sensitivity limited by quantum noise.

5.2. The DC bias microwave circuit

The device consists of a galvanically accessible microwave cavity, formed by a CPW that is shunted by an input capacitor C_s and shorted to ground at its far end by a JJ, as depicted in Figs. 5.1(a-c). The JJ is formed by a narrow constriction in the superconducting base-layer, which allows us to fabricate it in the same step as the microwave circuit. For details on the fabrication procedure, see Sec. 5.7.2 of the Supplemental Material [230]. Due to the shunt capacitor allowing low-frequency signals to pass through, but acting as a semi-transparent

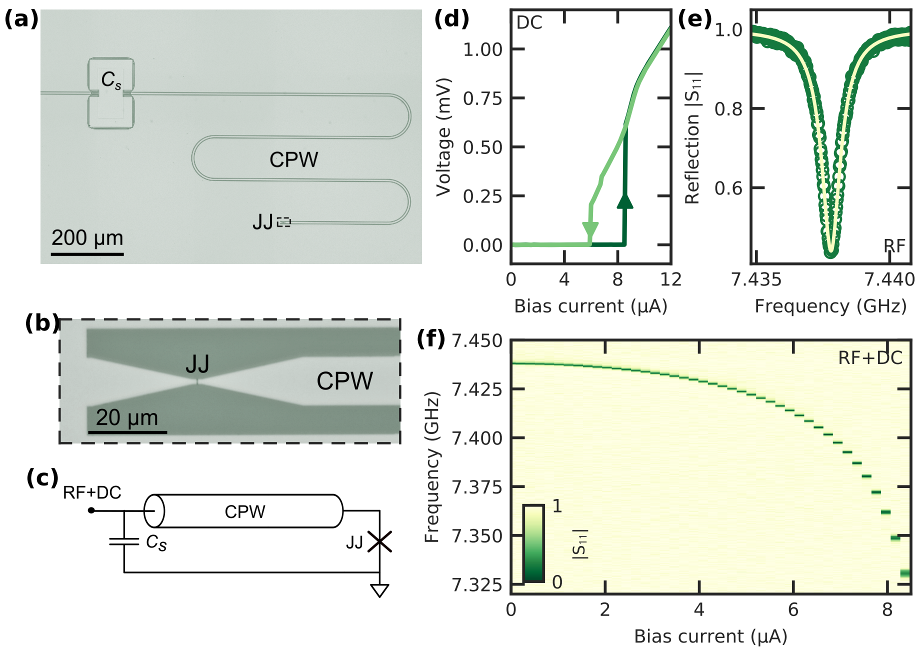

Figure 5.1: A coplanar microwave Josephson circuit with direct current bias. (a) Optical image of the measured device. It consists of a coplanar waveguide transmission line shunted to ground via a parallel plate capacitor C_s on the input, and the Josephson junction shorting the CPW center conductor to ground on the far end. (b) Optical close-up of the area around the JJ. (c) Schematic circuit layout. (d) Current-voltage characteristics of the JJ, measured by sweeping the bias current up and down (sweep direction indicated by arrows). (e) Normalized and background-corrected reflection $|S_{11}|$ of the device with zero bias current applied, see Sec. 5.7.3 of the Supplemental Material [230]. Circles: data, line: fit. (f) Reflection coefficient $|S_{11}|$ as a function of bias current. Since the Josephson inductance increases with bias current, the resonance frequency of the circuit shifts towards lower values.

mirror for microwave frequencies, our circuit allows for simultaneous measurements in the DC and RF regimes.

In the DC regime, the CPW center conductor acts as a long lead to the JJ, which we use to perform a current-voltage measurement to characterize the JJ. Upon applying an increasing DC bias current, the JJ switches from the superconducting to the voltage state and back again at switching and retrapping currents $I_\mathrm{s} \approx 8.5\,\mu\mathrm{A}$ and $I_\mathrm{r} \approx 6.1\,\mu\mathrm{A}$, as shown in Fig. 5.1(d). The observed hysteresis is most likely a combination of the capacitances of the CPW and shunt capacitor, and local heating in the junction area, see Refs. [166, 231–233] and Sec. 5.7.4 in the Supplemental Material [230].

In the RF regime, the JJ acts as a nonlinear inductor, with its inductance L_J depending on the amount of bias current I_b flowing through it, according to

$$L_\mathrm{J}(I_\mathrm{b}) = \frac{\Phi_0}{2\pi\sqrt{I_\mathrm{c}^2 - I_\mathrm{b}^2}}\,, \tag{5.1}$$

with I_c the critical current and Φ_0 the magnetic flux quantum. For zero bias current, both the impedance of shunt capacitor and of the JJ are small compared to the characteristic impedance of the CPW, i.e. $\omega L_J, 1/\omega C_s \ll Z_0$. The CPW can thus host a fundamental half-wavelength ($\lambda/2$) mode with current antinodes at both ends. When recording the reflected signal of the device using single-tone RF spectroscopy, the reflection signal shows a dip in the spectrum as seen in Fig. 5.1(e). We fit the data using the reflection coefficient of our circuit,

$$S_{11} = \frac{\kappa_e - \kappa_i - 2i\Delta}{\kappa_e + \kappa_i + 2i\Delta}\,, \tag{5.2}$$

with $\Delta = \omega - \omega_0$ the detuning between a drive at ω and the resonance frequency ω_0 and the external and internal loss rates κ_e and κ_i, respectively [37]. At zero bias current, we find a resonance frequency of $\omega_0 = 2\pi \times 7.438$ GHz, and linewidths of $\kappa_e = 2\pi \times 624$ kHz and $\kappa_i = 2\pi \times 261$ kHz. Here, the external loss rate κ_e describes how much signal leaks to the feedline, while κ_i captures intracavity losses such as due to dielectrics or radiation, see Sec. 5.7.3 of the Supplemental Material.

As we DC-bias the circuit, L_J increases, effectively shifting the voltage antinode closer to the JJ. This results in a continuously decreasing resonance frequency, tuning over approximately 108 MHz, see Fig. 5.1(f). We can approximate the bias current dependence of the cavity resonance frequency with a model describing a $\lambda/2$ CPW resonator terminated by a JJ via

$$\omega_0(I_b) = \omega_{\lambda/2}\frac{L_r + L_J(I_b, I_c)}{L_r + 2L_J(I_b, I_c)} \tag{5.3}$$

with $\omega_{\lambda/2}$ the resonance frequency of the CPW directly shorted to ground and L_r the total bare resonator inductance (see Sec. 5.7.3 of the Supplemental Material [230] and Ref. [208]). We use this model to fit the measured resonance frequencies in Fig. 5.2(a), from which we extract $\omega_{\lambda/2} = 2\pi \times 7.515$ GHz, $L_r = 3.401$ nH and $I_c = 9.157$ µA. The resonator inductance agrees with the value expected from our circuit design. The critical current as inferred from the microwave measurement is approximately 8 % larger than the DC switching current. We suspect that current noise in the DC line leads to premature switching of the JJ in the IV measurements, resulting in $I_s < I_c$, as discussed in Sec. 5.7.5 of the Supplemental Material [230] and Ref. [234]. On the other hand, the RF measurement is sensitive to the Josephson inductance, from which we can infer the critical current in a less perturbative way. We note that current-biasing a superconducting wire will also change its kinetic inductance L_k [54, 235]. However, while our device does possess a noticeable kinetic inductance fraction [236], the changes in L_k within the range of applied bias currents are negligible compared to L_J and we thus attribute the resonance frequency shift completely to the latter, see Sec. 5.7.3 of the Supplemental Material [230].

We note that upon increasing the DC bias current I_b, we observe an increase in internal loss rate κ_i of our device. We find that the dependence $\kappa_i(I_b)$ can be approximated by a constant term and exponential growth, which we ascribe to a combination of low-frequency electrical interference of the DC bias current, and phase diffusion across the JJ, see Supplemental Material Sec. 5.7.5.

5.3. Current detection by frequency up-conversion

Figure 5.2(a) illustrates the principle of current detection using the DC biased Josephson cavity. To detect small modulation currents, we drive the cavity on resonance $\omega_0(I_b)$ and simultaneously modulate the bias point I_b with a low-frequency signal $\delta I = I_\mathrm{LF}\cos\Omega t$, so that the total current is given by $I = I_\mathrm{b} + I_\mathrm{LF}\cos\Omega t$. The responsivity of the resonance frequency to bias current,

$$G_1 = \frac{\partial\omega_0}{\partial I_\mathrm{b}}\,, \tag{5.4}$$

exceeds $2\pi\times100\,\mathrm{MHz}\,\mu\mathrm{A}^{-1}$ for $I_\mathrm{b}\gtrsim 8\,\mu\mathrm{A}$. As a consequence, once the resonance frequency is modulated by I_LF, phase modulation leads to the generation of sidebands in the microwave drive tone reflection with $\omega = \omega_\mathrm{d} \pm n\Omega$, where $n\in\mathbb{Z}$. The reflected cavity field thus exhibits the drive tone together with the sidebands, as depicted in Fig. 5.2(b).

The general equation of motion for the amplitude field α of a harmonic high-Q oscillator with small nonlinearity β, written in the frame rotating with the drive, is given by

$$\alpha = \left[-i\left(\Delta + \beta|\alpha|^2\right) - \frac{\kappa}{2}\right]\alpha + \sqrt{\kappa_\mathrm{e}}S_\mathrm{in}\,, \tag{5.5}$$

with S_in the amplitude of the drive field in units of $\sqrt{\mathrm{Photons/Hz}}$ at ω, and β a small nonlinearity [237]. We consider the case in which the cavity resonance frequency is a function of an additional current given by $I = I_\mathrm{b} + \delta I = I_\mathrm{b} + I_\mathrm{LF}\cos\Omega t$, such that

$$\omega_0 = \omega_0(I_\mathrm{b}) + \sum_{m=1}^{n}\frac{\partial^m\omega_0}{\partial I^m}\delta I^m = \omega_I + \sum_{m=1}^{n} G_m\delta I^m\,. \tag{5.6}$$

The resulting field amplitude of the first order sidebands appearing at $\omega_0 \pm 1\Omega$ is

$$|S_{\pm1}|^2 = \frac{\kappa_\mathrm{e}\alpha_0^2G_1^2I_\mathrm{LF}^2}{\kappa^2 + 4(\Delta\pm\Omega)^2}\,. \tag{5.7}$$

In our experiment, we chose $\Omega = 2\pi\times1\,\mathrm{kHz}$ and $I_\mathrm{LF} = 10\,\mathrm{nA}$. In this case, $\Omega\ll\kappa$ and red (S_-) and blue (S_+) sidebands have approximately equal amplitudes, see Sec. 5.7.7 of the Supplemental Material [230]. Note that even higher order contributions from the current still contribute to the $\pm1\Omega$ sideband, but those contributions can be neglected for relatively weak modulation.

To explore the parameter space of our device, we performed a series of current-mixing measurements for different values of bias current I_b, drive detuning Δ and drive amplitude S_in, for all of which we observe excellent agreement between experiment and theory: As can be seen in Fig. 5.3(a), for the case of varying bias current and as expected from Eqs. (5.3),(5.7), the first order sideband vanishes for zero bias current. As we increase the DC bias current, the increasing Josephson inductance leads to an increased responsivity $\partial\omega_0/\partial I_\mathrm{b}$, which in turn results in a growing sideband amplitude. Assuming all other parameters remain constant, the sideband amplitude should keep growing until the bias current reaches the critical current of the JJ, at which point the junction switches to the normal state, effectively destroying the device response. However, already at $I_\mathrm{b}\approx0.75\,I_\mathrm{c}$ the sideband amplitude exhibits a maximum value and begins to decrease subsequently. The origin for this phenomenon lies in the growth of κ_i for increasing I_b as described earlier, which limits the maximum achievable sideband amplitude, see Sec. 5.4.2 and Sec. 5.7.5 of the Supplemental Material [230].

Operating the device at constant bias current and drive power P_in but sweeping the drive tone with respect to the cavity resonance similarly reduces the sideband amplitude, which is

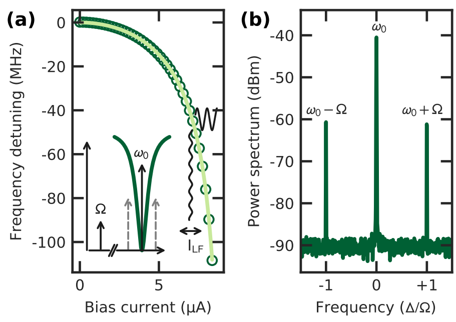

Figure 5.2: Current detection by frequency up-conversion. (a) Cavity resonance frequency for increasing DC bias current, showing a total frequency shift of 108 MHz. Circles: measured data, line: fit to resonance frequency using Eq.(5.3). Inset: sketched measurement scheme in the frequency domain. By driving the cavity on resonance $\omega = \omega_0$ and simultaneously modulating with a low frequency current $\delta I = I_{\text{LF}} \cos \Omega t$, the cavity generates sidebands to the drive tone at $\omega_0 \pm \Omega$ (dashed grey arrows). (b) The power spectrum of the reflected field at $I_{\text{b}} = 2.5\,\mu\text{A}$, containing the input pump signal at ω_0 and the first order sidebands due to mixing at $\omega_0 \pm \Omega$. The noise floor sets a lower limit on the smallest detectable sideband amplitude. The sideband amplitude allows us to directly calibrate the noise floor and thus the sensitivity from the signal-to-noise ratio, here SNR $\approx$ 30 dB.

reflected in both the theoretical model and our measurements, see Fig. 5.3(b). We attribute deviations of the model from the data to an effectively increased cavity linewidth resulting from a noise-induced fluctuating cavity frequency.

Finally, when setting the detuning back to zero and sweeping the drive power, we initially observe a linear increase of the sideband amplitude, see Fig. 5.3(c). This is in good agreement with the intracavity field dependence with pump power of a linear cavity. However, due to the nonlinearity of the JJ and the resulting Kerr anharmonicity of the circuit, our device enters the Duffing regime for large input powers, resulting in the observable reduction of the sideband amplitude: The anharmonicity results in a down shifted resonance frequency given by $\omega_0' = \omega_0 - |\alpha_0|^2\beta$. In the measurement depicted in Fig. 5.3(c), the only varying parameter is the pump power, which means that in the Duffing regime the drive acquires an increase in detuning for increased power, resulting in a decreased sideband amplitude, as we saw earlier.

5.4. CURRENT SENSITIVITY

Having established the validity of our theoretical framework, we calculate the current sensitivity $\mathcal{S}_I$ of our device. This quantity captures the minimum current that the device is able to discriminate from the noise floor. We obtain this quantity by extracting the signal-to-noise ratio (SNR) of the first sideband amplitude: Since we know the amplitude of our ingoing LF current signal, we can convert the sideband amplitude and noise floor to currents as described in Sec. 5.7.9 of the Supplemental Material [230]. We obtain

$$\mathcal{S}_I = \frac{I_{\text{LF}}}{\sqrt{\text{ENBW} \times 10^{(\mathcal{S}-\mathcal{N})/10}}}, \tag{5.8}$$

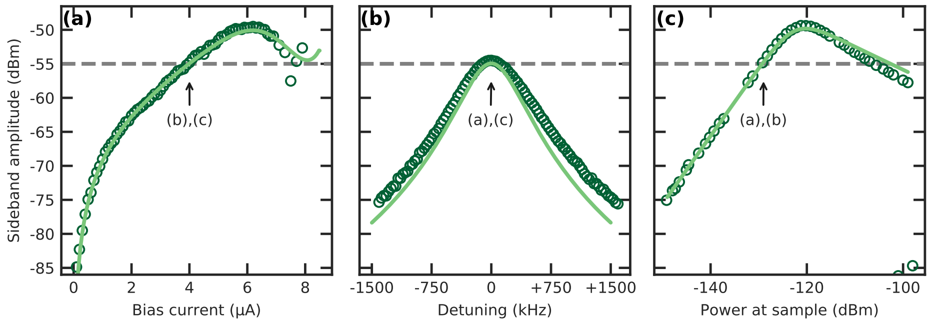

Figure 5.3: Exploring the parameter space for the first order sideband amplitude. (a) Sideband height for changing bias current setpoint at fixed input power and zero detuning. (b) Sideband height for changing drive detuning at fixed input power and bias current. (c) Sideband height for changing input power at fixed bias current and detuning. Circles: measured data, solid lines: calculated amplitude via input-output theory, dashed grey line: calculated sideband amplitude at $I_b = 4\,\mu A$, $\Delta = 0$ and $P_{in} = -129$ dBm. Arrows indicate the setpoints for the other respective panels.

with ENBW the equivalent noise bandwidth of the spectrum analyzer [238], and S and N the amplitudes of the sideband and the noisefloor in dBm, respectively.

5.4.1. MEASURED DEVICE

We analyze $\mathcal{S}_I$ for a large range of bias currents and drive powers. The device sensitivities extracted via Eq. (5.8) are plotted in Figs. 5.4(a,b) for the measured and modeled data, respectively, showing good qualitative agreement. Linecuts through the 2D measured and simulated data at the best measured value of $\mathcal{S}_I$ show good quantitative agreement between theoretical model and measurement, see Figs. 5.4(c,d).

For a fixed bias current, the current sensitivity drops exponentially as a function of input power, reaching a minimum value of $\mathcal{S}_I = 8.9\,\mathrm{pA}/\sqrt{\mathrm{Hz}}$ at $I_b = 7.3\,\mu A$ and $P_{in} = -113$ dBm. Similarly, as a function of bias current and fixed input power, the current sensitivity drops rapidly over more than two orders of magnitude. Our theoretical calculations deviate from the measured data for very large input powers and bias currents, for which the model predicts sensitivity values larger than observed. This deviation might be due to minor differences in experimental and theoretical detuning: If the the pump tone ω_0 is slightly below the value of ω_0' in the limit of $n_{ph} \longrightarrow 0$, the pump will initially be slightly red-detuned ($\Delta < 0$) and move to blue-detuned ($\Delta > 0$) as the resonance shifts downward due to the Kerr nonlinearity, instead of starting on-resonance and becoming only blue-detuned as we increase P_{in}. Depending on the pump power at which $\Delta = 0$, the theory curve will underestimate the sideband amplitude for $\Delta > 0$, resulting in too large values of $\mathcal{S}_I$, as in Fig. 5.4(c) for $P_{in} \geq -120$ dBm.

As detailed in Sec. 5.7.8 of the Supplemental Material [230], the model follows the measured data more closely for high pump powers assuming an initially red detuned drive. This deviation is especially large for high bias currents because the anharmonicity grows with I_b. Thus, the cavity resonance shifts stronger with pump power and the drive is more likely to have a smaller detuning than expected for high P_{in}.

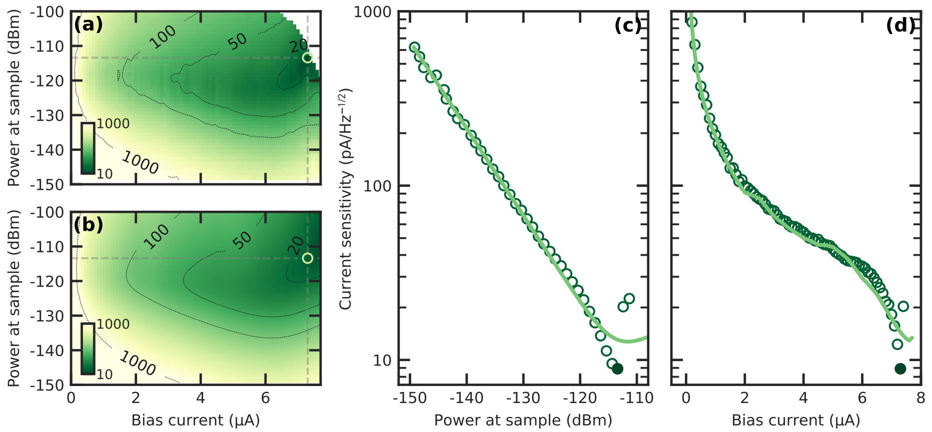

Figure 5.4: Finding the best device sensitivity. Current sensitivity in pA/$\sqrt{\text{Hz}}$ versus bias current and input power, as measured (a) and calculated (b). Dashed grey lines correspond to the linecuts in (c) and (d), circle marks the point of minimum measured sensitivity. Color scale is logarithmic from 10 to 1000, black lines mark contour lines of sensitivity values as labeled. (b) Sensitivity at 7.3 µA versus pump power (vertical line in (a,b)). We attribute discrepancies at high P_{in} to differences in Δ between measurement and theory. (c) Sensitivity at P_{in} = −113 dBm versus bias current (horizontal line in (a,b)). Circles: measured data, lines: model, full circle: minimum measured sensitivity.

5

5.4.2. Limitations of present device and setup

Optimum sensitivity would be achieved for zero pump detuning, maximum pump power and biasing the device close to I_c, see Fig. 5.4(a),(b). In our experiment we were unable to operate the device in a stable regime for bias currents greater than $0.9\,I_c$, after which the JJ occasionally switched to the normal state, destroying the RF resonance. We attribute this to a significant ac current induced by the microwave drive on the order of 1 µA, see Supplemental Material Sec. 5.7.6. Together with the DC bias, the total current at the JJ reaches close to I_c, thus constraining the available parameter space.

Additionally, we observed exponential increase of the internal loss rate for large bias currents. These effects are presumably due to random phase diffusion across the junction and electrical interference in our setup, see Sec. 5.7.5 of the Supplemental Material [230]. Most notably, at elevated bias currents spurious sidebands at integer multiples of 50 Hz appear in the measured spectra, which are due to insufficient isolation between the DC and RF electronics. Using the same approach as for the intended signal, we can quantify the current noise due to mains power to 170 pA $\approx I_{\text{LF}}/60$. Improving the setup should allow us to move to even higher bias currents, gaining in $\mathcal{S}_I$. In addition, the resonance frequency shift due to anharmonicity places an upper bound on the maximum input power.

In an optimized measurement, shifting the pump frequency with pump power in order to remain closer to resonance should allow us to gain more than 10 dB, reaching a minimum of 2.7 pA/$\sqrt{\text{Hz}}$, see Sec. 5.7.8 of the Supplemental Material [230].

5.4.3. Modeled optimized device

In order to improve $\mathcal{S}_I$, we propose a slightly changed circuit layout that follows naturally from the measured device and is immediately implementable: Instead of a transmission line shorted to ground by a single JJ, we propose to incorporate the Josephson inductance into the transmission line itself, by means of a diluted JJ metamaterial [239]. The optimized design would then be a transmission line directly shorted to ground, with the CPW center conductor made up of a series of identical unit cells, each composed of a combination of linear and Josephson inductance (L_0, L_J) and a capacitance to ground (C_0), as depicted in Fig. 5.5(a). Following the approach to circuit quantization presented in Ref. [240] and methods from Refs. [165, 241, 242], we derive the resonance frequency of this CPW as

$$\omega_0(I_\mathrm{b}) = \frac{\pi}{N\sqrt{C_0(L_\mathrm{J}(I_\mathrm{b}) + L_0)}}\,, \tag{5.9}$$

in the limit of large N, as detailed in Sec. 5.7.11 of the Supplemental Material [230]. To maximize the responsivity G_1 of the device via maximizing the participation ratio $\eta_\mathrm{J} = L_\mathrm{J}/(L_0 + L_\mathrm{J})$ per unit cell, we propose a CPW with center conductor and gap sizes $1/10$ of the current design and a reasonably short unit cell length of 1 µm. This would result in $L_0 = 842$ fH, $L_\mathrm{J} = 35.9$ pH and $C_0 = 169$ aF per unit cell, see Ref. [243] and Sec. 5.7.11 of the Supplemental Material [230]. For an initial resonance frequency at $\omega_0 = 2\pi \times 7.5$ GHz, the device would require approximately 845 unit cells, resulting in a total device length of 845 µm, much more compact than our present layout. Such an optimized device offers a significantly larger $G_1 \approx 4\,\mathrm{GHz\,\mu A^{-1}}$ with a relative frequency shift $\delta\omega_0/\omega_0 \approx 50\,\%$. Assuming the same internal losses as for our measured device and additionally increasing the external coupling, e.g. by reducing the shunt capacitor to $1/2$ of its current area, this device would be able to achieve sensitivities as low as $0.17\,\mathrm{pA}/\sqrt{\mathrm{Hz}}$, a factor of 54 improvement to our presented design, as shown in Fig. 5.5(b).

We note that in an ideal experiment, the drive frequency should be tuned for increasing drive power in order to account for the Kerr-shift of the resonance to lower frequencies, thus minimizing Δ and maximizing α_0. Implementing this measurement scheme would allow us to achieve sensitivities down to $50\,\mathrm{fA}/\sqrt{\mathrm{Hz}}$. Since this estimation does not take parametric amplification into account, we expect it to be an upper bound to the experimentally achievable $\mathcal{S}_I$: Utilizing quantum-limited parametric amplification built into the device would allow us to gain approximately 20 dB [208, 220, 239], providing noise levels down to $5\,\mathrm{fA}/\sqrt{\mathrm{Hz}}$.

5.5. Conclusion

We presented a Josephson parametric upconverter and demonstrated current sensitivities down to $8.9\,\mathrm{pA}/\sqrt{\mathrm{Hz}}$ which makes our compatible with TES readout, and derived an analytical model that accurately reproduces the measured data and is immediately applicable to other device architectures. We estimate that future devices using increased Josephson participation ratios, and using the intrinsic Kerr-nonlinearity for four-wave parametric amplification built into the detection cavity, should allow for an improved $\mathcal{S}_I \sim 5\,\mathrm{fA}/\sqrt{\mathrm{Hz}}$, orders of magnitude better than state of the art KPUPs and limited by the fundamental quantum noise of the cavity.

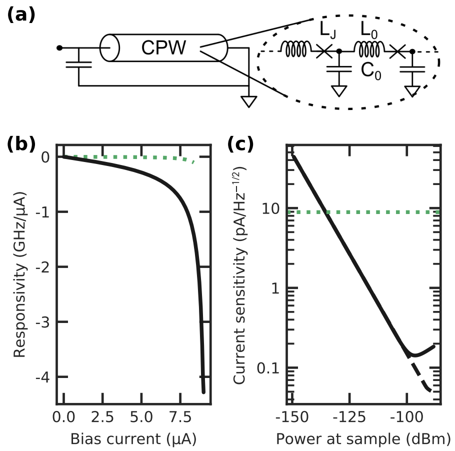

Figure 5.5: Estimated sensitivities for optimized device design. (a) Instead of a linear CPW shorted to ground by a nonlinear Josephson junction, the optimized device is a diluted JJ meta material with a CPW center conductor based on a Josephson junction array, directly shorted to ground. (b) Frequency responsivity G_1 for the optimized (solid line) and current device (dotted line). Due to the dominating Josephson inductance, the optimized device tunes further with bias current. (c) Predicted $\mathcal{S}_I$ for the optimized device. Dotted line indicates the minimum experimentally achieved sensitivity of 8.9 pA/$\sqrt{\text{Hz}}$ with the present design. For the JJ array CPW, we predict sensitivities as low as 170 fA/$\sqrt{\text{Hz}}$ (solid line). The sensitivity curves upwards for high pump powers due to the nonlinearity in the circuit. Choosing the pump frequency to be continuously close to resonance for high drive powers, the predicted sensitivity would drop down to 50 fA/$\sqrt{\text{Hz}}$ (dashed line). Parametric amplification could reduce the sensitivity one order of magnitude further by reducing the contribution of the noise of the cryogenic HEMT amplifier in the readout noise of the cavity.

5.6. Methods

5.6.1. Data availability

All raw and processed data as well as supporting code for measurement libraries, data processing and figure generation is available in Zenodo [211].

5.6.2. Input-output formalism

Starting from Eq. (5.5), with the steady-state solution α_0, the reflection coefficient is given by

$$S_{11} = -1 - \sqrt{\kappa_e}\frac{\alpha_0}{S_{\text{in}}} = -1 + \frac{2\kappa_e}{\kappa + 2i\Delta} \tag{5.10}$$

where the second equality holds in the limit $\beta \longrightarrow 0$ and which can be recognized as the usual reflection expression of circuit theory.

We now consider the case in which the cavity resonance frequency is a function of an additional current given by $I = I_b + \delta I$. With the resonance frequency given by Eq. (5.6), the new equation of motion reads

$$\dot{\alpha} = \left[-i\left(\Delta - \sum_{m=1}^{n} G_m \delta I^m\right) - \frac{\kappa}{2}\right]\alpha \\ -i\beta|\alpha|^2\alpha + \sqrt{\kappa_e} S_{in} \, . \tag{5.11}$$

With the Ansatz for the intracavity field $\alpha(t) = \alpha_0 + \delta\alpha(t)$ and assuming $|\alpha|^2 \approx \alpha_0^2$ we get

$$\delta\dot{\alpha} = \left[-i\left(\Delta - \sum_{m=1}^{n} G_m \delta I^m\right) - \frac{\kappa}{2}\right]\delta\alpha \\ +i\alpha_0 \sum_{m=1}^{n} G_m \delta I^m \, . \tag{5.12}$$

Let the modulation in current be of the form

$$\delta I = I_{LF} \cos \Omega t = I_- e^{-i\Omega t} + I_+ e^{+i\Omega t} \tag{5.13}$$

where $I_- = I_+ = I_{LF}/2$. Our Ansatz for $\delta\alpha$ is consequently

$$\delta\alpha = \sum_{m=1}^{n} a_{-m} e^{-mi\Omega t} + a_{+m} e^{+mi\Omega t} \, . \tag{5.14}$$

Inserting Eqs. (5.13),(5.14) into Eq. (5.12), we can group the terms by their frequency components and equalize each component individually in order to solve for the sideband coefficients $a_{\pm m}$. Each sideband output field can then be calculated via

$$S_{\pm m} = \sqrt{\kappa_e} a_{\pm m} \, . \tag{5.15}$$

We arrive at a compact result for the first order sidebands appearing at $\omega_0 \pm 1\Omega$:

$$S_{\pm 1} = \frac{\sqrt{\kappa_e}\alpha_0 G_1 I_{LF}}{-i\kappa + 2(\Delta \pm \Omega)} \, . \tag{5.16}$$

We calculated all $a_{\pm m}$ coefficients up to $m = 3$ using *Mathematica* v11.3.0.0 in the notebook `input-output formalism.nb`, which we subsequently converted to *python3* code using the notebook `Export to Python.nb` located in Zenodo [211].

5.6.3. CALCULATING THE STEADY-STATE SOLUTION

We can calculate α_0 by solving Eq. (5.5) for a large pump signal and treating the probe as a perturbation. Thus, let us assume that the solution has the form $\alpha(t) = \alpha_0 \exp[i\omega_p t]$ and the input signal $S_{in}(t) = S_p(t) = S_{po} \exp[i(\omega_p t + \phi)]$ is the pump signal. Since we are only interested in the steady-state solution, let $S_{po}, \alpha_0 \in \mathbb{R}$. Inserting this into Eq. (5.5), we get

$$\left(i\Delta + \frac{\kappa}{2}\right)\alpha_0 + i\beta\alpha_0^3 = \sqrt{\kappa_e} S_{po} e^{i\phi} \tag{5.17}$$

Multiplying this equation with its complex conjugate returns

$$\beta^2\alpha_0^6 + 2\Delta\beta\alpha_0^4 + \left(\Delta^2 + \frac{\kappa^2}{4}\right)\alpha_0^2 - \kappa_e S_{po}^2 = 0\,. \tag{5.18}$$

While this third-order polynomial in α_0^2 has multiple complex solutions, the ones relevant in our case are only real. In the high-power regime, our resonator will exhibit bifurcation and Duffing behavior, meaning there will be three real valued solutions to α_0^2: The largest, median and smallest one corresponding to the high, middle and low amplitude branch, respectively. For a given input field S_{po} and detuning Δ, the (up to three) solutions of this equation can be found either numerically or analytically. However, for the parameters used in our experiment, the solutions for α_0^2 are identical because our drive remains outside of the bifurcation regime. We can then use the corrected intracavity field for obtaining the sideband amplitudes by replacing the value of α_0 for the linear oscillator in Eq. (5.31).

Furthermore, taking the resonance frequency as the point where $\partial\alpha_0/\partial\omega = 0$, we can compute the frequency shift the cavity experiences as a result of the driving power by differentiating Eq. (5.18) with respect to ω as

$$\omega_0' = \omega_0 - |\alpha_0|^2\beta\,. \tag{5.19}$$

5.6.4. Higher order terms

Already for second order in δI, the prefactors are too complicated to write down in a short form, which is why we refer to the full analytical solutions in the *Mathematica* notebook `input-output formalism.nb` located on Zenodo [211]. We note that higher order corrections arising for terms in δI^m, have only negligible effects on the lower order forms. For the analysis in the main text, we therefore only make use of the closed form for the first order terms, and for the second order peaks in Fig. 5.6(b-d), only the second order terms were used.

We observe higher order sidebands over a wide range of operating points, with an exemplary spectrum exhibiting both first and second order peaks plotted in Fig. 5.6(a). Similar to Fig. 5.3(a), the second order sideband increases with DC bias current up to $I_b \approx 0.75\, I_c$ where the amplitude is limited by the increasing internal loss rate, see Fig. 5.6(b). As depicted in Fig. 5.6(c), finite drive detuning strongly suppresses the sideband amplitude similar to the first order peaks. The power dependence, see Fig. 5.6(c), also closely resembles the shape of the first order sideband, with maximum amplitude for high drive powers and subsequent decrease due to increasing drive detuning as a consequence of the downshift in resonance frequency due to the Kerr nonlinearity.

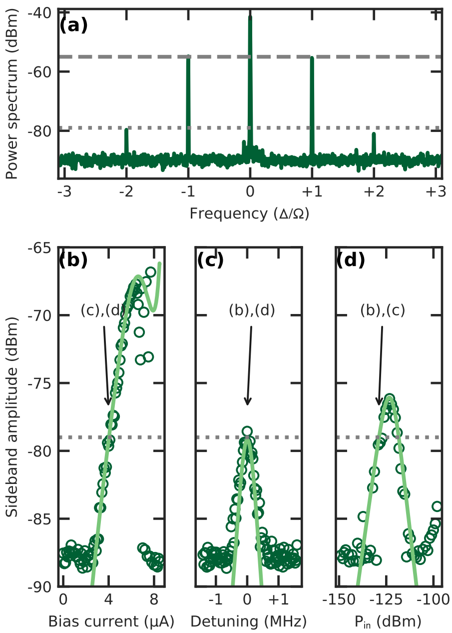

Figure 5.6: Exploring the parameter space for the second order sideband amplitude. (a) The power spectrum at the output at $I_0 = 4\,\mu A$, $\Delta = 0$ and $P_{\text{in}} = -129$ dBm containing the input pump signal at ω_0 and the first and second order sidebands due to mixing at $\omega_0 \pm \Omega$ and $\omega_0 \pm 2\Omega$. Dotted grey line corresponds to the one in panels (b-d), dashed grey line corresponds to the one in Fig. 5.3. (b) Sideband height for changing bias current setpoint at fixed input power and zero detuning for varying bias current. (c) Sideband height for changing drive detuning at fixed input power and bias current. (d) Sideband height for changing input power at fixed bias current and detuning. Circles: measured data, solid lines: calculated amplitude via input-ouput theory, dotted grey line: calculated sideband amplitude at $I_0 = 4\,\mu A$, $\Delta = 0$ and $P_{\text{in}} = -129$ dBm. Arrows indicate the setpoints for the other respective panels.

5.7. Supplementary Material: Current detection using a Josephson parametric upconverter

5.7.1. Measurement setup

Wiring configuration

All measurements were taken with the device mounted to the millikelvin stage of a *Bluefors LD400* dilution refrigerator with a base temperature of approximately 15 mK. The measurement setup is sketched in Fig. 5.7. We use in-house built, low-noise battery-powered electronics for DC measurements of the device: A voltage-controlled current source with an ideally infinite output impedance, and a voltmeter. For measurements involving current detection, we modulate the voltage controlled current source with an arbitrary waveform generator (AWG), model *DG1022Z* from *Rigol*. Microwave reflection measurements of the cavity are done using a vector network analyzer (VNA) from *Agilent*, model *PNA N5222A*. Signal generation and spectroscopy for current detection are done using signal generator *SMB 100A* (SG) and analyzer *FSV13* (SA), respectively, from *Rohde & Schwarz*. The VNA and SG paths are merged using directional couplers. Prior to the measurements on current detection, we calibrated the frequency dependent difference in attenuation between the signal paths VNA – device under test (DUT) and SG – DUT which we account for in all measurements and in the data analysis.

In order to minimize the influence of 50 Hz interference from mains powered equipment on our experiments, we place the DC electronics on an isolated rack and place all RF equipment on another one. We observed significant signal deterioration for elevated bias currents if the DC and RF electronics shared the same ground. For this reason, we placed additional DC blocks with separated inner and outer conductors on the RF input lines (PE8212 from *Pasternack*). Note that for the LF current modulation, we need to galvanically connect the AWG to our current source, which in turn leads to a potential source of significant 50 Hz interference (see Sec. 5.7.5 for more elaborate discussion on this topic).

The DC lines are heavily filtered using π-filters inside the room-temperature electronics, and homemade copper powder and two-stage RC-filters on the baseplate of the dilution refridgerator. The -3 dB cut-off for these filters is at around 30 kHz, well above the chosen modulation frequency of 1 kHz. To reduce the influence of stray magnetic fields, a passive μ-metal shield surrounds the DUT and entire 15 mK stage.

Measurement protocol for current detection

The measurements on current detection were performed using the following measurement scheme:

1. **Initialization and calibration** Turn off all outputs of RF instruments. Sweep the bias current back to zero and then to the next bias value. Set the VNA output power to low power and perform an S_{11} measurement from 7 GHz to 8 GHz. From this measurement, determine the resonance frequency f_0 as the frequency at which $|S_{11}|$ is minimum.

2. **Current detection for fix pump power and detuning** Turn off the output of the VNA. Set the RF drive from the SG to low power and the drive frequency to f_0. Turn on the LF modulation ($I_{\mathrm{LF}} = 10$ nA, $\Omega = 2\pi \times 1$ kHz). Trigger the SA to perform one measurement.

3. **Current detection for variable detuning** Keep the RF pump power at the same value and sweep the RF modulation frequency from $f_0 - 3$ MHz to $f_0 + 3$ MHz and for each detuning record the output signal using the SA.

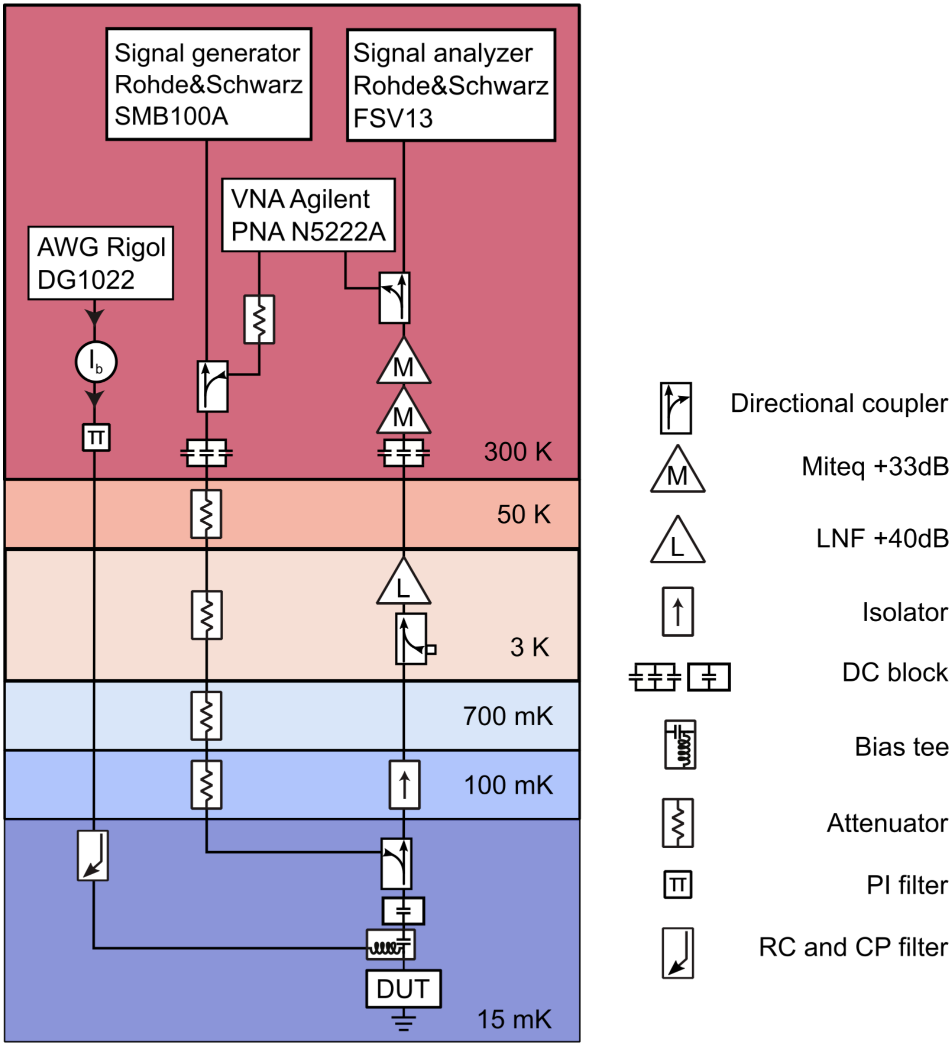

Figure 5.7: Measurement setup used for all measurements in this chapter. The directional coupler at the 3 K stage was terminated by a 50 Ω load at the coupled port. The bias current source is battery powered and voltage controlled, while all other equipment is mains powered. DC blocks at room temperature isolate both center and outer conductor, while the ones at 15 mK only isolate the center conductor. From the millikelvin stage to the HEMT at 3 K, we use superconducting cabling. Not shown are a passive μ-metal shield surrounding the millikelvin stage, as well as a cryogenic switch between DUT and bias-T to switch between the different samples on-chip, see Fig. 5.8.

5

4. Current detection for variable pump power Set the RF frequency back to f_0. Sweep the RF pump power and for each pump power record the output signal using the SA. After each pump power measurement, reinitialize the bias current and find the resonance frequency again in order to reduce the number of "dead" cases in which the Josephson junction switched to the voltage state prematurely.

ESTIMATION OF THE ATTENUATION AND AMPLIFICATION CHAIN

To estimate the attenuation chain, we use the thermal noise of our cryogenic high electron mobility transistor (HEMT) as a calibration source. The noise power due to the effective noise temperature $T_e \approx 2\,\mathrm{K}$ of the HEMT as given by the manufacturer is

$$P'_{\mathrm{N,in}} = k_B T_e \Delta f \approx 2.761 \times 10^{-23}\,\mathrm{W\,Hz^{-1}} \times 1\,\mathrm{kHz} \approx 2.761 \times 10^{-20}\,\mathrm{W} \approx -165.6\,\mathrm{dBm}\,, \quad (5.20)$$

where $\Delta f = 1\,\mathrm{kHz}$ is the measurement bandwidth of our setup. By averaging over a few S_{11} traces taken with the VNA in an area unaffected by our DUT, i.e. off-resonant to the cavity and thus leaving the background unaltered in power, we extract an average signal and standard deviation which we use to define the signal-to-noise ratio at the VNA, $\mathrm{SNR_{VNA}} = 34.5\,\mathrm{dB}$ for a VNA output power of 0 dBm.

In our setup, the added noise from the HEMT dominates over other noise sources, which we deduce from an increase in noise level when powering up the HEMT with the room temperature amplifiers already on. Therefore, the SNR at the VNA is identical to the one at the HEMT output, and we deduce the power arriving at the HEMT input to be $P_{\mathrm{in}} = -131.3\,\mathrm{dBm}$. Between DUT and HEMT, the signal travels a certain distance of cabling and passes through additional microwave components, see Fig. 5.7. On the way, the signal will have been reduced by X dB due to the mentioned components, hence the power arriving at the HEMT will be $P'_{\mathrm{in}} = 10^{-X/10} P_{\mathrm{in}}$, which results in an estimated attenuation of 129.3 dB of our VNA input line, assuming $X = 2\,\mathrm{dB}$ of cable loss between sample and HEMT.

We deduce the total gain of our amplification chain by calculating the average noise power measured with the SA, $P_{\mathrm{N,SA}} = -97.5\,\mathrm{dBm}$ in a 1 Hz bandwidth, and substracting from it the HEMT noise power $P'_{\mathrm{N,in}} = -195.6\,\mathrm{dBm}$ corresponding to the same bandwidth and the cable loss $X = 2\,\mathrm{dB}$, resulting in a total gain of 96.1 dB for the amplifier chain.

5.7.2. DEVICE FABRICATION

The device is fabricated in a four-step process in the *Kavli Nanolab* cleanroom of TU Delft, using a combination of electron beam lithography (EBL, EBPG5000+ from *Raith*), liftoff, sputtering (AC450 from *Alliance*), PECVD (PlasmaPro 80 from *Oxford Instruments*) and dry-etching (Fluorine reactive ion etcher from *Leybold Hereaus*). An optical micrograph of the fully packaged chip is shown in Fig. 5.8. The geometric device parameters are given in Table 5.1. In the following we describe the fabrication step by step.

Substrate We use a double-side polished high-resistivity ($> 6\,\mathrm{k\Omega\,cm}$, light P/Boron doping, 550 μm thickness) 4 inch silicon wafer from *IWS* as substrate for our device. The wafer is covered in positive electron beam resist (AR-P 6200.13, approximate thickness 550 nm) and exposed to define the pattern for alignment and dicing markers. We sputter-deposit 50 nm of Molybdenum-Rhenium (MoRe, RF magnetron sputtering in argon atmosphere from a 60 % Mo-40 % Re target) and lift off the resist-protected areas using an anisole bath and strong ultrasonication, followed by multiple acetone and isopropanol baths.

Table 5.1: Geometric device parameters

Symbol	Description	Value
s	CPW center conductor	10 µm
w	CPW gaps to ground	6 µm
t	Base layer thickness	20 nm
L'_g	Geometric inductance per length [243]	424 nH m^{-1}
C'_0	Geometric capacitance per length [243]	169 pF m^{-1}
l	CPW length, from end of shunt to JJ	6382 µm
A_s	Shunt capacitor area	57 800 µm^2
t_d	Dielectric layer thickness	140 nm

We subsequently cover the wafer with photoresist (HPR 504, 1.2 µm thick) and dice it into 14 mm × 14 mm chips for easier handling during fabrication.

Base layer We pattern the Josephson junction together with the base layer and ground planes in a single lift-off step using AR-P 6200.09 (200 nm) and 20 nm of sputtered Aluminum-Silicon (AlSi, reactive DC magnetron sputtering in argon atmosphere from a 99 % Al-1 % Si target). Lift-off is done by placing the chip in the bottom of a beaker with room-temperature anisole and strong ultrasonication for a few minutes.

Dielectric layer For the shunt dielectric layer, we deposit 140 nm amorphous silicon at 90 °C using PECVD. Patterning is done with EBL of a double-layer resist (PMMA 950K A4 and AR-N 7700.18) and reactive ion etching in a SF_6 + He atmosphere. The resist layers are in-situ removed using O_2 plasma.

Top shunt plate The top plate of the shunt capacitor is fabricated with an additional lift-off step using the same resist as for the alignment markers, and sputtering 100 nm AlSi.

Packaging To fit our printed circuit board (PCB), the chip is again covered in photoresist and trimmed down to 10 mm × 10 mm. After washing off the photoresist in a series of acetone and isopropanole baths, the chip is glued to our copper sample holder, to which the PCB is mounted, using cryogenic GE varnish. Electrical connections to the device are made using wedge-bonding on a Westbond wirebonder with aluminum wire bonds. We place a small copper lid on the chip to protect it from dirt and to suppress box modes of a bigger copper lid screwed onto the copper base, which accomodates the SMA connectors.

5.7.3. GENERAL DEVICE PARAMETERS

REFLECTION COEFFICIENT

The reflection coefficient of a transmission line with a shunt capacitor to ground on the input side and shorted to ground on the far end is given by

$$S_{11}(\omega, \kappa_i, \kappa_e) = \frac{\kappa_e - \kappa_i - 2i\Delta}{\kappa_e + \kappa_i + 2i\Delta} = -1 + \frac{2\kappa_e}{\kappa + 2i\Delta} \tag{5.21}$$

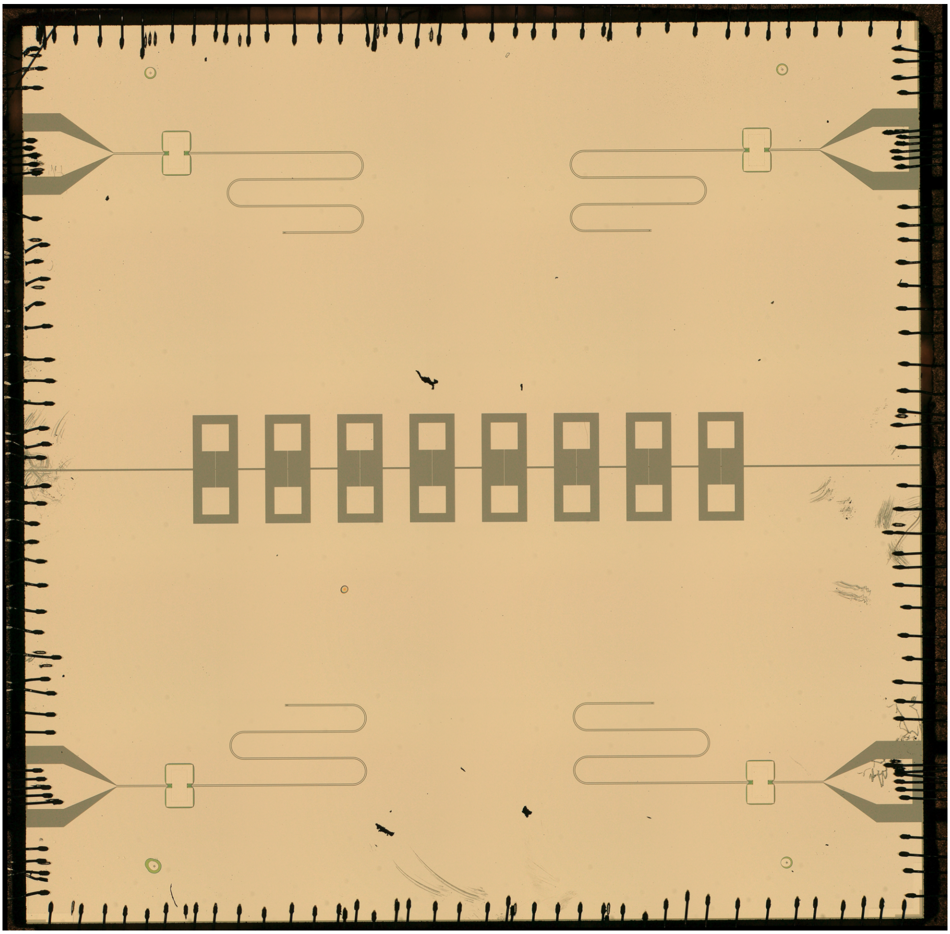

Figure 5.8: The full chip. Microscope image of the full chip, wirebonded to the PCB used for measurements. The chip hosts four different devices: The CPW with single JJ discussed in the main text (bottom left), a reference cavity with the same geometry shorted to ground (top left), and two devices shorted to ground by superconducting interference devices (SQUIDs) with loop sizes 8 µm × 9 µm (top right) and 5 µm × 5 µm (bottom right). Structures in the chip center are used for room-temperature DC tests. Chip size is 10 mm × 10 mm.

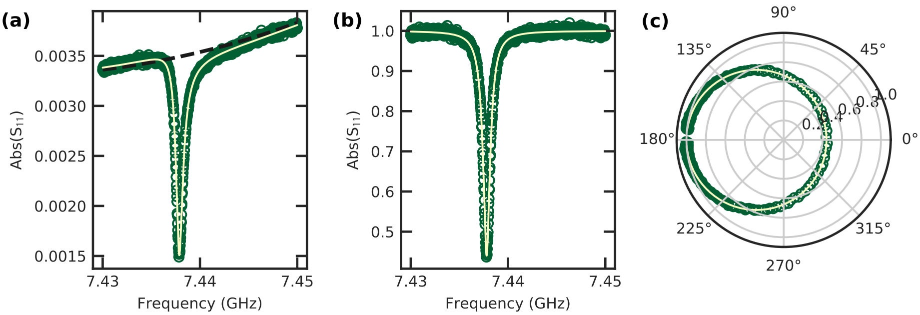

Figure 5.9: Data and fit of the reflection coefficient. (a) Absolute value of S_{11} as measured (markers) with fit (solid line) taking into account background (dashed line). (b) Absolute value of the reflection coefficient S_{11} versus frequency after removing the oscillating background. (c) Polar plot of the absolute value of S_{11} versus phase, without background and rotation in the complex plane. Markers: data, solid lines: fits according to Eq. (5.21).

with the detuning from resonance, $\Delta = \omega - \omega_0$ and the internal, external and total loss rates κ_i, κ_e and $\kappa = \kappa_e + \kappa_i$. Broadly speaking, the external loss rate describes signal loss of the DUT to the feedline, while the internal loss rate describes losses due to effects like radiation or dielectrics. Following Ref. [37], we infer $\kappa_e = 2/(\pi\omega_0 Z_0^2 C_s^2)$ for a CPW with impedance Z_0 matched to that of a feedline. There is no analytical expression for κ_i.

The real response function is however distorted by the complex microwave background which arises due to impedance mismatches in our measurement setup, as can be seen in Fig. 5.9(a). For this reason, we model the measured S_{11} spectra using the above model for an ideal device multiplied by a complex microwave background and a rotation in the complex plane:

$$S'_{11}(\omega, \kappa_i, \kappa_e, \theta) = \left(a + b\omega + c\omega^2\right) e^{i(a'+b'\omega)} \left\{e^{i\theta}\left[S_{11}(\omega, \kappa_i, \kappa_e) + 1\right] - 1\right\} \qquad (5.22)$$

Our fitting algorithm first detects the resonance as the frequency corresponding to the maximum phase derivative and fits the background signal by removing a certain window around the resonance frequency. In a second step, it fits the modified model to the full data set keeping the background parameters fixed, and finally refits all background and model parameters once more starting from the previously fitted values. A result of this fitting procedure, with background removed, is shown in Fig. 5.9(b,c).

Kinetic inductance estimation

Our AlSi films have a significant kinetic inductance contribution due to their small thickness of only 20 nm. We estimate the kinetic inductance fraction by performing a finite element electromagnetic simulation using *Sonnet* v16.56 (Sonnet Software Inc., 2018) of the reference device (shorted to ground on the same chip, thus excluding the Josephson inductance) which results in an expected resonance due to only geometry at $\omega_g = 2\pi \times 8.83$ GHz. We compare this value with the measured value of $\omega_k = 2\pi \times 7.56$ GHz. The kinetic inductance fraction is

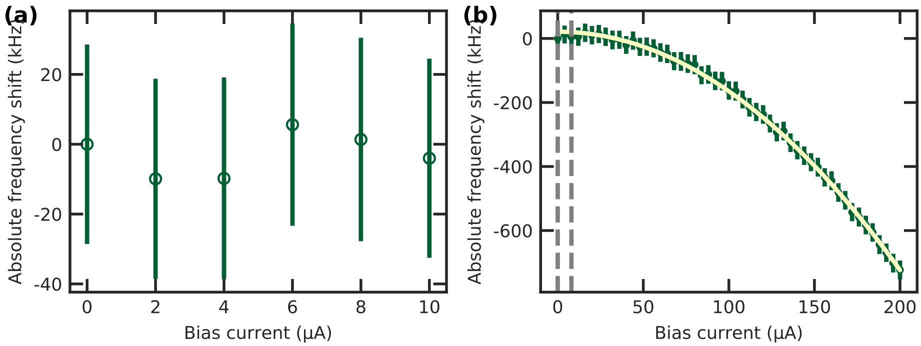

Figure 5.10: Frequency shift of the reference CPW shorted to ground. (a) Within the bias range for the device in the main text, $I_{0,\max} = 8\,\mu\text{A}$, the fluctuations in resonance frequency of the reference device are not due to kinetic inductance but remain within the range of our fit errors for the resonance frequency. (b) Biasing the reference resonator up to 200 μA allows us to extract the characteristic current for the kinetic inductance of the superconductor, $I_* \approx 7.35\,\text{mA}$. Markers: data with error bars, solid line: fit to Eq. (5.24), dashed lines: range of applied bias currents for JPUP experiments in main text.

5

given by [236]

$$\eta_\mathrm{k} = \frac{L'_\mathrm{k}}{L'_\mathrm{k} + L'_\mathrm{g}} = 1 - \left(\frac{\omega_\mathrm{k}}{\omega_\mathrm{g}}\right)^2 \tag{5.23}$$

which has a value of 0.267 in our device, hence $L'_\mathrm{k} = 154\,\text{nH}\,\text{m}^{-1}$. This changes the characteristic impedance of our CPW from the geometric value of 50.1 Ω to 58.5 Ω. Kinetic inductance also increases as a function of DC bias current via $L_\mathrm{k}(I) = L_\mathrm{k}(0)\left[1 + (I/I_*)^2\right]$ with the characteristic current I_* [235]. The resulting downshift of the resonance frequency can be described by

$$\omega_0(I_\mathrm{b}) = \frac{\omega_0(0)}{\sqrt{1 + \eta_\mathrm{k} I_\mathrm{b}^2 / I_*^2}}\,. \tag{5.24}$$

We emphasize however that in the JJ device, the sheet kinetic inductance is not the relevant tuning parameter: Biasing the reference device up to 10 μA does not show a trend; instead the fluctuations in f_0 remain within the fitting errors, see Fig. 5.10(a). Only when applying bias currents up to 200 μA, well beyond the values used for the measurements presented in the main text, does the resonance frequency of the reference device shift to lower frequencies, as shown in Fig. 5.10(b). We fit the data using Eq. (5.24), extracting $I_* \approx 7.35\,\text{mA}$. This supports our claim that we can exclude kinetic inductance as an additional source of tuning the resonance frequency via applied bias currents and instead identify the Josephson inductance as the relevant tuning parameter.

Resonance frequency versus current due to Josephson inductance

Adapting the calculation for a Josephson terminated transmission line cavity given in Ref. [208] to our device, we find for the current dependence of the cavity resonance frequency

$$\omega_0(I_b) = \omega_{\lambda/2} \frac{L_r + L_J(I_b, I_c)}{L_r + 2L_J(I_b, I_c)} , \tag{5.25}$$

with L_r the total device inductance, $\omega_{\lambda/2}$ the resonance frequency without the JJ and L_J the Josephson inductance given in Eq. (5.1) of the main text. We use this model to fit the measured resonance frequencies and extract $\omega_{\lambda/2} = 2\pi \times 7.515$ GHz, $L_r = 3.401$ nH and $I_c = 9.157$ µA. From the device geometry and kinetic inductance estimation, we expect $L_r = (L_g' + L_k')l = 3.689$ nH, which is in acceptable agreement with the fit value.

5.7.4. On the hysteresis of switching currents in our DC measurements

Accodring to a simple RCSJ model, hysteresis in Josephson junctions should occur only for JJ quality factors $Q = R\sqrt{2eI_cC_J/\hbar} > 1$, with the junction capacitance C_J [166]. We perform finite element simulations with *Sonnet* v16.56 (Sonnet Software Inc., 2018) to estimate the stray capacitance of the metal leads in direct vicinity of the JJ (two 1 µm × 1 µm pads separated by 200 nm) to be $C_J = 5.2$ fF. Together with $R = 108\ \Omega$ and $I_c = 9.157$ µA, the junction would have $Q \approx 1.3$. For $Q \gtrsim 1$, the ratio between retrapping and critical current can be approximated as $I_r/I_c = 4/\pi Q$. Hence, in order to satisfy our measured values, $Q = 4/\pi \times I_c/I_r \approx 1.91$, which would be reached for $C_J \approx 11$ fF. Likely, the geometric capacitance of the CPW and the surrounding ground planes significantly contributes and dominates the circuit capacitance: Already including a 50 µm portion of the CPW increases C_J to 14 fF, satisfying this requirement. Additionally, we note that local heating in the junction area can also play a significant role, reducing I_r further [231–233].

5.7.5. On the increased loss rates for increased bias current

We observed an increase in the internal and external loss rates of the JJ terminated device for increased bias current, as can be seen in Fig. 5.11(a). We can fit the loss rates quite accurately with a phenomenological exponential model of the form

$$\kappa(I_b) = \kappa_0 + \kappa_1 \exp\left[\frac{I_b}{I_\sim}\right] . \tag{5.26}$$

The extracted parameters for the device presented in the main text are given in Tab. 5.2. While κ_e should not directly depend on bias current, we do observe a slight increase, possibly due to changes in the impedance, linewidth broadening due to the increased $\partial\omega_0/\partial I_b$ or shifting the cavity through cable resonances. Regarding the increase in internal loss rate, we identified the following mechanisms as most likely:

Electrical interference While we physically disconnect all mains-powered equipment from our battery powered DC electronics, and placed DC blocks for both inner and outer conductors on the RF inputs to the fridge, we still notice a significant amount of 50 Hz interference on the measured spectra for high bias currents, see Fig. 5.12(a). We calculate the magnitude of the spurious signals to be approximately 170 pA, which corresponds to 1.7 % of I_{LF} or $1.86 \times 10^{-5}\ I_c$. We assume that this interference is always present

Table 5.2: Extracted loss rate parameters for the main text device.

Loss rate	$\kappa_0/2\pi$ (kHz)	$\kappa_1/2\pi$ (Hz)	$I_\sim$ (nA)
Internal	256.16 ± 3.74	78.41 ± 11.86	777.89 ± 11.96
External	537.41 ± 2.11	0.021 ± 0.035	487.43 ± 52.40

but only has noticeable effects for large $\partial\omega_0/\partial I_\mathrm{b}$. Since our RF spectroscopy measurement takes more than 1 s, the measured linewidth is effectively broadened by the moving cavity, induced by small-scale 50 Hz modulations. While more insight could potentially have been gained by performing switching histogram measurements, the small magnitude of the spurious interference compared to the JJ switching current should only slightly affect DC measurements.

Note that the situation is significantly worse for an unoptimized setup, when noise couples to the DC electronics via a shared ground. This is the case when bolting the power strip (into which the VNA and SA are plugged in) to the metal housing of the rack on which the battery-powered DC electronics sit. In this case, the cavity spectrum is extremely broadened and starts to resemble two dips for high I_0, severely limiting the tuning range (c.f. Fig. 5.12(b) without, and Fig. 5.1(f) of the main text with isolation of the battery electronics from mains powered equipment). We estimate the interfering current signal for this case to be 150 nA to 250 nA, significantly limiting any device operation in either DC or RF. The measurement setup could be further improved by choosing a LF modulation frequency which is not a higher order multiple of 50 Hz, such as 1111 Hz, instead of 1000 Hz.

5

We note that there might be other frequencies at which interfering signals couple into our device. For example, the acoustic vibrations of the pulse tube needed to provide continuous cooling power in a dry dilution refrigerator have been shown to induce periodic current spikes in the 5 kHz to 10 kHz range of up to a few nA [244], which would lead to a significant increase in κ_i. Since our DC lines use only a small portion of coaxial cable at the mK stage and are otherwise twisted loom pairs up to room temperature, we expect this contribution to be small. Nevertheless, current noise by itself cannot completely account for the observed increased loss rates with bias current because $\kappa_\mathrm{i}(I_\mathrm{b})$ is not simply proportional to $\partial\omega_0/\partial I_\mathrm{b}(I_\mathrm{b})$.

Phase diffusion The shorted reference device exhibits constant κ_i and κ_e upon DC bias up to 200 µA, at which point the mixing chamber starts to heat as we surpass the cooling power of 14 µW for the *LD400 Bluefors* since the power dissipated in our 2.7 kΩ low-pass filters reaches up to 108 µW. In contrast, the temperature did not increase when measuring the JJ device. We therefore rule out quasiparticles (due to radiation or thermal excitations [166]) in the CPW as a significantly contributing loss mechanism. Instead, phase diffusion across the JJ can play a significant role as the bias current approaches I_c. Applying a DC bias current tilts the Josephson energy potential, enhancing the chance of phase-slip and quantum tunneling events, which can lead to dissipation even without switching to the normal state, as long as the phase particle is able to settle in the next washboard-potential minimum [245].

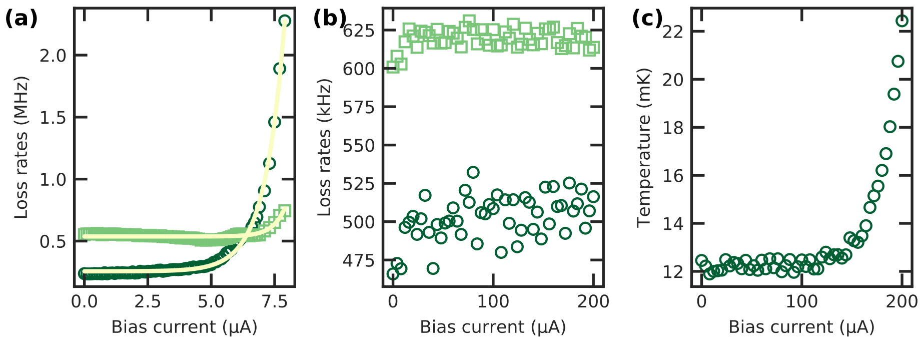

Figure 5.11: Bias current dependent cavity loss rates. (a) Internal (◯) and external (□) loss rates versus bias current of the JJ terminated device. The measured values can be described by the exponential model (lines) from Eq. (5.26). (b) Internal (◯) and external (□) loss rates of the reference device. We do not observe an increase in loss rate up to 200 μA. (c) Base temperature during measurement of (b). As we exceed the fridge cooling power, the mixing chamber plate heats up, but without any clear effect on κ_i and κ_e.

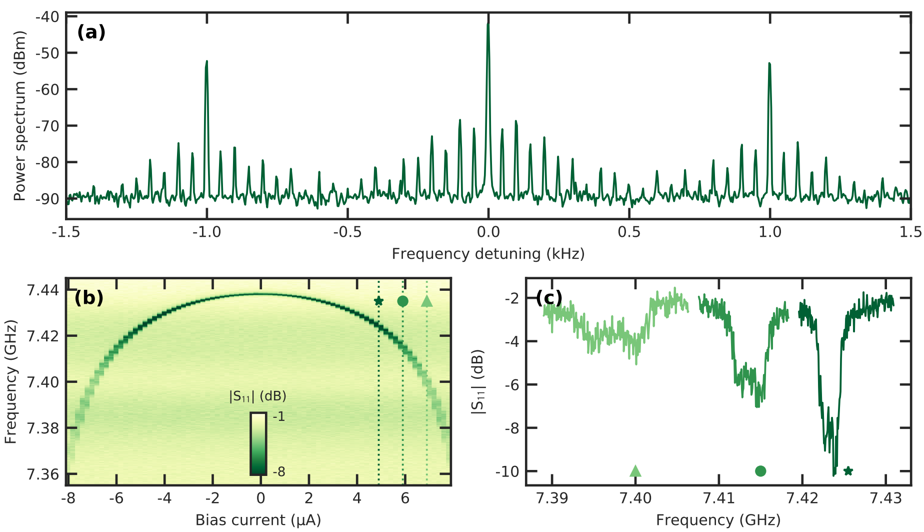

Figure 5.12: Mains power interference. (a) Current-mixing output spectrum taken at 7.1 μA bias current for the device in the main text. Peaks at zero frequency and ±1 kHz correspond to the cavity-resonant continuous wave pump tone and the mixing sidebands, respectively. Even with mains powered equipment separated from battery electronics, spurious peaks appear at integer multiples of 50 Hz, corresponding to current signals of approximately 170 pA. (b) $|S_{11}|$ measurements of the same device in the same cooldown, but with 50 Hz interference coupling to the DC electronics via a common ground. (c) Linecuts through (b) at various bias currents as indicated in (b). For high bias currents, the resonance splits into two dips, clearly hinting at significant current noise, which we estimate to be 150 nA to 250 nA.

5.7.6. ESTIMATING THE AC CURRENT AT THE JUNCTION

The current along a $\lambda/2$ resonator shorted to ground on both ends is given by

$$I(x) = I_0 \cos\left(\pi \frac{x}{l_0}\right) \tag{5.27}$$

where l_0 is the physical length of the cavity on the chip, I_0 is the current amplitude in the current antinodes and x is the coordinate along the resonator with $0 \leq x \leq l_0$. To find the peak current for a given intracavity energy α_0^2, we equalize the total energy related to the current with the intracavity energy

$$\alpha_0^2 = \frac{1}{2}\int_0^{l_0} L' I^2(x)\mathrm{d}x = \frac{l_0}{4} L' I_0^2 \tag{5.28}$$

The peak microwave current in the antinode is therefore given by

$$I_0 = \sqrt{\frac{4\alpha_0^2}{L' l_0}}. \tag{5.29}$$

The intracavity energy for a resonant drive on the other hand is given by

$$\alpha_0^2 = 4P_{\mathrm{in}}\frac{\kappa_\mathrm{e}}{\kappa^2} \tag{5.30}$$

5

in the linear regime. For an input power of -110 dBm, we then get a microwave current of $I_0 \approx 1.86\,\mu\mathrm{A}$ using $\kappa_\mathrm{e} = 2\pi \times 0.5\,\mathrm{MHz}$ and $\kappa = 2\pi \times 1\,\mathrm{MHz}$ as observed for about $I_\mathrm{b} \approx 7\,\mu\mathrm{A}$. From the impedance of the junction at this operation point $Z_\mathrm{J} \approx 3\mathrm{i}\,\Omega$, we estimate that the actual current through the junction is reduced to about 0.8 to 0.9 of the antinode current due to the boundary condition being not an ideal short. The intracavity microwave current is therefore capable of explaining the suppression of the DC critical current (premature switching) with increasing microwave power.

5.7.7. DIFFERENCE BETWEEN FIRST ORDER RED AND BLUE SIDEBANDS

As derived in the main text, to first order in δI, the coefficients describing the sideband amplitudes are

$$a_{\pm 1} = \frac{\alpha_0 G_1 I_{\mathrm{LF}}}{-i\kappa + 2(\Delta \pm \Omega)}\,. \tag{5.31}$$

Without changing the device, our peak height will increase if we modulate the current stronger ($I_{\mathrm{LF}} \uparrow$) or slower ($\Omega \downarrow$), and by pumping harder ($S_{\mathrm{in}} \uparrow$). With the same setup, increasing the current responsivity ($G_1 \uparrow$) would likewise enhance the peak height. Moreover, for small LF modulations $\Omega \ll \kappa$, the peaks for red and blue sidebands should be equal in amplitude. In fact, the absolute difference between the two sidebands scales with

$$|a_{-1}|^2 - |a_{+1}|^2 \propto \frac{16\Delta\Omega}{\left(\kappa^2 + 4(\Delta+\Omega)^2\right)\left(\kappa^2 + 4(\Delta-\Omega)^2\right)} \to 0\,, \tag{5.32}$$

for $\kappa \gg \Omega$. Our experiments with $\kappa \gtrsim 2\pi \times 750\,\mathrm{kHz} \gg \Omega = 2\pi \times 1\,\mathrm{kHz}$ support this statement, as we did not observe systematic differences between red and blue sidebands (cf Fig. 5.13) over the entire parameter space.

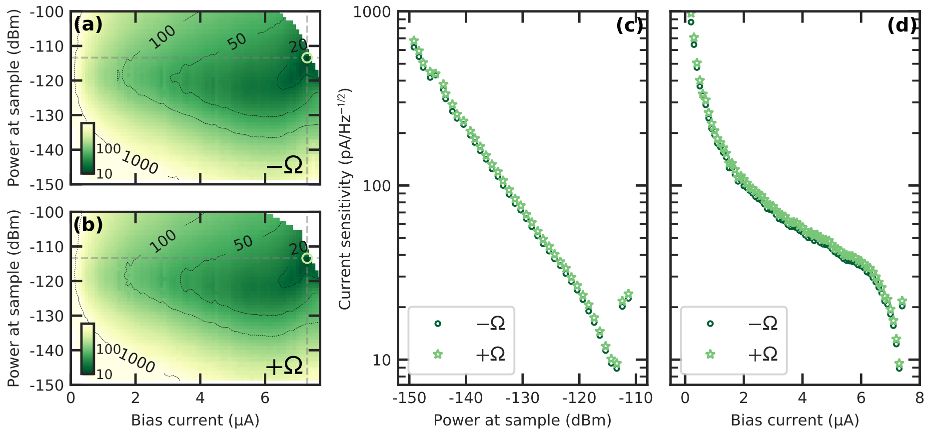

Figure 5.13: Comparison of blue and red sideband. Current sensitivity in pA/$\sqrt{\text{Hz}}$ versus bias current and input power, as measured for $-\Omega$ (a, see Fig. 5.4 of the main text) and $+\Omega$ (b). Dashed grey lines correspond to the linecuts in (c) and (d), circle marks the point of minimum measured sensitivity. (b) Sensitivity at 7.3 μA versus pump power (vertical line in (a,b)). (c) Sensitivity at -113 dBm versus bias current (horizontal line in (a,b)). ∘: $-\Omega$ sideband, ★: $+\Omega$ sideband. Minimum sensitivities are 8.90 pA/$\sqrt{\text{Hz}}$ and 9.52 pA/$\sqrt{\text{Hz}}$, respectively. Within the traced out parameter space, we observed no systematic differences between red and blue first order sidebands.

5.7.8. Current detection in the high power regime

Driving the cavity on resonance for high powers

To counteract the detuning acquired from the downshift in resonance frequency for high pump powers due to the device nonlinearity, in an ideal measurement configuration the drive tone would also be shifted correspondingly. As depicted in Fig. 5.14, in such a situation, the sideband amplitude would keep increasing by more than 10 dB, resulting in a minimum $\mathcal{S}_I$ = 2.6 pA/$\sqrt{\text{Hz}}$.

Deviations between data and theory for high powers

We observe deviations between the measured and modelled current sensitivity at high drive powers. As stated in the main text, assuming an initially red-detuned drive, i.e. $\Delta < 0$ in the limit of $|\alpha| \rightarrow 0$ could explain this behavior. In Figure 5.15, we plot the data with the original model, and add an initial detuning of -600 kHz to the drive tune. While in this case the sensitivity is overestimated for small drive powers, the model follows the measured data closer for high powers than the calculations for zero initial detuning.

5.7.9. Calculating the current sensitivity

The current sensitivity is defined by

$$\mathcal{S}_I = \frac{\sigma_I}{\sqrt{\text{ENBW}}}\,, \tag{5.33}$$

with σ_I the magnitude of the current noise and ENBW the equivalent noise bandwidth of the spectrum analyzer. In our experiment, the DUT converts the current modulation I_{LF} into

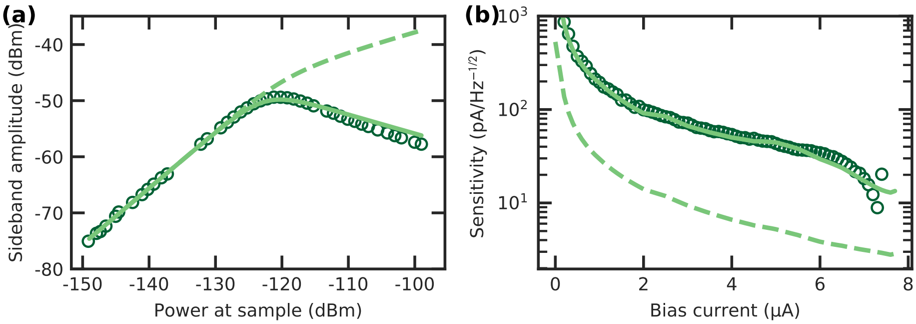

Figure 5.14: Driving the cavity on resonance. (a) Data (circles) and model with (solid line) and without (dashed line) detuning of the first order sideband amplitude at $I_0 = 4\,\mu$A, see Fig. 5.3(c) of the main text. Tuning the drive to be matched to the resonance results in a further increased sideband amplitude of more than 10 dB. (b) Data (circles) and model (solid line) of the first order sideband amplitude at $P_{in} = -113$ dBm, see Fig. 5.4(d) of the main text. Dashed line corresponds to modelled sensitivity at maximum drive power with shifted drive frequency.

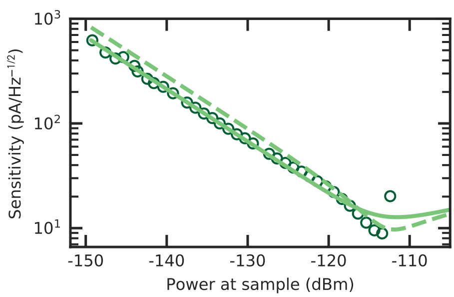

Figure 5.15: Deviations between data and theory for high powers. (a) Data (circles) and model (lines) for current sensitivity versus input power for the first order sideband amplitude at $I_0 = 7.3\,\mu$A, see Fig. 5.4(c) of the main text. Solid line corresponds to the same model as in the main text, dashed line has −600 kHz extra detuning added, corresponding to an initially red-detuned drive. This way, better matching between data and theory is achieved for high pump powers

an up-converted voltage signal, which we detect as the amplitude of the sidebands as $P_{\text{LF}} = 10^{S/10}$ in W, with S the signal height in dBm. Additionally, we record the noise floor amplitude $P_{\text{N}} = 10^{N/10}$ which sets the minimum detectable power, and the signal to noise ratio SNR $= 10^{(S-N)/10}$. Since the detected power is proportional to the square of the voltage field, which in turn is proportional to the input current, $P \propto V^2 \propto I_{\text{LF}}^2$, we can infer the equivalent white current noise level of the HEMT and the sensitivity via

$$\sigma_I = \frac{I_{\text{LF}}}{\sqrt{10^{(S-N)/10}}} \tag{5.34}$$

$$\mathcal{S}_I = \frac{I_{\text{LF}}}{\sqrt{\text{ENBW} \times 10^{(S-N)/10}}} \,. \tag{5.35}$$

For a Gaussian filter such as the one used in our setup, ENBW $= 1.065 \times$ RBW, with RBW the resolution bandwidth of the spectrum analyzer which was set to 5 Hz for all measurements [238]. In practice, we extract the sideband amplitude from the measured spectra as the peak power value at the expected $\omega_0 \pm m\Omega$ and compute the noise floor as the average of the remaining data points.

5.7.10. DATA VISUALIZATION

Our raw measurements include a significant number of outliers in current sensitivity, visible as bright spots and streaks in Fig. 5.16(a). These are due to absent sidebands of all integer multiples of Ω, resulting in apparent negligible SNR and $\mathcal{S}_I > 1000\,\text{pA}/\sqrt{\text{Hz}}$ for these operating points. The streaks between 7 µA to 8 µA are due to the pump frequency not correctly adjusted to compensate for the shift due to changing bias current, resulting in very large detuning and undetectable sidebands. For the remaining outliers, the pump was adjusted correctly, yet still no sidebands appear in the measurement spectra. We attribute this to the AWG output randomly not being turned on, thus no input modulation was applied and no sidebands produced. To exclude these outliers from further analysis, we chose to discard data points differing by more than 50 % from the value expected from theory, and subsequently interpolated the missing experimental data from the surrounding remaining data points.

5.7.11. MODELING THE JOSEPHSON ARRAY CPW

To model a Josephson junction array transmission line resonator, we use N unit cells of length l, a transmission line inductance per unit length L', a capacitance per unit length C' and a lumped element Josephson inductance L_{J}, as depicted in Fig. 5.17 and Fig. 5.5(a) of the main text. Each unit cell has the inductance $L_n = L'l + L_{\text{J}} = L_0 + L_{\text{J}}$ and the capacitance $C_n = C'l = C_0$.

FULL ANALYTICAL MODEL

In order to derive an analytical model, we follow the approach to circuit quantization presented in Ref. [240]. The admittance matrix $\mathbf{Y}$ which relates voltages v_n of a node n to the current injected by a hypothetical infinite impedance source i_n following

$$\mathbf{Yv} = \mathbf{i} \tag{5.36}$$

5

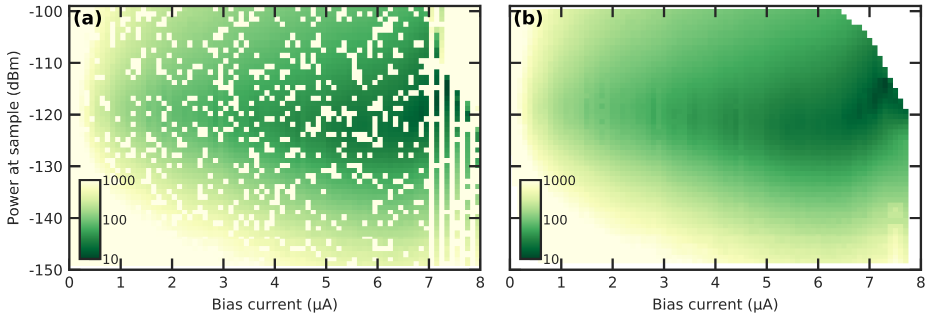

Figure 5.16: Interpolating the dataset. Raw (a) and interpolated (b) measured current sensitivities in pA/$\sqrt{\mathrm{Hz}}$ of the -1Ω sideband for all applied bias currents and pump powers. Outliers with large values of $\mathcal{S}_I$ are due to off-resonant drive tones (streaks) or absent LF modulation (speckles) due to errors in the measurement setup, resulting in no mixing at all (see text for details). The data in (b) corresponds to Fig. 5.4(a) of the main text, with modified colorscale for enhanced visibility.

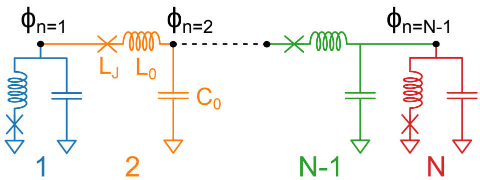

Figure 5.17: The JJ array CPW. Circuit schematic of a transmission line resonator consisting of N unit cells based on series and parallel combinations of lumped linear inductors L_0, capacitors C_0 and Josephson junctions L_J, used for deriving an analytical expression for the resonance frequency and anharmonicity. The ϕ_n indicate the flux at the individual circuit nodes. Colors mark different unit cells, with unit cell number indicated below each element group. Note that while there are N unit cells, there are only $N-1$ circuit nodes.

is explicitly written as

$$\underbrace{\begin{pmatrix} 2Y_\mathrm{s}(\omega)+Y_\mathrm{g}(\omega) & -Y_\mathrm{s}(\omega) & & 0 \\ -Y_\mathrm{s}(\omega) & \ddots & \ddots & \\ & \ddots & \ddots & -Y_\mathrm{s}(\omega) \\ 0 & & -Y_\mathrm{s}(\omega) & 2Y_\mathrm{s}(\omega)+Y_\mathrm{g}(\omega) \end{pmatrix}}_{\mathbf{Y}} \begin{pmatrix} v_1 \\ v_2 \\ \vdots \\ v_{N-1} \end{pmatrix} = \begin{pmatrix} i_1 \\ i_2 \\ \vdots \\ i_{N-1} \end{pmatrix} \tag{5.37}$$

where we have defined the admittances of the series and parallel blocks of the chain by $Y_\mathrm{s}(\omega) = 1/(i\omega(L_\mathrm{J}+L_0))$ and $Y_\mathrm{g}(\omega) = i\omega C_0$ respectively. Such a tridiagonal Toeplitz matrix [241] has well known eigenvalues ζ_m and eigenvectors e_m, given here by

$$\zeta_m(\omega) = 2\left[1-\cos\left(\frac{\pi m}{N}\right)\right] + \frac{Y_\mathrm{g}(\omega)}{Y_\mathrm{s}(\omega)} \tag{5.38}$$

$$e_m(n) = \sqrt{\frac{2}{N}}\sin\left(\frac{\pi m\, n}{N}\right) \tag{5.39}$$

for $m \in [1, N-1]$. Normal mode frequencies ω_m are those which cancel the determinant of $\mathbf{Y}$. Since the determinant is proportional to the product of eigenvalues $\zeta_m(\omega)$, the frequencies of the $N-1$ modes satisfy $\zeta_m(\omega_m) = 0$,

$$\omega_m = \sqrt{\frac{2 - 2\cos\left(\frac{\pi m}{N}\right)}{(L_J + L_0)C_0}} \,. \tag{5.40}$$

The zero-point fluctuations in flux across the first inductive element (series combination of junction and inductor) for a mode m is determined by the imaginary part of the derivative of the admittance $Y_1 = (i_1/v_1)_{i_n=0,n\neq1}$, evaluated at ω_m. To obtain Y_1, we write the admittance matrix as $\mathbf{Y} = \mathbf{U}\mathbf{D}\mathbf{U}^T$ where $\mathbf{D}$ is the diagonal matrix with m-th diagonal element ζ_m, and $\mathbf{U}$ is a matrix whose m-th row is e_m. Using this form to invert Eq. (5.36) leads to

$$\begin{pmatrix} v_1 \\ v_2 \\ \dots \\ v_{N-1} \end{pmatrix} = \mathbf{U}\mathbf{D}^{-1}\mathbf{U}^T \begin{pmatrix} i_1 \\ 0 \\ \dots \\ 0 \end{pmatrix} \tag{5.41}$$

leading to

$$\begin{aligned} Y_1(\omega) &= \frac{NY_s(\omega)}{\sum_{m=0}^{N-1}\frac{1}{a_m(\omega)}} \\ a_0(\omega) &= 1 \\ a_m(\omega) &= \frac{1 + 2\frac{Y_s(\omega)}{Y_g(\omega)}(1 - \cos(\pi m/N))}{1 + \cos(\pi m/N)}) \text{ for } m > 0\,. \end{aligned} \tag{5.42}$$

To compute its derivative, evaluated at ω_m, we rewrite Y_1 as

$$Y_1(\omega) = a_m(\omega)\frac{NY_s(\omega)}{1 + \sum_{m'=0}^{N-1}\frac{a_m(\omega)}{a_{m'}(\omega)}\delta_{mm'}} \tag{5.43}$$

with $\delta_{mm'}$ the Kronecker delta, such that

$$\frac{\partial Y_1(\omega)}{\partial\omega} = \frac{\partial a_m(\omega)}{\partial\omega}\frac{NY_s(\omega)}{1 + \sum_{m'=0}^{N-1}\frac{a_m(\omega)}{a_{m'}(\omega)}\delta_{mm'}} + a_m(\omega)\frac{\partial}{\partial\omega}\left[\frac{NY_s(\omega)}{1 + \sum_{m'=0}^{N-1}\frac{a_m(\omega)}{a_{m'}(\omega)}\delta_{mm'}}\right]\,. \tag{5.44}$$

Since $a_{m'}(\omega_m) \propto \lambda_{m'}(\omega_m) = 0$ if $m' \neq m$, evaluating the derivative at ω_m and taking its imaginary part yields

$$\begin{aligned} \mathrm{Im}Y_1'(\omega_m) &= \mathrm{Im}\left(\left.\frac{\partial Y_1(\omega)}{\partial\omega}\right|_{\omega=\omega_m}\right) \\ &= \mathrm{Im}\left(NY_s(\omega_m)\left.\frac{\partial a_m(\omega)}{\partial\omega}\right|_{\omega=\omega_m}\right) \\ &= \frac{NC_0}{1 - \cos^2(\pi m/N)}\,. \end{aligned} \tag{5.45}$$

The zero-point fluctuations in flux across the first inductive elements for a mode m is then given by [165, 240]

$$\phi_{\mathrm{zpf},1,m} = \sqrt{\frac{\hbar}{\omega_m \,\mathrm{Im} Y_1'(\omega_m)}} \,. \tag{5.46}$$

The definition of flux [242] $\phi_n(t) = \int_{-\infty}^{t} v_n(\tau)d\tau$ translates in the frequency domain to $\phi_n(\omega) = i\omega v_n(\omega)$. So knowing the relation between the node voltage amplitudes at a frequency ω_m, given by the coefficients $e_m(n)$, is sufficient to convert the fluctuations in flux at the first node to another. We are interested in the fluctuations in flux across the nth inductive element which is given by

$$\phi_{\mathrm{zpf},n,m} = \phi_{\mathrm{zpf},1,m} \frac{e_m(n) - e_m(n-1)}{e_m(1)} \tag{5.47}$$

for $n \in [1, N]$. The fluctuations in flux across the nth junction are then

$$\left(\frac{L_\mathrm{J}}{L_\mathrm{J} + L_0}\right) \phi_{\mathrm{zpf},n,m} \tag{5.48}$$

This leads to the total anharmonicity A_m for a mode m

$$A_m = \frac{1}{2\phi_0^2 L_\mathrm{J}} \left(\frac{L_\mathrm{J}}{L_\mathrm{J} + L_0}\right)^4 \sum_{n=1}^{N} \phi^4_{\mathrm{zpf},n,m} \tag{5.49}$$

where $\phi_0 = \hbar/2e$ is the reduced flux quantum.

Given an initial resonance frequency for zero bias current of 7.5 GHz and the CPW parameters as specified in the main text for a 1 µm wide CPW, we can use Eq. (5.40) to calculate the relation between unit cell length and number of unit cells, see Fig.5.18(a). Compared to the device in the main text, the JJ CPW can be significantly shorter, e.g. $l_0 = 845$ µm for a unit cell length $l = 1$ µm. The higher the number of unit cells, the shorter the individual unit cells, which leads to an increase in the participation ratio of the Josephson inductance to the total inductance per unit cell,

$$\eta_\mathrm{J} = \frac{L_\mathrm{J}}{L_\mathrm{J} + L_0} \,, \tag{5.50}$$

and the smaller the contribution of normal inductance $1-\eta_\mathrm{J}$, see Fig.5.18(b). The anharmonicity has a maximum of 6.8 kHz for a unit cell number $N = 154$ which corresponds to $\eta_\mathrm{J} = 2/3$, but drops rapidly for larger N.

Motivated by a larger current responsivity for large η_J, our proposed device has 845 unit cells and $\eta_\mathrm{J} = 97.7\,\%$. All parameters are detailed in Tab. 5.3. We plot the calculated resonance frequency and anharmonicity for the proposed device design in Fig. 5.5 from the main text as a function of bias current in Fig. 5.19. Since Josephson inductance dominates, resulting in the resonance frequency tuning by more than 55 %.

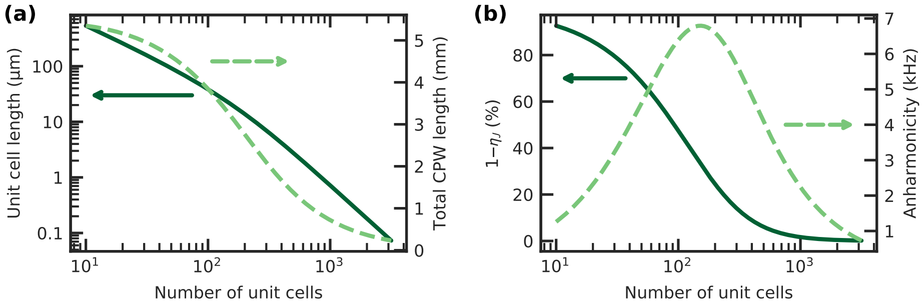

Figure 5.18: Device parameters for the JJ CPW. (a) Unit cell length l (solid, left) and total CPW length l_0 (dashed, right) for varying unit cell number N. (b) Normal inductance per unit cell (solid, left) and device anharmonicity (dashed, right) for varying unit cell number N. All quantities are calculated with the full analytical model for a resonance frequency at 7.5 GHz.

Table 5.3: Device parameters for the proposed JJ CPW

Symbol	Description	Value
s	CPW center conductor	1 µm
w	CPW gaps to ground	0.6 µm
t	Base layer thickness	80 nm
l	Unit cell length	1 µm
N	Number of unit cells	845
l_0	total CPW length	845 µm
L_J	Josephson inductance per unit cell	35.9 pH
L_0	Normal inductance per unit cell	842 fH
C_0	Geometric capacitance per unit cell	169 aF

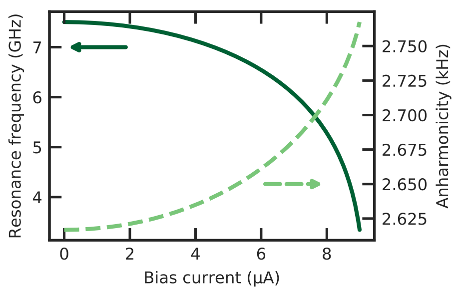

Figure 5.19: Bias current tuning of the 1 µm JJ CPW. Solid line: Resonance frequency versus bias current for the proposed JJ CPW device. Dashed line: Anharmonicity versus bias current for the proposed JJ CPW device. Arrows indicate corresponding axes.

Analytical model in the limit of large N

We now study the fundamental mode ($m = 1$) of an array with many unit-cells ($N \gg 1$). By Taylor expanding the cosine of Eqs. (5.40) and (5.45), the fundamental mode frequency and derivative of the admittance are then given by

$$\omega_1 \simeq \frac{\pi}{N\sqrt{C_0(L_\mathrm{J}+L_0)}} \tag{5.51}$$

$$\mathrm{Im}Y_1'(\omega_1) \simeq \frac{N^3}{\pi^2}C_0\,. \tag{5.52}$$

The quantity which relates zero-point fluctuations in phase accross the nth unit cell to the zero-point fluctuations of the first unit-cell can be simplified to

$$\frac{e_m(n)-e_m(n-1)}{e_m(1)} \simeq \frac{\sin(\frac{\pi n}{N})-\sin(\frac{\pi n}{N}-\frac{\pi}{N})}{\frac{\pi}{N}} \simeq \cos\left(\frac{\pi n}{N}\right) \tag{5.53}$$

Plugging these quantities into the expression of the anharmonicity, leads to

$$A_1 \simeq \frac{\hbar^2}{2\phi_0^2 L_\mathrm{J}}\frac{N^2C_0(L_\mathrm{J}+L_0)}{\pi^2}\left(\frac{L_\mathrm{J}}{L_\mathrm{J}+L_0}\right)^4\frac{\pi^2}{N^4C_0^2}\sum_{n=1}^{N}\cos^4\left(\frac{\pi n}{N}\right) \tag{5.54}$$

$$= \frac{3\pi^2}{4N^3}\left(\frac{L_\mathrm{J}}{L_\mathrm{J}+L_0}\right)^3\frac{e^2}{C_0} \tag{5.55}$$

where $\phi_0 = \hbar/2e$ is the reduced flux quantum and we made use of the relation $\sum_{n=1}^{N}\cos(n\pi/N)^4 = 3N/8$.

Alternative derivation

We assume that the fundamental cavity mode $m = 1$ of the JJ array CPW has current antinodes at both ends, i.e. we are dealing with a $\lambda/2$ cavity such that the resonator length $l_1 = \lambda_1/2$ with the resonance wavelength λ_1. The resonance frequency of the fundamental mode dependent on N and l is given by

$$\omega_1 = \frac{\pi}{N\sqrt{C'l\,(L'l+L_\mathrm{J})}}\,, \tag{5.56}$$

which is equivalent to Eq. (5.51). For given C', L', L_J, ω_1 and N, this allows for the calculation of the needed unit cell length l.

As we are working with a half-wavelength mode, the basic relation between the resonance frequency and the zero-point fluctuation flux per length in the limit of a continuous flux distribution is given by

$$\frac{1}{2}\hbar\omega_1 = \int_0^{\lambda_1/2}\frac{\Phi'^2_\mathrm{zpf}}{L'_n}dx \tag{5.57}$$

where $L'_n = L_n/l$ and $\Phi'_\mathrm{zpf} = \Phi'_z\cos\left(\frac{2\pi}{\lambda_1}x\right)$ is the flux per length of transmission line. This corresponds to

$$\Phi'_z = \sqrt{\frac{\hbar\omega_1 L'_n}{l_1}}\,. \tag{5.58}$$

Hence, the flux of the nth junction is approximately given by

$$\Phi_n = \frac{L_\mathrm{J}}{L_n} \Phi'_z l \cos\left(\frac{2\pi}{\lambda_1}\left[n - \frac{1}{2}\right] l\right) \tag{5.59}$$

where the first factor takes into account that only part of the flux is across the junction. With the Josephson energy $E_\mathrm{J} = \frac{\Phi_0^2}{4\pi^2 L_\mathrm{J}}$, the anharmonicity is given by

$$A = \frac{12\pi^2}{6L_\mathrm{J}\Phi_0^2} \sum_{n=1}^{N} \Phi_n^4 \tag{5.60}$$

$$= \frac{2e^2\omega_1^2}{N^2} \frac{L_\mathrm{J}^3}{L_n^2} \sum_{n=1}^{N} \cos^4\left(\frac{\pi}{N}\left[n - \frac{1}{2}\right]\right) \tag{5.61}$$

$$= \frac{3\pi^2}{4N^3} \left(\frac{L_\mathrm{J}}{L_\mathrm{J} + L_0}\right)^3 \frac{e^2}{C_0}\,, \tag{5.62}$$

where we have used the fact that the cosine sum for values $N > 2$ is equal to $3N/8$, which is identical to the result of the full analytical model in the limit of large N, see Eq. (5.55).

5

6

Conclusion

6.1. The results of this thesis

In this thesis, we presented studies on hybrid Josephson junction – DC bias microwave circuits. We studied both the fundamental properties of graphene Josephson junctions at microwave frequencies, and used the circuit which we developed for detection of very small currents.

Chapter 3 featured the integration of a graphene Josephson junction into a superconducting microwave circuit. Using an analytical circuit model and the previously calibrated parameters of a DC bias cavity allowed us to quantitatively extract the Josephson inductance from microwave measurements. This showed significant deviations between the value extrapolated from DC measurements, consistent with a skewed current phase relation. Analysis of the subgap resistance of the junction from the microwave losses of the resonance suggests that graphene Josephson junctions are a feasible platform for building gate-tunable microwave qubits.

In chapter 4, we took a closer look at the underlying physics of the Josephson inductance of these graphene devices, namely the current-phase relation. The high-frequency response of the devices, together with circuit calibration, allows for a direct way of extracting the Josephson inductance of our junctions. As in chapter 3, this value does not agree with the one estimated from the DC measured switching current of any of the junctions, with some DC values being larger and others being smaller than the ones observed in the microwave regime. By analysing the DC current response of the microwave resonance, we found low-frequency current noise to have significantly reduced the switching current measured at DC. The noise source is most likely poor isolation between the battery powered DC electronics and mains powered high frequency equipment via a shared ground at room temperature. The remaining deviations can be attributed to a forward-skewed current phase relation. We were able to quantify this skew, and with it the resulting anharmonicity of the Josephson energy potential, which is reduced to the case of a purely sinusoidal CPR.

6

We finally turned to a sensing application of our combined transmission line resonators and Josephson junctions in chapter 5. Inspired by kinetic inductance parametric upconverters for radiation detection, we used the responsivity of the resonance frequency of our devices to bias current to detect small, low-frequency current modulations. To simplify fabrication, we chose a single-layer constriction Josephson junction fabricated in the same step as the base layer of an aluminum film instead of graphene Josephson junctions (which would also have been feasible for this measurement). We were able to formulate an analytical model using input-output theory, which compared well with the measured data as a function of bias current set point, frequency detuning and and drive power. With a minimum sensitivity of $8.9\,\mathrm{pA\,Hz^{-1/2}}$ and a tunability of more than 100 MHz, the device is compatible with state-of-the-art techniques. We then used these results to extrapolate the sensitivity of an optimized design, featuring a Josephson transmission line, with the center conductor of the DC bias cavity replaced by unit cells consisting of short pieces of linear inductors and Josephson junctions. The same scheme as for the measured device would enable current sensitivities as low as $50\,\mathrm{fA\,Hz^{-1/2}}$, and drop another 20 dB to $5\,\mathrm{fA\,Hz^{-1/2}}$ by using in-built quantum-limited Josephson parametric amplification.

6.2. The road ahead

As we have seen in Chapters 3 and 4, with current technology and fabrication, encapsulated graphene Josephson junctions are not an immediately scalable option for quantum Josephson devices. This is mainly due to the remaining high intrinsic losses, which are likely limiting graphene transmon qubits such as the ones in Refs. [117, 177].

The two main issues that need to be addressed in order to improve this are (1) disorder at the graphene-metal interface and (2) the cumbersome BN encapsulation: Dry-etching using $CHF_3 + O_2$ in order to make galvanic contacts with the graphene layer can add surface defects in the silicon area close to the junction, providing a number of loss channels. It would therefore be beneficial to pre-pattern graphene or at least remove residual stacks, but this significantly adds to fabrication complexity. BN encapsulation on the other hand remains non-scalable as long as it cannot be done on a wafer scale. In particular, the hydrogen bubbles at BN/G interfaces limit device usability, since annealing in forming gas at 400 °C degrades the MW properties of the superconducting layer used for the MW circuitry and can potentially lead to surface defects in the silicon layer. Recent work by Sonntag *et al.* [246] on BN crystals grown at atmospheric pressure shows promise for large-scale BN deposition, which could advance the field in this regard.

A more viable route in the immediate future, which could be investigated in parallel, are unencapsulated Josephson junctions based on CVD-grown single layer graphene with top contacts. A possible fabrication scheme for this process could feature the following steps: (1) Pre-pattern all metal layers including bottom gate, (2) cover bottom gate by local sputtering of dielectric, (3) transfer SLG on wafer scale, (4) pattern SLG using O_2 plasma, (5) contact SLG using Ti/Al evaporation. The use of CVD graphene would have the significant advantage of wafer scale processing, enabling rapid prototyping and significantly larger throughput than both manual and automatic exfoliation and heterostructure assembly of graphene and boron nitride. It remains to be seen if the device quality would be sufficient for coherent devices.

From the perspective of DC bias cavities, there are a few possible follow-up projects:

The DC bias cavities could be improved further, as they are currently likely limited by dielectric losses originating from depositing the shunt capacitor dielectric. As described in chapter 2, side-coupled coplanar resonators made from the same NbTiN film as our DC bias cavities showed internal quality factors more than ten times higher our best devices. Dielectric losses at the metal-substrate interface are therefore not to blame. Similarly, radiative losses are unlikely the dominant source due to the coplanar geometry. However, the DC bias cavity fabrication in its current state requires three steps (compared to one for $\lambda/4$ resonators) and dielectric deposition on the entire superconducting surface with subsequent patterning. Switching dielectrics to low-temperature deposited low-loss materials such as aluminum oxide or silicon could enable much lower internal loss rates and more coherent devices [247].

Future research could examine our circuit layouts for various applications: For one, the Josephson transmission line resonator which we proposed in chapter 5 should be straightforward to build, since it requires no design changes to the existing recipe. This would put our analytical model to the test, and could result in record low levels of current sensitivities.

Alternatively, instead of current-biasing our devices, voltage-biased Josephson junctions inside coplanar waveguide cavities have recently shown to exhibit coherent radiation, and were hence dubbed Josephson lasers [248, 249]. The emission frequency of these recent implementations lies in the gigahertz range and is highly coherent, which makes them attractive for on-chip microwave sources. However, the existing approaches are limited to a fixed frequency with only a few % of frequency tuning. Additionally, the circuit design relies on introducing DC leads to a cavity at voltage nodes, which can be affected by lithographic errors. Using the shunt capacitor DC bias cavities would allow for arbitrary frequency targeting: Since the input port of the DC and high frequency signals are identical, there are no constraints on the length of the circuit. Building a low-frequency resonator simply by extending the transmission line length, shorted by a Josephson junction to ground, could result in a megahertz Josephson laser, enabling a significantly larger frequency span than existing devices by using the cavity overtones in addition to the fundamental mode.

The road ahead might even feature a renaissance of all-superconducting DC circuits for computing applications. With cryotrons still being pursued both for memory applications and training neural networks [250, 251], and the discovery of field effect in all-superconducting devices [252, 253], we can only wait and see what is to come.

A

Collection of DC data of graphene Josephson devices

Here, we provide additional data of current-voltage curves of graphene Josephson junctions and SQUIDs embedded in DC bias microwave cavities. Specifically, we take a closer look at nonlinear features in the IVCs of our devices when the junction is biased above its critical current, which are present regardless of device, gate voltage or magnetic field. Additionally, we investigate the effect of microwave radiation on the IVCs of our devices.

A

A.1. FISKE STEPS

In the IV traces of all gJJ devices embedded in MW cavities, we found peculiar oscillations for bias currents exceeding I_c, in particular on the retrapping branch, as shown in Fig. A.1. These oscillations occured without any MW probe tone applied, and seemed to be largely independent of gate voltage or magnetic field. Upon closer inspection of the IV curves, we found that these oscillations stem from steps in the measured voltage, as shown in Fig. A.2.

We attribute these to Fiske-like oscillations, due to the JJ probing its electromagnetic environment [254–256]: A voltage-biased Josephson junction is known to emit radiation according to the second Josephson relation,

$$\frac{\partial\delta}{\partial t} = \frac{2e}{\hbar}V(t) \tag{A.1}$$

where δ is the phase across the junction. This Josephson radiation can resonantly excite any present cavity modes with frequency $\omega_n = n2eV/\hbar$, $n \in \mathbb{Z}$. In a current-voltage trace of a JJ, this results in steps at voltages

$$V_n = \frac{\hbar}{2e}\omega_n = \frac{v_{\mathrm{ph}}\pi}{L}n \tag{A.2}$$

with the phase velocity v_{ph} and the cavity length L.

Fiske steps are usually known to occur as a result of standing electromagnetic waves in a cavity formed by the Josephson junction itself, and are hence prominent in large-area JJ [257–259]. However in our devices, there is a patterned $\lambda/2$ MW cavity surrounding the gJJ which can form a pronounced cavity mode.

In Fig. A.2, we show a subset of IVs that exhibit such voltage steps as a function of gate voltage and magnetic field, respectively. Steps occur at integer multiples of approximately 16.7 µV, which corresponds to a resonance frequency of 8.1 GHz, deviating by about 2 % from the expected resonance frequency $f_r \approx 8.3$ GHz our MW circuits are designed for (see Chapter 4). We note that specifically in the device shown here, we were unable to detect a cavity resonance when performing spectroscopy using a vector network analyzer due to large internal losses from residual normal metal around the JJ. Nevertheless, the DC data shows the sensitivity of the JJ to its environment, even if internal losses are high.

A.2. SHAPIRO STEPS

In addition to voltage steps arising from self-oscillations of the JJ due to its electromagnetic environment, irradiating the JJ with microwaves can also lead to steps in the measured voltage, the so-called Shapiro steps [35, 132, 260, 261]. We recorded several IV traces of graphene Josephson devices under MW radiation with varying frequency and power. Here, we noted significant differences between power sweeps of a gJJ embedded in a low-loss MW cavity (Fig. A.3), and a gSQUID inside a MW cavity with high internal losses (Fig. A.4).

Shapiro steps of the gSQUID as a function of drive frequency are shown in Fig. A.5. Clearly, the voltage steps occur at multiple integer heights of $V = 2e\omega/\hbar$.

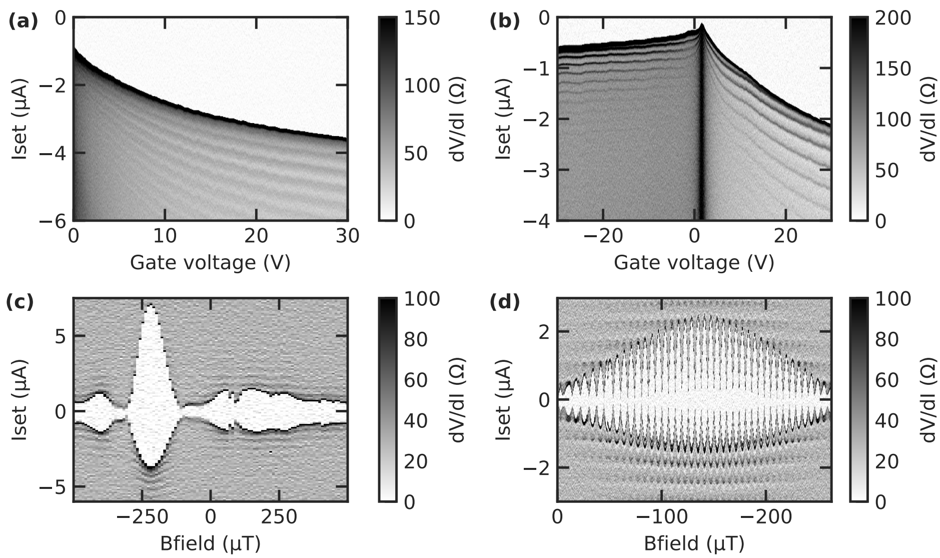

Figure A.1: Fiske-oscillations in gJJs embedded in MW resonance circuits. We observe oscillations in the differential resistance for numerous devices as a function of gate voltage **(a,b)** and magnetic field **(c,d)**. Devices in **(a)** and **(c)** are identical and correspond to the main text/ballistic one in Chapters 3 and 4, panel **(b)** is from the reference/diffusive device in the same chapters. The device in panel **(d)** is a gSQUID embedded in a MW DC bias cavity that did not show any MW response due to residual normal graphene areas around the SQUID. Offsets in magnetic field in panels **(c,d)** are due to flux focusing and trapping due to large areas of the chip covered by superconducting ground plane.

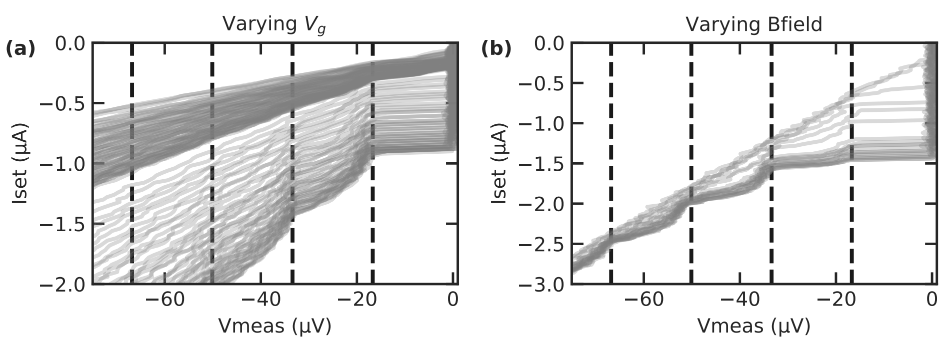

Figure A.2: Fiske-steps in the IVs of gJJs versus gate voltage and magnetic field. Panel **(a)** is the return branch of IVs taken as a function of gate voltage of the gSQUID in Fig. A.1(d). Panel **(b)** are linecuts through panel (c) of Fig. A.1. Dashed lines at integer multiples of 16.7 µV correspond to a resonance frequency of 8.1 GHz.

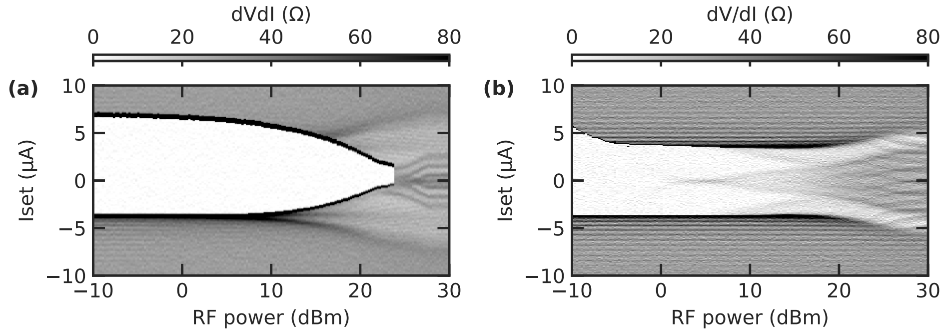

Figure A.3: Shapiro steps of a gJJ in a low-loss MW cavity at **(a)** 5 GHz (off-resonant) and at **(b)** 8.1 GHz (on-resonance). Oscillations in the differential resistance in **(b)** above I_c are due to Fiske-like steps (see section A.1)

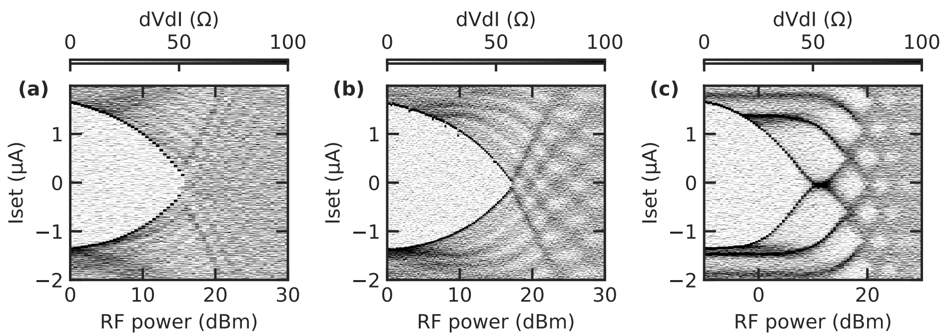

Figure A.4: Shapiro steps of a gSQUID in a high-loss MW cavity at **(a)** 3 GHz, **(b)** 5 GHz and **(c)** 8 GHz. The device is designed to exhibit a resonance at approximately 8.3 GHz.

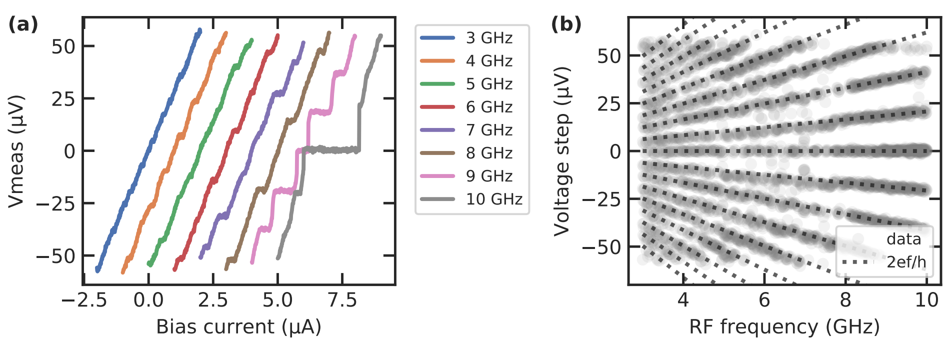

Figure A.5: Shapiro steps of a gSQUID in a high-loss MW cavity at varying drive frequency. The device is designed to exhibit a resonance at approximately 8.3 GHz. The voltage steps follow multiple integer values of $2e\omega/\hbar$.

B

Tips for operating the EBPGs at the TU Delft Kavli Nanolab

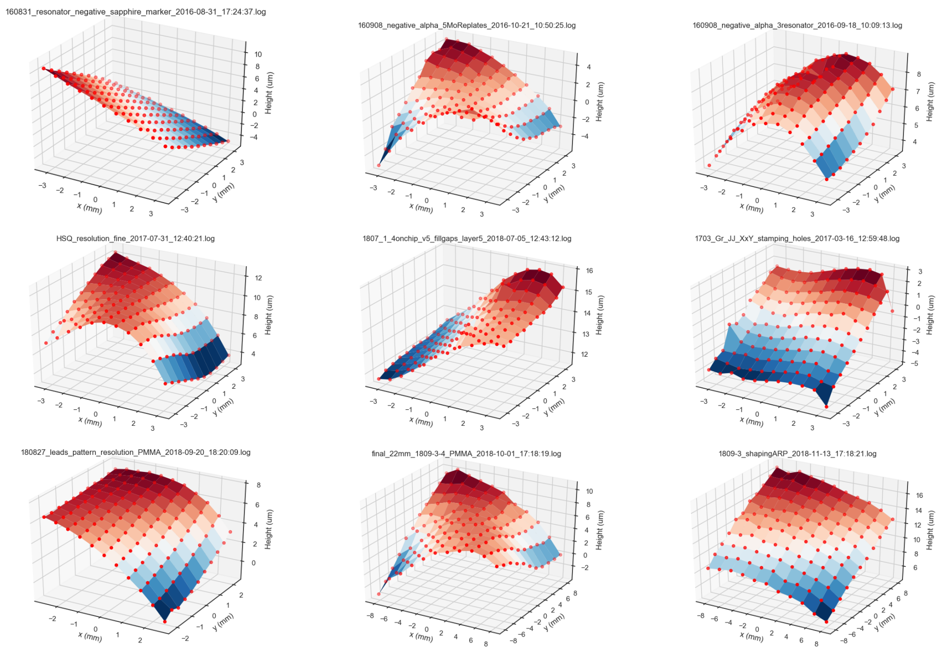

Figure B.1: A selection of heightmaps of different samples and different substrates, exposed on the EBPG 5000+ and the EBPG 5200. Sample heights are aligned with three height screws with which tilt can be adjusted for. Substrate bending can be due to the clamps holding the chip in place.

B.1. Height adjustment

When mounting chips on the EBPG sample holder, the chip needs to be held in place by clamps, while the holder height, tilt and rotation can be adjusted using micrometer screws. Naturally, the substrate never ends up completely horizontal due to manual errors, but in addition to surface tilt, bending also occurs regularly: Clamping the chip down with the holder clamps leads to tension and bending of the chip of up to several micrometers per mm, see Fig. B.1. These height differences can lead to distortions or stitching in the exposed pattern if not accounted for: The electron beam is focused only at one height. If height measurement is deactivated in cjob, the EBPG will not adjust the focus and patterns exposed this way can exhibit gaps reminiscent of stitching errors, or become overexposed. For this reason, activating beam height adjustment should be standard practice and can lead to significant improvements in patterning quality.

B.2. Stitching errors

We occasionally encountered stitching errors in our patterns, especially on the EBPG5000+, as shown in Fig. B.2. These defects manifest themselves as cuts or offsets at the main field borders, between parts of the pattern written by the ebeam. Each part of a pattern within a main field, approximately 700 µm × 700 µm, will be exposed without any stage movement or height adjustment. Stitching errors thus usually occur at the borders between main fields.

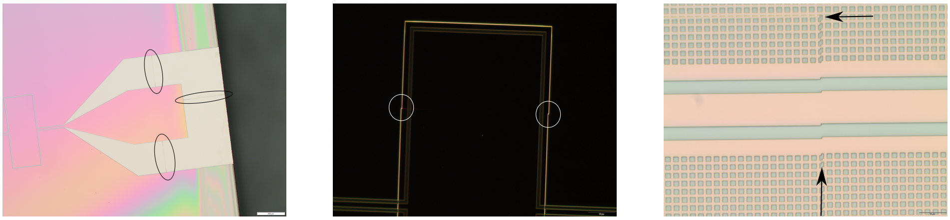

Figure B.2: Stitching errors encountered on the EBPG5000+. Parts of the pattern are unexposed (left, as marked by the black ellipsoids) or offset from each other (center and right, marked by ellipsoids and arrows), leading to severe defects in the circuit pattern.

Aside from the beam being out of focus, as discussed above, these can also be due to unusually large drifts over time in the piezoelectronics of the EBPG. To minimize the risk of encountering these issues, the following points should always be checked when setting up a job file:

Height measurements To eliminate errors due to the beam being out of focus, enable automatic height adjustment in cjob. Note that the job will fail if the measured height is out of range.

Exposure time Minimizing exposure time can reduce the susceptibility to drift errors. Techniques to consider are to change to a bigger beam, or to switch pattern polarity, e.g. by switching between a negative and a positive resist, or patterning with lift-off versus dry-etching.

Main field placement Choosing the main field placement such that the most critical parts of a pattern are not crossing main field borders can limit the effect of stitching. This can be achieved e.g. by changing the mainfield size to a more a suitable value, choosing *floating* main field placement, and selecting *follow geometry* as writing order.

Separate exposures Stitching-sensitive parts of a pattern can be split off from those that are less susceptible to stitching errors, and be exposed separately within one job. For example, the holey ground used in superconducting microwave circuits for flux trapping should be split off from the coplanar waveguides, since CPWs should not have stitching errors, while defects in the ground plane are not critical.

B.3. EBEAM ALIGNMENT

Here, we provide information, tips and tricks on how ebeam alignment works and how to implement it reliably on the Raith EBPG 5000+ and 5200 in the TU Delft Kavli cleanroom. This is important because when writing patterns onto a chip, you will need to specify the location of where on the chip you want your pattern to be. In the case of single-layer exposure, you can simply note down the coordinates of two opposite corners of your chip, from which you can calculate the chip center. This point can then be forwarded to the EBPG as location for the exposure.

B.3.1. Alignment of various layers to each other

It is good practice to add alignment marks to your pattern in case you will want to do another ebeam step on your sample. Note that even combining ebeam and photolithography steps are possible is suitable markers are chosen. Obviously, for multiple steps you will want to have a very good alignment of the individual steps with respect to the previous layers. There are various types of ebeam markers available in cjob. In our group we usually make use of rectangular markers that are 20 µm × 20 µm. Depending on the polarity, i.e. whether these will be elevated (positive) or holes (negative), these markers are called RP20 or RN20, respectively. Depending on how good your alignment needs to be you might do with just one set of markers

How marker search works

There are two ways for searching for and aligning to markers:

1. Manually: This is only possible in `operator` mode: Move to the marker positions (e.g. via `almic2ebpg` or directly via `mpos`, turn on the SEM and align to the markers. This way you can align to any recognizable structure with known position. You should only use this if the machine cannot recognize your markers, e.g. due to dirt on top.

2. Automatically: This method should be used preferably because the EBPG's software algorithm is much better than a human. In your cjob file you need to tell the ebeam which marker type (RECT for rectangular metallic, TOPO for topographic makers), POSitive or NEGative tone and what size they are. Rectangular markers can have lengths ranging from 20 µm to 100 µm.

The default markers, as they are on the sample holders, are `RECT POS 20,20`, or `RP20`.

For an automatic marker search, the EBPG starts at the specified position and scans outwards in a rectangular spiral, while at the same time measuring the contrast. In the end, once it measures a step of significant contrast and length that matches the specified marker type, it will stop. If it doesn't find anything, it will abort after a certain radius. The marker search parameters are:

- expected contrast `CONTRA` (default 97 %)
- maximum radius `ISRAD` (default 50 µm, at most half a scan field)
- step `ISXSTP, ISYSTP` (default 30 % marker size)

General rules for good alignment

Note that you should keep a free area (recommended are >100 µm × 100 µm) around each marker. This will help to avoid search failures due to confusion with other features. Also note that your markers should not be too close to your patterns, since marker search exposes the sample at a very high dose.

At least three markers are needed for correcting rotation, shift and scaling. However, it is recommended to use four markers to also account for shear and perspective distortion because the SEM detector is placed at an angle, which can lead to image distortions.

For most precise alignment (specs of the EBPG5000 and 5200 are below 10 nm) these steps should be followed:

- Do not use manual marker search. The EBPG is usually better than a human.

- Never use markers twice. Especially small beams can be extremely sensitive to any dirt on your markers, so make sure you have enough backup markers (at least one set per step). Scanning markers during alignmnt leads to contamination from carbon deposition, potentially rendering them useless for future steps.
- Do both rough and fine alignment: Do one alignment on R20 at the exposure level, one R20 alignment at the layout level, and one R10 alignment at the pattern level
- Use small markers for fine alignment (i.e. RN10/RP10 as the last alignment step)
- Put all patterns to be exposed inside the area enclosed by the markers.
- The pattern should be within 500 μm of each marker, meaning markers should not be spaced further apart than 1 mm from each other.

Rough alignment

- If the EBPG cannot find your markers, you might consider manual marker search (set marker type to `JOY` and run job as `operator`). Alignment will be significantly worse in this case, but at least you might be able to expose
- Dirt on your markers can lead to the EBPG not recognizing them or, worse, misinterpreting edges, so that your pattern will be scaled or even misaligned.
- For alignment down to approximately 1 μm, it is not necessary to put all of your pattern inside an area enclosed by your markers. For a 10 mm × 10 mm chip, you can for example place your markers at ±3000 μm, ±4000 μm and still expose and align all the way to the outside of the chip edge (with worse alignment the further outside the marker area you expose)

B.3.2. Example workflow of high-accuracy alignment on a large chip

This is an example workflow from Felix' device *1809.3* exposed on 14 November 2018 at 17:04:55. The pattern to be exposed is located on a 22 mm × 22 mm chip, further divided into four 10 mm × 10 mm chips, each with three DC bias cavities. At the end of two of each cavities per chip, there is a graphene JJ with several ebeam steps, which require high-accuracy alignment to each other. As an example we will cover the alignment for the third exposure, *shapingARP*. Note that every single pattern is different from the others, so we cannot simply use the same patterns for each junction, but require individual patterns, hence the large number of patterns and colors, see Fig. B.3.

First step: Alignment at the exposure level

Since we have several chips on the big one, we will first get the mapping of the entire large chip. For this, we find the four outermost markers, which in this case is RN20 at (±6500,±8100), see Fig. B.4.

Second step: Alignment at the layout level

Now that we have the general orientation of our large chip, we go into each of the four sub-chips and align the beam to four chip-markers. For the bottom-left chip, this is for example RN20 at (-6500,-8100), (-6500,-1900), (-3500,-1900), (-3500,-8100), see Fig. B.5. Note that we also use keystone correction here.

B

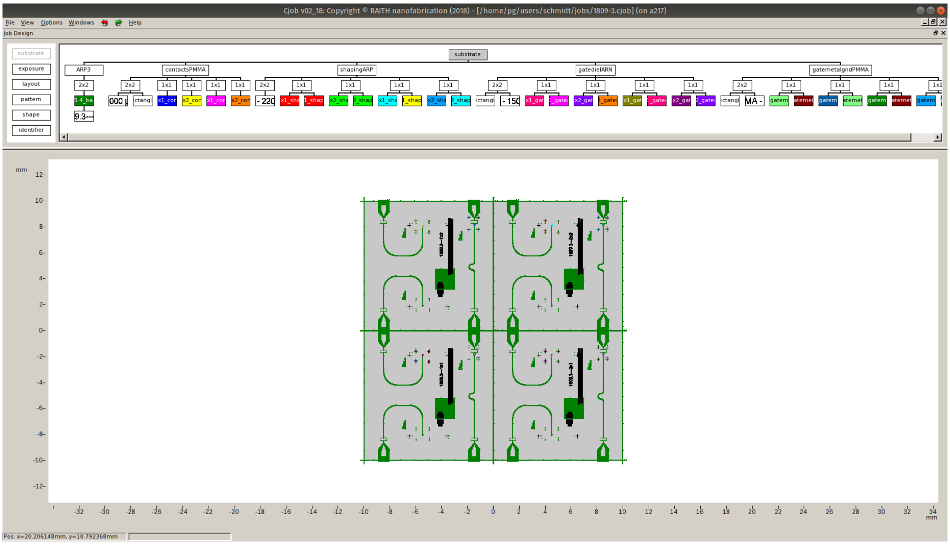

Figure B.3: Cjob file for device 1809.3

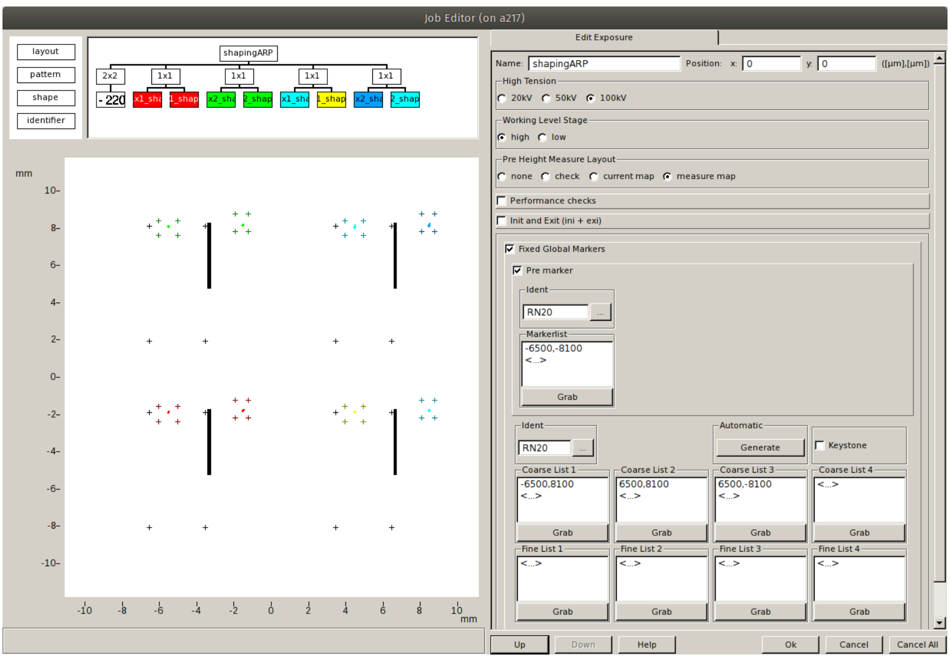

Figure B.4: First step: Alignment at the exposure level

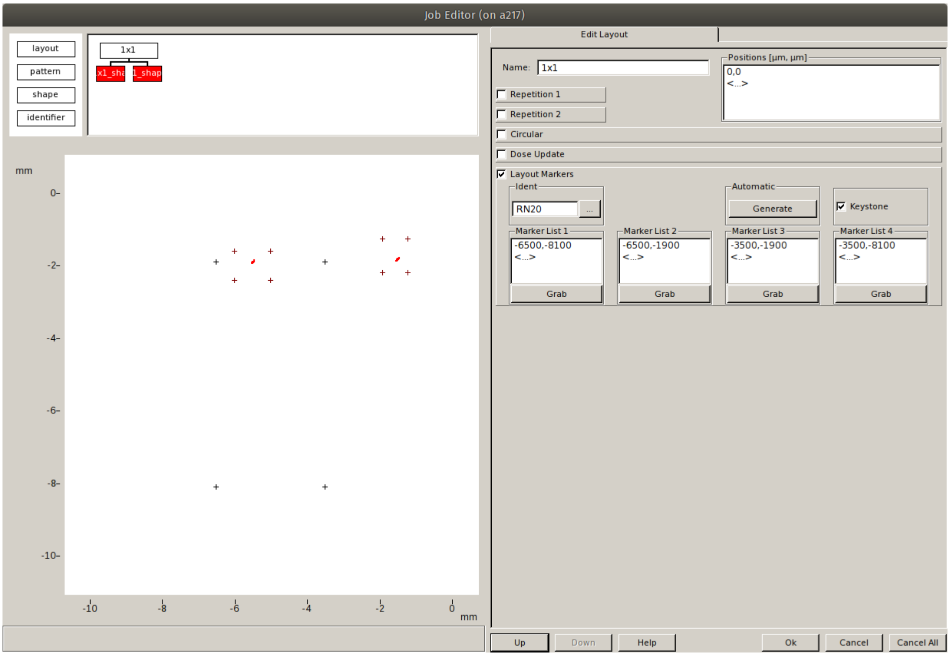

Figure B.5: Second step: Alignment at the layout level

THIRD STEP: ALIGNMENT AT THE PATTERN LEVEL

On each chip we will do two exposures with different patterns for two bias cavities. Since the patterns are spaced far apart, we choose to do a separate alignment for each exposure with very closely spaced markers. We now also switch to RN10 markers, since these are smaller and therefore the marker search is less likely to expose too much resist around our sample. Here for example the marker group of RN10 is (-1900,-2200), (-1200,-2200), (-1200,-1250), (-1900,-1250), see Fig. B.6. The xdistance between two markers is 700 µm, the ydistance 950 µm. Note that we also use keystone correction here.

HOW DID THE JOB GO?

Let's take a look at the log file, located on the ebpg5200 under `pg/users/schmidt/log/`, filename `1809-3_shapingARP_2018-11-14_170455.log`. Marker search starts in line 1831:

```
1831 Locating pre-alignment marker find_RN20 @ position
         45157.000000,44783.000000 [um] (absolute)
1832 Entered USER-DEFINED marker search routine findmarker
1833
1834 Executing /home/pg/.naf/bin/findmarker RN20
1835 PG_IMAGE_FINE_SIZE not defined
1836 getstringpar(): status =1088 =E_NOMAPSEL, set to HILL_I_NORMAL, type =-1,
         returned ""
1837 Current position 45157.000, 44783.000 corresponds to absolute position
         45157.000, 44783.000 (map "")
```

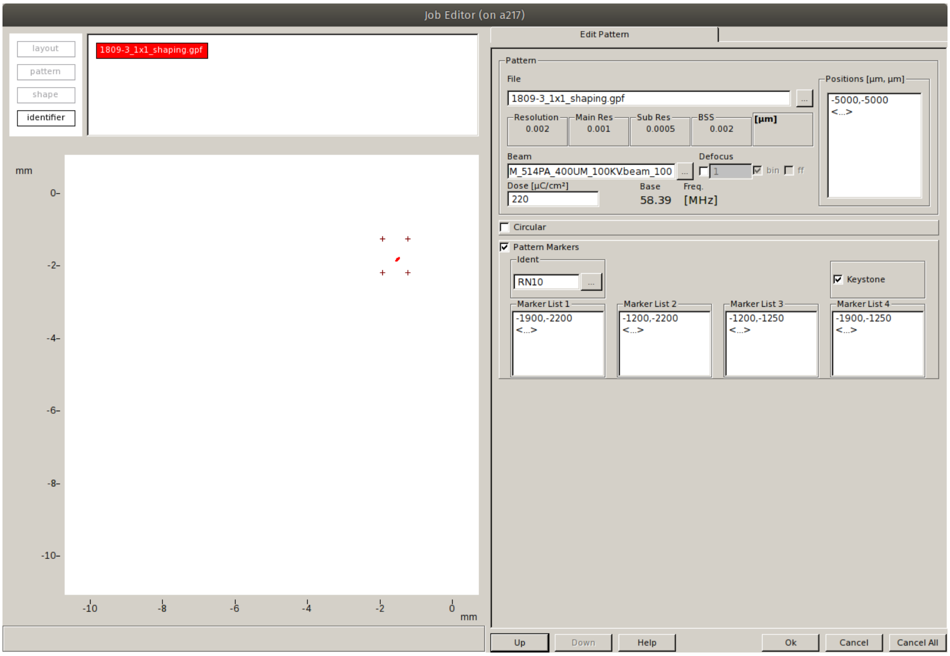

Figure B.6: Third step: Alignment at the pattern level

```
1838 The measured height at expected marker position 45157.000,44783.000 is
         18.7 micron, compensating
1839 Searching marker "RN20" at 45157.000, 44783.000 and found at 45167.510,
         44783.300
1840 Searching marker "RN20" at 45157.000,44783.000 and found at
         45167.510,44783.300, tababs /meas 45157.203,44776.097
1841   found @ 45.167510,44.783300
1842                  found marker @ position 45167.510400,44783.300050 [um]
                        (absolute)
```

Clearly, there was some misalignment between the actual marker position and the one specified for the job (10 µm in x, 0.3 µm in y). Note that the EBPG already compensates for the measured sample height at the marker (l. 1838) (see also Sec. B.1). Next, the marker search continues with the other three markers (ll. 1875-1909):

```
1875 pg select map substrate cjob_shapingARP
1876 cjob_align (pre)
1877 Entered USER-DEFINED marker search routine findmarker
1878
1879 Executing /home/pg/.naf/bin/findmarker RN20
1880 PG_IMAGE_FINE_SIZE not defined
1881 getstringpar(): status =0, type =10, returned "cjob_shapingARP"
1882 Current position -6500.000, 8100.000 corresponds to absolute position
         45167.510, 60983.300 (map "cjob_shapingARP")
```

```
The measured height at expected marker position -6500.000,8100.000 is 11.3 micron, compensating
Searching marker "RN20" at -6500.000, 8100.000 and found at -6522.129, 8099.725
Searching marker "RN20" at -6500.000,8100.000 and found at -6522.129,8099.725, tababs /meas 45135.510,60976.133
Locating align marker 1 find_RN20 at position -6500.000000,8100.000000 (-6500.000000,8100.000000) (cjob_shapingARP)
Entered USER-DEFINED marker search routine findmarker

Executing /home/pg/.naf/bin/findmarker RN20
PG_IMAGE_FINE_SIZE not defined
getstringpar(): status =0, type =10, returned "cjob_shapingARP"
Current position 6500.000, 8100.000 corresponds to absolute position 58167.510, 60983.300 (map "cjob_shapingARP")
The measured height at expected marker position 6500.000,8100.000 is 0.7 micron, compensating
Searching marker "RN20" at 6500.000, 8100.000 and found at 6477.666, 8117.098
Searching marker "RN20" at 6500.000,8100.000 and found at 6477.666,8117.098, tababs /meas 58135.341,60993.509
  found
Locating align marker 2 find_RN20 at position 6500.000000,8100.000000 (6500.000000,8100.000000) (cjob_shapingARP)
Entered USER-DEFINED marker search routine findmarker

Executing /home/pg/.naf/bin/findmarker RN20
PG_IMAGE_FINE_SIZE not defined
getstringpar(): status =0, type =10, returned "cjob_shapingARP"
Current position 6500.000, -8100.000 corresponds to absolute position 58167.510, 44783.300 (map "cjob_shapingARP")
The measured height at expected marker position 6500.000,-8100.000 is 8.2 micron, compensating
Searching marker "RN20" at 6500.000, -8100.000 and found at 6499.656, -8083.052
Searching marker "RN20" at 6500.000,-8100.000 and found at 6499.656,-8083.052, tababs /meas 58156.871,44793.346
  found
Locating align marker 3 find_RN20 at position 6500.000000,-8100.000000 (6500.000000,-8100.000000) (cjob_shapingARP)
  found
```

We can see that the EBPG found all three markers, but it detected significant shifts:

- Marker 1 was found at -6522.129, 8099.725 versus at -6500.000, 8100.000 (22.1 µm, 0.3 µm)
- Marker 2 was found at 6477.666, 8117.098 versus at 6500.000, 8100.000 (22.3 µm,17.1 µm)
- Marker 3 was found found at 6499.656, -8083.052 versus at 6500.000, -8100.000 (0.3 µm, 16.9 µm)

This implies nonnegligible scaling and rotation. Good thing we did marker search! These shifts can be reduced if you do the rotation alignment very precise. I seemed to have been a bit sloppy here, but the EBPG can still account for this without any problems.

The EBPG then continues with searching the markers in the second step, at the layout patterns (ll. 2744-2801):

```
2744 /home/pg/users/schmidt/jobs/RN20.mar
2745 cjob_do: layout: 1x1
2746 centre          [um] : 0.000000,0.000000
2747 origin          [um] : 0.000000,0.000000
2748 cells                : 1,1
2749 current mapping      : cjob_shapingARP
2750 mapping              : cjob_1x1
2751 pg select map substrate cjob_shapingARP
2752 centre          [um] : 0.000000,0.000000 (cjob_shapingARP)
2753 cjob_align (do)
2754 Entered USER-DEFINED marker search routine findmarker
2755
2756 Executing /home/pg/.naf/bin/findmarker RN20
2757 PG_IMAGE_FINE_SIZE not defined
2758 getstringpar(): status =0, type =10, returned "cjob_shapingARP"
2759 Current position -6500.000, -8100.000 corresponds to absolute position
         45167.371, 44782.876 (map "cjob_shapingARP")
2760 The measured height at expected marker position -6500.000,-8100.000 is
         18.5 micron, compensating
2761 Searching marker "RN20" at -6500.000, -8100.000 and found at -6499.856,
         -8099.553
2762 Searching marker "RN20" at -6500.000,-8100.000 and found at
         -6499.856,-8099.553, tababs /meas 45165.938,44780.110
2763 align marker 1: -6500.000000,-8100.000000,find_RN20
2764 align marker 2: -6500.000000,-1900.000000,find_RN20
2765 align marker 3: -3500.000000,-1900.000000,find_RN20
2766 align marker 4: -3500.000000,-8100.000000,find_RN20
2767 Locating align marker 1 find_RN20: -6500.000,-8100.000
         (-6500.000,-8100.000)
2768 Entered USER-DEFINED marker search routine findmarker
2769
2770 Executing /home/pg/.naf/bin/findmarker RN20
2771 PG_IMAGE_FINE_SIZE not defined
2772 getstringpar(): status =0, type =10, returned "cjob_shapingARP"
2773 Current position -6500.000, -1900.000 corresponds to absolute position
         45158.955, 50982.933 (map "cjob_shapingARP")
2774 The measured height at expected marker position -6500.000,-1900.000 is
         16.2 micron, compensating
2775 Searching marker "RN20" at -6500.000, -1900.000 and found at -6499.918,
         -1899.681
2776 Searching marker "RN20" at -6500.000,-1900.000 and found at
         -6499.918,-1899.681, tababs /meas 45157.700,50980.158
2777   found @ -6499.856,-8099.553 (absolute: 45167.515,44783.323)
2778 Locating align marker 2 find_RN20: -6500.000,-1900.000
```

```
(-6500.000,-1900.000)
Entered USER-DEFINED marker search routine findmarker

Executing /home/pg/.naf/bin/findmarker RN20
PG_IMAGE_FINE_SIZE not defined
getstringpar(): status =0, type =10, returned "cjob_shapingARP"
Current position -3500.000, -1900.000 corresponds to absolute position 48158.908, 50986.942 (map "cjob_shapingARP")
The measured height at expected marker position -3500.000,-1900.000 is 13.8 micron, compensating
Searching marker "RN20" at -3500.000, -1900.000 and found at -3499.941, -1899.714
Searching marker "RN20" at -3500.000,-1900.000 and found at -3499.941,-1899.714, tababs /meas 48157.674,50984.175
  found @ -6499.918,-1899.681 (absolute: 45159.037,50983.252)
Locating align marker 3 find_RN20: -3500.000,-1900.000 (-3500.000,-1900.000)
Entered USER-DEFINED marker search routine findmarker

Executing /home/pg/.naf/bin/findmarker RN20
PG_IMAGE_FINE_SIZE not defined
getstringpar(): status =0, type =10, returned "cjob_shapingARP"
Current position -3500.000, -8100.000 corresponds to absolute position 48167.324, 44786.885 (map "cjob_shapingARP")
The measured height at expected marker position -3500.000,-8100.000 is 16.1 micron, compensating
Searching marker "RN20" at -3500.000, -8100.000 and found at -3499.889, -8099.631
Searching marker "RN20" at -3500.000,-8100.000 and found at -3499.889,-8099.631, tababs /meas 48165.902,44784.120
  found @ -3499.941,-1899.714 (absolute: 48158.966,50987.229)
Locating align marker 4 find_RN20: -3500.000,-8100.000 (-3500.000,-8100.000)
  found @ -3499.889,-8099.631 (absolute: 48167.435,44787.254)
```

Obviously, the first alignment on the exposure level was already quite good, since we now already have alignment precision to our marker positions on the sub-micron level. This is good enough for most cases, but not for multi-step patterns at with submicron dimension which require very precise feature alignment, in this case below 100 nm.

As a last step, we search for the RN10 markers at the pattern level (ll. 2840-2895):

```
2840 Layout Cell 1 1 of 1x1
2841 /home/pg/users/schmidt/jobs/RN10.mar
2842 lay_dose_update =+,0.000000,0
2843 cjob_do: expose pattern, started at 17:18:16
2844
2845 pg select map substrate cjob_1x1
2846 centre       [um] : 0.000000,0.000000 (cjob_1x1)
2847 cjob_align (do)
2848 Entered USER-DEFINED marker search routine findmarker
```

```

Executing /home/pg/.naf/bin/findmarker RN10
PG_IMAGE_FINE_SIZE not defined
getstringpar(): status =0, type =10, returned "cjob_1x1"
Current position -1900.000, -2200.000 corresponds to absolute position 49759.338, 50689.349 (map "cjob_1x1")
The measured height at expected marker position -1900.000,-2200.000 is 13.4 micron, compensating
Searching marker "RN10" at -1900.000, -2200.000 and found at -1900.017, -2200.002
Searching marker "RN10" at -1900.000,-2200.000 and found at -1900.017,-2200.002, tababs /meas 49758.077,50686.574
align marker 1: -1900.000000,-2200.000000,find_RN10
align marker 2: -1200.000000,-2200.000000,find_RN10
align marker 3: -1200.000000,-1250.000000,find_RN10
align marker 4: -1900.000000,-1250.000000,find_RN10
Locating align marker 1 find_RN10: -1900.000,-2200.000 (-1900.000,-2200.000)
Entered USER-DEFINED marker search routine findmarker

Executing /home/pg/.naf/bin/findmarker RN10
PG_IMAGE_FINE_SIZE not defined
getstringpar(): status =0, type =10, returned "cjob_1x1"
Current position -1200.000, -2200.000 corresponds to absolute position 50459.322, 50690.277 (map "cjob_1x1")
The measured height at expected marker position -1200.000,-2200.000 is 13.0 micron, compensating
Searching marker "RN10" at -1200.000, -2200.000 and found at -1200.016, -2200.023
Searching marker "RN10" at -1200.000,-2200.000 and found at -1200.016,-2200.023, tababs /meas 50458.060,50687.497
  found @ -1900.017,-2200.002 (absolute: 49759.321,50689.347)
Locating align marker 2 find_RN10: -1200.000,-2200.000 (-1200.000,-2200.000)
Entered USER-DEFINED marker search routine findmarker

Executing /home/pg/.naf/bin/findmarker RN10
PG_IMAGE_FINE_SIZE not defined
getstringpar(): status =0, type =10, returned "cjob_1x1"
Current position -1200.000, -1250.000 corresponds to absolute position 50458.025, 51640.278 (map "cjob_1x1")
The measured height at expected marker position -1200.000,-1250.000 is 12.6 micron, compensating
Searching marker "RN10" at -1200.000, -1250.000 and found at -1200.006, -1250.035
Searching marker "RN10" at -1200.000,-1250.000 and found at -1200.006,-1250.035, tababs /meas 50456.797,51637.506
  found @ -1200.016,-2200.023 (absolute: 50459.305,50690.253)
Locating align marker 3 find_RN10: -1200.000,-1250.000 (-1200.000,-1250.000)
```

```
Entered USER-DEFINED marker search routine findmarker

Executing /home/pg/.naf/bin/findmarker RN10
PG_IMAGE_FINE_SIZE not defined
getstringpar(): status =0, type =10, returned "cjob_1x1"
Current position -1900.000, -1250.000 corresponds to absolute position
    49758.041, 51639.349 (map "cjob_1x1")
The measured height at expected marker position -1900.000,-1250.000 is
    13.0 micron, compensating
Searching marker "RN10" at -1900.000, -1250.000 and found at -1900.006,
    -1250.009
Searching marker "RN10" at -1900.000,-1250.000 and found at
    -1900.006,-1250.009, tababs /meas 49756.803,51636.566
  found @ -1200.006,-1250.035 (absolute: 50458.020,51640.243)
Locating align marker 4 find_RN10: -1900.000,-1250.000
    (-1900.000,-1250.000)
  found @ -1900.006,-1250.009 (absolute: 49758.035,51639.341)
```

At this stage, the misalignment is below 100 nm for each marker. This is sufficient and the EBPG continues by exposing the pattern.

C

Information on home-made lowpass filters

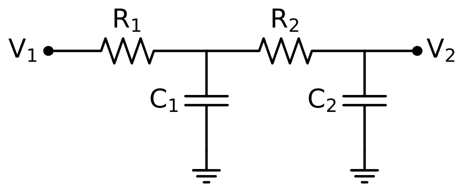

Figure C.1: Circuit schematic of a two-stage lowpass RC filter.

C

C.1. LOW-PASS RC FILTER COMPONENTS

For an overview of the different types of lumped frequency filters, for example to design a filter with a different cut-off frequency, we refer the reader to the OKAWA Electric design calculators[1]. The low-pass filters used in this thesis consist of two-stage RC filters, see Fig. C.1 with the following values: $R_1 = 470\,\Omega$[2], $R_2 = 2\,\mathrm{k}\Omega$[3], $C_1 = 10\,\mathrm{nF}$[4], $C_2 = 470\,\mathrm{pF}$[5]. The connectors for the filter PCBs can also be bought on Farnell[6]. Our PCBs require surface mount devices of type **0805** or **2012 metric**.

When ordering, care needs to be taken on the resistor type: There are *thin/metal* and *thick film* resistors. Resistors of type *thick film* should not be used, as they typically use Ruthenium oxide as resistive film with a large temperature coefficient. Hence, once cooled to lower temperatures, these resistors will dramatically change resistance. Instead, we use *thin film* or *metal electrode leadless faces* (MELF) resistors. These have a very low temperature coefficient, so they are much more stable. MELF resistors are cylindrical, so assembling them can be tricky since they easily roll away, but typically have higher voltage and power ratings.

There are also different types of SMD capacitors. The ones used in this thesis are of type *C0G (NP0)* dielectric, which provide high-quality temperature stability. SMD capacitors rated *GCM* (automotive grade) are to be preferred over *GRM* (general purpose), as they have a higher reliability rating, which is especially important for cryogenic experiments.

To assemble the lowpass filters, we apply solder paste to the metal pads of our PCBs at *DEMO* at TU Delft, place the SMD elements on the necessary locations, and either cure the solder paste using a heat gun or a dedicated oven. The connectors are subsequently soldered on using a standard solder iron.

C.2. COPPER POWDER FILTERS

We here provide the detailed recipe we used to make our own copper-powder filters, based on a recipe shared with us by Jason Mensingh at QuTech, Delft. These filters usually consist of a

[1] http://sim.okawa-denshi.jp/en/Fkeisan.htm

[2] Farnell 121-5922 MMU01020C4700FB300 - Surface Mount MELF Resistor, 470 Ω, MMU 0102 Series, 100 V, Metal Film, 100 mW, ±1 %

[3] Farnell 171-7632 ERA6ARB202V - SMD Chip Resistor, 0805 [2012 Metric], 2 kΩ, ERA6A Series, 100 V, Metal Film, 125 mW. Alternatively: Farnell 121-5939 MMU01020C2001FB300 - Surface Mount MELF Resistor, 2 kΩ, MMU 0102 Series, 100 V, Metal Film, 200 mW, ±1 % (these are round ones)

[4] Farnell 882-0074 GRM2195C1H103JA01D - SMD Multilayer Ceramic Capacitor, 10 000 pF, 50 V, 0805 [2012 Metric], ±5 %, C0G / NP0, GRM Series

[5] Farnell 180-0825 C0805C471J2GACTU - SMD Multilayer Ceramic Capacitor, 470 pF, 200 V, 0805 [2012 Metric], ±5 %, C0G / NP0

[6] 134-2652 19-70-1-TGG - RF / Coaxial Connector, SMA Coaxial, Edge Launch Jack, Solder, 50 ohm, Beryllium Copper

long meandering transmission line on a PCB connectorized with SMA connectors and encased in a copper box. To suppress high-frequency radiation above 1 GHz, the box is then filled with copper powder epoxy. Due to the chemical nature of this process, it is highly recommended to do all of this in a fumehood in a chemical lab and to follow standard laboratory procedures.

C.2.1. INGREDIENTS AND TOOLS

- Resin-hardener epoxy combination *Poly-Pox injecteerhars*[7]
  - 200 g resin (*hars*)
  - 100 g hardener (*harder*)
- Copper powder from SigmaAldrich[8]
- (TU Delft) paper coffee cup
- BD Plastikpak 2 mL syringe 300185[9]
- KimtechScience small wipes 05511[10]
- HUBY-340 cotton swabs[11]
- spatula
- scissors
- precision scale

C

C.2.2. INSTRUCTIONS

- Fill 10 g resin into the coffee cup and add 5 g hardener
- Stir for a few minutes using the spatula. The mixture should be slightly yellow, clear and very liquid. Bubbles are normal.
- Carefully, and in the fumehood add 79.5 g copper powder. The total weight should read 94.5 g
- Stir again for a few minutes, until there are no more visible grains, also in the edges of the cup. The mixture should look like quite viscous liquid Nutella.
- At this point it is safe to work outside of the fume hood. Cut down the walls of the coffee cup using the scissors. This will make it easier to fill the syringe.

[7] https://www.polyservice.nl/epoxyhars-sets/374-poly-pox-injecteerhars.html?search_query=injecteer&results=8
[8] Copper powder (spheroidal), 10 µm to 25 µm, 98 %, Product no. 326453, CAS 7440-50-8, https://www.sigmaaldrich.com/catalog/product/aldrich/326453?lang=en&region=NL
[9] https://www.lab-shop.co.uk/liquid-handling-4597/plastipak-sterile-disposable-syringes-4469/plastipak-300185-sterile-disposable-425054.htm
[10] http://www.kcprofessional.com/en-us/products/wipers/specialty-wipers/05511
[11] http://www.cleancross.net/english/products/threeinch_slim.html#BB-001

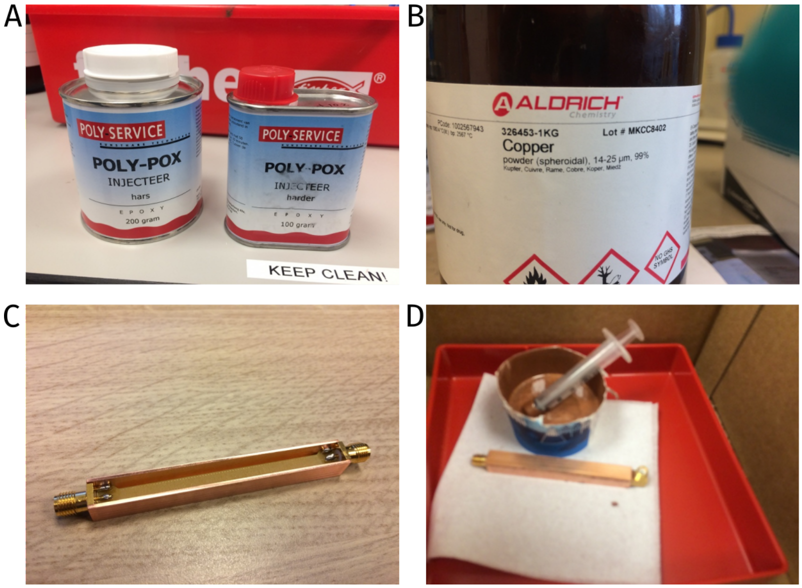

Figure C.2: Making copper powder filters. A, Resin and hardener from *POLY-SERVICE*. **B,** Copper powder from *SigmaAldrich*. **C,** PCB with soldered SMA connectors, inside the bottom part of its copper housing. **D,** Dried copper powder mixture, together with a finished copper powder filter.

- Fill the syringe from the cup. One syringe should be enough for one of our usual rectangular copper boxes.
- Slowly squirt the mixture into the copper box. Be careful, as the epoxy has very low viscosity! Slightly overfill the box.
- Put the lid on and press it onto the bottom piece. Then, using the swab, clean off spilled-over epoxy.
- Leave the rest of the mixture with the syringe next to the copper powder filter box for about a day. The next day, if the mixture inside the cup is solid, then it will also be solid inside the box. This is because the epoxy is hardened through a chemical reaction, not evaporation.

C.2.3. TESTING THE FILTER

- Measure the filter resistance using a handheld multimeter. Typical through-resistance is around $3\,\Omega$, while center pin to ground should be open.
- Connect the filter to a VNA and measure the transmission using cryocompatible cables at RT.
- Dunk the filter into liquid nitrogen and repeat the measurements repeatedly.
- Note that when taking the filter back out of nitrogen, the inside might be shorted to ground because of air moisture. The readings should be back to normal after one hour.

D

Miscellaneous source code

All source code presented here can also be found on my gist github profile.[1]

D.1. MATPLOTLIB COLORMAPS FOR SPYVIEW

Spyview[2] is a very useful piece of software for quick data visualization and exploration. It does however come with only a limited set of outdated colormaps. The following source code describes how to generate .ppm files based on the matplotlib colormaps that can be used for Spyview:

Listing D.1: ppm_for_spyview.py

```
import numpy as np
from matplotlib import cm, pyplot
import array

# PPM info
width =1
height =255
maxval =255

for cmap_name in pyplot.colormaps(): # all matplotlib colormaps
    # get data from matplotlib colormap
    cmap = cm.get_cmap(cmap_name)

    cw_array =[]
    for xval in np.linspace(0, 1, height):
        cw_raw =list(np.rint(np.array(cmap(xval)[:3]) *maxval).astype(int))
        # from raw data only take RBG, not alpha
        # convert to array for numerical treatment, *255 to go to RGB
            space, then convert array elements to int
        cw_array.extend(cw_raw)

    # PPM header
    ppm_header =f'P6 {width} {height} {maxval}\n'

    # PPM image data (filled with blue)
    image =array.array('B', cw_array)

    # Save the PPM image as a binary file
    with open(cmap_name + '.ppm', 'wb') as f:
        f.write(bytearray(ppm_header, 'ascii'))
        image.tofile(f)
```

[1] https://gist.github.com/feschmidt
[2] https://github.com/gsteele13/spyview

D.2. EBEAM HEIGHT MAP VISUALIZATION

The Raith EBPGs have the capability to record the height of the chip before exposure by measuring the angular reflection of a laser beam off the chip surface. The following is a python file to extract this data from the log files in a user folder on either one of the TU Delft EBPGs, and plot these height maps as single pngs.

Listing D.2: all_logs_to_png.py

```
import glob
import logging
import matplotlib.pyplot as plt
from mpl_toolkits.mplot3d import Axes3D
import numpy as np
import pandas as pd
import seaborn as sns
sns.set()
sns.set_style('white')
sns.set_style('ticks')
import traceback

ebeam =input("For which ebeam is the analysis supposed to be run?\n")

logfiles =sorted(glob.glob(f'log_{ebeam}/*.log'))
print(logfiles)

# Look for the following line:
key1 ='Measured/(skipped) heights [um] on the substrate:'
key2 ='Measured/(skipped) and estimated/[not counting] heights [um] on
    the substrate:'
# Below strings are unused
c00 = 'C00' # DC
c10 = 'C10' # x
c01 = 'C01' # y
c20 = 'C20' # x*x
c11 = 'C11' # x*y
c02 = 'C02' # y*y
c30 = 'C30' # x*x*x
c21 = 'C21' # x*x*y
c12 = 'C12' # x*y*y
c03 = 'C03' # y*y*y

for myfile in logfiles:

    filename =myfile.split('/')[-1]
    print(myfile)
    print(filename)

    with open(myfile, 'rb') as f:
        #read_data = f.read()
        i = 0
```

```
    for line in f:
        i += 1
        try:
            print(i, "-->", line.decode('UTF8').strip('\n'))
        except Exception as e:
            logging.error(traceback.format_exc())
            # Logs the error appropriately.

startlog =False
setbreak =False
thelog =[]
with open(myfile, 'rb') as f:
    #read_data = f.read()
    i = 0
    for line in f:
        i += 1
        try:
            theline =line.decode('UTF8').strip('\n')
            if setbreak:
                print(filename)
                break
            if startlog and not setbreak:
                print(i, "-->", theline)
                thelog.append(theline)
            if theline ==key1:
                startlog =True
            if 'fit' in theline:
                setbreak =True
        except Exception as e:
            logging.error(traceback.format_exc())
            # Logs the error appropriately.

if startlog:
    x = []
    y = []
    hs = []
    for newline in thelog:
        if key2 ==newline:
            break
        newline =newline.split()
        if 'M' in newline:
            h = []
            for i, item in enumerate(newline):
                if i ==0:
                    y.append(float(item))
                elif i ==1:
                    continue
                else:
                    if item =='*.*': # for height measurements out of
                         range
```

D

```
                    h.append(np.nan)
                elif '%ENG_W_SHOUHM' in item:
                    h.append(np.nan)
                    break
                else:
                    h.append(float(item))
        hs.append(h)
    elif '+--->' in newline:
        for i, item in enumerate(newline):
            if i > 1:
                x.append(float(item))

x = np.array(x)
y = np.array(y)
hs = np.array(hs)
dx = abs(x[-1] - x[0])
dy = abs(y[-1] - y[0])
DX = np.linspace(-dx / 2, dx / 2, len(x))
DY = np.linspace(-dy / 2, dy / 2, len(y))

try:
    fig, ax =plt.subplots()
    # ax.imshow(hs,extent=(x.min(), x.max(), y.max(), y.min()))
    heightmap =ax.imshow(hs,
                         extent=(-dx / 2, dx / 2, -dy / 2, dy / 2),
                         cmap='RdBu_r')
    cbar =plt.colorbar(heightmap)
    cbar.set_label('Height (um)')
    plt.xlabel('x (mm)')
    plt.ylabel('y (mm)')
    plt.title(filename)
    plt.tight_layout()
    plt.savefig(f'png_{ebeam}/2d/{filename}.png',
        bbox_inches='tight')
    #     plt.show()
    plt.close()

    X, Y =np.meshgrid(DX, DY)
    ax = plt.axes(projection='3d')
    ax.plot_surface(X, Y, hs, cmap='RdBu_r', edgecolor='none')
    ax.scatter3D(X, Y, hs, c='red')
    ax.set_title(filename)
    ax.set_xlabel('x (mm)')
    ax.set_ylabel('y (mm)')
    ax.set_zlabel('Height (um)')
    plt.tight_layout()
    plt.savefig(f'png_{ebeam}/2d/{filename}3D.png',
                bbox_inches='tight')
    #     plt.show()
    plt.close()
```

```
        except Exception as e:
            logging.error(traceback.format_exc())
            # Logs the error appropriately.

    else:
        print(f'no height measurement in {filename}')
```

D

Acknowledgements

Going down, party time
My friends are gonna be there too.

AC⚡DC [262]

Doing my PhD was by no means a one-man job. Without the help, encouragement and support from countless people, this research would not have been possible. The following people played a very important role in me traveling down this road.

I was lucky to have two promotors, both with a curiosity for modern physics, and always trying to modernize their research infrastructure. **Gary**, you are a great motivator and not only found the right words of encouragement when things were not going as planned, especially in the beginning of my PhD, but also leaped into action to deal with "political issues". In addition to me being drawn to Canadians, your curiosity in many different fields of physics was what got me hooked to join your group. Thank you for your support, especially for the encouraging words on starting a family and making it possible for me to work remotely. Thank you also to **Anton**, my second promotor. It was always very refreshing, and at times eye-opening, to get another PI's perspective on both science and work place procedures. Keep *Plotocop* going, I'm looking forward to its future generations. I would also like to thank all independent members of the committee for taking the time to evaluate this dissertation and giving me valuable feedback to improve the quality of this work.

To the people of SteeleLab: `Henlo fr13nd` **Mark**, my fellow graphene team member! We had a good whirl at merging DC bias cavities with graphene and boron nitride flakes. It was a great moment when we saw the first graphene resonance, and a sad one when you left for the far north. Thank you for (among other things) introducing me to VR, surreal memes, and touring Manchester, Teddington, Villard-de-Lans and Helsinki. I'm looking forward to many more instances of Orang and Meme man! **Martijn**, thank you for teaching me sarcasm and saying no to my supervisor. Sorry for not bringing back the bicycles, but then again you had the cleaning personnel take care of my samples. Current events forbid me to nominate paranymphs, but rest assured I would have liked to return the favor. **Marios**, I enjoy our conversations, especially during these crazy times, on all things PhD and family related. **Mario**, a big thank you for teaching me the intricacies of circuit anharmonicity, and the collaboration on the current detection paper. I'm glad our trip overseas turned out to be so much fun. **Byoung-moo**, I'm glad you can finally harvest the crops of your super-ambitious project. Good luck with finishing things up! **Sarwan**, I loved our obstacle runs together. Keep mastering the membranes, workouts and cooking, and best of luck for the future! I know you have great support with **Adrián**, who introduced me to the (currently) best Pizza bakery in Delft. Keep the flag of `stlab/utils` flying! **Daniel**, thank you for teaching me about microwave and superconducting physics, and the continuous flow of elegant mathematical derivations. You were a great roommate to have on the Casimir ski trip! Also thank you to the other half of the QOMSIM team, **Inês**! We had a great collaboration on the current detection, and I wish you two all the best for your future.

Fingers crossed you keep up the success! **Jasper**, you still have your entire PhD roller coaster ahead of you. Hold on tight, and it shall be a good ride. **Hadi**, it was nice to have a second 2D materials researcher in the group. Best of luck with your research on the other side of the road. **Fatemeh**, good to see your measurements are running, good luck!

In addition to me investigating graphene Josephson junctions, there were two other people in SteeleLab who pursued rather exotic topics, out of the scope of the central group theme: **Nikos**, from the first time talking to you during my interview I knew that we would get along quite well. Thank you for letting me crash on your couch on my first day of work, the good times in Boston, NYC and our office. I wish you and your family all the best for the future. Thank you **Yıldız**, the Turkish lady, for an always open ear for troubles, and for trusting me with your challenges. Good luck with the final sprint to the finish line!

I would also like to thank all Bachelor and Master students who I supervised for showing me what it takes to improve my supervision skills: In alphabetical (and chronological!) order, **Artiom, Daniël, Eagan** and **Pieter**.

Over the years, I have made some great friends in other groups of the department of Quantum Nanoscience. **Sabina** and **Maria**, thank you for the many nice coffee and lunch breaks. Sabina, thank you for lending me your ladder, and congratulations again and good luck with your position as assistant professor! Maria, I was lucky to have experienced your excellent cooking skills. Thank you for treating us to some real Moroccan food in terms of quality and quantity. **Nandini**, I still remember talking to you about monolayer MoS_2 at the stamping setup and working in the "Death Lab" on the fourth floor. I am glad you were able to start again at *QuTech*, and am looking forward to the next *Macarena* dance at one of your house parties. **Moritz**, I think we started interacting regularly when teaching QM1, but in addition to that, I also enjoyed us being cleanroom nerds and our conversations about our personal lives. Thank you for taking over for me in the PhD council, and good luck together with **Rob** for the remainder of your project! Rob, not only at work, but also at Krashna, I had a great time with you around. Thank you for the proofreading! **Claus**, eating ribs at *Wijnhaven* was a fun event, we have to do it again in the future! **Luigi**, you always managed to catch me off-guard when greeting me as "Mr. Felix"! I will gladly remember our time together on the PhD council and the discussions on how to etch and sputter things in the cleanroom. In addition, **Edouard**, **Martin**, **Andreas**, **Igor**, **Miguel**, **Rasa**, **Jérémie** and **Joeri**, good luck with your current and future research and I am looking forward to our next conversations, be it on scientific or other topics.

During my time at *QN* I had the pleasure to share an office with great people from various places: **Mari Carmen**, you and I almost started on the same day, in the same third-floor-hidden-away office and, as it turned out, were both well acquainted with Mark! My move to D110 separated us, but I'm glad we have still kept in contact. Fellow office mates of D110, **Lorenzo, Magda, Nikos, Su-Hyun, Marc** and **Jie**, thank you for the discussions on both scientific and other matters.

In the cleanroom, I was privileged to get to interact with some great lithography experts: **David** and **Ale**, thank you both for advice and chats on completely different topics, and sharing some of the best tips and tricks to increase the process quality. **James, Willemijn** and **Srijit**. We were frenemies and internal competition from day One. Even though things were not easy, I am glad we made it out okay. The *Kavli Nanolab* cleanroom itself would not be standing without the following people: **Frank, Marc, Eugene, Pauline, Ewan, Marco vdK, Marco B, Charles, Anja, Arnold, Hozanna, Ron, Roel** and **Lodi**. You not only keep things from blowing up, but also up and running, even though it sometimes is the Wild West in there. It was an amazing experience

to be able to work in probably one of the best equipped university cleanrooms worldwide.

I would like to extend a “Heel erg bedankt” to the support staff and technicians of *Quantum Nanoscience*: **Etty, Maria, Marijke, Erika** and **Heleen**. Thank you for taking care of so many administrative requests, never freaking out about the messy receipts for reimbursements and the countless hours of solving Basware related quirks and bugs. **Tino, Ronald** and **Tom**, you always kept things rolling and never got tired of our requests to building new setups or sample holders. Thank you to the entire team at *DEMO*, especially **Erik** and **Jack**, for support in electrical matters and building the IVVI modules. Thank you also to the great technicians at *QuTech*, in particular **Jason, Raymond, Raymond** and **Marijn**, for support regarding electronics, PCBs and low-pass and copper powder filters. In addition, all PIs at *QN* deserve to be mentioned as well for enabling a dynamic and modern work environment: **Sonia, Simon, Toeno, Andrea, Sander, Herre, Yaroslav** and **Kobus**.

Many of my former colleagues at *QN* have long left the department, but shall not be forgotten here. **Ranko**, a big “Hvala” for introducing me to Krashna, singing along with me during all these years, your insight to Montenegro, and the constant reminders to have more fun in my life. **Willeke**, I admire your brave switch to the industry, and it seems you made a great choice. Singing and going on tour together are some of my best memories of my time in Delft. **João**, I enjoyed our chats in *QN* and our brief time together at Krashna. **Holger**, the first *EP III* guy from Würzburg, your spot-on questions on induced superconductivity and the underlying physics in my experiments were always a great challenge, which forced me to think hard about what it was I was measuring. Thank you for that, and the fun we had as a group in Boston and New York. **Chris**, yet another dude from NRW in the flatlands. Even though we didn’t interact much during our shared time in Delft, I am glad we kept in touch now that we both moved back to Germany. All the best to you and Jasmin.

As already hinted above, singing in the *Delftse Studenten Muziek Gezelschap Krashna Musika* and especially the interactions with other choir members were a great balance to research. Thank you to all the friends I have made there, particularly, **Alexey**, **Christina**, **Jaime**, **Luca**, **Ozan** and **Tommaso**. I will try to make it to as many future concerts as I can, and I miss singing already.

Zu guter Letzt möchte ich mich noch ganz herzlich bei meiner Familie bedanken. **Mama** und **Papa**, danke dass ihr mich immer unterstützt, sowohl finanziell als auch emotional, meine Umzüge mitmacht und mich besuchen kommt, egal wohin es mich verschlägt. Ganz besonderer Dank gilt **Katrin** und **Felicitas**: Katrin, die gemeinsamen Jahre zusammen in Würzburg haben uns stark gemacht für die Zeit in Delft und Breyell. Schön, dass das jetzt ein Ende hat, und wir gemeinsam weitermachen können. Danke für alles, du bist für mich die Beste und ich liebe dich! Felicitas, du rückst alles nochmal in eine neue Perspektive und zeigst mir, was im Leben wirklich wichtig ist. Schön, dass du bei uns bist!

Curriculum Vitæ

Felix Erik Schmidt

12-11-1991	Born in Cologne, Germany.

Education

2002–2010	Secondary School Heinrich-Böll Gymnasium Troisdorf, Germany (2002-2007) Bev Facey Community High School, Sherwood Park, Canada (2007-2008) Heinrich-Böll Gymnasium Troisdorf, Germany (2008-2010)
2010	Military Service as IT soldier Sector for Information Technology, Airforce Base Köln-Wahn
2011–2016	BSc and MSc Nanostructure Technology Julius-Maximilians-Universität Würzburg *BSc Thesis:* Optimization of Tunnel Barriers for Spin Injection in Graphene *MSc Thesis:* Graphene – Hexagonal Boron Nitride Heterostructures *Supervisor:* Prof. Dr. C. Gould
2016-2020	PhD Physics Technische Universiteit Delft *Thesis:* Josephson junctions in superconducting coplanar DC bias cavities: Fundamental studies and applications *Promotors:* Prof. Dr. G.A. Steele and Dr. A. Akhmerov

List of Publications

4. **Felix E. Schmidt**, Mark D. Jenkins, Kenji Watanabe, Takashi Taniguchi and Gary A. Steele, *Probing the current-phase relation of graphene Josephson junctions using microwave measurements*, arXiv 2007.09795.

3. **Felix E. Schmidt**, Daniel Bothner, Ines C. Rodrigues, Mario F. Gely, Mark D. Jenkins, and Gary A. Steele, *Current detection using a Josephson parametric upconverter*, arXiv 2001.02521 (accepted for publication in Phys. Rev. Applied).

2. Sudhir Kumar Sahu, Jaykumar Vaidya, **Felix Schmidt**, Digambar Jangade, Arumugam Thamizhavel, Gary Steele, Mandar M Deshmukh and Vibhor Singh, *Nanoelectromechanical resonators from high-T_c superconducting crystals of $Bi_2Sr_2Ca_1Cu_2O_{8+\delta}$*, *2D Materials* **6**, 2 (2019).

1. **Felix E. Schmidt**[*], Mark D. Jenkins[*], Kenji Watanabe, Takashi Taniguchi and Gary A. Steele, *A ballistic graphene superconducting microwave circuit*, *Nature Communications* **9**, 4069 (2018).

[*]These authors contributed equally.

References

[1] A. Savage, *The Origin of "The Only Difference Between Screwing Around and Science Is Writing It Down",* (2015).

[2] H. Mujtaba, *AMD EPYC Rome CPUs Feature 39.54 Billion Transistors, IOD Detailed,* (accessed 2020-04-20).

[3] G. E. Moore, *Cramming more components onto integrated circuits, Reprinted from Electronics, volume 38, number 8, April 19, 1965, pp.114 ff.* IEEE Solid-State Circuits Society Newsletter **11**, 33 (2006).

[4] D. Buck, *The Cryotron-A Superconductive Computer Component,* Proceedings of the IRE **44**, 482 (1956).

[5] D. C. Brock, *Will the NSA Finally Build Its Superconducting Spy Computer? - IEEE Spectrum,* (accessed 2020-04-20).

[6] B. Josephson, *Possible new effects in superconductive tunnelling,* Physics Letters **1**, 251 (1962).

[7] P. W. Anderson and J. M. Rowell, *Probable Observation of the Josephson Superconducting Tunneling Effect,* Physical Review Letters **10**, 230 (1963).

[8] D. McDonald, R. Peterson, C. Hamilton, R. Harris, and R. Kautz, *Picosecond applications of Josephson junctions,* IEEE Transactions on Electron Devices **27**, 1945 (1980).

[9] W. Anacker, *Josephson Computer Technology: An IBM Research Project,* IBM Journal of Research and Development **24**, 107 (1980).

[10] T. D. Clark, R. J. Prance, and A. D. C. Grassie, *Feasibility of hybrid Josephson field effect transistors,* Journal of Applied Physics **51**, 2736 (1980).

[11] W. Gallagher, *Three-terminal superconducting devices,* IEEE Transactions on Magnetics **21**, 709 (1985).

[12] A. L. Robinson, *IBM Drops Superconducting Computer Project: Problems with a high-speed memory chip would delay a Josephson junction computer long enough for semiconductors to catch up,* Science **222**, 492 (1983).

[13] R. P. Feynman, *Simulating physics with computers,* International Journal of Theoretical Physics **21**, 467 (1982).

[14] J. M. Martinis, M. H. Devoret, and J. Clarke, *Quantum Josephson junction circuits and the dawn of artificial atoms,* Nature Physics **16**, 234 (2020).

[15] M. Steffen, D. P. DiVincenzo, J. M. Chow, T. N. Theis, and M. B. Ketchen, *Quantum computing: An IBM perspective,* IBM Journal of Research and Development **55**, 13:1 (2011).

[16] F. Arute, K. Arya, R. Babbush, *et al.*, *Quantum supremacy using a programmable superconducting processor,* Nature **574**, 505 (2019).

[17] A. Linn, *With new Microsoft breakthroughs, general purpose quantum computing moves closer to reality - Stories,* (accessed 2020-04-18).

[18] L. M. K. Vandersypen and M. A. Eriksson, *Quantum computing with semiconductor spins,* Physics Today **72**, 38 (2019).

[19] *On "Quantum Supremacy",* (accessed 2020-06-28).

[20] A. P. M. Place, L. V. H. Rodgers, P. Mundada, *et al.*, *New material platform for superconducting transmon qubits with coherence times exceeding 0.3 milliseconds,* arXiv:2003.00024 [cond-mat, physics:physics, physics:quant-ph] (2020), arXiv:2003.00024 [cond-mat, physics:physics, physics:quant-ph] .

[21] L. DiCarlo, J. M. Chow, J. M. Gambetta, *et al.*, *Demonstration of two-qubit algorithms with a superconducting quantum processor,* Nature **460**, 240 (2009).

[22] L. Casparis, M. R. Connolly, M. Kjaergaard, *et al.*, *Superconducting gatemon qubit based on a proximitized two-dimensional electron gas,* Nature Nanotechnology **13**, 915 (2018).

[23] T. Hyart, B. van Heck, I. C. Fulga, M. Burrello, A. R. Akhmerov, and C. W. J. Beenakker, *Flux-controlled quantum computation with Majorana fermions,* Physical Review B **88**, 035121 (2013).

[24] S. Thompson, M. Armstrong, C. Auth, *et al.*, *A Logic Nanotechnology Featuring Strained-Silicon,* IEEE Electron Device Letters **25**, 191 (2004).

[25] F. Fritz, *AMD Ryzen 5 3600 (Zen 2 | Matisse | IOD),* (2019).

[26] N. K. Langford, R. Sagastizabal, M. Kounalakis, *et al.*, *Experimentally simulating the dynamics of quantum light and matter at deep-strong coupling,* Nature Communications **8**, 1715 (2017).

[27] S. Shankland, *Take a look at Google's quantum computing technology,* (accessed 2020-04-20).

[28] G. De Lange, B. Van Heck, A. Bruno, *et al.*, *Realization of Microwave Quantum Circuits Using Hybrid Superconducting-Semiconducting Nanowire Josephson Elements,* Physical Review Letters **115**, 1 (2015).

[29] T. W. Larsen, K. D. Petersson, F. Kuemmeth, *et al.*, *Semiconductor-Nanowire-Based Superconducting Qubit,* Physical Review Letters **115**, 1 (2015).

[30] L. Casparis, T. W. Larsen, M. S. Olsen, *et al.*, *Gatemon Benchmarking and Two-Qubit Operations,* Physical Review Letters **116**, 150505 (2016).

[31] F. Luthi, T. Stavenga, O. W. Enzing, *et al.*, *Evolution of Nanowire Transmon Qubits and Their Coherence in a Magnetic Field,* Physical Review Letters **120** (2018), 10.1103/PhysRevLett.120.100502.

[32] Y.-P. Shim and C. Tahan, *Semiconductor-inspired design principles for superconducting quantum computing,* Nature Communications **7**, 11059 (2016).

[33] C. Tahan, *Graphene qubit motivates materials science,* Nature Nanotechnology **14**, 102 (2019).

[34] K. S. Novoselov, *Electric Field Effect in Atomically Thin Carbon Films,* Science **306**, 666 (2004).

[35] H. B. Heersche, P. Jarillo-Herrero, J. B. Oostinga, L. M. K. Vandersypen, and A. F. Morpurgo, *Bipolar supercurrent in graphene,* Nature **446**, 56 (2007).

[36] G.-H. Lee and H.-J. Lee, *Proximity coupling in superconductor-graphene heterostructures,* Reports on Progress in Physics **81**, 056502 (2018).

[37] S. J. Bosman, V. Singh, A. Bruno, and G. A. Steele, *Broadband architecture for galvanically accessible superconducting microwave resonators,* Applied Physics Letters **107**, 192602 (2015).

[38] V. E. Calado, S. Goswami, G. Nanda, *et al.*, *Ballistic Josephson junctions in edge-contacted graphene,* Nature Nanotechnology **10**, 761 (2015).

[39] M. Ben Shalom, M. J. Zhu, V. I. Fal'ko, *et al.*, *Quantum oscillations of the critical current and high-field superconducting proximity in ballistic graphene,* Nature Physics **12**, 318 (2015).

[40] G. E. Blonder, M. Tinkham, and T. M. Klapwijk, *Transition from metallic to tunneling regimes in superconducting microconstrictions: Excess current, charge imbalance, and supercurrent conversion,* Physical Review B **25**, 4515 (1982).

[41] C. W. J. Beenakker, *Universal limit of critical-current fluctuations in mesoscopic Josephson junctions,* Physical Review Letters **67**, 3836 (1991).

[42] M. Titov and C. W. J. Beenakker, *Josephson effect in ballistic graphene,* Physical Review B **74** (2006), 10.1103/PhysRevB.74.041401.

[43] A. Kringhøj, L. Casparis, M. Hell, *et al.*, *Anharmonicity of a superconducting qubit with a few-mode Josephson junction,* Physical Review B **97**, 060508 (2018).

[44] F. E. Schmidt, M. D. Jenkins, K. Watanabe, T. Taniguchi, and G. A. Steele, *A ballistic graphene superconducting microwave circuit,* Nature Communications **9**, 4069 (2018).

[45] T. Laeven, B. Nijholt, M. Wimmer, and A. R. Akhmerov, *Enhanced proximity effect in zigzag-shaped Majorana Josephson junctions,* arXiv:1903.06168 [cond-mat] (2019), arXiv:1903.06168 [cond-mat] .

[46] L. Bretheau, J. I.-J. Wang, R. Pisoni, K. Watanabe, T. Taniguchi, and P. Jarillo-Herrero, *Tunnelling spectroscopy of Andreev states in graphene,* Nature Physics **13**, 756 (2017).

[47] C. W. J. Beenakker, Colloquium *: Andreev reflection and Klein tunneling in graphene,* Reviews of Modern Physics **80**, 1337 (2008).

[48] M. Göppl, A. Fragner, M. Baur, *et al.*, *Coplanar waveguide resonators for circuit quantum electrodynamics,* Journal of Applied Physics **104**, 113904 (2008).

[49] J. Zmuidzinas, *Superconducting Microresonators: Physics and Applications,* Annual Review of Condensed Matter Physics **3**, 169 (2012).

[50] P. K. Day, H. G. LeDuc, B. A. Mazin, A. Vayonakis, and J. Zmuidzinas, *A broadband superconducting detector suitable for use in large arrays,* Nature **425**, 817 (2003).

[51] A. Blais, R.-S. Huang, A. Wallraff, S. M. Girvin, and R. J. Schoelkopf, *Cavity quantum electrodynamics for superconducting electrical circuits: An architecture for quantum computation,* Physical Review A **69**, 062320 (2004).

[52] A. A. Clerk, K. W. Lehnert, P. Bertet, J. R. Petta, and Y. Nakamura, *Hybrid quantum systems with circuit quantum electrodynamics,* Nature Physics **16**, 257 (2020).

[53] A. Blais, S. M. Girvin, and W. D. Oliver, *Quantum information processing and quantum optics with circuit quantum electrodynamics,* Nature Physics **16**, 247 (2020).

[54] M. R. Vissers, J. Hubmayr, M. Sandberg, S. Chaudhuri, C. Bockstiegel, and J. Gao, *Frequency-tunable superconducting resonators via nonlinear kinetic inductance,* Applied Physics Letters **107**, 062601 (2015).

[55] F. Chen, A. J. Sirois, R. W. Simmonds, and A. J. Rimberg, *Introduction of a dc bias into a high-Q superconducting microwave cavity,* Applied Physics Letters **98**, 132509 (2011).

[56] S.-X. Li and J. B. Kycia, *Applying a direct current bias to superconducting microwave resonators by using superconducting quarter wavelength band stop filters,* Applied Physics Letters **102**, 242601 (2013).

[57] S. Mahashabde, E. Otto, D. Montemurro, S. de Graaf, S. Kubatkin, and A. Danilov, *Fast tunable high Q-factor superconducting microwave resonators,* (2020), arXiv:2003.11068 .

[58] *Qucs project: Quite Universal Circuit Simulator,* (accessed 2020-06-28).

[59] P. W. Anderson and A. H. Dayem, *Radio-Frequency Effects in Superconducting Thin Film Bridges,* Physical Review Letters **13**, 195 (1964).

[60] N. Papadopoulos, *Mesoscopic Transport in 2D Materials and Heterostructures*, Ph.D. thesis, TU Delft (2019).
[61] Y. Zhang, L. Zhang, and C. Zhou, *Review of Chemical Vapor Deposition of Graphene and Related Applications,* Accounts of Chemical Research **46,** 2329 (2013).
[62] L. Lin, B. Deng, J. Sun, H. Peng, and Z. Liu, *Bridging the Gap between Reality and Ideal in Chemical Vapor Deposition Growth of Graphene,* Chemical Reviews **118,** 9281 (2018).
[63] L. Banszerus, M. Schmitz, S. Engels, *et al.*, *Ballistic Transport Exceeding 28 μm in CVD Grown Graphene,* Nano Letters **16,** 1387 (2016).
[64] D. Neumaier, S. Pindl, and M. C. Lemme, *Integrating graphene into semiconductor fabrication lines,* Nature Materials **18,** 525 (2019).
[65] A. S. Mayorov, R. V. Gorbachev, S. V. Morozov, *et al.*, *Micrometer-Scale Ballistic Transport in Encapsulated Graphene at Room Temperature,* Nano Letters **11,** 2396 (2011).
[66] D. A. Bandurin, I. Torre, R. K. Kumar, *et al.*, *Negative local resistance caused by viscous electron backflow in graphene,* Science **351,** 1055 (2016).
[67] Y. Cao, V. Fatemi, A. Demir, *et al.*, *Correlated insulator behaviour at half-filling in magic-angle graphene superlattices,* Nature **556,** 80 (2018).
[68] Y. Cao, V. Fatemi, S. Fang, *et al.*, *Unconventional superconductivity in magic-angle graphene superlattices,* Nature **556,** 43 (2018).
[69] X. Du, I. Skachko, A. Barker, and E. Y. Andrei, *Approaching ballistic transport in suspended graphene,* Nature Nanotechnology **3,** 491 (2008).
[70] P. Rickhaus, R. Maurand, M.-H. Liu, M. Weiss, K. Richter, and C. Schönenberger, *Ballistic interferences in suspended graphene,* Nature Communications **4,** 2342 (2013).
[71] N. Mizuno, B. Nielsen, and X. Du, *Ballistic-like supercurrent in suspended graphene Josephson weak links,* Nature Communications **4,** 2716 (2013).
[72] D.-K. Ki and A. F. Morpurgo, *High-Quality Multiterminal Suspended Graphene Devices,* Nano Letters **13,** 5165 (2013).
[73] R. Maurand, P. Rickhaus, P. Makk, *et al.*, *Fabrication of ballistic suspended graphene with local-gating,* Carbon **79,** 486 (2014).
[74] P. Rickhaus, P. Makk, K. Richter, and C. Schönenberger, *Gate tuneable beamsplitter in ballistic graphene,* Applied Physics Letters **107,** 251901 (2015).
[75] P. Rickhaus, M.-H. Liu, P. Makk, *et al.*, *Guiding of Electrons in a Few-Mode Ballistic Graphene Channel,* Nano Letters **15,** 5819 (2015).
[76] P. Rickhaus, *Electron Optics in Ballistic Graphene*, Ph.D. thesis, University of Basel (2015).
[77] C. R. Dean, a. F. Young, I. Meric, *et al.*, *Boron nitride substrates for high-quality graphene electronics,* Nature Nanotechnology **5,** 722 (2010).
[78] T. Taniguchi and K. Watanabe, *Synthesis of high-purity boron nitride single crystals under high pressure by using Ba–BN solvent,* Journal of Crystal Growth **303,** 525 (2007).
[79] M. Zastrow, *Meet the crystal growers who sparked a revolution in graphene electronics,* Nature **572,** 429 (2019).
[80] J. Xue, J. Sanchez-Yamagishi, D. Bulmash, *et al.*, *Scanning tunnelling microscopy and spectroscopy of ultra-flat graphene on hexagonal boron nitride,* Nature Materials **10,** 282 (2011).
[81] R. Decker, Y. Wang, V. W. Brar, *et al.*, *Local Electronic Properties of Graphene on a BN Substrate via Scanning Tunneling Microscopy,* Nano Letters **11,** 2291 (2011).
[82] L. A. Ponomarenko, A. K. Geim, A. A. Zhukov, *et al.*, *Tunable metal–insulator transition in double-layer graphene heterostructures,* Nature Physics **7,** 958 (2011).
[83] F. Amet, *Novel Phenomena Driven by Interactions and Symmetry Breaking in Graphene*, Ph.D. thesis, Stanford University (2014).
[84] A. K. Geim and I. V. Grigorieva, *Van der Waals heterostructures,* Nature **499,** 419 (2013).
[85] K. S. Novoselov, A. Mishchenko, A. Carvalho, and A. H. Castro Neto, *2D materials and van der Waals heterostructures,* Science **353,** aac9439 (2016).
[86] P. Blake, K. S. Novoselov, A. H. C. Neto, *et al.*, *Making graphene visible,* Applied Physics Letters **91,** 063124 (2007), arXiv:0705.0259 .
[87] S. Masubuchi, M. Morimoto, S. Morikawa, *et al.*, *Autonomous robotic searching and assembly of two-dimensional crystals to build van der Waals superlattices,* Nature Communications **9,** 1413 (2018).
[88] A. Castellanos-Gomez, M. Buscema, R. Molenaar, *et al.*, *Deterministic transfer of two-dimensional materials by all-dry viscoelastic stamping,* 2D Materials **1,** 011002 (2014).
[89] F. Pizzocchero, L. Gammelgaard, B. S. Jessen, *et al.*, *The hot pick-up technique for batch assembly of van der Waals heterostructures,* Nature Communications **7,** 11894 (2016).
[90] P. J. Zomer, M. H. D. Guimarães, J. C. Brant, N. Tombros, and B. J. van Wees, *Fast pick up technique for high quality heterostructures of bilayer graphene and hexagonal boron nitride,* Applied Physics Letters **105,** 013101 (2014).

[91] S. J. Haigh, A. Gholinia, R. Jalil, *et al.*, *Cross-sectional imaging of individual layers and buried interfaces of graphene-based heterostructures and superlattices,* Nature Materials **11**, 764 (2012).

[92] E. Khestanova, F. Guinea, L. Fumagalli, A. K. Geim, and I. V. Grigorieva, *Universal shape and pressure inside bubbles appearing in van der Waals heterostructures,* Nature Communications **7**, 12587 (2016).

[93] H. Ghorbanfekr-Kalashami, K. S. Vasu, R. R. Nair, F. M. Peeters, and M. Neek-Amal, *Dependence of the shape of graphene nanobubbles on trapped substance,* Nature Communications **8**, 15844 (2017).

[94] N. Levy, S. A. Burke, K. L. Meaker, *et al.*, *Strain-Induced Pseudo-Magnetic Fields Greater Than 300 Tesla in Graphene Nanobubbles,* Science **329**, 544 (2010).

[95] *KLayout Layout Viewer And Editor,* (accessed 2020-06-28).

[96] *LibreCAD - Free Open Source 2D CAD,* (accessed 2020-06-28).

[97] L. Wang, I. Meric, P. Y. Huang, *et al.*, *One-Dimensional Electrical Contact to a Two-Dimensional Material,* Science **342**, 614 (2013).

[98] G. Nanda, J. L. Aguilera-Servin, P. Rakyta, *et al.*, *Current-Phase Relation of Ballistic Graphene Josephson Junctions,* Nano Letters (2017), 10.1021/acs.nanolett.7b00097.

[99] M. Popinciuc, V. E. Calado, X. L. Liu, A. R. Akhmerov, T. M. Klapwijk, and L. M. K. Vandersypen, *Zero-bias conductance peak and Josephson effect in graphene-NbTiN junctions,* Physical Review B **85**, 205404 (2012).

[100] V. Mourik, K. Zuo, S. M. Frolov, S. R. Plissard, E. P. A. M. Bakkers, and L. P. Kouwenhoven, *Signatures of Majorana Fermions in Hybrid Superconductor-Semiconductor Nanowire Devices,* Science **336**, 1003 (2012).

[101] M. J. Jackson, *Microfabrication and Nanomanufacturing* (CRC Taylor & Francis, Boca Raton, 2006).

[102] M. J. Rooks, E. Kratschmer, R. Viswanathan, J. Katine, R. E. Fontana, and S. A. MacDonald, *Low stress development of poly(methylmethacrylate) for high aspect ratio structures,* Journal of Vacuum Science & Technology B: Microelectronics and Nanometer Structures **20**, 2937 (2002).

[103] B. Cord, J. Lutkenhaus, and K. K. Berggren, *Optimal temperature for development of poly(methylmethacrylate),* Journal of Vacuum Science & Technology B: Microelectronics and Nanometer Structures **25**, 2013 (2007).

[104] H. Namatsu, *Three-dimensional siloxane resist for the formation of nanopatterns with minimum linewidth fluctuations,* Journal of Vacuum Science & Technology B: Microelectronics and Nanometer Structures **16**, 69 (1998).

[105] D. J. Thoen, B. G. C. Bos, E. A. F. Haalebos, T. M. Klapwijk, J. J. A. Baselmans, and A. Endo, *Superconducting NbTin Thin Films With Highly Uniform Properties Over a 100 mm Diameter Wafer,* IEEE Transactions on Applied Superconductivity **27**, 1 (2017).

[106] B. H. Schneider, S. Etaki, H. S. J. van der Zant, and G. A. Steele, *Coupling carbon nanotube mechanics to a superconducting circuit,* Scientific Reports **2**, 599 (2012).

[107] B. H. Schneider, *Suspended Carbon Nanotubes Coupled to Superconducting Circuits.*, Ph.D. thesis, TU Delft (2014).

[108] N. N. Iosad, B. D. Jackson, F. Ferro, *et al.*, *Source optimization for magnetron sputter-deposition of NbTiN tuning elements for SIS THz detectors,* Superconductor Science and Technology **12**, 736 (1999).

[109] C. J. H. Keijzers, *Josephson Effects in Carbon Nanotube Mechanical Resonators and Graphene.*, Ph.D. thesis, TU Delft (2012).

[110] M. Aziz, D. Christopher Hudson, and S. Russo, *Molybdenum-rhenium superconducting suspended nanostructures,* Applied Physics Letters **104**, 233102 (2014).

[111] V. Singh, B. H. Schneider, S. J. Bosman, E. P. J. Merkx, and G. A. Steele, *Molybdenum-rhenium alloy based high-Q superconducting microwave resonators,* Applied Physics Letters **105**, 222601 (2014).

[112] K. J. G. Götz, S. Blien, P. L. Stiller, *et al.*, *Co-sputtered MoRe thin films for carbon nanotube growth-compatible superconducting coplanar resonators,* Nanotechnology **27**, 135202 (2016).

[113] S. Blien, K. J. G. Götz, P. L. Stiller, *et al.*, *Towards carbon nanotube growth into superconducting microwave resonator geometries: Nanotube growth into superconducting microwave resonators,* physica status solidi (b) **253**, 2385 (2016).

[114] A. W. Draelos, M.-T. Wei, A. Seredinski, *et al.*, *Supercurrent Flow in Multiterminal Graphene Josephson Junctions,* Nano Letters **19**, 1039 (2019).

[115] F. Amet, C. T. Ke, I. V. Borzenets, *et al.*, *Supercurrent in the quantum Hall regime,* Science **352**, 966 (2016).

[116] J. O. Island, G. A. Steele, H. S. J. van der Zant, and A. Castellanos-Gomez, *Thickness dependent interlayer transport in vertical MoS_2 Josephson junctions,* 2D Materials **3**, 031002 (2016).

[117] J. G. Kroll, W. Uilhoorn, K. L. van der Enden, *et al.*, *Magnetic field compatible circuit quantum electrodynamics with graphene Josephson junctions,* Nature Communications **9**, 1 (2018).

[118] V. A. Seleznev, M. A. Tarkhov, B. M. Voronov, *et al.*, *Deposition and characterization of few-nanometers-thick superconducting Mo–Re films,* Superconductor Science and Technology **21**, 115006 (2008).

[119] J. M. Mannion, M. S. Wellons, C. R. Shick, G. A. Fugate, B. A. Powell, and S. M. Husson, *Ambient aging of rhenium filaments used in thermal ionization mass spectrometry: Growth of oxo-rhenium crystallites and anti-aging strategies,* Heliyon **3**, e00232 (2017).

[120] J. M. Mannion, C. R. Shick, Jr., G. A. Fugate, M. S. Wellons, B. A. Powell, and S. M. Husson, *Rhenium filament*

oxidation: Effect on TIMS performance and the roles of carburization and humidity, Talanta **168**, 183 (2017).

[121] J. Lisenfeld, A. Bilmes, A. Megrant, *et al.*, *Electric field spectroscopy of material defects in transmon qubits,* npj Quantum Information **5**, 105 (2019).

[122] J. B. Johnson, *Thermal Agitation of Electricity in Conductors,* Physical Review **32**, 97 (1928).

[123] H. Nyquist, *Thermal Agitation of Electric Charge in Conductors,* Physical Review **32**, 110 (1928).

[124] F. Giazotto, T. T. Heikkilä, A. Luukanen, A. M. Savin, and J. P. Pekola, *Opportunities for mesoscopics in thermometry and refrigeration: Physics and applications,* Reviews of Modern Physics **78**, 217 (2006).

[125] M. Sarsby, N. Yurttagül, and A. Geresdi, *500 microkelvin nanoelectronics,* Nature Communications **11**, 1492 (2020).

[126] A. T. Jones, C. P. Scheller, J. R. Prance, Y. B. Kalyoncu, D. M. Zumbühl, and R. P. Haley, *Progress in Cooling Nanoelectronic Devices to Ultra-Low Temperatures,* Journal of Low Temperature Physics (2020), 10/gg3ffh.

[127] S. Krinner, S. Storz, P. Kurpiers, *et al.*, *Engineering cryogenic setups for 100-qubit scale superconducting circuit systems,* EPJ Quantum Technology **6**, 2 (2019).

[128] M. J. Persky, *Review of black surfaces for space-borne infrared systems,* Review of Scientific Instruments **70**, 2193 (1999).

[129] R. Barends, J. Wenner, M. Lenander, *et al.*, *Minimizing quasiparticle generation from stray infrared light in superconducting quantum circuits,* Applied Physics Letters **99**, 113507 (2011).

[130] J. Baselmans, S. Yates, P. Diener, and P. de Visser, *Ultra Low Background Cryogenic Test Facility for Far-Infrared Radiation Detectors,* Journal of Low Temperature Physics **167**, 360 (2012).

[131] D. J. van Woerkom, A. Geresdi, and L. P. Kouwenhoven, *One minute parity lifetime of a NbTiN Cooper-pair transistor,* Nature Physics **11**, 547 (2015).

[132] G.-H. Lee, S. Kim, S.-H. Jhi, and H.-J. Lee, *Ultimately short ballistic vertical graphene Josephson junctions,* Nature Communications **6**, 6181 (2015).

[133] K. S. Novoselov, V. I. Fal′ko, L. Colombo, P. R. Gellert, M. G. Schwab, and K. Kim, *A roadmap for graphene,* Nature **490**, 192 (2012).

[134] E. D. Walsh, D. K. Efetov, G.-H. Lee, *et al.*, *Graphene-Based Josephson-Junction Single-Photon Detector,* Physical Review Applied **8** (2017), 10.1103/PhysRevApplied.8.024022.

[135] J. M. Martinis, *Course 13 Superconducting qubits and the physics of Josephson junctions,* in *Les Houches*, Vol. 79 (Elsevier, 2004) pp. 487–520.

[136] M. A. Castellanos-Beltran, *Development of a Josephson Parametric Amplifier for the Preparation and Detection of Nonclassical States of Microwave Fields*, Ph.D. thesis, University of Colorado, Boulder (2010).

[137] G. J. Dolan, *Offset masks for lift-off photoprocessing,* Applied Physics Letters **31**, 337 (1977).

[138] L. J. Zeng, S. Nik, T. Greibe, *et al.*, *Direct observation of the thickness distribution of ultra thin AlO_x barriers in $Al/AlO_x/Al$ Josephson junctions,* Journal of Physics D: Applied Physics **48**, 395308 (2015).

[139] L. Zeng, D. T. Tran, C.-W. Tai, G. Svensson, and E. Olsson, *Atomic structure and oxygen deficiency of the ultrathin aluminium oxide barrier in $Al/AlO_x/Al$ Josephson junctions,* Scientific Reports **6**, 29679 (2016).

[140] J. A. Schreier, A. A. Houck, J. Koch, *et al.*, *Suppressing charge noise decoherence in superconducting charge qubits,* Physical Review B **77**, 180502 (2008).

[141] M. Sandberg, C. M. Wilson, F. Persson, *et al.*, *Tuning the field in a microwave resonator faster than the photon lifetime,* Applied Physics Letters **92**, 203501 (2008).

[142] W. Liang, M. Bockrath, D. Bozovic, J. H. Hafner, M. Tinkham, and H. Park, *Fabry - Perot interference in a nanotube electron waveguide,* Nature **411**, 665 (2001).

[143] F. Miao, S. Wijeratne, Y. Zhang, U. C. Coskun, W. Bao, and C. N. Lau, *Phase-Coherent Transport in Graphene Quantum Billiards,* Science **317**, 1530 (2007).

[144] A. F. Young and P. Kim, *Quantum interference and Klein tunnelling in graphene heterojunctions,* Nature Physics **5**, 222 (2009).

[145] S. Cho and M. Fuhrer, *Massless and massive particle-in-a-box states in single- and bi-layer graphene,* Nano Research **4**, 385 (2011).

[146] Y. Wu, V. Perebeinos, Y.-m. Lin, T. Low, F. Xia, and P. Avouris, *Quantum Behavior of Graphene Transistors near the Scaling Limit,* Nano Letters **12**, 1417 (2012).

[147] L. Campos, A. Young, K. Surakitbovorn, K. Watanabe, T. Taniguchi, and P. Jarillo-Herrero, *Quantum and classical confinement of resonant states in a trilayer graphene Fabry-Pérot interferometer,* Nature Communications **3** (2012), 10.1038/ncomms2243.

[148] I. V. Borzenets, F. Amet, C. T. Ke, *et al.*, *Ballistic Graphene Josephson Junctions from the Short to the Long Junction Regimes,* Physical Review Letters **117** (2016), 10.1103/PhysRevLett.117.237002.

[149] M. T. Allen, O. Shtanko, I. C. Fulga, *et al.*, *Observation of Electron Coherence and Fabry–Perot Standing Waves at a Graphene Edge,* Nano Letters **17**, 7380 (2017).

[150] M. Zhu, M. B. Shalom, A. Mishchsenko, V. Fal'ko, K. Novoselov, and A. Geim, *Supercurrent and multiple Andreev reflections in micrometer-long ballistic graphene Josephson junctions,* Nanoscale **10**, 3020 (2018).

[151] C. D. English, D. R. Hamilton, C. Chialvo, I. C. Moraru, N. Mason, and D. J. Van Harlingen, *Observation of non-sinusoidal current-phase relation in graphene Josephson junctions,* Physical Review B **94** (2016), 10.1103/PhysRevB.94.115435.

[152] H. Paik, D. I. Schuster, L. S. Bishop, *et al.*, *Observation of High Coherence in Josephson Junction Qubits Measured in a Three-Dimensional Circuit QED Architecture,* Physical Review Letters **107**, 240501 (2011).

[153] N. N. Iosad, A. B. Ermakov, F. E. Meijer, B. D. Jackson, and T. M. Klapwijk, *Characterization of the fabrication process of Nb/Al–AlN$_x$/Nb tunnel junctions with low R_nA values up to 1 $\Omega\mu m^2$,* Superconductor Science and Technology **15**, 945 (2002).

[154] S. K. Tolpygo, D. J. C. Amparo, R. T. Hunt, J. A. Vivalda, and D. T. Yohannes, *Subgap Leakage in Nb/Al-AlO$_x$/Nb Josephson Junctions and Run-to-Run Reproducibility: Effects of Oxidation Chamber and Film Stress,* IEEE Transactions on Applied Superconductivity **23**, 1100305 (2013).

[155] C.-X. Liu, F. Setiawan, J. D. Sau, and S. Das Sarma, *Phenomenology of the soft gap, zero-bias peak, and zero-mode splitting in ideal Majorana nanowires,* Physical Review B **96**, 054520 (2017).

[156] W. Chang, S. M. Albrecht, T. S. Jespersen, *et al.*, *Hard gap in epitaxial semiconductor–superconductor nanowires,* Nature Nanotechnology **10**, 232 (2015).

[157] M. Kjaergaard, F. Nichele, H. J. Suominen, *et al.*, *Quantized conductance doubling and hard gap in a two-dimensional semiconductor–superconductor heterostructure,* Nature Communications **7**, 12841 (2016).

[158] T. Ö. Rosdahl, A. Vuik, M. Kjaergaard, and A. R. Akhmerov, *Andreev rectifier: A nonlocal conductance signature of topological phase transitions,* Physical Review B **97**, 045421 (2018).

[159] J. Koch, T. M. Yu, J. Gambetta, *et al.*, *Charge-insensitive qubit design derived from the Cooper pair box,* Physical Review A **76**, 042319 (2007).

[160] J. D. Hunter, *Matplotlib: A 2D Graphics Environment,* Computing in Science Engineering **9**, 90 (2007).

[161] F. E. Schmidt, M. D. Jenkins, K. Watanabe, T. Taniguchi, and G. Steele, *Data And Code For "A Ballistic Graphene Superconducting Microwave Circuit",* (2018).

[162] M. D. Jenkins and F. E. Schmidt, *Measurement and Analysis scripts for "A ballistic graphene superconducting microwave circuit",* Zenodo (2018).

[163] D. M. Pozar, *Microwave Engineering*, 4th ed. (Wiley, Hoboken, NJ, 2012).

[164] T. Van Duzer and C. W. Turner, *Principles of Superconductive Devices and Circuits*, 2nd ed. (Prentice Hall, Upper Saddle River, N.J, 1999).

[165] S. E. Nigg, H. Paik, B. Vlastakis, *et al.*, *Black-Box Superconducting Circuit Quantization,* Physical Review Letters **108**, 240502 (2012).

[166] M. Tinkham, *Introduction to Superconductivity*, 2nd ed. (McGraw-Hill, Inc., New York, 1996).

[167] H. Courtois, M. Meschke, J. T. Peltonen, and J. P. Pekola, *Origin of Hysteresis in a Proximity Josephson Junction,* Physical Review Letters **101** (2008), 10.1103/PhysRevLett.101.067002.

[168] I. V. Borzenets, U. C. Coskun, H. T. Mebrahtu, Y. V. Bomze, A. I. Smirnov, and G. Finkelstein, *Phonon bottleneck in graphene-based Josephson junctions at millikelvin temperatures,* Physical Review Letters **111** (2013), 10.1103/PhysRevLett.111.027001, arXiv:1212.6297 .

[169] C. W. Groth, M. Wimmer, A. R. Akhmerov, and X. Waintal, *Kwant: A software package for quantum transport,* New Journal of Physics **16**, 063065 (2014).

[170] J.-D. Pillet, C. H. L. Quay, P. Morfin, C. Bena, A. L. Yeyati, and P. Joyez, *Andreev bound states in supercurrent-carrying carbon nanotubes revealed,* Nature Physics **6**, 965 (2010).

[171] J. C. Cuevas and A. L. Yeyati, *Subharmonic gap structure in short ballistic graphene junctions,* Physical Review B **74**, 180501 (2006).

[172] P. Dubos, H. Courtois, B. Pannetier, F. K. Wilhelm, A. D. Zaikin, and G. Schön, *Josephson critical current in a long mesoscopic S-N-S junction,* Physical Review B **63**, 064502 (2001).

[173] F. E. Schmidt, M. D. Jenkins, K. Watanabe, T. Taniguchi, and G. A. Steele, *Probing the current-phase relation of graphene Josephson junctions using microwave measurements,* arXiv:2007.09795 [cond-mat] (2020), arXiv:2007.09795 [cond-mat] .

[174] F. E. Schmidt, M. D. Jenkins, K. Watanabe, T. Taniguchi, and G. A. Steele, *Data and code for "Probing the current-phase relation of graphene Josephson junctions using microwave measurements",* (2020).

[175] B. Josephson, *Supercurrents through barriers,* Advances in Physics **14**, 419 (1965).

[176] A. A. Golubov, M. Y. Kupriyanov, and E. Il'ichev, *The current-phase relation in Josephson junctions,* Reviews of Modern Physics **76**, 411 (2004).

[177] J. I.-J. Wang, D. Rodan-Legrain, L. Bretheau, *et al.*, *Coherent control of a hybrid superconducting circuit made with graphene-based van der Waals heterostructures,* Nature Nanotechnology **14**, 120 (2019).

[178] R. Rifkin and B. S. Deaver, *Current-phase relation and phase-dependent conductance of superconducting point contacts from rf impedance measurements,* Physical Review B **13**, 3894 (1976).

[179] F. E. Schmidt, D. Bothner, I. C. Rodrigues, M. F. Gely, M. D. Jenkins, and G. A. Steele, *Current detection using a*

Josephson parametric upconverter, (2020), arXiv:2001.02521 .

[180] M. I. Katsnelson, *Zitterbewegung, chirality, and minimal conductivity in graphene,* The European Physical Journal B **51**, 157 (2006).

[181] K. Ziegler, *Robust Transport Properties in Graphene,* Physical Review Letters **97**, 266802 (2006).

[182] J. Tworzydło, B. Trauzettel, M. Titov, A. Rycerz, and C. W. J. Beenakker, *Sub-Poissonian Shot Noise in Graphene,* Physical Review Letters **96**, 246802 (2006).

[183] M. Fuechsle, J. Bentner, D. A. Ryndyk, M. Reinwald, W. Wegscheider, and C. Strunk, *Effect of Microwaves on the Current-Phase Relation of Superconductor–Normal-Metal–Superconductor Josephson Junctions,* Physical Review Letters **102** (2009), 10.1103/PhysRevLett.102.127001.

[184] I. Hagymási, A. Kormányos, and J. Cserti, *Josephson current in ballistic superconductor-graphene systems,* Physical Review B **82** (2010), 10.1103/PhysRevB.82.134516.

[185] A. M. Black-Schaffer and J. Linder, *Strongly anharmonic current-phase relation in ballistic graphene Josephson junctions,* Physical Review B **82**, 184522 (2010).

[186] P. Rakyta, A. Kormányos, and J. Cserti, *Magnetic field oscillations of the critical current in long ballistic graphene Josephson junctions,* Physical Review B **93**, 224510 (2016).

[187] E. Boaknin, V. E. Manucharyan, S. Fissette, *et al.*, *Dispersive microwave bifurcation of a superconducting resonator cavity incorporating a Josephson junction,* (2007), arXiv:cond-mat/0702445 .

[188] A. M. Portis, H. Chaloupka, M. Jeck, H. Piel, and A. Pischke, *Power-induced switching of an HTS microstrip patch antenna,* Superconductor Science and Technology **4**, 436 (1991).

[189] M. Hein, W. Diete, M. Getta, *et al.*, *Fundamental limits of the linear microwave power response of epitaxial Y-Ba-Cu-O films,* IEEE Transactions on Appiled Superconductivity **7**, 1264 (1997).

[190] J. Wosik, L.-M. Xie, K. Nesteruk, D. Li, J. H. Miller, and S. A. Long, *Power handling capabilities of superconducting YBCO thin films: Thermally induced nonlinearity effects,* Journal of Superconductivity **10**, 97 (1997).

[191] J. M. Martinis, K. B. Cooper, R. McDermott, *et al.*, *Decoherence in Josephson Qubits from Dielectric Loss,* Physical Review Letters **95**, 210503 (2005).

[192] A. D. O'Connell, M. Ansmann, R. C. Bialczak, *et al.*, *Microwave dielectric loss at single photon energies and millikelvin temperatures,* Applied Physics Letters **92**, 112903 (2008).

[193] D. Gunnarsson, J.-M. Pirkkalainen, J. Li, *et al.*, *Dielectric losses in multi-layer Josephson junction qubits,* Superconductor Science and Technology **26**, 085010 (2013).

[194] B. Dassonneville, M. Ferrier, S. Guéron, and H. Bouchiat, *Dissipation and Supercurrent Fluctuations in a Diffusive Normal-Metal–Superconductor Ring,* Physical Review Letters **110** (2013), 10.1103/PhysRevLett.110.217001.

[195] M. Ferrier, B. Dassonneville, S. Guéron, and H. Bouchiat, *Phase-dependent Andreev spectrum in a diffusive SNS junction: Static and dynamic current response,* Physical Review B **88**, 174505 (2013).

[196] B. Dassonneville, A. Murani, M. Ferrier, S. Guéron, and H. Bouchiat, *Coherence-enhanced phase-dependent dissipation in long SNS Josephson junctions: Revealing Andreev bound state dynamics,* Physical Review B **97**, 184505 (2018).

[197] C. M. Wilson, T. Duty, M. Sandberg, F. Persson, V. Shumeiko, and P. Delsing, *Photon Generation in an Electromagnetic Cavity with a Time-Dependent Boundary,* Physical Review Letters **105**, 233907 (2010).

[198] X. Zhou, V. Schmitt, P. Bertet, *et al.*, *High-gain weakly nonlinear flux-modulated Josephson parametric amplifier using a SQUID array,* Physical Review B **89**, 214517 (2014).

[199] E. Scheer, P. Joyez, D. Esteve, C. Urbina, and M. H. Devoret, *Conduction Channel Transmissions of Atomic-Size Aluminum Contacts,* Physical Review Letters **78**, 3535 (1997).

[200] M. F. Goffman, C. Urbina, H. Pothier, J. Nygård, C. M. Marcus, and P. Krogstrup, *Conduction channels of an InAs-Al nanowire Josephson weak link,* New Journal of Physics **19**, 092002 (2017).

[201] P. Pandey, R. Kraft, R. Krupke, D. Beckmann, and R. Danneau, *Andreev reflection in ballistic normal metal/graphene/superconductor junctions,* Physical Review B **100**, 165416 (2019).

[202] I. Sochnikov, L. Maier, C. A. Watson, *et al.*, *Nonsinusoidal Current-Phase Relationship in Josephson Junctions from the 3D Topological Insulator HgTe,* Physical Review Letters **114**, 066801 (2015).

[203] M. J. A. Stoutimore, A. N. Rossolenko, V. V. Bolginov, *et al.*, *Second-Harmonic Current-Phase Relation in Josephson Junctions with Ferromagnetic Barriers,* Physical Review Letters **121**, 177702 (2018).

[204] A. Assouline, C. Feuillet-Palma, N. Bergeal, *et al.*, *Spin-Orbit induced phase-shift in Bi2Se3 Josephson junctions,* Nature Communications **10**, 126 (2019).

[205] A. Murani, B. Dassonneville, A. Kasumov, *et al.*, *Microwave Signature of Topological Andreev level Crossings in a Bismuth-based Josephson Junction,* Physical Review Letters **122**, 076802 (2019).

[206] M. Wallquist, V. S. Shumeiko, and G. Wendin, *Selective coupling of superconducting charge qubits mediated by a tunable stripline cavity,* Physical Review B **74**, 224506 (2006).

[207] W. Wustmann and V. Shumeiko, *Parametric resonance in tunable superconducting cavities,* Physical Review B **87**, 184501 (2013).

[208] S. Pogorzalek, K. G. Fedorov, L. Zhong, *et al.*, *Hysteretic Flux Response and Nondegenerate Gain of Flux-Driven Josephson Parametric Amplifiers,* Physical Review Applied **8**, 024012 (2017).

[209] J. M. Kivioja, T. E. Nieminen, J. Claudon, O. Buisson, F. W. J. Hekking, and J. P. Pekola, *Weak coupling Josephson junction as a current probe: Effect of dissipation on escape dynamics,* New Journal of Physics **7**, 179 (2005).

[210] U. C. Coskun, M. Brenner, T. Hymel, V. Vakaryuk, A. Levchenko, and A. Bezryadin, *Distribution of Supercurrent Switching in Graphene under the Proximity Effect,* Physical Review Letters **108**, 097003 (2012).

[211] F. E. Schmidt, D. Bothner, I. C. Rodrigues, M. F. Gely, M. D. Jenkins, and G. A. Steele, *Data and processing for "Current detection using a Josephson parametric upconverter",* (2020).

[212] D. J. Goldie, A. V. Velichko, D. M. Glowacka, and S. Withington, *Ultra-low-noise MoCu transition edge sensors for space applications,* Journal of Applied Physics **109**, 084507 (2011).

[213] B. Cabrera, R. M. Clarke, P. Colling, A. J. Miller, S. Nam, and R. W. Romani, *Detection of single infrared, optical, and ultraviolet photons using superconducting transition edge sensors,* Applied Physics Letters **73**, 735 (1998).

[214] A. J. Miller, S. W. Nam, J. M. Martinis, and A. V. Sergienko, *Demonstration of a low-noise near-infrared photon counter with multiphoton discrimination,* Applied Physics Letters **83**, 791 (2003).

[215] F. Gay, F. Piquemal, and G. Genevès, *Ultralow noise current amplifier based on a cryogenic current comparator,* Review of Scientific Instruments **71**, 4592 (2000).

[216] S. W. Henderson, J. R. Stevens, M. Amiri, *et al.*, *Readout of two-kilopixel transition-edge sensor arrays for Advanced ACTPol,* in *SPIE Astronomical Telescopes + Instrumentation*, edited by W. S. Holland and J. Zmuidzinas (Edinburgh, United Kingdom, 2016) p. 99141G.

[217] A. Kher, P. K. Day, B. H. Eom, J. Zmuidzinas, and H. G. Leduc, *Kinetic Inductance Parametric Up-Converter,* Journal of Low Temperature Physics **184**, 480 (2016).

[218] S. Doerner, A. Kuzmin, K. Graf, I. Charaev, S. Wuensch, and M. Siegel, *Compact microwave kinetic inductance nanowire galvanometer for cryogenic detectors at 4.2 K,* Journal of Physics Communications **2**, 025016 (2018).

[219] A. Kuzmin, S. Doerner, S. Singer, *et al.*, *Terahertz Transition-Edge Sensor With Kinetic-Inductance Amplifier at 4.2 K,* IEEE Transactions on Terahertz Science and Technology **8**, 622 (2018).

[220] J. Stehlik, Y.-Y. Liu, C. M. Quintana, C. Eichler, T. R. Hartke, and J. R. Petta, *Fast Charge Sensing of a Cavity-Coupled Double Quantum Dot Using a Josephson Parametric Amplifier,* Physical Review Applied **4**, 014018 (2015).

[221] A. B. Pavolotsky, D. Dochev, and V. Belitsky, *Aging- and annealing-induced variations in Nb/Al–AlOx/Nb tunnel junction properties,* Journal of Applied Physics **109**, 024502 (2011).

[222] U. S. Goteti, M. Denton, K. Krause, *et al.*, *Reliability Studies of Nb/AlOx/Al/Nb Josephson Junctions Through Accelerated-Life Electrical Stress Testing,* IEEE Transactions on Applied Superconductivity **29**, 1 (2019).

[223] S. Yanai and G. A. Steele, *Observation of enhanced coherence in Josephson SQUID cavities using a hybrid fabrication approach,* (2019), arXiv:1911.07119 .

[224] A. Wallraff, D. I. Schuster, A. Blais, *et al.*, *Strong coupling of a single photon to a superconducting qubit using circuit quantum electrodynamics,* Nature **431**, 162 (2004).

[225] F. Lecocq, I. M. Pop, Z. Peng, *et al.*, *Junction fabrication by shadow evaporation without a suspended bridge,* Nanotechnology **22**, 315302 (2011).

[226] R. Vijay, J. D. Sau, M. L. Cohen, and I. Siddiqi, *Optimizing Anharmonicity in Nanoscale Weak Link Josephson Junction Oscillators,* Physical Review Letters **103**, 087003 (2009).

[227] O. Kennedy, J. Burnett, J. Fenton, *et al.*, *Tunable Nb Superconducting Resonator Based on a Constriction Nano-SQUID Fabricated with a Ne Focused Ion Beam,* Physical Review Applied **11**, 014006 (2019).

[228] I. C. Rodrigues, D. Bothner, and G. A. Steele, *Coupling microwave photons to a mechanical resonator using quantum interference,* Nature Communications **10**, 5359 (2019).

[229] D. Bothner, I. C. Rodrigues, and G. A. Steele, *Photon-Pressure Strong-Coupling between two Superconducting Circuits,* (2019), arXiv:1911.01262 .

[230] *See Supplemental Material at [URL will be inserted by publisher] for details on device fabrication, device parameters, hysteresis of switching currents, measurement setup, data processing and mathematical derivations.* .

[231] W. J. Skocpol, M. R. Beasley, and M. Tinkham, *Self-heating hotspots in superconducting thin-film microbridges,* Journal of Applied Physics **45**, 4054 (1974).

[232] D. Hazra, L. M. A. Pascal, H. Courtois, and A. K. Gupta, *Hysteresis in superconducting short weak links and μ-SQUIDs,* Physical Review B **82**, 184530 (2010).

[233] N. Kumar, T. Fournier, H. Courtois, C. B. Winkelmann, and A. K. Gupta, *Reversibility Of Superconducting Nb Weak Links Driven By The Proximity Effect In A Quantum Interference Device,* Physical Review Letters **114**, 157003 (2015).

[234] R. L. Kautz and J. M. Martinis, *Noise-affected I-V curves in small hysteretic Josephson junctions,* Physical Review B **42**, 9903 (1990).

[235] A. J. Annunziata, D. F. Santavicca, L. Frunzio, *et al.*, *Tunable superconducting nanoinductors,* Nanotechnology **21**, 445202 (2010).

[236] J. Gao, J. Zmuidzinas, B. A. Mazin, P. K. Day, and H. G. Leduc, *Experimental study of the kinetic inductance fraction of superconducting coplanar waveguide,* Nuclear Instruments and Methods in Physics Research Section A: Accelerators, Spectrometers, Detectors and Associated Equipment Proceedings of the 11th International Workshop on Low Temperature Detectors, **559**, 585 (2006).

[237] C. Eichler and A. Wallraff, *Controlling the dynamic range of a Josephson parametric amplifier,* EPJ Quantum Technology **1**, 2 (2014).

[238] C. Rauscher, V. Janssen, and R. Minihold, *Fundamentals of Spectrum Analysis*, 9th ed. (Rohde & Schwarz, München, 2016).

[239] L. Planat, R. Dassonneville, J. P. Martínez, *et al.*, *Understanding the Saturation Power of Josephson Parametric Amplifiers Made from SQUID Arrays,* Physical Review Applied **11**, 034014 (2019).

[240] M. F. Gely and G. Steele, *QuCAT: Quantum Circuit Analyzer Tool in Python,* New Journal of Physics (2019), 10/ggf2wk.

[241] S. Noschese, L. Pasquini, and L. Reichel, *Tridiagonal Toeplitz matrices: Properties and novel applications,* Numerical Linear Algebra with Applications **20**, 302 (2013).

[242] U. Vool and M. Devoret, *Introduction to quantum electromagnetic circuits,* International Journal of Circuit Theory and Applications (2017), 10/gbn6sw.

[243] R. N. Simons, *Coplanar Waveguide Circuits, Components, and Systems*, edited by K. Chang, Wiley Series in Microwave and Optical Engineering (John Wiley & Sons, Inc., New York, USA, 2001).

[244] R. Kalra, A. Laucht, J. P. Dehollain, *et al.*, *Vibration-induced electrical noise in a cryogen-free dilution refrigerator: Characterization, mitigation, and impact on qubit coherence,* Review of Scientific Instruments **87**, 073905 (2016).

[245] J. M. Kivioja, T. E. Nieminen, J. Claudon, O. Buisson, F. W. J. Hekking, and J. P. Pekola, *Weak coupling Josephson junction as a current probe: Effect of dissipation on escape dynamics,* New Journal of Physics **7**, 179 (2005).

[246] J. Sonntag, J. Li, A. Plaud, *et al.*, *Excellent electronic transport in heterostructures of graphene and monoisotopic boron-nitride grown at atmospheric pressure,* 2D Materials (2020), 10/ggs4pf.

[247] A. A. Adamyan, S. E. Kubatkin, and A. V. Danilov, *Tunable superconducting microstrip resonators,* Applied Physics Letters **108**, 172601 (2016).

[248] F. Chen, J. Li, A. D. Armour, *et al.*, *Realization of a single-Cooper-pair Josephson laser,* Physical Review B **90**, 020506 (2014).

[249] M. C. Cassidy, A. Bruno, S. Rubbert, *et al.*, *Demonstration of an ac Josephson junction laser,* Science **355**, 939 (2017).

[250] E. Toomey, M. Onen, M. Colangelo, B. A. Butters, A. N. McCaughan, and K. K. Berggren, *Bridging the Gap Between Nanowires and Josephson Junctions: A Superconducting Device Based on Controlled Fluxon Transfer,* Physical Review Applied **11**, 034006 (2019).

[251] M. Onen, B. A. Butters, E. Toomey, T. Gokmen, and K. K. Berggren, *Design and characterization of superconducting nanowire-based processors for acceleration of deep neural network training,* Nanotechnology **31**, 025204 (2020).

[252] G. De Simoni, F. Paolucci, P. Solinas, E. Strambini, and F. Giazotto, *Metallic supercurrent field-effect transistor,* Nature Nanotechnology **13**, 802 (2018).

[253] F. Paolucci, G. De Simoni, P. Solinas, *et al.*, *Magnetotransport Experiments on Fully Metallic Superconducting Dayem-Bridge Field-Effect Transistors,* Physical Review Applied **11**, 024061 (2019).

[254] M. D. Fiske, *Temperature and Magnetic Field Dependences of the Josephson Tunneling Current,* Reviews of Modern Physics **36**, 221 (1964).

[255] R. E. Eck, D. J. Scalapino, and B. N. Taylor, *Self-Detection of the ac Josephson Current,* Physical Review Letters **13**, 15 (1964).

[256] D. D. Coon and M. D. Fiske, *Josephson ac and Step Structure in the Supercurrent Tunneling Characteristic,* Physical Review **138**, A744 (1965).

[257] V. M. Krasnov, N. Mros, A. Yurgens, and D. Winkler, *Fiske steps in intrinsic $Bi_2Sr_2CaCu_2O_{8+x}$ stacked Josephson junctions,* Physical Review B **59**, 8463 (1999).

[258] N. Yabuki, R. Moriya, M. Arai, *et al.*, *Supercurrent in van der Waals Josephson junction,* Nature Communications **7**, 10616 (2016).

[259] L. Li, H. Zhang, Y.-H. Yang, and G.-X. Miao, *High-Quality Epitaxial MgB_2 Josephson Junctions Grown by Molecular Beam Epitaxy,* Advanced Engineering Materials **19**, 1600792 (2017).

[260] S. Shapiro, *Josephson Currents in Superconducting Tunneling: The Effect of Microwaves and Other Observations,* Physical Review Letters **11**, 80 (1963).

[261] R. L. Kautz, *Noise, chaos, and the Josephson voltage standard,* Reports on Progress in Physics **59**, 935 (1996).

[262] AC/DC, *Highway to Hell,* (1979).